ANALYSIS OF FULL-SCALE SEA-TRIALS MANOEUVRING DATA AND DEVELOPMENT AND VALIDATION OF A MOTION-SIMULATION MODEL FOR THE AUV "MUN EXPLORER"

MANOJ THOMAS ISSAC

Analysis of Full-Scale Sea-Trials Manoeuvring Data and Development and Validation of a Motion-Simulation Model for the AUV "MUN Explorer"

by

© Manoj Thomas Issac

B. Tech., University of Kerala, India (1999)
M. Tech., Indian Institute of Technology, Madras (2002)

A thesis submitted to the
School of Graduate Studies
in partial fulfillment of the requirements
for the degree of
Doctor of Philosophy

Faculty of Engineering and Applied Science
Memorial University of Newfoundland

September 2011

St. John's Newfoundland

Abstract

Autonomous Underwater Vehicles (AUVs) are free-swimming underwater robots capable of navigating on its own by means of the various sensors it carries onboard. AUVs are rapidly emerging as an important tool in ocean exploration. Designers of AUVs rely increasingly on hydrodynamic models as a design tool particularly for the initial phases of vehicle development. These models allow the designer a means for determining the inherent motion behaviour of a proposed vehicle even before its construction and testing.

The research work addressed in this thesis is aimed at evaluating the performance of a hydrodynamic motion simulation model developed based on the *component build-up method* for torpedo-shaped underwater vehicles. The model is derived in a form that only requires the specification of the vehicle's geometry, and the lift, drag and moment characteristics of its constituent elements: the hull, control surfaces, propulsion system etc. The total hydrodynamic load acting on the vehicle is obtained by summing up the loads from each of these components. Such a model, developed by previous researchers at Memorial University of Newfoundland (MUN) for a streamlined AUV was available for use in this research. However, this model was never validated against experimental data. In order to validate the model and establish the performance envelope it was necessary to test the simulation model against all possible mission scenarios that a typical AUV would encounter. This required an extensive set of manoeuvring data from real vehicles that resembled a wide range of mission scenarios.

The availability of a new *Explorer* class AUV at Memorial University (the *MUN Explorer*) facilitated the performing of a series of free-running manoeuvring trials at sea. This included straight-line tests, turning circles, zigzags in horizontal and vertical planes and helix manoeuvres. The responses of the vehicle to different manoeuvres are reported in detail in this thesis and formed a major portion of this research. This formed a

database, which encompass a range of mission scenarios, against which the simulated response of the vehicle could be compared. Apart from providing a dataset for validation purpose, these manoeuvring trials also provided valuable information on the performance and capabilities of the *Explorer*, which belongs to the class of a large commercial AUV, and is one of the only seven *Explorers* operational around the world to date.

In order to simulate the above manoeuvres, it was necessary to modify the existing hydrodynamic model to one that can capture the specific features of the new AUV – the *MUN Explorer*. A second model of the *MUN Explorer*, with a different tail plane configuration from the original, was also developed to study and compare the control plane actions between the two configurations. The ease with which the model was adapted from one vehicle to another as well as the ease with which the model can be reconfigured exemplifies the overriding advantage of using the *component build-up* method and the generic nature of the hydrodynamic model as well.

A select number of manoeuvres were simulated using one of the models. Preliminary results from the simulation of steady state manoeuvres show reasonable-to-good agreement with the measured data. The vehicle responses to manoeuvring trials, simulation of a few of these manoeuvres and their comparisons and validation are considered to be some of the main contributions made in this research work.

O the depth of the riches both of the wisdom and knowledge of God! how unsearchable are his judgments, and his ways past finding out!

For who hath known the mind of the Lord? or who hath been his counsellor?

Or who hath first given to him, and it shall be recompensed unto him again?

For of him, and through him, and to him, are all things: to whom be glory for ever. Amen

Romans 11: 33 – 36 (KJV)

Thesis Supervisor: **Dr. Neil Bose**
Title: Professor of Maritime Hydrodynamics, Director, Australian Maritime College (AMC) - National Centre for Maritime Engineering and Hydrodynamics, University of Tasmania, Launceston TAS 7250, Australia

Thesis Supervisor: **Dr. Christopher D. Williams**
Title: Senior Research Engineer, National Research Council Canada, Institute for Ocean Technology, St. John's, NL, A1B 3T5, Canada

Thesis Supervisor: **Dr. Ralf Bachmayer**
Title: Associate Professor, Chair for Ocean Technology, Memorial University of Newfoundland, St. John's, NL, A1B 3X5, Canada

Acknowledgements

This thesis would not have been possible but for the grace of God and the support of a number of people.

I would like to express my deepest gratitude to Dr. Neil Bose for providing me with this opportunity, whose relentless support, guidance and encouragement throughout this program tremendously helped me in making it to the finish, while at the same time being tolerant and understanding. I am so grateful to Dr. Christopher D. Williams for his consistent support and guidance throughout this research work. I am indebted to him for the immense amount of time that was spent in discussion and preparation of this thesis. My heartfelt thanks to Dr. Ralf Bachmayer for his persistent encouragement and the help he was in times of need. Above all, I consider myself to be very fortunate to have worked under the guidance of these great people.

I would like to thank the Natural Sciences and Engineering Research Council (NSERC) and the School of Graduate Studies, Memorial University of Newfoundland, for the funding to support this research. It is my pleasure to thank all the colleagues at the Marine Environmental Research Lab for Intelligent Vehicles (MERLIN) of Memorial University who made this thesis possible; especially Sara Adams, Moqin He, Haibo Niu, Ron Lewis and Peter King. A special thanks goes to the National Research Council's, Institute for Ocean Technology for providing me the office space, library facilities, technical support and access to their facilities throughout this research. Thanks are also due to International Submarine Engineering Ltd. (ISE), Vancouver, BC, for their technical support and advice in times of need.

There were several teachers and friends who played a crucial role in guiding me to embark on this journey; in particular I want to pay my regards to dear friends, Dr. Vinu

Unnithan and Dr. Santhosh Sathyapal who were instrumental in changing the course of my life and encouraged me to fulfill my dreams. Sweet memories shared with and nice ambiences provided by friends in St. John's are unforgettable. I shall also never forget the support and endless love extended to me by the Swamidas's.

Words do not suffice to express my devotion and gratitude to my parents and brother who have been a constant source of inspiration throughout my life and have always encouraged me to go for a long innings in my academic pursuits. I do thank my parents-in-law and brother-in-law for having faith in me, for their support and for the beautiful people they are. Last but not least, I am indebted to my wife, Jenny, and son, David, for their support, prayers, joy and comfort they have been and also for their understanding.

Table of Contents

List of Figures

List of Tables

List of Symbols

A	Angle of attack of the hull
A_{CP}	Reference area (planform) of the control planes
A_p	Planform area of the hull
A_{po}	Planform area of the hull from the nose to the station x_0
A_{ref}	Reference area (general use)
a_e	Effective aspect ratio of a control plane
B	Buoyant force vector
B	Magnitude of buoyancy force
b_{CP}	Control plane span
C_A	Axial force coefficient
CB	Centre of buoyancy of the vehicle
C_{DB0}	Drag coefficient of the bare hull at zero angle of attack
C_{Dc}	Crossflow drag coefficient (general use)
$C_{DF(\alpha=0)}$	Fore-drag coefficient at zero angle of attack
CE	Centre of effort (for the hull)
CG	Center of gravity of the vehicle
C_l, C_d	2-D lift and drag coefficient (general use)
C_L, C_D,	Lift and drag coefficient (general use)
C_M	Moment coefficient (general use)
C_N	Normal force coefficient
CP	Centre of pressure (for the control planes)

c	Chord length of the control plane
D_p	Diameter of the propeller
f_N	Normal force on the hull at a particular station along the length
$\boldsymbol{F}$	Force vector, $\boldsymbol{F} = [X\,Y\,Z]^{\mathrm{T}}$
$\boldsymbol{F}_C$	Control forces
$\boldsymbol{F}_E$	Environmental forces
$\boldsymbol{F}_I$	Ideal fluid forces – 'Added Mass'
$\boldsymbol{F}_R$	Real fluid forces – 'Damping'
$\boldsymbol{F}_S$	Static (hydrostatic) forces – weight and buoyancy
$\boldsymbol{F}_H, \boldsymbol{G}_H$	Total hydrodynamic forces and moments
$\boldsymbol{F}_S, \boldsymbol{G}_S$	Total hydrostatic forces and moments
F_{xFins}, F_{yFins}, F_{zFins}	External forces acting on the fins along the three axis x, y and z, respectively
F_{xHull}, F_{yHull}, F_{zHull}	External forces acting on the hull along the three axis x, y and z, respectively
F_{xProp}, F_{yProp}, F_{zProp}	Forces generated by the propeller acting along the three axis x, y and z, respectively
f_L	Lift force on the hull at a particular station along the length
f	fineness ratio
$f_{CD,}$	A scale factor to convert 2D drag data into 3D drag data for control planes
$\boldsymbol{G}$	Moment vector, $\boldsymbol{G} = [K\,M\,N]^{\mathrm{T}}$
G_{xFins}, G_{yFins}, G_{zFins}	External moments acting on the fins about the three axis x, y and z, respectively
G_{xHull}, G_{yHull}, G_{zHull}	External moments acting on the hull about the three axis x, y and z, respectively
G_{xProp}, G_{yProp}, G_{zProp}	Forces generated by the propeller acting along the three axis x, y and z, respectively
$\mathbf{I}_3$	Identity matrix of the order (3 x 3)

$\mathbf{I}$	Inertia tensor
I_x, I_y, I_z	Moments of inertia about the x_B, y_B and z_B axis respectively
I_{xz}, I_{yz}, I_{xy}	Products of inertia about the x_B-y_B, y_B-z_B and z_B-x_B axis respectively
$\boldsymbol{J}_1$	Matrix to transform the translational velocity from body-fixed frame to the Earth-fixed reference frame
$\boldsymbol{J}_2$	Matrix to transform angular velocity from body-fixed frame to Earth-fixed reference frame
$\boldsymbol{J}_1^T$	Transpose of the matrix, $\boldsymbol{J}_1$
$\boldsymbol{J}_1^{-1}, \boldsymbol{J}_2^{-1}$	Inverse of the matrices, $\boldsymbol{J}_1$ and $\boldsymbol{J}_2$
J	Advance ratio
K, M, N	Moments acting about the three coordinate axes x, y and z respectively
K_Q	Torque coefficient for the propeller
K_T	Thrust coefficient for the propeller
k'	Rotational added mass coefficient
k_1, k_2	Longitudinal and transverse added mass coefficient, respectively
L	Length of the hull
L_{ref}	A reference length (general use)
$\mathcal{L}, \mathcal{D}$	Lift and drag forces acting on a body (general use)
$\mathcal{L}_H, \mathcal{D}_H$	Lift and drag forces on the hull
$\mathcal{L}_{HCP}, \mathcal{D}_{HCP}$	Lift and drag forces on the horizontal control plane
$\mathcal{L}_{VCP}, \mathcal{D}_{VCP}$	Lift and drag forces on the vertical control plane
LOA	Overall length of the vehicle
m	Wet mass of the vehicle
$\mathbf{M_A}$	Augmented apparent mass matrix
n	Propeller revolutions per second (RPS)
n_a	Propeller RPM during the acceleration phase

n_d	Propeller RPM during the deceleration phase
p, q, r	Roll, Pitch and Yaw rates, respectively
$\dot{p}, \dot{q}, \dot{r}$	Angular acceleration in the body-fixed frame
Q	Torque developed by the propeller
q_0	Free-stream dynamic pressure
$\boldsymbol{R}_{x,\phi}$	Principal rotation matrix describing a rotation angle of ϕ about the x-axis
$\boldsymbol{R}_{y,\theta}$	Principal rotation matrix describing a rotation angle of θ about the y-axis
$\boldsymbol{R}_{z,\psi}$	Principal rotation matrix describing a rotation angle of ψ about the z-axis
R	Radius of turn (general usage)
R	Resistance of the vehicle to motion through a fluid (general use)
R_{BH}	Resistance of the bare hull to motion through a fluid
R_{CP}	Resistance of the control plane to motion through a fluid
$\mathrm{R_a}$	Actual radius of turn measured from experiments
$\mathrm{R_c}$	Commanded radius of turn
Re_n	Cross-flow Reynolds Number
$\mathrm{R_{sim}}$	Simulated radius of turn
$\mathbf{r}$	An arbitrary vector
$\boldsymbol{r}_{CE}$	Position vector of the centre of effort (hull) from the origin of the body-fixed frame
$\boldsymbol{r}_{CP}$	Position vector of the centre of pressure (control plane) from the origin of the body-fixed frame
r'	Nondimensional turning rate
r_x	Hull radius at station x along the length
r_{x0}	Hull radius at station x_0 along the length
$\mathbf{S}$	Augmented matrix of rigid-body coupling coefficients

$\mathbf{S}(\mathbf{v}_2)$	A skew-symmetric matrix representing the cross product of $\mathbf{v}_2 \times \bullet$
S	Cross-sectional area of the hull
S_b	Cross-sectional area at the base of the hull
S_{x0}	Cross-sectional area of the hull at station x_0
$\boldsymbol{T}$	Transformation matrix from body-fixed to Earth-fixed reference frame
T	Thrust developed by the propeller
T_0	Drag of the vehicle at the initial equilibrium velocity, V_0
t	Thrust deduction factor
u, v, w	Translational velocities (surge, sway and heave) in body-fixed reference frame, respectively
$\dot{u}, \dot{v}, \dot{w}$	Linear acceleration in the body-fixed frame
u_{CE}, v_{CE}, w_{CE}	Components of velocity at the centre of effort of the hull along the body-fixed axes
u_{CP}, v_{CP}, w_{CP}	Components of velocity at the centre of pressure of the control plane
u_{tp}, v_{tp}, w_{tp}	Translational velocities of flow in the 'X' tail coordinate axes system.
V_0	Approach speed of the vehicle
V_0	Initial equilibrium velocity
V	Velocity (scalar)
V_a	Average inflow speed to the propeller
V_{acc}	Forward speed of the vehicle at a given propeller RPM during the acceleration phase
V_B	Volume of the body (hull)
$V_{CE,}$	Magnitude of velocity at the centre of effort of the hull
V_{CP}	Magnitude of velocity at the centre of pressure of the control plane

V_{dec}	Forward speed of the vehicle at a given propeller RPM during the deceleration phase
v_c	In-line current velocity
$\mathbf{W}$	Weight force vector
W	Magnitude of weight force
X, Y, Z	Forces acting along the three coordinate axes x, y and z respectively
X_{cg}, Y_{cg}, Z_{cg}	Location of the centre of gravity of the vehicle with respect to an arbitrary Earth-fixed frame
X_E, Y_E, Z_E	Coordinate axis of the Earth-fixed reference frame
$X_{HCP}, Y_{HCP}, Z_{HCP}$	Total force on the horizontal control plane in the body-fixed axes
$X_{VCP}, Y_{VCP}, Z_{VCP}$	Total force on the vertical control plane in the body-fixed axes
x, y, z	Coordinate axis of the body-fixed reference frame
x_B, y_B, z_B	Position of centre of buoyancy from the origin of the body-fixed frame
x_{CE}, y_{CE}, z_{CE}	Distance of the centre of effort from the centre of mass in the body-fixed frame
x_{CP}, y_{CP}, z_{CP}	Distance of the centre of pressure of the control plane from the centre of mass in the body-fixed frame
x_E, y_E, z_E	Coordinates of the position of the CG of the vehicle in the Earth-fixed frame
$\dot{x}_E, \dot{y}_E, \dot{z}_E$	Rate of change of position of the vehicle or translational velocities in the Earth-fixed frame
x_G, y_G, z_G	Position of centre of gravity of the vehicle from origin of the body-fixed frame
x_{tp}, y_{tp}, z_{tp}	Coordinate axes of the 'X' tail control planes oriented at 45° to the body-fixed axes.
x_0	Hull station up till which the potential theory is valid
x_1	Hull station where the rate of change of cross-sectional area first reaches its maximum negative value
x_{ac}	Aerodynamic force centre measured from the tip of the nose

x_{CE}	Distance to the hydrodynamic centre from the centre of gravity
x_m	Longitudinal distance of pitching moment centre from the nose
x_p	Distance from the nose to the centroid of the plan-form area
Y_0, Z_0	Amplitude or width-of-path of the horizontal and vertical zigzag trajectory respectively
α, α'	Angle of attack
β, β'	Angle of side-slip
ΔR	Difference between actual radius of turn and commanded radius
ΔV	Difference in speeds (V_{acc} - V_{dec}) of the vehicle for the same propeller RPM
δ_1, δ_2	Deflection angles of the *MUN Explorer* AUV dive planes
$\delta_3, \delta_4, \delta_5, \delta_6$	Deflection angles of the *MUN Explorer* AUV tail planes
δP_D	Effective control plane angle representing the combined effect of the two dive planes in producing pitch motion
δR_D	Effective control plane angle representing the combined effect of the two dive planes in producing roll motion
δR	Effective control plane angle representing the combined effect of the four tail planes in producing roll motion
δP	Effective control plane angle representing the combined effect of the four tail planes in producing pitch motion
δY	Effective control plane angle representing the combined effect of the four tail planes in producing yaw motion
δ_{HCP}	Deflection of the horizontal control plane
δ_{VCP}	Deflection of the vertical control plane
Φ	Hull role angle
Φ_B	Angle by which the coordinate axis of the 'X' planes is oriented with respect to the body-fixed axis
ϕ, θ, ψ	Euler angles- Roll, Pitch and Yaw, respectively

$\dot{\phi}\ \dot{\theta}\ \dot{\psi}$.	Rate of angular displacements in the Earth-fixed frame
η_0	Propeller open-water efficiency
η	Ratio of cross-flow drag coefficient for a body of finite fineness ratio to that for a body of infinite fineness ratio
$\boldsymbol{\eta}$	Vector representing the position and orientation of the vehicle expressed in the inertial reference frame, $\boldsymbol{\eta} = [\boldsymbol{\eta}_1, \boldsymbol{\eta}_2]^T$
$\boldsymbol{\eta}_1$	Position of the CG of the vehicle in the inertial reference frame $\boldsymbol{\eta}_1 = [x_E, y_E, z_E]^T$
$\boldsymbol{\eta}_2$	Orientation of the vehicle in the inertial reference frame $\boldsymbol{\eta}_2 = [\phi, \theta, \psi]^T$
$\dot{\boldsymbol{\eta}}_1$	Vector representing the translational velocities in the Earth-fixed frame, $\dot{\boldsymbol{\eta}}_1 = [\dot{x}_E \quad \dot{y}_E \quad \dot{z}_E]^T$
$\dot{\boldsymbol{\eta}}_2$	Vector representing the rate of angular displacements in the Earth-fixed frame, $\dot{\boldsymbol{\eta}}_2 = [\dot{\phi} \quad \dot{\theta} \quad \dot{\psi}]^T$
$\boldsymbol{\nu}$	Vector representing the translational and rotational velocities in the body-fixed frame, $\boldsymbol{\nu} = [\boldsymbol{\nu}_1, \boldsymbol{\nu}_2]^T$
$\boldsymbol{\nu}_1$	Vector of translational velocities along the body-fixed axes, $\boldsymbol{\nu}_1 = [u\ v\ w]^T$
$\boldsymbol{\nu}_2$	Vector of angular velocities about the body-fixed axes, $\boldsymbol{\nu}_2 = [p\ q\ r]^T$
$\boldsymbol{\nu}_{CE}$	Velocity vector at the centre of effort in body-fixed frame, $\boldsymbol{\nu}_{CE} = [u_{CE}\ v_{CE}\ w_{CE}]^T$
$\boldsymbol{\nu}_{CP}$	Velocity vector at the centre of pressure in body-fixed frame, $\boldsymbol{\nu}_{CP} = [u_{CP}\ v_{CP}\ w_{CP}]^T$
$\dot{\mathbf{v}}_1, \dot{\mathbf{v}}_2$	Linear and angular acceleration vectors in the body-fixed axes
ρ	Density of the fluid
ω	Taylor wake fraction

List of Abbreviations

AHRS	Attitude Heading Reference System
ARCS	Autonomous Remotely Controlled Submersible
ASE	Analytical and Semi-Empirical Method
AUG	Autonomous Underwater Glider
AUV	Autonomous Underwater Vehicle
BAUV	Biomimetic Autonomous Underwater Vehicle
CBM	Component Build-up Method
CSCOUT	Canadian Self-Contained Off-the-shelf Underwater Testbed
DATCOM	DATa COMpendium
DVL	Doppler Velocity Log
GPS	Global Positioning System
IOT	Institute for Ocean Technology
ISE	International Submarine Engineering
MUN	Memorial University of Newfoundland
NRC	National Research Council, Canada
ROV	Remotely Operated Vehicle
UUV	Unmanned Underwater Vehicle

Chapter 1

Introduction

Autonomous Underwater Vehicles (AUVs) are self-propelled robotic platforms that can perform a predefined mission completely unmanned while spending all or part of their duty cycle(s) submerged. Autonomous Underwater Vehicles (AUVs) are one of the two categories of vehicles that belong to a generic group called Unmanned Underwater Vehicles (UUVs), the other being Remotely Operated Vehicles (ROVs). While an AUV performs a mission without being constantly monitored or supervised by a human operator, an ROV requires continuous instructions from a human operator via tethered cable or acoustic link.

1.1 Applications of Autonomous Underwater Vehicles

The commercial potential of UUVs was not recognized until the discovery of offshore oil and gas supplies in the North Sea. Since then, ROVs have been extensively used throughout the offshore industry, whereas in both military and commercial sectors, the usage of AUVs was limited. However, the need to operate and explore extreme depths in hostile environments, prompted by the offshore industry and the quest for deep oceans research has heightened the development of AUV technology. Further, the scientific demand for high-resolution spatial and temporal ocean observation data is increasing. A number of oceanographic problems require quality data acquisition without disturbing the ocean environment. Ship-borne methods can introduce errors in measurements due to the disturbance caused by towed instrument packages, samplers or by the ship itself. The potential of AUV technology in undersea surveys and the significant improvement in the quality of data acquired using these platforms, compared to the traditional ocean observation platforms like ships and buoys, is gradually being recognized as a replacement for conventional ship-borne methods.

Autonomous Underwater Vehicle technology is an area of rapid development and the capabilities of these vehicles increased significantly over the past two decades. Operational ranges have gone up to hundreds of kilometres and depth ranges have extended to 6000 m, making most of the ocean depths (about 97%) accessible worldwide [MacNaughton, 2005]. In the case of certain AUVs belonging to the class of gliders the operational ranges have exceeded 3000 km [Griffiths *et al*, 2007]. The development of AUVs has potential application in scientific, industrial and military sectors, thus taking humans out of water [Griffiths, 2003]. The potential applications of AUVs range from hydrographic and sub-bottom surveys, environmental monitoring, iceberg profiling, mine reconnaissance, cable laying, cable/pipeline inspection, to name a few. The ocean research done well with AUVs today are mid-water transects, geophysical surveys and physical oceanographic missions in the upper water column [Sibenac *et al*, 2004]. In hostile weather conditions where surface operations are unsafe; in regions covered by ice where deployment of manned submersibles are risky and tethered vehicles are of limited use, AUVs hold the best promise for freely working on the seafloor and collecting spatial datasets. AUVs have already been used for under ice applications such as laying cables [Butler & Hertog (1993), Ferguson (2003)] and surveying the underside of ice [Yeo, 2008]. Theseus was the largest AUV built and held the record for the longest AUV mission – 440 km, all of which was under-ice. It was deployed in the Arctic in 1995 and 1996 for laying fibre-optic cables up to 220 km [Ferguson, 1998]. In the recent years, the capability of doing unsupervised AUV mission in ice-covered areas has advanced significantly [Ferguson, 2009]. Crees *et al*, (2010) reports the successful deployment of National Resources Canada's (NRCan) *Arctic Explorer* in the Canadian high Arctic (~ 79° N, 115° W) in March/April 2010. The AUV spent 10 days completely under ice before being successfully recovered. During this period, the AUV accomplished close to 1000 km of under-ice survey while transiting at an average speed of 1.5 m/s at an altitude of 130 m above the seabed and reaching depths of over 3160 m. This was reported as a major technological feat as the *Arctic Explorer* conducted the longest ever completely under-ice AUV mission in such a challenging environment [Tam *et al*, (2011)].

Mission requirements dictate the assembly of an array of components – sensor packages, navigation units, batteries, payloads, to be carried on-board the AUV, which in turn determine the size of the envelope while the energy storage requirements and ease of construction define its shape.

1.2 Classification of Autonomous Underwater Vehicles

Autonomous underwater vehicles are now being developed by a wide range of organizations for an almost wider range of tasks. According to the information published in *Jane's Underwater Technology* (Fennel, 2007), there were over 200 different types of vehicles built to date then. It will be difficult to classify them into distinctly different groups as several of them have overlapping features. However, a broad classification based on their role and shapes are as follows:

1.2.1 Classification based on role

The most apt method of classification is that based on the three distinct but overlapping roles for AUVs:

a) *Research AUVs*
b) *Industrial AUVs and*
c) *Military AUVs*

It is likely that some AUVs conceived and designed for one role will be used in other roles. For these AUVs, their classification may be considered as 'dynamic'. As per the "*Recommended Code of Practice*" [Brown *et al*, 2000], published by the *Society of Underwater Technology*, the three different classes have significantly different access rights in the legally recognised range of maritime boundaries.

1.2.2 Classification based on shape

The hydrodynamic form of the AUV determines the propulsion energy required, as well as stability and manoeuvrability at various operating speeds. The most common shapes among them are:

a) The *torpedo shape*: is mainly cylindrical with a hemispherical or semi-ellipsoidal nose and a long tapering after body. Autosub, Explorer, REMUS, GAVIA, Odyssey Class III-Caribou are some examples of torpedo-shaped AUVs (see Figure 1.1).

b) The *low-drag shape*: has a varying diameter lengthwise starting with a nearly semi-elliptical forebody and afterbody tapering to a point. HUGIN 3000, Odyssey II series are examples of low-drag shaped (see Figure 1.2).

c) The *flatfish type*: is another set of vehicles that have a flat rectangular hull. Vehicles like NPS ARIES, CETUS, PHOENIX, ATLAS MARIDAN, are some examples of this shape, which are currently in use (see Figure 1.3).

Explorer **Autosub**

Fig. 1.1 Torpedo-shaped AUVs

HUGIN 1000 AUV **Odyssey Class II**

Fig. 1.2 Low drag shaped AUVs

Maridan MARTIN AUV

NPS AUV

Fig 1.3 Flat fish-type AUVs

There are two other classes of streamlined underwater vehicles that add themselves to the fleet of AUVs but differ from the conventional type of AUVs by means of their propulsion system. They are the Autonomous Underwater Gliders (AUGs) and Biomimetic Autonomous Underwater Vehicles (BAUVs). Gliders are buoyancy driven vehicles propelled by changes in buoyancy while moving in a saw-tooth shaped gliding trajectory. This class of vehicles are distinguished by four inter-related operating characteristics: the use of buoyancy propulsion, a saw-tooth operating pattern, long duration and relatively slow operating speed, [Davis *et al,* (2003), Bachmayer *et al*, (2006)]. Some of the gliders that are currently in operation are the *Slocum* glider, *Seaglider*, *Spray* etc (see Figure 1.4). On the other hand, biomimetic AUVs are those that mimic fish-like motions thereby replacing the conventional propulsion system powered by rotary propellers. Draper Laboratory's Vorticity Control Unmanned Undersea Vehicle (VCUUV), in Figure 1.5, for instance, is the first mission-scale autonomous underwater vehicle that uses vorticity controlled propulsion and manoeuvring, which was modelled by mimicking the morphology and kinematics of a large yellowfin tuna [Anderson & Kerrebrock, 2004].

Spray glider   ***Slocum*** glider

Fig. 1.4 Autonomous Underwater Gliders (AUGs)

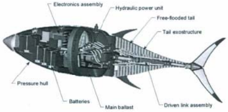

Fig. 1.5 Draper Laboratory's VCUUV – A biomimetic AUV

Apart from the above-mentioned shapes, there are also slow speed AUVs which look like ROVs. These are generally called work-class AUVs and can be classified into two: Intervention AUVs and Inspection AUVs. Both classes of vehicle are slow speed, hovering type AUVs and hence do not necessarily possess a streamlined body. Moreover, an intervention AUV would normally be equipped with manipulator arms unlike an inspection AUV. A few of the AUVs today, which are equipped with manipulators are SAUVIM (Semi Autonomous Underwater Vehicle for Intervention Mission) and ALIVE (AUV for light interventions on deepwater subsea fields) etc.

However, due to limited on-board power, the manipulator arms preferred for intervention AUVs are energy-efficient electrically actuated arms rather than electrohydraulic arms found in intervention ROVs [Marani, *et al*, 2006]. Figure 1.6 shows a couple of examples of intervention AUVs.

SAUVIM AUV
University of Hawaii

ALIVE AUV
Cybernetics, France

Fig. 1.6 Intervention AUVs

A streamlined body is characteristic of a long range cruising type or survey-class AUV. This is essential for reducing the fluid drag and consequently the energy requirement for propulsion. As a result, a good number of cruising type AUVs in operation today are streamlined and also axisymmetric. The discussions that follow in this thesis focus only on axisymmetric streamlined underwater vehicles.

Bane and Ferguson (1987) evaluated the performance characteristics of two of the above streamlined shapes (*torpedo shape* and *low-drag shape*) to obtain the effects of shape on performance and their relative merits and demerits. For the two shapes presented by them, the weight and volume occupied by the payload and all subsystems, other than propulsion and energy, were the same. The low drag and hence the less power required, plus the low structural weight are the advantages of a *low-*

drag shaped vehicle, while constraints like fixed shape, requirement for a docking cradle and costlier fabrication constitute the difficulties. On the other hand, the ease of fabrication of a cylindrical section and feasibility of modular interchange outweigh the demerits like increased drag, structural weight and greater radius-of-turn for a *torpedo-shaped* vehicle. The scope of this thesis is centred on *torpedo-shaped* vehicles which are characterized by a parallel mid-body section having a semi-ellipsoidal nose section attached forward of it and a faired tail section attached to its aft end.

1.3 Methods of Modelling Vehicle Dynamics

Simulation of subsea vehicles in the time domain has been used for many years as a way to predict motions of these vehicles in advance of prototype trials. The development started in the 1940s with the need to predict the motions of naval submarines in the design phase [Kalske, 1992]. Important factors to be studied were operating limits, the establishment of valid control strategies, and the ability to perform prescribed manoeuvres as effectively as possible. The design of motion controllers, the training of vehicle operators and even aspects of mission planning and the development of tactics all rely upon realistic simulation of the underwater vehicle.

A dynamics model based on theory and empirical data is often built to characterise the behaviour of a vehicle, which in turn provides an efficient platform for vehicle control system development. The standard submarine equations of motion derived by Gertler & Hagen (1967) and later revised by Humphreys (1976) and Feldman (1979) offer a general framework for the development of the vehicle equations of motion. The dynamics of the vehicle are represented by six equations, one for each degree of freedom. Hydrodynamic coefficients are commonly used to characterize the vehicle response. These are coefficients that quantify the forces on the vehicle as a function of its attitude and motion. The use of hydrodynamic coefficients in a simulation can provide very realistic results, as long as the coefficients are accurately determined.

The hydrodynamic forces and moments that enter into the equations of motion for an underwater vehicle as coefficients are usually classified into three general categories: static, rotary and acceleration [Gertler, 1972]. The *static* coefficients are due to the components of linear velocity of the body relative to the fluid; the *rotary* coefficients are due to components of angular velocity. The *static* and *rotary* coefficients are primarily due to viscous flow and these velocity-dependent terms can be treated as damping effects. The *acceleration* coefficients, on the other hand, are due to either linear or angular acceleration components and can be interpreted as the added mass of the vehicle. Within limited ranges, the coefficients may vary linearly with respect to the appropriate variable, and thus may be utilized as *static*, *rotary* and *acceleration* derivatives in linearized equations of motion for the purpose of establishing the stability of the vehicle.

The uncertainty involved in the determination of hydrodynamic coefficients of a given vehicle introduces error into the final simulation result. A number of methods are available for the determination of the hydrodynamic coefficients and Goheen (1991) gives an overview of some of these. They tend to fall into one of the following two broad categories:

1.3.1 Test-based methods

a) Conventional Captive Model Testing

The simplest experiments involve holding the model at a fixed position and attitude below a towing carriage. Towing the model in this manner produces data from which the *static coefficients* can be determined.

A Rotating Arm device can hold the model at a fixed radius and attitude below an arm that rotates at a constant angular speed. Towing the model in this manner produces data from which the *rotary coefficients* can be determined. One disadvantage of the rotating arm is that the persistence of the wake produces a non-quiescent flow condition through which the model must pass, beyond the first revolution of the arm.

The Planar Motion Mechanism (PMM) can also be used to force the model to move along an arc-of-a-circle, or, along a sinusoidal or zigzag trajectory. Towing the model in this manner produces data from which the *rotary coefficients* can be determined. The model attitude can be set so that the longitudinal axis of the model is tangent to the trajectory, or the model can be set at a particular drift angle to the trajectory. One disadvantage of the PMM is that the arcs of a circle are of short length; so much less data per run can be collected compared to using a rotating arm device.

For the *acceleration coefficients*, the PMM can in theory be used to accelerate the model in the surge and sway directions, and to accelerate the model in the yaw sense. However, the limits on the acceleration available from the towing carriage and from the actuators within the PMM make this approach difficult or not practical. Since potential flow methods have shown to provide good estimates of the hydrodynamic loads, often referred to as "added-mass" and "added-inertia" effects, it is preferable to use such numerical methods to obtain the "acceleration" coefficients.

b) Free-Swimming Test Approach

One of the possibilities for evaluating the manoeuvring capability of a subsea vehicle is to perform model tests with a self-propelled physical scale-model in a water tank. This will focus on making a preliminary characterization of the vehicle's manoeuvring performance. System Identification (SI) methods can be used for modelling the dynamic performance from the experimental data. In system identification problems or inverse problems, the fundamental properties of the system are to be determined from observed behaviour of that system, obtained using a free-swimming (self-propelled) physical model. Some experiments are performed on the system; a mathematical model is then fitted to the recorded motion data by assigning suitable numerical values to its parameters.

SI modelling trials are reasonably accurate compared to other modelling methods and require less effort at the experimental stage, as they dispense with the need for a towing tank and PMM. However, an overriding disadvantage of the test-based methods is that they require a scale model of the vehicle to be built.

1.3.2 Predictive methods

Predictive methods offer an attractive alternative to test-based methods when the vehicle is still in its design stages, or when costs prohibit a full-scale or model-scale testing program. Predictive methods are most likely to yield good results when applied to streamlined vehicles since their behaviour can perhaps be more easily predicted.

vehicle dynamics model with a different tail plane configuration was also developed. This second model with '+' tail planes were used to simulate some manoeuvres performed by the original vehicle with 'X' tail planes, in an attempt to study if there is a possible way of mapping the 'X' tail planes action to '+' tail planes action.

1.5 Organization of the Thesis

The research work reported in this thesis is organized into chapters that describe each important portion of the work in detail – hydrodynamics model of the AUV, experimental set-up and vehicle features, manoeuvring trials and data analysis, development and modification of hydrodynamics model, simulation results and the general conclusions. Further, each chapter consists of a brief introduction to the main body of its content and finishes with a summary of its content.

Chapter 2 describes the mathematical model developed using the component build-up method. It also gives a review of literature on some of the work done on AUVs using the described method. It ends with a summary highlighting the need for experimental data from real vehicles for validation of the hydrodynamic model.

Chapter 3 describes the experimental vehicle and the experimental set-up used for this research work. It introduces the *MUN Explorer* AUV and describes its features and the various methods and measures adopted to accomplish the task of performing the manoeuvring experiments.

Chapter 4 presents a detailed analysis of all the different types of manoeuvres that were performed at sea using the *MUN Explorer* AUV. The different manoeuvres that were performed include straight-line tests or acceleration-deceleration tests, turning circles, horizontal and vertical zigzags and helix manoeuvres. Results and observations from data analysis of all these manoeuvres are presented in this chapter, which forms a major portion of this thesis and is considered to be a major contribution of the thesis.

Chapter 5 describes the simulation model modified specifically to capture the geometric features of the *MUN Explorer* AUV. It focuses on sections of the hydrodynamic model that have undergone major changes, particularly to accommodate the geometric and inertial parameters and the dynamics of the control planes arranged in an 'X' tail configuration.

Chapter 6 presents a set of simulations that were performed and compares the simulation results with the measured results from experiments in an effort to evaluate the performance of the hydrodynamic model. Only a small subset of the actual tests has been simulated and presented in this thesis.

Chapter 7 highlights the conclusions arrived at from the above research work, emphasizing the major contributions of this thesis and at the same time laying out recommendations for some future works.

A portion of the work contained in this thesis has already been peer-reviewed and published in open literature, the list of which is presented at the end of Bibliography.

Chapter 2

The Vehicle Dynamics Model

The design and development of an Autonomous Underwater Vehicle (AUV) is a very complex and expensive task. The designers of AUVs, therefore, increasingly rely on computer models as a design tool to develop the vehicle geometry and controllers. A reliable model is one that can predict or simulate the behaviour of a vehicle realistically and such a model would greatly reduce the need for an often expensive, lengthy and risky process of prototype testing and therefore be particularly advantageous during the initial phases of vehicle design and development. However, one of the major challenges in creating such a computer model is that the vehicle dynamics must be accurately represented.

The vehicle dynamics model constitutes only one of a number of elements that makes up a typical AUV simulation environment; some others being a controller, a mission planner, a collision detection module etc [Brutzman *et al.*, 1992]. The function of the vehicle dynamics model is to represent the vehicle's interaction with the surrounding fluid in which it operates. The dynamics model described throughout this chapter is based on the *component build-up* method that was originally developed by Nahon (1996) for the ARCS AUV and later adapted to the Canadian Self-Contained Off-the-shelf Underwater Testbed or the C-SCOUT AUV. The C-SCOUT is a streamlined AUV designed and built by the graduate students at Memorial University of Newfoundland and work term students employed by the National Research Council's Institute for Ocean Technology (formerly known as the Institute for Marine Dynamics). Details regarding the design, construction and preliminary testing of the C-SCOUT AUV can be found in Curtis *et al* (2000), Curtis (2001a) and Curtis *et al* (2001b).

In order to characterise the motion of the physical vehicle, a dynamics model based on the *component build-up* or the *body build-up* method of Nahon (1996) was developed by Perrault (2002) and Evans (2003) using MATLAB™ and SIMULINK™. This Simulink model is a modular, non-linear model based on the Newton-Euler equations of motion. Conventionally, the forcing functions in the Newton-Euler equations of motion are written as a Taylor Series Expansion. This requires the physical model testing of the vehicle in order to determine the coefficients of the Taylor Series Expansion, otherwise known as the hydrodynamic derivatives. The model developed for C-SCOUT by Perrault (2002) and Evans (2003) and described through this chapter is also based on the Newton-Euler equations of motion but the forcing function, in this case, is constructed from lift, drag and moments acting on various components of the vehicle derived from analytical and semi-empirical (ASE) relations that only require specification of vehicle geometry. The lift and drag forces are then applied to the centre of pressure of each component and the overall force is obtained by summing up the individual contributions; hence the name *component build-up* method. The advantage of this method is that the forces acting on the components can, for the most part, be determined from semi-empirical expressions. However, this approach needs to be verified and validated against full-scale test results. Another advantage of this hydrodynamic model is that it can be easily adapted to vehicles of similar shape (streamlined axisymmetric) as will be seen in later chapters where this model was modified to simulate the manoeuvres performed by a similar (axisymmetric) but different (in size) vehicle – the *MUN Explorer* AUV. The scope of this research was to validate this simulation model against experimental results obtained from full-scale manoeuvring trials.

This chapter is aimed at describing the dynamics and hydrodynamics that underlies the motion simulation model of an axisymmetric streamlined underwater vehicle that is built based on a *component build-up* method. A review of literature on the hydrodynamic modelling of underwater vehicles using the component build-up method is also presented at the end of this chapter.

2.1 Dynamics and Hydrodynamics

One of the important aspects of modelling vehicle dynamics is to predict the trajectory of the vehicle in space: the position and orientation of the vehicle with respect to time. An underwater vehicle moving in 3D space has six degrees of freedom (DOF) and therefore six independent coordinates are necessary to determine the position and orientation of the vehicle. The first three coordinates, $\boldsymbol{\eta}_1 = [x_E, y_E, z_E]^T$, and their time derivatives describe the position and translational motion along x, y and z-axes, while the last three coordinates, $\eta_2 = [\phi, \theta, \psi]^T$ and their time derivatives describe the orientation and rotational motion of the vehicle. The six degrees of motion, for a marine vehicle, are defined as: *surge, sway, heave, roll, pitch* and *yaw* (see Fig. 2.1).

2.1.1 Frames of Reference

The motion of a body in space subjected to external forces is governed by Newton's Second Law of Motion. However, Newton's laws are valid only in a non-accelerating frame of reference, often called a Newtonian or inertial frame. What constitutes an inertial frame depends on the physical and temporal scale of the problem being addressed. The only way to define an inertial frame is that it is a frame of reference attached to one or more physical bodies of a scale much larger than the problem under study, and such that the Second Law of Motion applies to an acceptable degree of accuracy for motion of a body with respect to this frame [McGhee *et. al,* 2000].

A commonly used inertial coordinate system is the local "flat Earth" system with an arbitrarily selected point on the surface of the Earth as its origin. This is a good approximation since the motion of the Earth hardly affects low speed undersea vehicles and so the acceleration of a point on the surface of the Earth is usually neglected. Therefore, as long as the vehicle speed relative to the Earth is far below orbital velocity, an Earth-fixed reference frame can be considered to be inertial. Normally, the inertial frame has its coordinate axes X_E, Y_E and Z_E directed in the local north, east and down directions respectively.

In modern physics, the very concept of motion cannot be defined except as the "relative displacement" of one body with respect to another. Therefore, in order to represent a vehicle's motions as well as its position and orientation a second reference frame is required: one which moves with respect to the inertial frame. This moving frame of reference is conveniently fixed to the vehicle and is called the body-fixed reference frame. The origin of the body-fixed frame is usually chosen to be at the centre of gravity (CG) of the vehicle and is essential for specifying the orientation of the vehicle. This body-fixed coordinate system is also an *xyz* system with the axes *x*, *y*, and *z* directed towards the nose, starboard and keel-ward directions respectively.

2.1.2 Euler Angles and Coordinate Transformations

The *reference orientation* for a rigid body is one in which all of its body-fixed axes are aligned with the corresponding Earth-fixed reference frame. In general, a body can be rotated away from this reference orientation by rotating it about one or more of the axes of the Earth-fixed reference frame. The angles by which this body-fixed reference frame is rotated about the inertial X_E, Y_E and Z_E axes are termed roll (ϕ), pitch (θ) and yaw (ψ) respectively. These angles, which collectively describe the orientation of the body-fixed frame with respect to the inertial frame, are called *Euler angles* and are denoted by the vector, η_2. Thus the position (η_1) and orientation (η_2) vectors are described with respect to the inertial or Earth-fixed reference frame and they represent the six independent coordinates (6 DOF) of a rigid body moving in 3D space.

$$\eta = [\eta_1, \eta_2]^T = [x_E, y_E, z_E, \phi, \theta, \psi]^T$$

The translational and angular velocities of the rigid body are expressed in the body-fixed reference frame. The translational velocity components surge (u), sway (v) and heave (w), which describe the translational motion of the centre of gravity of the rigid body along the x, y, and z-axes of body-fixed frame respectively are represented by the vector, ν_1. The rotational rates about the same axes are roll-rate (p), pitch-rate (q) and yaw-rate (r) respectively and are represented by the vector, ν_2.

$$\nu = [\nu_1, \nu_2]^T = [u, v, w, p, q, r]^T$$

The position and orientation of the vehicle, represented by the vector, η, are obtained by numerical integration of the linear and angular velocity components of the vector, ν, but only after they are transformed to the Earth-fixed coordinate system. In order to transform the linear and angular velocity components from one coordinate system to another, two transformation matrices, $J_1(\eta_2)$ and $J_2(\eta_2)$, are necessary.

Translational Velocity Transformation

The translational velocity transformation from body-fixed coordinates to the Earth-fixed coordinates is performed by the rotation matrix, $J_1(\eta_2)$ expressed as follows:

$$\begin{bmatrix} \dot{x}_E \\ \dot{y}_E \\ \dot{z}_E \end{bmatrix} = J_1(\eta_2) \begin{bmatrix} u \\ v \\ w \end{bmatrix} \quad \text{or} \quad \dot{\eta}_1 = J_1(\eta_2)\nu_1 \tag{2.1}$$

Conventionally, J_1 is described by three rotations and the order of these rotations is not arbitrary. In guidance and control applications it is common to use the xyz-convention specified in terms of Euler angles for the rotations [Fossen, 1994]. The above order of rotations and the Euler angle definitions are not unique but just the standard convention adopted in naval architecture and there are 12 possible distinct choices for Euler angles [McGhee, 2000]. The rotation sequence is written as:

$$J_1(\eta_2) = R^T_{z,\psi} R^T_{y,\theta} R^T_{x,\phi} \tag{2.2}$$

The notation, $R_{i,\alpha}$ represents the principal rotation matrix describing a rotation angle of α about the i-axis. The principal or elementary rotation matrices $R_{x,\phi}$, $R_{y,\theta}$, and $R_{z,\psi}$ about the local north, east and down axes respectively are defined as:

$$R_{x,\phi} = \begin{bmatrix} 1 & 0 & 0 \\ 0 & c\phi & s\phi \\ 0 & -s\phi & c\phi \end{bmatrix} \quad R_{y,\theta} = \begin{bmatrix} c\theta & 0 & -s\theta \\ 0 & 1 & 0 \\ s\theta & 0 & c\theta \end{bmatrix} \quad R_{z,\psi} = \begin{bmatrix} c\psi & s\psi & 0 \\ -s\psi & c\psi & 0 \\ 0 & 0 & 1 \end{bmatrix}$$

where s · = sin(·) and c · = cos(·). Also, note that $R_{i,\alpha}$ satisfy the condition $RR^T = R^T R = I$.

The above expression (2.2) when expanded yields

$$J_1(\eta_2) = \begin{bmatrix} \cos\psi\cos\theta & -\sin\psi\cos\phi + \cos\psi\sin\theta\sin\phi & \sin\psi\sin\phi + \cos\psi\cos\phi\sin\theta \\ \sin\psi\cos\theta & \cos\psi\cos\phi + \sin\phi\sin\theta\sin\psi & -\cos\psi\sin\phi + \sin\theta\sin\psi\cos\phi \\ -\sin\theta & \cos\theta\sin\phi & \cos\theta\cos\phi \end{bmatrix} \tag{2.3}$$

The coordinate transformation matrix, $J_1(\eta_2)$, is an orthogonal matrix, i.e., $J_1^T J_1 = I$ and hence the inverse linear velocity transformation can be written as:

$$\begin{bmatrix} u \\ v \\ w \end{bmatrix} = J_1^{-1}(\eta_2) \begin{bmatrix} \dot{x}_E \\ \dot{y}_E \\ \dot{z}_E \end{bmatrix} = J_1^T(\eta_2) \begin{bmatrix} \dot{x}_E \\ \dot{y}_E \\ \dot{z}_E \end{bmatrix} \quad \text{i.e.} \quad v_1 = J_1^{-1}(\eta_2)\dot{\eta}_1$$

Angular Velocity Transformation

The body-fixed angular velocity vector, $v_2 = [p \quad q \quad r]^T$, and the Euler rate vector, $\dot{\eta}_2 = [\dot{\phi} \quad \dot{\theta} \quad \dot{\psi}]^T$, are related through the transformation matrix, $J_2(\eta_2)$ as:

$$\begin{bmatrix} \dot{\phi} \\ \dot{\theta} \\ \dot{\psi} \end{bmatrix} = J_2(\eta_2) \begin{bmatrix} p \\ q \\ r \end{bmatrix} \quad \text{or} \quad \dot{\eta}_2 = J_2(\eta_2) v_2 \tag{2.4}$$

This relationship should not be interpreted as a coordinate transformation because the Euler angles cannot be treated as coordinates. They simply express how the body-fixed coordinate system is oriented with respect to the inertial reference frame. Hence, the transformation matrix J_2 does not satisfy the orthogonal transformation property i.e. $J_2^{-1} \neq J_2^T$ [Fossen, 1991]. The orientation of the body-fixed frame with respect to the inertial reference frame can be expressed as:

$$v_2 = \begin{bmatrix} \dot{\phi} \\ 0 \\ 0 \end{bmatrix} + R_{x,\phi} \begin{bmatrix} 0 \\ \dot{\theta} \\ 0 \end{bmatrix} + R_{x,\phi} R_{y,\theta} \begin{bmatrix} 0 \\ 0 \\ \dot{\psi} \end{bmatrix} = J_2^{-1}(\eta_2)\dot{\eta}_2 \tag{2.5}$$

where

$$J_2^{-1}(\eta_2) = \begin{bmatrix} 1 & 0 & -\sin\theta \\ 0 & \cos\phi & \cos\theta\sin\phi \\ 0 & -\sin\phi & \cos\theta\cos\phi \end{bmatrix} \Rightarrow J_2(\eta_2) = \begin{bmatrix} 1 & \sin\phi\tan\theta & \cos\phi\tan\theta \\ 0 & \cos\phi & -\sin\phi \\ 0 & \sec\theta\sin\phi & \sec\theta\cos\phi \end{bmatrix} \tag{2.6}$$

Note that $J_2^{-1} \neq J_2^T$ and hence they are not orthogonal. The expression (2.5) can now be expanded as:

$$\begin{bmatrix} p \\ q \\ r \end{bmatrix} = \begin{bmatrix} 1 & 0 & -\sin\theta \\ 0 & \cos\phi & \cos\theta\sin\phi \\ 0 & -\sin\phi & \cos\theta\cos\phi \end{bmatrix} \begin{bmatrix} \dot{\phi} \\ \dot{\theta} \\ \dot{\psi} \end{bmatrix} \tag{2.7}$$

The inverse of the above expression given by equation (2.4) is expanded as:

$$\begin{bmatrix} \dot{\phi} \\ \dot{\theta} \\ \dot{\psi} \end{bmatrix} = \begin{bmatrix} 1 & \sin\phi\tan\theta & \cos\phi\tan\theta \\ 0 & \cos\phi & -\sin\phi \\ 0 & \sec\theta\sin\phi & \sec\theta\cos\phi \end{bmatrix} \begin{bmatrix} p \\ q \\ r \end{bmatrix} \tag{2.8}$$

Note that $J_2(\eta_2)$ becomes singular at a pitch angle of $\theta = \pm 90^\circ$. This is one of the limitations of the Euler angle representation. This results in loss of numerical accuracy for Euler angles close to $\theta = 90^\circ$. An additional limitation of Euler angles is with respect to computation time. The transformations require the calculation of six trigonometric functions, which are computationally expensive [Biddle, 2003]. In such cases, the Euler representations may be replaced by alternative ones such as quaternions [Kane *et al.*, 1983], which eliminates singularities. Autonomous underwater vehicles of the kind that is discussed through this thesis, however for most practical purposes, do not operate in or near the region of a pitch angle close to 90° and hence for the model described through this thesis, the Euler representation is used. The detailed derivation of matrices $J_1(\eta_2)$ and $J_2(\eta_2)$ can be found in sources such as Craig (1989), Fossen (1994), McGhee *et. al.*, (2000) etc.

The two transformation matrices $J_1(\eta_2)$ and $J_2(\eta_2)$ can now be combined to give a single 6 x 6 transformation matrix and the kinematic equations from the above discussions can be summarized in vector form as follows:

$$\begin{bmatrix} \dot{\eta}_1 \\ \dot{\eta}_2 \end{bmatrix} = \begin{bmatrix} J_1(\eta_2) & 0_{3\times3} \\ 0_{3\times3} & J_2(\eta_2) \end{bmatrix} \begin{bmatrix} v_1 \\ v_2 \end{bmatrix} \tag{2.9}$$

or, in compact form, it can be written as

$$\dot{\eta} = Tv$$

where T is the transformation matrix $\begin{bmatrix} J_1(\eta_2) & 0_{3\times3} \\ 0_{3\times3} & J_2(\eta_2) \end{bmatrix}$

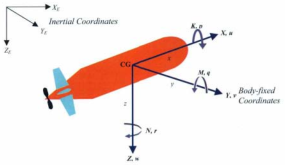

Fig. 2.1 Inertial and body-fixed coordinate system

2.2 Rigid Body Dynamics

The motion of an AUV in 3D space is based on the physics of rigid body motion in a fluid and is described in terms of the Newton-Euler laws of motion, where the rate of change of momentum of a rigid body is equated to the force or moment causing that change.

$$\boldsymbol{F} = m\dot{\boldsymbol{v}}_1 + \boldsymbol{v}_2 \times m\boldsymbol{v}_1 \qquad (2.10)$$

$$\mathrm{G} = \mathrm{I}\dot{v}_2 + v_2 \times \mathrm{I}v_2 \qquad (2.11)$$

where m is the wet mass of the vehicle, $\boldsymbol{F} = [X, Y, Z]^{\mathrm{T}}$ represent the forces acting along the three coordinate axes (x, y, z), $\boldsymbol{G} = [K, M, N]^{\mathrm{T}}$ represents the moments about these three axes, while $\mathbf{v}_1$ and $\mathbf{v}_2$ are the linear and angular velocity vectors as discussed before. A schematic diagram of the body-axis coordinate system is shown in Figure 2.1 with the arrows indicating the directions of positive forces and moments. It also shows the positive directions of linear and angular velocities.

$$m[\dot{u}-vr+wq-x_G(q^2+r^2)+y_G(pq-\dot{r})+z_G(pr+\dot{q})]=X$$
$$m[\dot{v}-wp+ur-y_G(r^2+p^2)+z_G(qr-\dot{p})+x_G(qp+\dot{r})]=Y$$
$$m[\dot{w}-uq+vp-z_G(p^2+q^2)+x_G(rp-\dot{q})+y_G(rq+\dot{p})]=Z$$

$$\begin{aligned}&I_x\dot{p}+(I_z-I_y)qr-(\dot{r}+pq)I_{xz}+(r^2-q^2)I_{yz}+(pr-\dot{q})I_{xy}\\&+m[y_G(\dot{w}-uq+vp)-z_G(\dot{v}-wp+ur)]\end{aligned}=K \qquad (2.12)$$

$$\begin{aligned}&I_y\dot{q}+(I_x-I_z)rp-(\dot{p}+qr)I_{xy}+(p^2-r^2)I_{zx}+(qp-\dot{r})I_{yz}\\&+m[z_G(\dot{u}-vr+wq)-x_G(\dot{w}-uq+vp)]\end{aligned}=M$$

$$\begin{aligned}&I_z\dot{r}+(I_y-I_x)pq-(\dot{q}+rp)I_{yz}+(q^2-p^2)I_{xy}+(rq-\dot{p})I_{zx}\\&+m[x_G(\dot{v}-wp+ur)-y_G(\dot{u}-vr+wq)]\end{aligned}=N$$

The equations of motion are usually expressed in the body-fixed reference frame since the inertial properties of the vehicle are constant in that frame as long as no ballast material is ingested or ejected. Using SNAME (1950) notations, the equations (2.10) and (2.11) can be expanded in its component form (2.12) as consisting of six equations; one for each degree of freedom. The first three equations represent the equilibrium of forces in the x, y and z body-fixed directions while the last three equations represent the equilibrium of moments about each of the body-fixed axes, x, y and z. A detailed derivation of the rigid body equations of motion can be found in Abkowitz (1969), Fossen (1994) or any standard textbooks of Engineering Mechanics, e.g., Hibbeler (1995).

2.3 External Forces

The external forces and moments which act on the body, however, by their nature are uncertain. These forces and moments can be broken down into six forcing functions –

one for each degree of freedom (DOF). In a component build-up method, the forcing function in each DOF can further be broken down as contributions from each of the vehicle components – hull, control planes, appendages, propellers etc. The external forces acting along the body axes x, y, z are shown by the first three equations in (2.13) and the remaining three equations defines the moments about the x, y, z axes respectively:

$$
\begin{aligned}
F_x &= F_{x\,Hull} + F_{x\,Fins} + F_{x\,Prop} \\
F_y &= F_{y\,Hull} + F_{y\,Fins} + F_{y\,Prop} \\
F_z &= F_{z\,Hull} + F_{z\,Fins} + F_{z\,Prop} \\
G_x &= G_{x\,Hull} + G_{x\,Fins} + G_{x\,Prop} \\
G_y &= G_{y\,Hull} + G_{y\,Fins} + G_{y\,Prop} \\
G_z &= G_{z\,Hull} + G_{z\,Fins} + G_{z\,Prop}
\end{aligned}
\qquad (2.13)
$$

The nature of the forces, which contribute to each set of forces, can be treated and analyzed separately.

$$\Sigma \boldsymbol{F} = \boldsymbol{F}_S + \boldsymbol{F}_I + \boldsymbol{F}_R + \boldsymbol{F}_C + \boldsymbol{F}_E \text{; } \Sigma \boldsymbol{G} = \boldsymbol{G}_S + \boldsymbol{G}_I + \boldsymbol{G}_R + \boldsymbol{G}_C + \boldsymbol{G}_E$$

$\boldsymbol{F}_S, \boldsymbol{G}_S$ - Static (hydrostatic) forces and moments– weight and buoyancy

$\boldsymbol{F}_I, \boldsymbol{G}_I$ - Ideal fluid forces and moments – "Added Mass"

$\boldsymbol{F}_R, \boldsymbol{G}_R$ - Real fluid forces and moments – "Damping"

$\boldsymbol{F}_C, \boldsymbol{G}_C$ - Control forces and moments

$\boldsymbol{F}_E, \boldsymbol{G}_E$ - Environmental forces and moments

Environmental Forces (F_E)

These are external forces that are induced by environmental effects such as ocean waves and ocean currents. At present these forces are assumed to be zero although the simulation model is capable of handling crosscurrents. The effect of waves can be safely discarded considering the fact that in most cases AUVs spend much of their operational time in the deep waters.

Hydrostatic Forces (F_S) – Weight and Buoyancy

The hydrostatic forces of buoyancy and weight always act in the z-direction of the Earth fixed axes. The resultant of the buoyancy and weight vector is given by $\mathbf{W} - \mathbf{B}$ as these forces act in opposite direction, and are usually represented by a system of forces and moments in the body fixed axes.

$$F_S = \mathbf{W} - \mathbf{B}$$

$\mathbf{W}$ acts at the CG (x_G, y_G, z_G) of the vehicle while $\mathbf{B}$ acts at the CB (x_B, y_B, z_B) of the vehicle. The magnitude of the resultant force is W – B and its components along the body axes x, y, z, are given below:

$$\begin{aligned} F_{S,x} &= -(W - B)\sin\theta \\ F_{S,y} &= (W - B)\cos\theta\sin\phi \\ F_{S,z} &= (W - B)\cos\theta\cos\phi \end{aligned} \tag{2.14}$$

The moments produced by these forces are given by the cross product

$$\mathbf{G} = \mathbf{r} \times \mathbf{F}$$

where, **r**, is the position vector describing the location of centre of buoyancy, CB, with respect to the centre of gravity, CG, of the vehicle. The moments described by the above equation can be represented in component form as shown in Equation (2.15). These moments are calculated about the axes of an arbitrary frame oriented the same as the body frame, but not necessarily coincident with it.

$$\begin{aligned} G_{S,x} &= (y_G W - y_B B)\cos\phi\cos\theta - (z_G W - z_B B)\sin\phi\cos\theta \\ G_{S,y} &= (z_G W - z_B B)\sin\theta - (x_G W - x_B B)\cos\phi\cos\theta \\ G_{S,z} &= (x_G W - x_B B)\sin\phi\cos\theta + (y_G W - y_B B)\sin\theta \end{aligned} \tag{2.15}$$

Theoretically, an autonomous underwater vehicle could be neutrally buoyant though in practice these vehicles are designed to be slightly positively buoyant. This is a safety feature built-in to the vehicles, which enables the vehicle to surface in case of a system error. If the vehicle is neutrally buoyant, then the weight is equal to the buoyant force, and there is no net hydrostatic force, i.e., the force equations (2.14) reduce to zero. However, the moment equations (2.15) do not reduce to zero.

For an AUV with symmetry about the vertical plane through the longitudinal centreline (*xz*-plane) $y_G = y_B = 0$. Further, the origin of the body-fixed reference frame is typically fixed at the centre of gravity in which case, $x_G = y_G = z_G = 0$. Under these conditions, equations (2.15) reduces to

$$\begin{aligned} G_{S,x} &= z_B B\sin\phi\cos\theta \\ G_{S,y} &= z_B B\sin\theta + x_B B\cos\phi\cos\theta \\ G_{S,z} &= -x_B B\sin\phi\cos\theta \end{aligned} \tag{2.16}$$

2.4 Determination of Hydrodynamic Loads

The hydrodynamic forces are typically expressed as functions of the body geometry, density of the fluid, the relative velocity of the body to the flow and the hydrodynamic coefficients. For example, the lift and drag forces can be expressed as:

$$\mathcal{L} = \frac{1}{2}\rho C_L A_{ref} V^2 \tag{2.17}$$

$$\mathcal{D} = \frac{1}{2}\rho C_D A_{ref} V^2 \tag{2.18}$$

where C_L and C_D are the lift and drag coefficients of the components – hull, appendages etc. These coefficients are function of the angle of attack, α and sideslip, β.

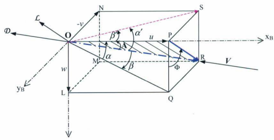

Fig. 2.2 Lift, Drag, α and β for a vehicle oriented arbitrarily to the flow

In order to express the lift and drag forces acting on the various components in the body frame, various frames and their corresponding rotation matrices are required. In

$$
\begin{aligned}
C_L &= \frac{(k_2 - k_1)}{A_{ref}} \sin 2\alpha \cos\frac{\alpha}{2} \int_0^{x_0} \frac{dS}{dx} dx + \frac{2\eta}{A_{ref}} \sin^2 \alpha \cos\alpha \int_{x_0}^{L} r c_{dc} dx \\
C_D &= \frac{(k_2 - k_1)}{A_{ref}} \sin 2\alpha \sin\frac{\alpha}{2} \int_0^{x_0} \frac{dS}{dx} dx + \frac{2\eta}{A_{ref}} \sin^3 \alpha \int_{x_0}^{L} r c_{dc} dx \qquad (2.27) \\
C_M &= \frac{(k_2 - k_1)}{A_{ref} L_{ref}} \sin 2\alpha \cos\frac{\alpha}{2} \int_0^{x_0} \frac{dS}{dx} (x_m - x) dx + \frac{2\eta}{A_{ref} L_{ref}} \sin^2 \alpha \cos\alpha \int_{x_0}^{L} r_x c_{dc} (x_m - x) dx
\end{aligned}
$$

The station x_0, which defines the portion of the body up to which the potential theory should be employed, can be determined from the following empirical relation provided by Hopkins (1951)

$$\frac{x_0}{L} = 0.378 + 0.527 \frac{x_1}{L} \qquad (2.28)$$

where x_1 is defined as the station on the body at a longitudinal distance from the nose at which the rate of change of cross-sectional area with respect to longitudinal distance has a maximum negative value. The other parameters in the equation (2.27) are the reference area A_{ref}, which in Hopkins equation was represented by $V_B^{2/3}$ and a characteristic length L_{ref}, which Hopkins represented by $V_B^{1/3}$. Hopkins suggests that better agreement could have been realized at higher angles of attack provided x_0 had been allowed to move forward along the body with increasing angle of attack. In general, Hopkins' formulations of lift and drag coefficients produced results, which were in good agreement with experimental data. However, with regards to the lift and drag characteristics, he could not conclude whether his method was a better choice than that of Allen and Perkins, as both methods produced good agreement with the experimental data.

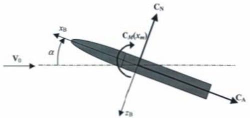

Fig. 2.3 Illustration of the Normal Force, Axial Force and Pitching Moment acting on the Hull

The aerodynamic force centre, x_{ac} measured from the nose tip is given by

$$x_{ac} = \left(\frac{x_m}{d} - \frac{C_M}{C_N}\right)d \tag{2.30}$$

Jorgensen compares the aerodynamic characteristics computed using his formulation with test data from nine different bodies of revolution obtained at a Mach number of 2.86. In comparing the variation of C_N, C_A and C_M with α, good agreement was reported between the computed and measured results, except for the axial force coefficient, C_A. Unfortunately, none of these tests were performed at subsonic speeds, which would have been of primary interest to us. Jorgensen, in his report, also examines the effect of Reynolds number on the normal force coefficient and aerodynamic centre position. His investigation reveals that the Reynolds number has a significant effect on both the C_N and x_{ac}/l throughout most of the α range as a result of the strong influence of the varying cross-flow drag coefficient, C_{Dc}. There is a considerable drop in the cross-flow drag coefficient, C_{Dc}, as cross-flow Reynolds number[1] Re_n increases from 10^5 to 10^6 followed by a gradual rise as Re_n increases from 10^6 to 10^7. This could in turn affect the computed normal force coefficient and aerodynamic centre position.

The cross-flow Reynolds number Re_n values for C-SCOUT AUV are between 0 and 800,000 calculated based on maximum diameter of the hull and cross-currents of up to 2 m/s [Perrault, 2002]. In the case of *MUN Explorer* AUV, which would be of interest to this thesis later, a similar calculation considering cross-currents up to 2 m/s would yield the cross-flow Reynolds number Re_n values roughly between 0 and 1,000,000.

Perrault (2002), in his doctoral thesis, used the integrated form of Hopkins' formulation while developing the hydrodynamic model for the C-SCOUT AUV, which is discussed through this Chapter. In his formulation, the potential term was integrated from the nose up to station x_0 and the viscous term was integrated for the remainder of the hull. After integration, Perrault arrived at the following equations (2.31).

$$C_L = (k_2 - k_1)\frac{S_{x0}}{A_{ref}}\sin 2\alpha \cos\frac{\alpha}{2} + \eta C_{Dc}\frac{(A_p - A_{p0})}{A_{ref}}\sin^2\alpha\cos\alpha \quad (2.31a)$$

$$C_D = C_{DF(\alpha=0)}\cos^3\alpha + (k_2 - k_1)\frac{S_{x0}}{A_{ref}}\sin 2\alpha \sin\frac{\alpha}{2} + \eta C_{Dc}\frac{(A_p - A_{p0})}{A_{ref}}\sin^3\alpha \quad (2.31b)$$

[1] $Re_n = Re \sin\alpha$, where Re is the free-stream Reynolds number calculated based on the maximum diameter of the body. [Kinematic viscosity of seawater, $\upsilon = \mu / \rho$ is 1.35×10^{-6} m^2/s]

$$C_M = (k_2 - k_1)\left(\frac{V_B - S_{x0}(x_0 - x_m)}{A_{ref}L_{ref}}\right)\sin 2\alpha \cos\frac{\alpha}{2} +$$

$$\eta C_{Dc}\left(\frac{A_P}{A_{ref}}\left(\frac{x_m - x_p}{L_{ref}}\right) - \frac{A_{P0}}{A_{ref}}\left(\frac{x_m - x_{p0}}{L_{ref}}\right)\right)\sin^2 \alpha \qquad (2.31c)$$

where

$$S_{x0} = \pi r_{x0}^2$$

is the cross-sectional area of the hull at the station x_0, where the radius of the hull is r_{x0}. The other parameters in the equation (2.31) are: A_p the plan-form area, A_{p0} the plan-form area up to station x_0 and x_{p0} is the distance from the nose to the centroid of the planform area A_{p0}.

Perrault's model, which uses Hopkins' formulation, had the limitation that it was only good for small angles of attack (say up to 20°). In an attempt to make the simulation applicable for large angles of attack, Evans (2003), in his Master's thesis, upgraded the work done by Perrault (2002) by adopting Jorgensen's formulation, which is capable of predicting the hydrodynamic characteristics at higher angles of attack. Jorgensen's equation (2.29) does not include the added mass factor in the potential terms. Excluding this term had an insignificant effect on the results, as the bodies considered by Jorgensen were mostly high fineness ratio bodies, for which this term works out to a value close to one. Since this is not always the case with AUVs, Evans modified Jorgensen's equations by including the added mass term:

$$C_N = (k_2 - k_1)\frac{S_b}{A_{ref}} \sin 2\alpha' \cos\frac{\alpha'}{2} + \eta C_{Dc} \frac{A_p}{A_{ref}} \sin^2 \alpha'; \quad 0^\circ \le \alpha \le 180^\circ$$

(2.32a)

$$C_A = C_{A\alpha=0^\circ} \cos^2 \alpha'; \qquad 0^\circ \le \alpha \le 90^\circ$$

(2.32b)

$$C_A = C_{A\alpha=180^\circ} \cos^2 \alpha'; \qquad 90^\circ \le \alpha \le 180^\circ$$

$$C_M = (k_2 - k_1)\left[\frac{V_B - S_b(L - x_m)}{A_{ref} d}\right] \sin 2\alpha' \cos\frac{\alpha'}{2} + \eta C_{Dc} \frac{A_p}{A_{ref}} \left(\frac{x_m - x_c}{d}\right) \sin^2 \alpha';$$

$$0^\circ \le \alpha \le 90^\circ$$

and

(2.32c)

$$C_M = -(k_2 - k_1)\left[\frac{V_B - S_b x_m}{A_{ref} d}\right] \sin 2\alpha' \cos\frac{\alpha'}{2} + \eta C_{Dc} \frac{A_p}{A_{ref}} \left(\frac{x_m - x_c}{d}\right) \sin^2 \alpha';$$

$$90^\circ \le \alpha \le 180^\circ$$

where

$$\alpha' = \alpha \qquad \text{for} \qquad 0^\circ \le \alpha \le 90^\circ$$

$$\alpha' = 180^\circ - \alpha \qquad \text{for} \qquad 90^\circ \le \alpha \le 180^\circ$$

Due to the fact that the equations (2.32) were intended for a blunt based body, Evans (2003) used the maximum cross-section of the hull for S_b.

Centre of Effort (CE) of the Hull

The centre of effort of the hull is an imaginary point in the hull where the lift and drag forces are assumed to act and about which the hydrodynamic moment is zero. Both Perrault and Evans considered the centre of effort to be common to roll, pitch and yaw due to the axisymmetric nature of the C-SCOUT hull. The centre of effort was calculated as follows:

$$\text{Normal Force (NF)} * x_{CE} = \text{Pitching Moment (PM)}$$

$$\left(\frac{NF}{\frac{1}{2}\rho V^2 A_{ref}}\right) \times x_{CE} = \left(\frac{PM}{\frac{1}{2}\rho V^2 A_{ref} L_{ref}}\right) L_{ref} \;\Rightarrow\; C_N \times x_{CE} = C_M \times L_{ref}$$

$$x_{CE} = L_{ref} \frac{C_M}{C_N} \tag{2.33}$$

such that the centre of effort is a function of the characteristic length and the ratio of moment and normal force coefficient.

It remains to be seen how well these formulations, derived based upon the geometry of the vehicle, could predict the hydrodynamic characteristics of an AUV. From the literature, it was evident that very few experimental data from AUV shapes exist to validate this theory. In the hydrodynamic model described through this thesis, the set of Jorgensen's equations modified by Evans (Eq. 2.32) were used.

Hull Forces

The lift and drag forces on the hull are described as

$$\mathcal{D}_H = \frac{1}{2}\rho C_D A_{ref} V_{CE}^2 \tag{2.34}$$

$$\mathcal{L}_H = \frac{1}{2}\rho C_L A_{ref} V_{CE}^2 \tag{2.35}$$

where C_L and C_D are the lift and drag coefficients of the hull, respectively, derived from the analytical and semi-empirical formulations presented in previous section, A_{ref} is the reference area, which in this case is the wetted surface area of the hull and V_{CE} is the magnitude of the velocity at the centre of effort

$$V_{CE} = \left(u_{CE}^2 + v_{CE}^2 + w_{CE}^2\right)^{\frac{1}{2}} \tag{2.36}$$

The velocity components u_{CE}, v_{CE} and w_{CE} at the centre of effort can be derived from those at the centre of mass as follows:

$$\begin{bmatrix} u_{CE} \\ v_{CE} \\ w_{CE} \end{bmatrix} = \begin{bmatrix} u \\ v \\ w \end{bmatrix} + \begin{bmatrix} p \\ q \\ r \end{bmatrix} \times \begin{bmatrix} x_{CE} \\ y_{CE} \\ z_{CE} \end{bmatrix} \tag{2.37}$$

where x_{CE} is the longitudinal position of the centre of effort as calculated by equation (2.33) and y_{CE} and z_{CE} are the distance from the centre of mass to the longitudinal axis of the hull along the y and z body-fixed axes.

The above equation (2.37) can also be written in vector notation as follows:

$$\boldsymbol{v}_{CE} = \boldsymbol{v}_1 + \boldsymbol{v}_2 \times \boldsymbol{r}_{CE} \tag{2.38}$$

Once the velocity components at the centre of effort are known, the angle of attack at the hull, A, and the roll angle, Φ, can be easily determined by making use of the set of equations (2.21).

$$\tan A = \left(\frac{\sqrt{v_{CE}^2 + w_{CE}^2}}{u_{CE}} \right) \tag{2.39}$$

$$\tan \Phi = \left(\frac{-v_{CE}}{w_{CE}} \right) \tag{2.40}$$

Based on equation (2.39), the angle, A, will lie between 0° and 180°. The 180° to 360° range is accounted for by the rotation angle, Φ, which specifies the velocity vector in the YZ-plane of the body-fixed frame.

The lift and drag forces in the lift-drag plane can be transformed into the body-fixed frame by the following rotation operation, as described in Perrault (2002)

$$\begin{bmatrix} X_{Hull} \\ Y_{Hull} \\ Z_{Hull} \end{bmatrix} = \begin{bmatrix} -\cos A & 0 & \sin A \\ \sin\Phi \sin A & \cos\Phi & \sin\Phi \cos A \\ -\cos\Phi \sin A & \sin\Phi & -\cos\Phi \cos A \end{bmatrix} \begin{bmatrix} D_H \\ 0 \\ L_H \end{bmatrix} \tag{2.41}$$

If, instead of lift and drag forces, the normal and axial forces are estimated, as with the case while using Jorgensen's equations, the above equation (2.41) reduces to the form below, as described in Evans (2003)

$$\begin{bmatrix} X_{Hull} \\ Y_{Hull} \\ Z_{Hull} \end{bmatrix} = \frac{1}{2}\rho A_{ref} V_{CE}^2 \begin{bmatrix} -1 & 0 & 0 \\ 0 & \sin\Phi & 0 \\ 0 & -\cos\Phi & 1 \end{bmatrix} \begin{bmatrix} C_A \\ C_N \\ 0 \end{bmatrix} \tag{2.42}$$

The moments generated by the hull forces about the centre of mass of the vehicle are calculated as follows:

$$\mathbf{G}_{Hull} = \mathbf{r}_{CE} \times \mathbf{F}_{Hull} \tag{2.43}$$

where $\mathbf{r}_{CE}$ is the position vector describing the location of the centre of effort of a component with respect to the centre of mass of the vehicle.

Evans (2003) notes that, based on the definition of the location of the centre of effort, described by (2.33), the method of calculating moments in (2.43) will produce the same result as a moment calculated with the use of the moment coefficient, described in (2.32c).

(b) *Control Plane Lift, Drag and Moment Coefficients*

The forces acting on the control planes are normally decomposed into lift and drag forces, acting perpendicular and parallel to the incoming flow, respectively. The C-SCOUT control planes have a NACA 0012 section profile. Lift, drag and moment coefficients for a variety of 2-D wing sections are readily available from sources such as Abbott and von Doenhoff (1959). However, marine vehicles such as underwater vehicles use control planes of low aspect ratios for which 3-D effects are predominant.

Whicker and Fehlner (1958) conducted a comprehensive study on wings of low aspect ratio, typical of AUVs, and derived semi-empirical expressions for estimating the lift and drag coefficients of control planes operating at small angle of attacks. Perrault

(2002) used these formulations, in his thesis, for estimating the lift and drag coefficients of the control planes but cautioned that at higher angles of attack, there was a need for further data. Evans (2003), however, desired a simulation that was capable of the full 360° range of angles. Only few researchers, such as Riegels (1958), Critzos *et. al.* (1955) etc., have looked at wide range of angles of attack. This is because of the limited usefulness of angles of attack beyond stall in aircraft operations. Evans (2003) used the 2D lift and drag coefficient data from Critzos *et al.,* (1955) for the C-SCOUT simulation in order to account for the full 360° range of angles of attack. In order to modify the 2D lift and drag coefficient data to make it apply for 3-D wing, methods presented in McCormick (1995) were utilized:

$$C_L = \frac{a_e C_l}{a_e + 2\left(\frac{a_e + 4}{a_e + 2}\right)} \tag{2.44}$$

$$C_D = f_{CD} C_d \tag{2.45}$$

where C_l and C_d are the 2-D lift and drag coefficients respectively and f_{CD} is a scale factor from *Figure 4.11* of McCormick (1995), used by Evans. Note that equation (2.44) is intended for linear angle of attack range before stall, but Evans assumed it to be applicable to the nonlinear range as well. The effective aspect ratio of the control plane a_e was defined as:

$$a_e = \frac{b_{CP}^2}{A_{CP}} \tag{2.46}$$

where b_{CP}^2 is the span (twice the distance between the root to tip of the control plane) and A_{CP} is the plan-form area of a pair of control planes, without including the area inside the hull.

Both Perrault and Evans ignored the pitching moment coefficient for the control planes as their contributions were assumed to be small.

Centre of Pressure (CP) of the Control Plane

The centre of pressure of the control plane for the C-SCOUT AUV was assumed to be at the quarter-chord point of the section at 42% of the halfspan out from the root chord [Perrault, 2002]. This control plane had a tapered plan-form.

Control Plane Forces

The base configuration of the C-SCOUT AUV has four control planes arranged in cruciform '+' configuration at the stern. In order to estimate the lift and drag forces on the control planes, only the flow along the chord, c, was considered, while the span-wise flow was neglected. This implies that (see Fig. 2.2) the flow that is relevant to the horizontal control planes (HCP) is

$$V_{CP}\cos(\beta) = \sqrt{u_{CP}^2 + w_{CP}^2} \tag{2.47}$$

while the flow that is relevant to the vertical control planes (VCP) is (see Fig. 2.2)

$$V_{CP}\cos(\alpha') = \sqrt{u_{CP}^2 + v_{CP}^2} \tag{2.48}$$

where V_{CP} is the magnitude of the velocity at the centre of pressure (CoP) of the control plane

$$V_{CP} = \sqrt{u_{CP}^2 + v_{CP}^2 + w_{CP}^2} \tag{2.49}$$

The components of velocity at the centre of pressure of each control plane u_{CP}, v_{CP} and w_{CP}, can be estimated from the knowledge of velocity at the CG of the vehicle as

$$\begin{bmatrix} u_{CP} \\ v_{CP} \\ w_{CP} \end{bmatrix} = \begin{bmatrix} u \\ v \\ w \end{bmatrix} + \begin{bmatrix} p \\ q \\ r \end{bmatrix} \times \begin{bmatrix} x_{CP} \\ y_{CP} \\ z_{CP} \end{bmatrix} \tag{2.50}$$

In vector notation, the above equation can be written as

$$\boldsymbol{v}_{CP} = \boldsymbol{v}_1 + \boldsymbol{v}_2 \times \boldsymbol{r}_{CP} \tag{2.51}$$

where $\boldsymbol{r}_{CP}$ is the position vector describing the location of the centre of pressure of the control plane with respect to the centre of mass of the vehicle.

The lift and drag coefficients of the control planes are a function of the control plane deflection and the angle of attack/sideslip of the hull. These angles denoted by α, β, α' and β' for each control plane are estimated using relationships shown in equation (2.19), (2.20), which requires the knowledge of velocities at the centre of pressures of each control planes. These velocities are determined by application of equation (2.51) to each control plane.

Horizontal Control Planes (HCP):

The lift and drag forces acting on the horizontal control planes, considering only the flow along the chord, are described as

$$D_{HCP} = \frac{1}{2}\rho C_D A_{CP} (V_{CP} \cos(\beta))^2 \tag{2.52}$$

$$L_{HCP} = \frac{1}{2}\rho C_L A_{CP} (V_{CP} \cos(\beta))^2 \tag{2.53}$$

where

$$\beta = \tan^{-1}\left(\frac{v_{CP}}{\sqrt{u_{CP}^2 + w_{CP}^2}}\right) \tag{2.54}$$

The lift and drag coefficients, C_L and C_D, are functions of the horizontal control plane deflection, δ_{HCP}, added to the angle of attack, α, of the hull, where

$$\alpha = \tan^{-1}\left(\frac{w_{CP}}{u_{CP}}\right) \tag{2.55}$$

Therefore, the lift and drag forces acting at the centre of pressure of the horizontal control planes can be expressed in the body-fixed frame as [see Perrault (2002) for details]:

$$\begin{bmatrix} X_{HCP} \\ Y_{HCP} \\ Z_{HCP} \end{bmatrix}_B = \begin{bmatrix} -\cos(\alpha) & 0 & \sin(\alpha) \\ 0 & 1 & 0 \\ -\sin(\alpha) & 0 & -\cos(\alpha) \end{bmatrix} \begin{bmatrix} D_{HCP} \\ 0 \\ L_{HCP} \end{bmatrix} \tag{2.56}$$

Vertical Control Planes (VCP):

The lift and drag forces acting on the vertical control planes, considering only the flow along the chord, are described as

$$\mathcal{D}_{VCP} = \frac{1}{2}\rho C_D A_{CP} \left(V_{CP}\cos(\alpha')\right)^2 \tag{2.57}$$

$$\mathcal{L}_{VCP} = \frac{1}{2}\rho C_L A_{CP} \left(V_{CP}\cos(\alpha')\right)^2 \tag{2.58}$$

where

$$\alpha' = \tan^{-1}\left(\frac{w_{CP}}{\sqrt{u_{CP}^2 + v_{CP}^2}}\right) \tag{2.59}$$

The lift and drag coefficients, C_L and C_D, are functions of the vertical control plane deflection, δ_{VCP}, added to the sideslip, β', of the hull, where

$$\beta' = \tan^{-1}\left(\frac{v_{CP}}{u_{CP}}\right) \tag{2.60}$$

Therefore, the lift and drag forces acting at the centre of pressure of the vertical control planes can be expressed in the body-fixed frame as [see Perrault (2002) for details]:

$$\begin{bmatrix} X_{VCP} \\ Y_{VCP} \\ Z_{VCP} \end{bmatrix}_B = \begin{bmatrix} -\cos(\alpha) & 0 & \sin(\alpha) \\ 0 & 1 & 0 \\ -\sin(\alpha) & 0 & -\cos(\alpha) \end{bmatrix} \begin{bmatrix} D_{VCP} \\ 0 \\ L_{VCP} \end{bmatrix} \tag{2.61}$$

External moments on the vehicle due to the control plane forces are expressed in the body fixed frame as follows:

$$\mathbf{G}_{CP} = \mathbf{r}_{CP} \times \mathbf{F}_{CP} \tag{2.62}$$

2.4.2 Rear Thruster

Evans (2003), for the C-SCOUT simulation, modelled the rear thruster simply as a force exerted along the longitudinal axis of the vehicle. At equilibrium, this thrust was equal to the drag force on the vehicle and therefore no acceleration occurred. Evans argues that once the vehicle is in motion, the thrust is inversely proportional to the forward velocity, u, and therefore simulates a propulsor with constant power output:

$$T = \frac{T_0 V_0}{u} \tag{2.63}$$

where T is the thrust and T_0 is equal to the drag of the vehicle at its initial equilibrium velocity, V_0.

2.5 Equations of Motion

The rigid body equations of motion represented by the equations (2.10) and (2.11) or (2.12) can be summarised into a matrix form as shown in Perrault (2002),

$$\begin{bmatrix}\mathbf{F}\\ \mathbf{G}\end{bmatrix} = \begin{bmatrix} m\mathbf{I}_3 & 0 \\ 0 & \mathbf{I}\end{bmatrix}\begin{bmatrix}\dot{\mathbf{v}}_1 \\ \dot{\mathbf{v}}_2\end{bmatrix} + \begin{bmatrix}\mathbf{S}(\mathbf{v}_2) & 0 \\ 0 & \mathbf{S}(\mathbf{v}_2)\end{bmatrix}\begin{bmatrix} m\mathbf{I}_3 & 0 \\ 0 & \mathbf{I}\end{bmatrix}\begin{bmatrix}\mathbf{v}_1 \\ \mathbf{v}_2\end{bmatrix} \tag{2.64}$$

$$= \begin{bmatrix} m\mathbf{I}_3 & 0 \\ 0 & \mathbf{I}\end{bmatrix}\begin{bmatrix}\dot{\mathbf{v}}_1 \\ \dot{\mathbf{v}}_2\end{bmatrix} + \begin{bmatrix}\mathbf{S}(m\mathbf{I}_3\mathbf{v}_2) & \mathbf{S}(m\mathbf{I}_3\mathbf{v}_2) \\ 0 & \mathbf{S}(\mathbf{v}_2)\mathbf{I} - \mathbf{S}(\mathbf{I}\mathbf{v}_2)\end{bmatrix}\begin{bmatrix}\mathbf{v}_1 \\ \mathbf{v}_2\end{bmatrix}$$

where $\mathbf{I}_3 = \begin{bmatrix}1 & 0 & 0\\ 0 & 1 & 0 \\ 0 & 0 & 1\end{bmatrix}$ and $\mathbf{S}$ ($\mathbf{v}_2$) is a skew-symmetric matrix given by

$$S(\mathbf{v}_2)=\begin{bmatrix} 0 & -r & q \\ r & 0 & -p \\ -q & p & 0 \end{bmatrix}$$

$\mathbf{I}$ is the inertia tensor given by

$$\mathbf{I}=\begin{bmatrix} I_{xx} & -I_{xy} & -I_{xz} \\ -I_{xy} & I_{yy} & -I_{yz} \\ -I_{xz} & -I_{yz} & I_{zz} \end{bmatrix}$$

The vectors $\mathbf{F}$ and $\mathbf{G}$ on the left-hand-side of the equation (2.64) represent, respectively, the external forces and moments acting on the vehicle causing its motion. These external forces can be summarized in matrix form as

$$\begin{bmatrix} \mathbf{F} \\ \mathbf{G} \end{bmatrix}=\begin{bmatrix} \mathbf{F}_S \\ \mathbf{G}_S \end{bmatrix}+\begin{bmatrix} \mathbf{F}_{\dot{\mathbf{v}}_1} & \mathbf{F}_{\dot{\mathbf{v}}_2} \\ \mathbf{G}_{\dot{\mathbf{v}}_1} & \mathbf{G}_{\dot{\mathbf{v}}_2} \end{bmatrix}\begin{bmatrix} \dot{\mathbf{v}}_1 \\ \dot{\mathbf{v}}_2 \end{bmatrix}+\begin{bmatrix} \mathbf{F}_H \\ \mathbf{G}_H \end{bmatrix} \tag{2.65}$$

where the first term on the RHS indicates the hydrostatic loads on the vehicle, the second term indicates the pressure induced forces and the last term indicates the nonlinear, viscous terms. Equating the right hand sides of equations (2.64) and (2.65) and rearranging the terms for acceleration, the equations of motion can be written as:

$$\left(\begin{bmatrix} m\mathbf{I}_3 & 0 \\ 0 & \mathbf{I} \end{bmatrix}-\begin{bmatrix} \mathbf{F}_{\dot{\mathbf{v}}_1} & \mathbf{F}_{\dot{\mathbf{v}}_2} \\ \mathbf{G}_{\dot{\mathbf{v}}_1} & \mathbf{G}_{\dot{\mathbf{v}}_2} \end{bmatrix}\right)\begin{bmatrix} \dot{\mathbf{v}}_1 \\ \dot{\mathbf{v}}_2 \end{bmatrix}$$

$$=\begin{bmatrix} \mathbf{F}_S \\ \mathbf{G}_S \end{bmatrix}+\begin{bmatrix} \mathbf{F}_H \\ \mathbf{G}_H \end{bmatrix}-\begin{bmatrix} \mathbf{S}(m\mathbf{I}_3\mathbf{v}_1) & \mathbf{S}(m\mathbf{I}_3\mathbf{v}_2) \\ 0 & \mathbf{S}(\mathbf{v}_2)\mathbf{I}-\mathbf{S}(\mathbf{I}\mathbf{v}_2) \end{bmatrix}\begin{bmatrix} \mathbf{v}_1 \\ \mathbf{v}_2 \end{bmatrix} \tag{2.66}$$

The above equation (2.66) is solved for the accelerations of the vehicle. The accelerations are integrated once to obtain the velocities (translational and angular); the velocities are then integrated to obtain the position and orientation of the vehicle.

$$\begin{bmatrix} \dot{\mathbf{v}}_1 \\ \dot{\mathbf{v}}_2 \end{bmatrix} = \mathbf{M}_A^{-1} \begin{bmatrix} \mathbf{F} \\ \mathbf{G} \end{bmatrix} \tag{2.67}$$

where $\mathbf{M}_A$ is the augmented apparent mass matrix.

2.6 Nonlinear Model of a Streamlined AUV: Implementation

The nonlinear model of the streamlined C-SOCUT AUV, developed by Perrault (2002) and later modified by Evans (2003), was implemented in MATLAB™ and SIMULINK™. At the heart of the model was a variable-time-step integrator solving a set of six second-order differential equations, one for each degree of freedom.

The procedures involved in implementing the nonlinear model can be summarized through the following steps:

1. An initial Earth-fixed state vector, $\boldsymbol{\eta}_0$, $\dot{\boldsymbol{\eta}}_0$ is selected.
2. The Earth-fixed velocity vector, $\dot{\boldsymbol{\eta}}$, is transformed into the body-fixed velocity vector $\boldsymbol{v}$ using the relation, $\boldsymbol{v} = \boldsymbol{T}^{-1}\dot{\boldsymbol{\eta}}$.
3. The velocity at the reference point (centre of pressure, centre of effort) of each component/element is calculated using the relationship for $\boldsymbol{V}$ in (2.38), (2.51).
4. The angles of attack and sideslip are calculated from the knowledge of the velocity components at each reference points using appropriate equations.

5. The lift coefficients for each component are calculated using appropriate equations.
6. The drag coefficients for each component are calculated using appropriate equations.
7. Dimensionalize the lift and drag forces for each component using the velocity at the centre of pressure/effort of each component according to equations for Lift (2.17) and Drag (2.18).
8. The resulting lift and drag forces are transformed to the body-axis through the angles of attack and sideslip.
9. The forces and moments acting on various components of the vehicle are summed and applied to the left hand side of equation (2.64). This enables the body-fixed acceleration vector $\dot{\boldsymbol{v}}$ to be calculated.
10. The acceleration vector, $\dot{\boldsymbol{v}}$ is then integrated to yield the body-fixed velocity vector, $\boldsymbol{v}$.
11. The velocity vector, $\boldsymbol{v}$ is transformed into the Earth-fixed reference frame to yield the velocity vector, $\dot{\boldsymbol{\eta}}$, using the relation $\dot{\boldsymbol{\eta}} = \boldsymbol{T}\boldsymbol{v}$.
12. The Earth-fixed velocity vector, $\dot{\boldsymbol{\eta}}$, is integrated to yield the position and orientation vector, $\boldsymbol{\eta}$.
13. If the trajectory in the Earth-fixed coordinate system is not complete, $\boldsymbol{\eta}$ and $\dot{\boldsymbol{\eta}}$ are looped back to step 2.

2.7 Review of Related Literature

The lack of accurate methods for predicting vehicle hydrodynamic characteristics, given the external geometric configuration of a typical AUV, has been a recurring problem and an uncertain process in the design of underwater vehicles. Currently, semi-empirical methods represent the state-of-the-art prediction technique and provide a viable means for analyzing many geometric variations during the initial stages of underwater vehicle development. This is because semi-empirical methods are algebraic in form and therefore computationally rapid and inexpensive. The heart of a semi-empirical method is the body build-up technique in which the hydrodynamic coefficients for isolated components are determined, interference effects between components are predicted and contributions summed up to the give the hydrodynamic coefficients of the complete vehicle. These coefficients are then utilized in the equations of motion to evaluate vehicle stability and performance as a function of the vehicle mass characteristics and external shape. Humphrey and Watkinson (1978) report that they have applied these techniques to the design and analysis of approximately 60 underwater vehicles. However, to the best of the author's knowledge, only very few literature exist in the public domain that used the *component build-up* or *body build-up* method as a means to modelling the behaviour of underwater vehicles. A literature review on the hydrodynamic modelling of underwater vehicles using the *component build-up method* (CBM) is presented below.

In 1973, the Hydromechanics Division at Naval Coastal Systems Center (NCSC) initiated a systematic approach for analytically determining the hydrodynamic coefficients of submersibles. The initial phase of this effort involved the adaptation of semi-empirical methods developed by the aerospace community for subsonic aircrafts such as *Stability and Control DATCOM*, to underwater vehicles. This new method devised by NCSC for submersibles was to overcome the deficiencies inherent in applying the methods used for subsonic aircraft analysis to underwater vehicles; in particular, the inability to account for the hydrodynamic characteristics of low aspect ratio fins. Thus, NCSC generated a database by systematically testing a wide range of typical submersible configurations. Using data obtained from the wind tunnel tests, NCSC developed a new semi-empirical method capable of predicting the hydrodynamic coefficients of both a complete vehicle configuration and individual vehicle components [Summey and Smith, (1981)]. Summey and Smith (1981) also predicted the hydrodynamic coefficients for three different submersibles using NCSC's new method and reported the findings to be better than the predictions from three[2] other methods. However, no details regarding this model or its derivation, which is based on the body build-up technique, were available from the literature.

An overriding advantage of using the *component build-up* method is that the hydrodynamic forces and moments acting on the vehicle are derived from empirical relations that require only specification of vehicle's geometry. Each component of the vehicle such as hull, control planes, thrusters etc, are modelled separately using simple hydrodynamic relations. The forces and moments acting on each of these components are summed up to give the external forces and moments acting on the complete vehicle. Further, this method also retains the inherent nonlinear nature of the vehicle model.

[2] USAF DATCOM methods, Hydroballistic Handbook methods, Analytical methods by Abkowitz & Paster

While reviewing the literature related to modelling underwater vehicles using the *component build-up method*, it became apparent that there existed two streams of researchers who applied the same method but in different ways. Both groups used the component build-up method to estimate the external load acting on the complete vehicle. One group of researchers used the external load estimates to derive the hydrodynamic derivatives, typical of the Taylor series expansion method, and utilized those coefficients in the equations of motion to simulate vehicle motions. Nahon (1993), Prestero (2001), Hwang (2003), Ridely *et al.* (2003), Havard (2004), de Barros *et al.,* (2008a; 2008b) are some of those researchers who used this *indirect* method. The hydrodynamic coefficient estimates thus obtained were often compared or validated with corresponding results from tow tank and PMM tests[3], CFD analysis etc. On the other hand, the second stream of researchers, instead of calculating the hydrodynamic derivatives from the external forces acting on the vehicle, computed the accelerations of the vehicle directly from the external forces and moments and integrated those estimates twice to predict the trajectory and orientation of the vehicle. The current work described through this thesis falls into the second category. Researchers who used this *direct* method in modelling underwater vehicle dynamics were Nahon (1996; 2006), Perrault (2002), Evans (2003), Evans & Nahon (2004), Buckham (2003), Lambert (2003) etc. However, validation of this approach was limited by extremely few experimental data from manoeuvring trials. Some salient features of the works of above researchers belonging to both categories are briefly described below.

[3] Resistance test, static yaw and pitch test, pure sway test, pure heave test, arc-of-a-circle test etc.

Nahon (1993) used the USAF DATCOM to predict the hydrodynamic coefficients necessary for the simulation of the ARCS vehicle - an autonomous underwater vehicle developed by the International Submarine Engineering (ISE) and used as a test bed for evaluating AUV technologies. The USAF DATCOM [Hoak & Finck, 1978] is intended to evaluate aircraft stability characteristics strictly from the aircraft's geometric shape parameters. The hydrodynamic derivatives thus determined for the ARCS AUV were compared with experimental results from full-scale vehicle tests reported in Hopkin and den Hertog (1993).

Prestero (2001), Ridley *et al.* (2003) derived hydrodynamic coefficients necessary for their dynamics models from first principles and semi-empirical relations. Prestero (2001) describes the development and verification of a 6-DOF nonlinear simulation model for the REMUS AUV while Ridley *et al.* (2003) describes the development of a nonlinear model for a torpedo shaped AUV developed at the Queensland University of Technology, Australia. The external forces and moments acting on the vehicles were all defined in terms of vehicle hydrodynamic coefficients. The simulated outputs from Prestero's (2001) model for step changes in rudder and horizontal stern plane deflections were verified with vehicle response to corresponding conditions at sea in the horizontal and vertical planes respectively. Ridley *et al.* (2003), on the other hand, does not verify the predicted coefficients but uses the coefficients in his model to simulate the AUV response under the action of various actuator inputs.

Hwang (2003) also used the component build-up approach to predict the linear and nonlinear hydrodynamic coefficients of the Long Term Mine Reconnaissance System (LMRS) autonomous unmanned underwater vehicle. Here the hydrodynamic model was validated against the results of hydrodynamic coefficients determined from the PMM tests conducted on a full-scale model. The comparisons were reported to have good agreement.

Further, since the body build-up technique predicts the overall hydrodynamic loads on the vehicle from the vehicle geometric components, any interference effect from the hull on a control plane is not properly modelled. On the other hand, the hydrodynamic derivatives determined from model testing will have this inherent effect included. It is well known that there exists some mutual interference between the components in a wing-body combination such that the total lift on the combination is different than the sum of the lift on the wing and body alone [Hoerner, (1965)]. This mutual interference effect between the lifting surface and the body may be significant, particularly in the case of an AUV, where the lifting surface is typically small in relation to the body size. It is therefore expected to be important to include the fin-body combination as units rather than in isolation.

Havard (2004), de Barros *et al*. (2008a; 2008b) are some researchers who along with using component build-up approach also considered the interaction effects between the components while modelling their AUVs. Havard (2004) makes use of the empirical methods from USAF DATCOM to derive the hydrodynamic derivatives for fin-body combinations, necessary for describing the hydrodynamic loads acting on the vehicle. The theory developed was successfully used to develop a hydrodynamic estimation software in MATLAB. The software was used to model the "MAYA" AUV for motions in the vertical plane. Since there were no experimental data available from MAYA AUV then to validate his results, the software was then used to model two other very similar AUVs: the REMUS and another torpedo shaped AUV developed by the Queensland University of Technology, Australia [Ridley *et al.* (2003)]. The results from a few selected simulations of the REMUS and the other AUV were compared with corresponding experimental data reported in Prestero (2001) and Ridley *et al.* (2003) respectively. Havard's (2004) model does not take into account thruster dynamics and duct-body interactions and also reports that much of the theory developed is adapted from the work of de Barros *et al.* (2004). In a later study, de Barros *et al.* (2008a) successfully applied the component build-up method for predicting AUV derivatives. The normal force and moment coefficients predicted for the bare-hull were found to be in good agreement with the results obtained from CFD methods. The normal force and moment coefficients derived were used to estimate the hydrodynamic derivatives of the MAYA AUV. The hydrodynamic derivatives thus obtained were used in the expression given by Lewis (1989) to calculate the radius during a steady turning manoeuvre which in turn was compared with the turning diameter of the vehicle obtained from sea trials. The same author, in yet another study [de Barros, 2008b], investigated the validity of the normal force and moment coefficients at nonlinear range of angles of attack. The normal force and moment coefficient estimates from analytical and CFD methods were compared with experimental results from the tank tests. The CFD method provided results that were in very good agreement with the experimental results and based on this observation the analytical expressions used for calculating the normal force and moment coefficients were modified. The modified expressions were shown to have improved the predictions considerably.

Apart from AUVs, the component build-up method has also been used for modelling other vehicles such as missiles, towed underwater bodies, gliders etc. Lesieutre *et al*, (1996; 2002) reports the development of an efficient aerodynamic prediction program for missiles using a component build-up method. However, no details regarding the derivation of the model were presented in any of the above literature. The component build-up method has also been used for modelling towed underwater vehicle systems. Buckham *et al.*, (2003) developed a dynamics model based on the component build-up method for a towed underwater vehicle system. This model is composed of a semi-submersible towing vehicle (DOLPHIN) connected to an active towfish (AURORA) by a discretized lumped-mass cable model. Here, the dynamics of both the towing vehicle and the towed vehicle are considered important because of their comparable masses. The validation of this model was reported in Lambert *et al.*, (2003). Overall, a good match between their simulation and sea trials was reported and any observed differences were attributed to simple discrepancies between the model and control gains. The model was further used to evaluate different turns in order to improve the performance of the system during U-turns. Stante *et al.* (2007) applied the component build-up method to model the SLOCUM ocean glider. The simulated results from the model were validated against available experimental data and the agreement between the two was reported to be reasonable.

Perrault (2002) developed a hydrodynamic model for the Baseline Configuration of the C-SCOUT AUV, based on the simplified dynamics model developed by Nahon (1996) for streamlined underwater vehicles. Perrault did not validate this model but rather used this simulation to study the sensitivity of motion response to variations in the geometric and hydrodynamic parameters. He also looked at the vehicle behaviour in the event of control plane faults such as jamming or loss of control planes during operation.

A major drawback to the simulations presented by the above researchers, who implemented the component build-up method, is a limitation to small angles of attack on the hull and control planes. Further, very few experimental data from AUVs were available to validate and establish a performance envelope to such models.

Evans (2003) desired a model that is capable of handling higher angles of attack and modified Perrault's work by incorporating formulations that can handle the full 360° angle of attack range. He argues that at low velocities or in cases of a cross current, the vehicle can experience an angle of attack of 90° on the hull and control planes and thus should be capable of handling such scenarios. In addition, Evans also incorporated the through-body thruster models, based on the work of Saunders (2003), to fully describe the Fully-Actuated Configuration of the C-SCOUT. The simulation was then used to evaluate and compare the stability and turning diameters of both configurations at various vehicle speeds and control plane deflections. In addition, a series of oceanographic sampling missions were also simulated to determine circumstances where one configuration of C-SCOUT would be beneficial over the other. However, Evans could not validate the C-SCOUT model against experimental data instead he adapted his simulation to the ISE ARCS vehicle and validated it using field data from ARCS vehicle. The ARCS simulation results were reported to be very close to those measured. However, the experimental results were limited to a couple of turning circles.

The hydrodynamic simulation model for the Baseline Configuration of C-SCOUT AUV, developed by Perrault (2002) and Evans (2003), lays the foundation for this research work, in which the primary focus was to validate the model against experimental data. With the exception of a few field test data from axisymmetric vehicles such as REMUS AUV, ARCS etc, there hardly seems to exist sufficient manoeuvring data from real vehicles to validate the mathematical models. Further, it remains to be seen up to what degree of accuracy can these formulations, derived based on the geometry of the vehicle, could predict the hydrodynamic characteristics of an AUV and thereby establish the limitations or performance bounds of these methods.

2.8 Conclusions

A nonlinear hydrodynamic model for a streamlined underwater vehicle was described through this chapter. This model is based on the component build-up or body build-up method in which the hydrodynamic loads acting on the vehicle are derived from empirical relations that require only the description of the vehicle geometry. Each component is modelled separately and the forces and moments from individual components are summed up to provide the total hydrodynamic load acting on the vehicle. The model described here was originally developed for the C-SCOUT autonomous underwater vehicle and was never validated against experimental data.

Of the vast literature that are available on the hydrodynamic modelling of AUVs, it was found that very few researchers have used the *component build-up* method and even fewer had sufficient experimental data available from AUVs to satisfactorily validate their model. Given the simplicity and ease with which a model of this kind can be developed, it would prove to be a quick and efficient means to modelling streamlined underwater vehicles if the performance bounds of such a model can be evaluated and established. Once bounds are known for inaccuracies that are inherent in prediction methods, better control approaches can be devised to deal with the uncertainties involved in the model. It is with this intention in mind that a series of manoeuvring experiments was proposed as part of this research work such that the data obtained could be used to establish the performance bounds of a hydrodynamic simulation model developed using the body build-up approach.

In the absence of experimental data from C-SCOUT AUV, the data necessary for validating the model was obtained from manoeuvring trials performed at sea using the new AUV that was available at the Memorial University of Newfoundland – the *MUN Explorer*, described in Chapter 3. As a result, a major portion of this research was dedicated to obtaining sufficient experimental data from full-scale testing of an axisymmetric streamlined AUV – the *MUN Explorer*, and the details of these experiments and data analyses are presented in Chapter 4. Consequently, the hydrodynamic model had to be adapted to that of *MUN Explorer* AUV and the changes that were necessary to make this modification will be described in Chapter 5.

Chapter 3

The *MUN Explorer* AUV: Vehicle Features and Experimental Setup

In June 2006, Memorial University of Newfoundland acquired a survey-class Autonomous Underwater Vehicle (AUV), the *MUN Explorer*, built by International Submarine Engineering Ltd., (ISE) in Port Coquitlam, British Columbia. This vehicle was funded by the Atlantic Canada Opportunities Agency (ACOA) through the Atlantic Innovation Fund (AIF). The *MUN Explorer* is a multi-user AUV primarily for research purposes in Newfoundland[1] and other parts of Canada and serves as a research platform for underwater sensor technologies such as underwater imaging and water quality sampling. Other potential areas of research for which the vehicle will be utilized are offshore environmental monitoring, seabed imaging, iceberg reconnaissance and characterization and vehicle dynamics testing.

[1] http://www.mun.ca/creait/MERLIN/auv.php

The availability of an *Explorer* at Memorial University facilitated the performing of a series of manoeuvring tests, required for this thesis work, during August / September of 2006. The entire test was carried out at Holyrood harbour situated 28 miles south-west of St. John's, Newfoundland. A topographical map of the location is shown later in this chapter (see Figure 3.5). The discussions that follow consist primarily of two sections: the first section gives an account of the structural and functional features of the AUV – *MUN Explorer* and the second section gives a description of the experimental setup, methods and measures adopted to perform the manoeuvring trials.

3.1 The *MUN Explorer* AUV

The *MUN Explorer* is a streamlined survey-class AUV and functions mainly as a sensor platform for undersea survey and offshore environmental monitoring purposes. The AUV is 4.5 m in length with a maximum mid-body diameter of 0.69 m and is designed to go as deep as 3000 m. It is propelled by a twin-blade propeller and can reach cruising speeds between 0.5 to 2.5 m/s. Manoeuvring of the vehicle in 3-D space is facilitated by six control-planes: four aft planes arranged in 'X' configuration and two dive planes on the forward payload section. To the aft of the vehicle is a retractable communications mast that can be raised to approximately 1.0 m above the body surface of the vehicle. The vehicle has a dry weight of 630 kg and can carry approximately 150 kg of scientific payload without having to add extra buoyancy in the form of syntactic foam. Figure 3.1 shows the *MUN Explorer* AUV before launch from a wharf at Holyrood, Newfoundland.

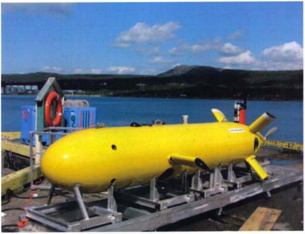

Fig. 3.1 *The MUN Explorer* AUV at Holyrood, Newfoundland

a. Structure

The *MUN Explorer* AUV is modular in structure consisting of a cylindrical main body blended perfectly with a nose cone at its front and a tapered tail section at its rear, giving it a hydrodynamically efficient streamlined shape, (see Figure 3.2). Except for the pressure hull, the majority of hull section is made of Glass Reinforced Plastic (GRP). This greatly reduces the overall weight of the vehicle.

The pressure hull is a cylindrical ring stiffened module made of 7075-T6 Aluminum, consisting of a cylinder section and 2 hemispherical end caps. The end-caps are joined to the cylinder using split aluminium clamps. The pressure hull provides all buoyancy to make the vehicle slightly positively buoyant, i.e., there is no additional buoyancy in the form of syntactic foam. Moreover, it also provides the necessary dry space for batteries, control electronics and dry payloads.

Immediately forward of the pressure hull is the free-flooding forward payload section. It is made of GRP. This section has the dive planes, forward lifting lug, towing lug, depth sensor, LinkQuest™ acoustic transponder and the ORE acoustic transponder mounted in it. Space is available inside this section for additional wet payload items.

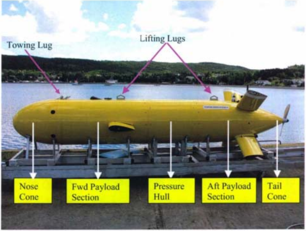

Fig. 3.2 Different modules of the *MUN Explorer* AUV

The free-flooding aft payload section made of GRP is to the rear of the pressure hull and it has a tapered end to connect to the tail cone section. Some navigation sensors and devices, such as the Doppler Velocity Log (DVL) and retractable communication mast are located in this section. There is also room for some additional wet payload in this section. The aft control planes are attached to the exterior of this section. Aft trim ballast is also located here. The tail cone is like a torpedo tail, and is designed to reduce the drag caused by the pressure drop at the end of the vehicle body. The propeller and the drive motor and gearbox are located in this section. Figure 3.2 shows the modular sections of AUV.

b. Control and Guidance

The Vehicle Control Computer (VCC) is the "brain" of the AUV that provides guidance and control using both sensors and actuators. It is an industrial rack mounted Inova Compact PCI computer with built-in expansion capability. It acquires data from all onboard instruments and sends this data to the Surface Control Console (SCC). It also receives commands from the surface or onboard control systems and generates commands to its actuators (eg. thrusters, planes). The VCC runs the QNX 4.25 operating system.

A network of computers on the surface, collectively called as the Surface Control Console (SCC), provide AUV with mission planning, monitoring and access to certain positioning sensors. It transmits all pilot commands to the vehicle and generates graphics text and diagnostics displays to provide information to the operator through a custom designed graphic user interface (GUI). The SCC is a standard 2U industrial style 19" rack-mount PC affixed to 19" rack-mount hardware inside the frame. The

SCC also runs the QNX 4.25 operating system. The SCC GUI displays the current state of most vehicle feedback information and accepts commands for actuators and instruments.

c. Communication Systems

Although an AUV is capable of autonomous operations, it is often advantageous to maintain a contact with the vehicle from the surface. This enables the operator to have occasional health checks and also ensures that the AUV sensors are logging useful information. The communication between the AUV (VCC) and surface console (SCC) is established by three different techniques. These systems are radio telemetry, underwater acoustic telemetry and hardwire deck cable.

i. Data Radio Telemetry Link

DataRadio system consists of a DataLinc Radio, a 4 Watt RF amplifier, dry coax, coax underwater connector, wet coax and antenna. The radio and amplifier are mounted aft on the electronic payload tray inside the pressure hull. The RF antenna is mounted on top of the telescoping mast; the wet coax exits the payload hull through a penetrator and runs through the telescoping mast cable management pulleys to the RF antenna.

The operator can select the radio telemetry link as the active telemetry link between the VCC and the SCC. The radio telemetry system is capable of high-speed communications with the surface console while the AUV is on the surface. For this communication, two wireless Ethernet Datalinc SRM6210E 900 MHz radio modems are used; one installed in the vehicle and the other on the surface console. The acoustic system is not functional at this time because the top-mounted transponder is out of the water. Power demand is not a concern since the system is switched off when the AUV is submerged. At the end of a mission, radio link is valuable to pilot the AUV to a safe recovery position and shut it down.

ii. Underwater Acoustic Telemetry

The underwater acoustic system consists of the LinkQuest™, electronic transducer mounted in the forward payload section. The LinkQuest system is used to transmit data between the AUV and its support ship when the AUV is underwater. It can be enabled from the SCC-GUI by the operator.

iii. Hardwire Deck Cable

A high-speed hardwired 100Mb industrial Ethernet cable with a RJ45 connector at the console end and a subcom 8-pin underwater connector at the vehicle end is used for working with the vehicle, when on the deck (wharf). This connection is meant for on-deck/onshore operations such as uploading mission plans, retrieving data after a day's mission as well as for normal pre and post-dive checks.

d. Navigation and Positioning

The navigation system of the vehicle consists of several different sensors to locate and orient the vehicle in 3-D space. A pressure sensor (Paroscientific - RS232 200Hz) located in the forward payload section measures the depth of vehicle below the water surface, while bottom avoidance and altitude are provided using a forward looking altimeter [Kongsberg Acoustic Altimeter (KSM1007)] located in the nose of the vehicle. The geographical coordinates of the position are obtained by means of a RDI velocity sensor (RDI 300 kHz DVL) when the vehicle is submerged. The Doppler Velocity Log (DVL) is an Acoustic Doppler Current Profiler (ADCP), which has four acoustic beams that measure velocity perpendicular to the four beams. The DVL uses this velocity and heading data to estimate the position. However, it needs to be initialized or reset intermittently by position fixes from other sources such as a GPS when at the surface. The *MUN Explorer* uses a Sound Ocean Systems DGPS mounted on the retractable communications mast that determines precise positions (geographical coordinates) while the AUV is on the surface. Further, the vehicle uses an Attitude Heading and Reference System (Watson AHRS E304) to sense the vehicle attitudes (roll, pitch and heading) and angular rates (roll rate, pitch rate and yaw rate).

e. Propulsion and Manoeuvring

The AUV is propelled by a 0.65 m diameter high efficiency twin-bladed propeller driven by a Hathaway 48 VDC brushless motor coupled to a 3:1 planetary gear. The vehicle can achieve a maximum speed of 2.5 m/s. The propeller is blended into the tail cone to maintain attached flow for better hydrodynamics.

Manoeuvring of the vehicle in 3-D space is facilitated by six control planes – four aft planes arranged in "X" configuration (see Figure 3.3) and two hydroplanes or dive planes which assist with precise depth and roll control. By altering the deflection angle of each aft plane, the vehicle yaw, pitch and roll can be controlled independently. Further, with proper control of the vehicle pitch, the vehicle depth can also be controlled using only the aft planes. The optional twin foreplanes are not always needed, but they can be useful if there is a need for independent depth and pitch control as, for e.g., in a precision terrain-following operation. The planes have a NACA 0024 section. Each control plane is controlled independently by a 24 Volt brushless DC motor that resides inside the control plane body and each plane has its own positive pressure oil compensator attached.

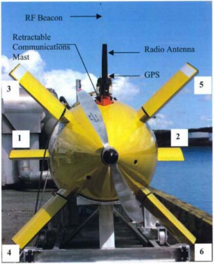

Fig. 3.3 The "X"- tail configuration and the dive planes with the numbering

f. Energy System

The primary source of energy is a bank of E-One Moli Energy 1.3 kWh Lithium ion battery modules. Each module is furnished with a cell monitoring and charging system to manage its output. There is room for 12 such modules and these are housed inside the pressure hull. At the time of test, the *MUN Explorer* used two sets of batteries while the remaining vacant space was occupied by lead blocks of equivalent weight as that of the battery module. The vehicle operates on a bus voltage of 48 VDC.

g. Emergency Systems

Generally, AUVs are equipped with devices that make the task of locating it simple. This is necessary at the end of a mission, during bad weather or darkness when the vehicle has to be recovered by the support ship (or other platforms). A GPS receiver can locate the exact position of the vehicle while the AUV is on the surface. In addition, the vehicle is equipped with a xenon flasher (Novatech ST-400-AR) and a radio beacon (Novatech RF-700A1) built by Novatech Design Ltd., as emergency devices (see Figure 3.3). They are independently powered by their own batteries. The strobe-light automatically turns itself on when the illumination is poor or at night and indicates to the surrounding area of the presence of the AUV; in good light the strobe light is off. The radio beacon is also self-powered and automatically turns itself on when the vehicle is on the surface, so that the vehicle can be found by using the corresponding radio direction finder when in range. The GPS antenna, radio telemetry antenna, RF beacon and strobe light are all mounted on top of the retractable communications mast. On diving, the mast automatically retracts into the hull and remains flush to the hull. When radio communication is needed or a GPS position fix is necessary, the vehicle can climb near the surface at low speed and the mast can be extended approximately 1.0 m above the vehicle body to reach out of the water. To locate the AUV when it is submerged an acoustic device must be relied upon. *MUN*

Explorer uses a self-powered ORE LXT 4336 vehicle transducer as an emergency locator. A general layout of the *MUN Explorer* AUV with its various component instruments and sensors are shown in Figure 3.4.

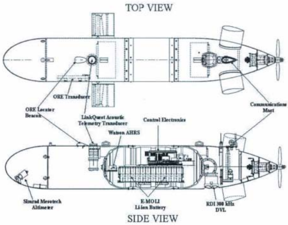

Fig. 3.4 A general layout of the *MUN Explorer* AUV (**Courtesy**: ISE Ltd.)

The above section gave a brief description on the structural and functional features of the *Explorer* AUV. More information and details about the *Explorer* class AUV can be found in *Technical Manuals*[2] supplied by ISE Ltd. Memorial University operates one of the only seven *Explorer* class AUVs that are operational around the world as of date; the others being IFREMER in France, University of Southern Mississippi (USA), University of Bremen (Germany) and Natural Resources Canada (NRCan).

[2] A list of ISE Technical Manuals used for reference are listed at the end of Bibliography

IFREMER operates two *Explorer* class AUVs particularly for seabed survey missions [Rigaud *et al.*, 2004]. *Eagle Ray*[3] is another *Explorer* class AUV owned by the National Institute for Undersea Science and Technology at the University of Southern Mississippi. The National Undersea Research Centre at the University of North Carolina, Wilmington, has operated the same vehicle for high-resolution habitat mapping of deep offshore areas[4]. The Centre for Marine Environmental Sciences (MARUM) at the University of Bremen (Germany) also operates an *Explorer* class AUV called *SEAL*, mainly used for generating high-resolution maps of the seafloor[5]. Lately, in 2009, ISE built two 5000 m rated *Explorer* AUVs for Natural Resources Canada (NRCan) to conduct long distance surveys under Arctic ice in support of Canada's claim under Article 76 of the UN Convention on the Law of the Sea [Tam *et al.*, 2011].

[3] http://www.usm.edu/niust/uvtchome3.htm
[4] http://www.uncw.edu/nurc/auv/oculina2006/summary
[5] http://www.marum.de/en/AUV.html

3.2 Experimental Setup: Deployment, Execution & Recovery

All manoeuvring trials using the *MUN Explorer* AUV were carried out, during the summer of 2006, in Holyrood harbour situated approximately 45 km (*Lat.* = 47.388 and *Long.* = -53.135) south-west of St. John's, Newfoundland. This sheltered body of water had the requisite depth and spread along with the onshore facilities, to carry out all the intended tests. A topographical map of the location as seen in the mission planning software "FleetManager" is shown in Figure 3.5. The water depth ranged from 10 m to 50 m or more in a span of 1 to 2 km and was more than sufficient for all the intended tests.

Fig. 3.5 Topography of the location – Holyrood, as seen in "FleetManager"

3.2.1 Deployment and Recovery

AUVs can either be launched from the shore or from a support vessel depending upon the mission. In our case, due to favourable site conditions and the limited scope of the test, the deployment of the vehicle was done from the wharf using a boom truck. Once the vehicle was launched, it was towed to a safe distance away from the wharf before any missions were executed (see Figure 3.6). *MUN Explorer* AUV used two sets of Li ion batteries and these were able to provide an operating time of approximately little more than two hours. When the vehicle has surfaced at the end of a day's missions, the vehicle computer was shutdown by sending commands from the surface control console (SCC) over radio telemetry and the vehicle was towed closer to the wharf from where it was recovered by the boom truck.

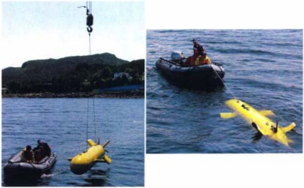

Fig. 3.6 Deployment of AUV from the wharf and tow away to a safe distance

3.2.2 Mission Planning and Execution

The operations control station on the surface (SCC) was housed in a container located on the wharf, which consisted of two PCs in a network: the operator console and the other a mission planning workstation (MPW). The operator console displays vehicle information in graphical and text forms and also accepts commands for actuators and instruments. The operator console runs on a QNX 4.25 Operating System. The mission planning console runs the graphical chart display and mission supervision software "FleetManager". It aids in preparing the mission plans and is run on a Windows XP platform.

The "FleetManager" is a software developed by the company Advanced Concept and System Architecture[6] (ACSA), France and is dedicated to supervision of multiple vehicles and mission planning. "FleetManager" is used for mission planning, vehicle's mission file generation, and real-time supervision. The system is based on C-Map software.

AUV missions are defined as ASCII text files. The "FleetManager" contains tools and features allowing one to create missions with both drawing tools and a text editor that understands the AUV mission file syntax. It contains mission task verbs, built-in keywords and comments. For instance, *entry label* and *goto* are two built-in keywords which are used for looping and jumping within a mission. The task verbs fall into two categories: geographic tasks and other. The geographic tasks are related to a geographical position (latitude and longitude) and are generated graphically. The list of

6 A.C.S.A Underwater GPS, http://www.underwater-gps.com

geographic task verbs includes *target*, *line_follow*, *circle* and *circle_current*. Each geographic task has a configurable vertical mode (depth or altitude); a vertical setpoint, a speed mode and a speed setpoint. Samples of few of the *task verbs* and their syntax as used in a typical mission plan file are shown in *Appendix* – A. The other types of tasks include the ability to turn equipment on or off for a specific part of a mission.

FleetManager permits the user to create manual and automatic routes. By using a series of geographic task verbs, a manual route can be defined as a series of waypoints. By changing depth or altitude setpoints at each point, it is possible to create virtually any trajectory in 3D-space. A built-in editor enables the user to improve the routes, specific geographic parameters such as vertical mode, speed etc. The mission files after creation are saved with the extension '.mis'. Since the mission plans are simple text files, any text editor can be used to create and modify them.

The mission plan files generated using the mission planning console was later transferred to the operator console which in turn was downloaded to the VCC by means of one of the communication links discussed in previous section. In order to overcome the time delay in loading the missions one at a time over data radio telemetry link, it was decided to use the hardwire Ethernet link whereby the whole missions for the day can be downloaded to the VCC quickly, before the launch of the vehicle. As a result several missions consisting of similar manoeuvres were collected together and compiled into a single large mission file with each mission demarcated by an unique label number (*entry_label*). The missions were also designed in such a way that after the completion of each mission (manoeuvre) the vehicle comes to the surface before starting the next mission. This informed the operator on the surface about the completion of a manoeuvre. The data from all instruments were logged on to the VCC during the entire operating period. All data were collected at a sampling frequency of 10 Hz. The log files were later uploaded to the SCC for further analysis using the same hardwire Ethernet link, once after the vehicle was recovered on to the wharf.

3.3 Conclusion

The above discussion has summarized the various features and functions of the *MUN Explorer* AUV that was used for the free-running tests. The experimental set-up and procedures adopted for performing the sea trials were also discussed. A series of standard manoeuvres were planned. These included straight-line test (acceleration/deceleration), turning circles, horizontal and vertical zigzags and a helix. The horizontal plane manoeuvres were performed at a depth of approximately 3 m below the surface so as to avoid any surface disturbance. The depth changing manoeuvres were performed between 3 m and 15 m depth of water. Finally, in order to excite all 6 degrees-of-freedom of the vehicle a helix manoeuvre was also performed. The results and observations from the data analysis of these manoeuvring trials are presented in *Chapter 4*. A summary of the entire content of this chapter, describing the vehicle features, experimental set-up while including samples of vehicle responses from each of the different kinds of manoeuvres were published in Issac *et al* (2007a).

Chapter 4

Manoeuvring Experiments Using the *MUN Explorer* AUV: Data Analysis, Observations

Manoeuvring, in naval architectural terms, can be defined as the controlled change in the direction of motion of a marine vehicle. Manoeuvring characteristics can be obtained by changing or maintaining a pre-defined course and speed of the vehicle in a systematic manner by means of working controls. The controls, in the case of an autonomous underwater vehicle, are control planes and propellers, which enable the vehicle to be manoeuvred in a 3-D space or in all six degrees-of-freedom (DOF).

During a mission, an AUV may undergo different manoeuvring scenarios such as a complete 180° turn ('U' turn) at the end of a survey line or circling around an object or some geophysical features, such as a hydrothermal vent etc., as in times of monitoring. Yet another time it may need to execute a severe turn during obstacle avoidance or frequent depth changes while following a rugged seabed terrain. Further, when AUVs are deployed to observe objects or features that are 1000s of meters deep, it is likely to spiral down in circles to such depths rather than dive along an inclined path, as this latter requires the AUV to be launched far away from the desired location. All these different scenarios demand a high degree of manoeuvrability in order to achieve reasonable position and attitude control.

Traditionally, naval architects have adopted certain standard manoeuvres in order to assess the path-keeping (stability) and path-changing (control) abilities of a marine vehicle. These manoeuvres, some of which may correspond to the above-mentioned scenarios, excite one or more degrees-of-freedom of a vehicle during a typical manoeuvre. The most common manoeuvres often adopted are spiral manoeuvres, zigzag manoeuvres and turning manoeuvres. While spiral manoeuvres and zigzag manoeuvres determine the stability and control characteristics of the vehicle respectively, the turning manoeuvres determine the turning abilities of a vehicle. Keeping the above scenarios in mind, manoeuvring trials were designed to be performed using the *MUN Explorer* AUV; the primary object of which was to obtain data for the validation of the motion simulation model, described in Chapter 2, and at the same time assess the behaviour of the vehicle. Hence, different types of manoeuvres were performed which included a straight-line test involving acceleration-deceleration, turning circles, zigzag tests in horizontal and vertical planes as well as a helix manoeuvre.

This chapter is dedicated to describing the results and observations from the analysis of experimental data obtained from manoeuvring trails performed using an axisymmetric streamlined AUV - the *MUN Explorer*. It also highlights practical difficulties and limitations that were met while carrying out a particular type of manoeuvre.

4.1 Preliminary Steps in Post-Processing the Data

During a typical mission, the AUV records a host of parameters measured by the different sensors and instruments onboard the vehicle. A list of the different parameters that are logged on to the Vehicle Control Computer (VCC) hard drive during a typical mission is presented in Section-1 of *Appendix*-A. These parameters include information on vehicle position, attitude, heading, speed, propeller rpm, depth, altitude, control plane deflections, power input to various sensors, actuators to name a few. Since the focus of these manoeuvring trails were to study the vehicle dynamics and not to use the AUV as a sensor platform, only a subset of the dataset, which pertained to the vehicle kinematics, was necessary for data analysis. The kinematic parameters are parameters that refer to the position, velocity and acceleration of the vehicle. However, some of these parameters cannot be used directly as obtained from the VCC, but required some corrections or modifications while post-processing. For example, in certain cases, such as in the case of position information, a transformation of coordinates was necessary to the position data while in certain other cases, such as in the case of control plane deflections, a modification in defining the parameters were necessary so as to explain the results. These issues are addressed in the following subsections.

4.1.1 Control Plane Deflections and Sign Conventions

Manoeuvring in 3-D space, in the case of the *MUN Explorer* AUV, is facilitated by six control planes – two dive planes fitted forward of the C.G of the vehicle and four tail planes fitted on the aft faired tail portion of the vehicle in an 'X' configuration as shown in Figure 4.1 (see also Fig. 3.3).

A vehicle with X-tail configuration uses all four fins to produce the necessary control forces to manoeuvre in the horizontal or vertical plane, unlike the cruciform '+' shape which uses a pair of fins for pitch and an orthogonal pair for yaw control. In the discussions that follow, the control plane deflections play a crucial role in understanding the behaviour of the vehicle during a manoeuvre. Hence, it is useful to have a brief explanation of the sign conventions used by the vehicle manufacturer and the consequent changes they bring about in the vehicle motion. This is explained through the following sketches.

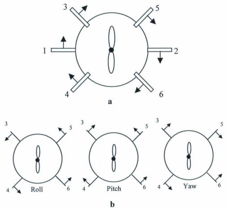

Fig. 4.1 Sketches showing the positive sign conventions for control plane deflection: Arrows show the direction in which the trailing edge is deflected (View: Looking from Rear)

The sketch above (Figure 4.1a) shows the sign convention adopted by the vehicle manufacturer. The arrows show the positive direction of deflection of the trailing edge of the control plane. In other words, a positive deflection is obtained by a right-hand-rule with the thumb pointing away from the body of the vehicle. Figure 4.1b shows the tail fin configuration for positive *pure-roll*, *pure-pitch* and *pure-yaw* control of the vehicle. By the term *pure*, it is implied that such a configuration of fins with each fin having the same magnitude of deflection ($|\delta_3| = |\delta_4| = |\delta_5| = |\delta_6|$) tends to produce a turn (rotation) to the positive direction. It means there is little or no coupling of angular motions. But if the fins have different magnitudes of deflection ($|\delta_3| \neq |\delta_4| \neq |\delta_5| \neq |\delta_6|$) in the same configuration they may produce a coupled motion. Since all four fins are used during manoeuvres, it becomes difficult to represent the vehicle behaviour with respect to each control plane deflection. A convenient way to represent the combined effect of all the four control planes is to describe them in terms of a single effective control plane angle as given by the following formulae [Hemsch and Nielsen, 1986]:

$$\delta P = \frac{\delta_3 + \delta_4 - \delta_5 - \delta_6}{4} \tag{4.1}$$

$$\delta Y = \frac{\delta_3 - \delta_4 + \delta_5 - \delta_6}{4} \quad \text{and} \tag{4.2}$$

$$\delta R = \frac{-\delta_3 - \delta_4 - \delta_5 - \delta_6}{4} \tag{4.3}$$

where δP, δY and δR stand for the effective individual (single) control plane angle for pitch, yaw and roll control respectively. A positive value of δY implies that the particular configuration of the tail fins have a tendency to turn the vehicle to starboard.

The dive planes also engage in assisting pitch and roll motions of the vehicle and their combined effect can be expressed as:

$$\delta P_D = \frac{-\delta_1 + \delta_2}{2} \text{ and } \delta R_D = \frac{-\delta_1 - \delta_2}{2} \tag{4.4}$$

This representation was found to be useful for presenting the results and discussions that follow in Section 4.2.

4.1.2 Data Acquisition and Coordinate Transformation

The vehicle is equipped with a navigation and positioning system that consists of several different sensors to locate and orient the vehicle in 3-D space. In order to locate the position of an object in 3-D space, first of all, an Earth fixed or inertial reference system X_E, Y_E, Z_E has to be defined and to locate an object in such a Cartesian coordinate system, at least three coordinates (x, y, z) are necessary. These position coordinates are supplied by the different sensors that are onboard the vehicle. The horizontal position coordinates were obtained as *latitudes* and *longitudes* from instruments like the GPS as well as the Doppler Velocity Log (DVL), which are located in the aft payload section of the vehicle. The GPS receiver can locate the exact position[1] (*Lat.*, *Long.*) of the vehicle when the AUV is on the surface. The DVL uses position fixes from the GPS to initialize its position. Estimates are then made of position by the process of deduced reckoning (DR), when the vehicle is submerged. These position fixes obtained, as geographical coordinates (Latitudes and Longitudes),

[1] Prior to May 2000, the full accuracy of the US tracking station Terrestrial Reference Frame (TRF) was not made available to non-military users. In the transfer of this TRF to satellite positions, positional accuracies were deliberately worsened by a feature known as selective availability (SA). In May 2000, this intentional degradation of the GPS signals was officially switched off. *A Guide to Coordinate Systems in Great Britain – An introduction to mapping coordinate systems and the use of GPS datasets with Ordnance Survey mapping.*

have to be converted to Cartesian coordinates (x, y). The z coordinate or the depth information is obtained from the pressure sensor mounted inside the forward payload section. Thus the three position coordinates (x, y, z) locates the vehicle in 3-D space. However, they do not represent the C.G of the vehicle as the sensors, which measure these readings, are mounted at different locations inside the vehicle. Knowing the offsets of the sensors with respect to the C.G of the vehicle and taking into account the roll (ϕ), pitch (θ) and yaw (ψ) motions of the vehicle, the coordinates of the C.G can be easily computed.

The location of the vehicle (C.G) does not necessarily give any information about the orientation or attitude of the vehicle. The primary source of this information is the Watson Attitude Heading and Reference System (Watson AHRS E304) mounted in the pressure hull, which provides roll, pitch and heading attitude as well as the angular rates (roll rate p, pitch rate q and yaw rate r) of the vehicle. The Watson AHRS consists of three solid-state angular rate sensors, which measure the angular rates, and these signals are coordinate transformed and then integrated to produce attitude and heading outputs. A second set of independent measurements of the attitudes, heading (ψ), pitch (θ) and roll (ϕ) feedback are available from the DVL as well. In order to know the orientation of the vehicle, a new reference frame X, Y, Z fixed to the body has to be defined. With its origin chosen as the C.G of the vehicle (see Figure 4.2), the positive directions of the X-axis points forward along the longitudinal axis, the Y-axis is to the starboard side and the Z-axis is pointed downwards and is perpendicular to both X and Y, respectively.

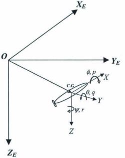

Fig. 4.2 Sketch showing the Earth fixed and Body fixed coordinate axes

The origin O of the local earth fixed coordinate system X_E, Y_E, Z_E, was arbitrarily chosen to be a point on the wharf, projected to the water surface, from which the AUV was launched and whose geographical coordinates (Long. = -53.135 and Lat. = 47.388) were known from the GPS records. The positive direction of the X_E-axis aligned with the true North direction while the Y_E-axis pointed towards the East. The x and y coordinates of the vehicle in Cartesian system was estimated with respect to the origin O for all missions that proceeded from south-to-north direction. However, there were exceptions to this convention when missions were run in the opposite directions – i.e., from north to south, as it was with the case of vertical zigzags, where the origin O was shifted to the starting point at the northern end. In all cases, the positive direction of Z_E axis pointed vertically down.

All data logging by the VCC reflects the GPS referenced time in UTC at a configurable desired rate. The list of parameters to be logged are modified on the

Surface Control Console (SCC) and archived with the mission plan files for future reference. All data was acquired at a sampling frequency of 10 Hz and was saved to the VCC hard drive as Comma Separated Variable (CSV) logfiles throughout the entire test.

4.1.2.1 Convert Geographical Coordinates to Rectangular Coordinates

The DVL is the primary source of speed information when the AUV is submerged and also provides backup altitude, heading, pitch and roll attitudes[2]. The altitude is measured by acoustic echo sounding. The DVL uses four acoustic beams to send sound pulses to the seafloor and listens for their echo. It then calculates the height above the seafloor based on the time taken for the echo to return and calculates the speed of the vehicle over the ground based on the measurement of the Doppler Frequency Shift of the waves returning to the DVL[3].

In the absence of an Inertial Navigation System (INS), the most basic navigation system in an AUV utilizes position estimates by mathematically integrating the heading and speed over time, referred to as deduced Reckoning. The compasses are digital, offering AUVs a reasonably accurate heading estimates while the position estimates are obtained in metric units. However, to estimate the current position of the AUV, the DVL needs to be initialized by position fixes from other instruments such as a GPS. Once the initial position is known, the current position of the vehicle can be estimated by a simple algorithm, which converts the X and Y position in rectangular coordinates (in metric units) to an absolute position in geographic coordinates -

[2] MUN EXPLORER 27-B02-3000 AUV: Control System Specification, Doc. No. ISE-R054-SPC-002-01

[3] http://oceanexplorer.noaa.gov/explorations/08auvfest/logs/may15/may15.html

latitude and *longitude*. This conversion algorithm used by the manufacturer is described in the *Technical Manual*[4] and is reproduced in Section-2 of *Appendix*-A.

As mentioned above, the AUV position information estimated by the DVL and obtained from the log files, are in geographical coordinates. To convert the geographical coordinates to Cartesian coordinates, the above algorithm is simply reversed.

This is one of the primary steps involved in post-processing of the mission data, which eventually provides the position coordinates (*x, y, z*) of the C.G of the vehicle. Once the position estimate of the C.G of the vehicle is obtained, other kinematic parameters can be derived from it.

4.1.2.2 Estimation of Earth and Body fixed Translational Velocities

The position vector (η_1) and orientation vector (η_2) of the vehicle, according to the notations used in Fossen (1994), are described relative to the inertial reference frame or the earth fixed frame while the translational and angular velocities of the vehicle should be expressed in the body-fixed frame of reference. The knowledge of body fixed translational and angular velocities are essential to describing the vehicle behaviour during different manoeuvres. The vehicle attitude and heading information (η_2) as well as the angular rates (*p, q, r*) measured by the Watson AHRS are both available from the mission data. The only parameters that are not directly available from the data are the body fixed translational velocities (*u, v,* w). These quantities are derived from the position estimates.

[4] MUN EXPLORER 27-B02-3000 AUV – Technical Manual, Volume V, ACE Documentation.

The rate of change of position $[x, y, z]$ of the vehicle C.G in 3-D space gives the global velocity components $[\dot{x}, \dot{y}, \dot{z}]$. The translational velocity components (u, v, w) were derived from the global velocity components $(\dot{x}, \dot{y}, \dot{z})$ by a simple coordinate transformation knowing the vehicle attitudes $[\theta, \phi, \psi]$, otherwise known as *Euler angles*. This transformation is represented as follows:

$$\begin{bmatrix} u \\ v \\ w \end{bmatrix} = \mathbf{J}_1^{-1}(\boldsymbol{\eta}_2) \begin{bmatrix} \dot{x} \\ \dot{y} \\ \dot{z} \end{bmatrix} \text{ or } \mathbf{v} = \mathbf{J}_1^{-1}(\boldsymbol{\eta}_2)\dot{\boldsymbol{\eta}}_1$$

where $\mathbf{J}_1(\boldsymbol{\eta}_2)$ is an orthogonal transformation matrix described in *Section 2.1.2* of Chapter 2.

The above procedures described through *Section 4.1.2* were implemented in a MATLAB™ program as a preliminary step to post-processing the mission data.

The sections that follow describe in detail the manoeuvring trials that were performed using the *MUN Explorer* AUV. The trials consisted of straight-line tests (acceleration-deceleration tests), turning circles, zigzags in horizontal and vertical planes and helix manoeuvres. The following sections also include the methods and measures adopted for performing each type of test and discuss the results and observations made thereof.

4.2 Acceleration and Deceleration Tests – Data Analysis

An acceleration test is performed by increasing the speed of the vehicle from rest or from a particular ahead speed to a higher ahead speed while a deceleration test is performed by decreasing the speed of a vehicle from a particular speed to a lower value or allowing the vehicle to coast to rest (Lewis, 1989). However, this was not always possible with this underwater vehicle for the following reasons. In order to avoid any surface disturbance, the test was performed at a depth of approximately 3 m below the surface. To make the vehicle dive to a specified depth, the vehicle has to be moving at a considerable speed such that the control planes are effective in making it dive to the command depth. Once it has reached the command depth, it is difficult to maintain the vehicle at rest. Theoretically, an AUV is a neutrally buoyant vehicle. However, for practical reasons, an AUV is often designed to be slightly positively buoyant and therefore it becomes difficult or impossible to maintain the vehicle at rest at any depth except on the surface because the vehicle slowly tends to rise to the surface. Owing to the above difficulties, the tests were done in a little different manner from the conventional method.

The acceleration-deceleration or straight-line test was performed by changing the speed at regular intervals while the vehicle followed a straight-line path at approximately 3 m depth. The vehicle was programmed to start from the surface at a speed of 1.5 m/s, which enabled the vehicle to dive to 3 m depth. Allowing enough time to reach the prescribed depth and to level off, the actual mission started by changing the speed at regular intervals. Figure 4.3 shows the trajectory of the vehicle from a particular acceleration-deceleration test. The vehicle headed north in a straight line starting with a maximum set-speed of 2.5 m/s and reduced it in steps of 0.5 m/s until it reached 1 m/s towards the north end of the line. This constitutes the deceleration phase. The vehicle took a turn to starboard at the end of the line and started the acceleration phase by heading south in a straight line. Here it started with a minimum set-speed of 1 m/s and increased it in steps of 0.5 m/s to reach a maximum of 2.5 m/s towards the south end of the line. Each speed was maintained for a length-of-travel of 100 m and at no time during the mission did the vehicle come to a complete stop.

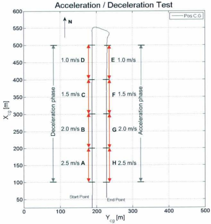

Fig. 4.3 Trajectory of the AUV from a straight-line test

The segments A, B, C, D, etc., denoted the length-of-travel for which a particular set-speed was maintained constant. The vehicle targets the waypoints picked on the map denoted by the start and end points of each segment, which lie in a straight line in the north-south direction. The test was repeated once more.

The drift or offset of the vehicle from the predefined straight line was estimated from the knowledge of the geographical coordinates of the waypoints. The two parallel lines were spaced 40 m apart with the abscissa of the deceleration phase line corresponding to a straight line passing through 187.5 m from the chosen origin while the acceleration phase line ran through 227.5 m. Any deviation of the vehicle coordinates (Y_{cg}) from these values indicated a drift of the vehicle from the actual straight course. The offset of the vehicle was calculated separately for the deceleration and acceleration phase. It was found from both the tests that during the deceleration phase, the vehicle drifted by about 0.17% and 0.3% laterally of the total distance traveled and almost all of this happened during the slow-speed regime denoted by segment D. This may have been due to the presence of a crosscurrent. This lateral drift in the case of acceleration phase was found to be slightly higher (0.55%) at segment E as the vehicle turned around and started from a slow speed of 1 m/s. Except for these two slow speed segments D and E, the vehicle maintained its course throughout the rest of its path.

Figure 4.4 shows the time series of forward speed and corresponding propeller RPM. The first-half of Figure 4.4 corresponds to the deceleration phase of the run and the latter half corresponds to the acceleration phase of the run. A closer look at the figure reveals that the propeller RPM for the acceleration phase is slightly lower than the propeller RPM for the deceleration phase and this difference is seen predominant at slower speeds. This discrepancy along with the previous observation of lateral drift indicates the presence of some crosscurrents whose in-line component has worked to the advantage of the vehicle in the acceleration phase.

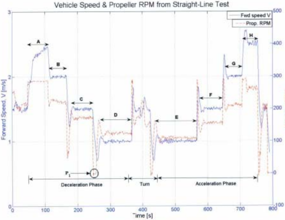

Fig. 4.4 Time series of speed and corresponding propeller RPM from the straight-line test

The forward speeds versus propeller RPM from both the tests are summarized in a single plot shown in Figure 4.5. Here, it becomes evident that the propeller RPM throughout the acceleration phase was lower than the propeller RPM during the deceleration phase, with the difference in propeller RPM growing larger at slower speeds. This indicates that the vehicle is more susceptible to in-line currents during slow speed. Further, there is a bit of scatter in the deceleration curve at the higher speed region, which corresponds to the segment A of figures 4.3 and 4.4. The segment A falls toward the beginning of the mission, soon after the dive, and the vehicle didn't quite hit the start point of segment A as it was still racing towards the command depth.

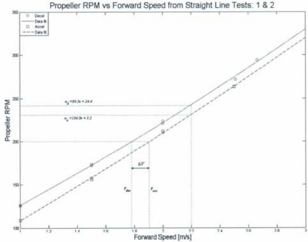

Fig. 4.5 Propeller RPM vs. forward speed for both acceleration and deceleration phases

From Figure 4.5, it is clear that for the same propeller RPM the vehicle has two different speeds during the two different phases; the difference in the speeds ΔV being brought about by the effect of in-line current. Conversely, the thrust required to maintain the same speed in one direction is different from thrust required to maintain the same speed in the opposite direction and hence the difference in propeller RPM[1]: n_d and n_a ($n_d > n_a$). As both the curves show a linear relationship, the true speed corresponding to the given RPM may be closer to the arithmetic mean of the two speeds: V_{dec} and V_{acc} ($V_{acc} > V_{dec}$). Extrapolating this information to zero RPM would give a rough estimate of the current velocity in the region. This is presented in Figure

[1] Note that here n is used to represent revolutions per minute (RPM). Later in the chapter it will be used to represent revolutions per second (rps).

4.6 where the difference in speed ΔV is plotted against the propeller RPM and the speed corresponding to zero propeller RPM denotes the current velocity, v_c. If a constant current is to be assumed in the region of the test (a reasonable assumption as the entire test was conducted within a span of less than 500 m), it is apparent from Figure 4.6 that the in-line current velocity, v_c, was around 0.2 m/s in the south direction. This would explain the reason for an increased propeller RPM during the deceleration phase while the vehicle was heading north.

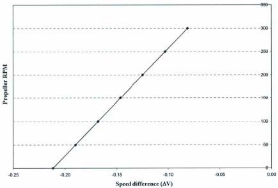

Fig. 4.6 Difference in speed ΔV between acceleration and deceleration phase, corresponding to the same propeller RPM

4.2.1 Acceleration, Deceleration and Stopping Time and Distance

The vehicle controller commands the vehicle to change its speed to the next set-speed as it arrived at the start point of each segment. Consequently, the vehicle responded by accelerating (decelerating) to the next set-speed. This transition from the initial approach speed to the next set-speed takes a while before the vehicle settles to the new steady speed. As a result the vehicle actually travelled a portion of the original 100 m long transect during this transition period and hence never really traveled the entire 100 m long segment at a particular set-speed. The time taken for the vehicle to reach the steady speed and the distance traveled during this transition time were estimated from the data. These are shown in the plots, Figure 4.7a and 4.7b.

In Figure 4.7a and Figure 4.7b, the change in speed and the distance traveled during the transition period are expressed in non-dimensional form. The change in speed is shown as a ratio of the actual speed to the initial approach speed, V_0. The *x*-axis represents the time in seconds taken by the vehicle to reach the steady speed. In all cases, the vehicle overshoots (undershoots) the command speed and later stabilizes to it. The distance traveled by the vehicle during this period is expressed in non-dimensional form as the number of vehicle lengths traveled.

Figure 4.7a shows the time taken and the distance traveled during the deceleration periods from both tests (1 & 2). The results from the first test are shown by *markers* of different shape, denoted by V1 and D1, while the results from the second tests are shown by *bold* (D2) and *dashed* (V2) lines. The V and D here represent the velocity and distance travelled by the vehicle respectively. It can be seen from the figure that the distance travelled by the vehicle during transition from one test almost exactly matched that obtained from the second test, except in the case of deceleration from 2.5 m/s to 2.0 m/s of the second test. Since this segment fell at the beginning of the mission, it so happened in the second test that the vehicle reached the start point coordinates of segment A before it had dived to the command depth. Hence, for this particular transition it is more reliable to depend on the results from the first test.

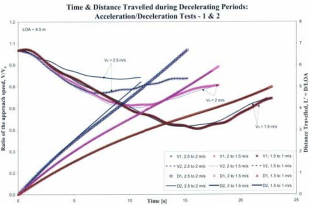

Fig. 4.7a Distance travelled by the vehicle during the transition from one speed to another in the deceleration phase

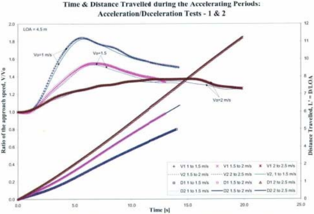

Fig. 4.7b Distance travelled by the vehicle during the transition from one speed to another in the acceleration phase

Figure 4.7b shows the time and distance travelled by the vehicle during the acceleration periods from both tests (1 & 2). From both the deceleration and the acceleration tests, the vehicle travelled the maximum distance during the transition between 2.0 and 2.5 m/s; the higher speed regimes. The vehicle travelled a distance of about 30 m (~ 6.5 LOA) as it decelerated from 2.5 m/s to a steady speed of 2.0 m/s and it travelled a distance of about 50 m (~ 11 LOA) when it accelerated from 2.0 m/s to a steady speed of 2.5 m/s. However, the time taken to reach steady speed was a maximum when the vehicle decelerated from 1.5 to 1.0 m/s, i.e., in segment D. Note that this segment was also influenced by water currents as discussed earlier.

Stopping Distance

Stopping distance is primarily of interest from the point of view of emergency manoeuvres such as avoiding collision, ramming etc. The results from the deceleration time and distance, shown in Figure 4.7a, could have been exploited to estimate the stopping distance, had the propeller stopped spinning during the deceleration periods. This was not the case though. However, a closer analysis of the time series of the propeller RPM revealed that the propeller actually stopped spinning (RPM = 0) for a short span of time (~ 9 s), which occurred when the vehicle decelerated from 1.5 to 1.0 m/s. This region of zero propeller RPM, denoted by P_1 in Figure 4.4, happened in both the tests at the same region, thus making it no accident. Therefore, this region of zero propeller RPM was exploited to make a rough estimate of the stopping distance. Since propeller RPM was zero during this period of 9 s, the scenario represented the case of a vehicle *coasting* to rest.

Speed Reduction and Distance Travelled at Zero RPM
Time Series: 282.2s to 291.3s: Test - 1

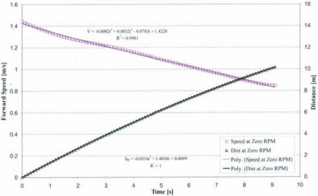

Speed Reduction and Distance Travelled at Zero RPM
Time Series: 247s to 255.9s: Test - 2

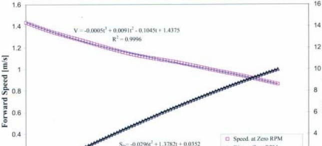

Fig. 4.8 Deceleration distances during zero propeller RPM from Tests 1 and 2

Figure 4.8 shows that portion of the time series, from both tests, during which the propeller RPM was recorded zero, which happened when the vehicle decelerated from 1.5 to 1.0 m/s. The distance traveled during this period of zero RPM is also plotted along with the deceleration curve. One of the two key factors affecting the stopping distance is the approach speed of the vehicle; the other being the inertial effect of the vehicle's mass and longitudinal added mass [Lewis, 1989]. The vehicle approach speed measured was 1.45 m/s, which was very close to the optimum operational speed ($\equiv$ 3 knots) of most AUVs including the *MUN Explorer*. The vehicle traveled a distance of about 10 m during this 9 s before the propeller started spinning again.

The stopping distance of the AUV from this operational speed of 1.45 m/s was roughly estimated by extrapolating the curves shown in Figure 4.8. By extrapolating the deceleration curve, the time taken by the vehicle to come to a complete stop ($V = 0$) can be determined. The time to reach zero speed thus estimated was around 17 s. Knowing this time, the stopping distance of the vehicle can be calculated from the expressions shown in the figure. This was estimated to be around 15 m.

4.2.2 Control Plane Angles for Straight Line Tests

The control plane deflections corresponding to each forward speed from both tests are shown in Tables 4.1 and 4.2. In an ideal straight-line test the control plane deflections should be zero or close to zero. However, from the Tables 4.1 and 4.2, it can be seen that the deflections are significant at slower speeds. The terms $\delta 1$, $\delta 2$, $\delta 3$, etc., are the measured control plane angles from the test and the numbering corresponds to the plane numbers shown in Figure 4.1. The effective individual control plane deflections

δP, δY, δR, δP_D and δR_D were calculated using expressions (4.1) through (4.4). For instance, δP for the case of 1 m/s in the deceleration phase can be calculated as follows:

$$\delta P = \frac{\delta_3 + \delta_4 - \delta_5 - \delta_6}{4}$$

$$= \frac{4.82 + 6.36 - (-6.18) - (-4.66)}{4} = 5.51^{\circ}$$

A positive value of δP or δY or δR implies that the given combination of plane deflections will tend to produce a positive attitude. For instance, a positive value of δY implies that the combination of control plane deflection would have a tendency to turn the vehicle to starboard. Further, the dive planes are effective in maintaining pitch and roll control as well. Their combined effects are given by the values δP_D and δR_D. The Tables also show the measured pitch and roll attitudes of the vehicle at each speed during the mission.

Table 4.1

Control Plane Deflection Angles and Calculated Effective Plane Angles for Straight Line Test - 1

			Dive Planes		Tail Plane				Dive Plane		Tail Plane comb.			Ang. Disp	
Seg.	**V**	**n**	**δ1**	**δ2**	**δ3**	**δ4**	**δ5**	**δ6**	**δP_D**	**δR_D**	**δP**	**δY**	**δR**	**Roll**	**Pitch**
	m/s	rpm	deg	deg	deg	deg	deg	deg	deg	deg	deg	deg	deg	ϕ, deg	θ, deg
	Deceleration Phase														
	2.66	294.4	0.34	-0.97	-0.23	0.98	-1.85	-0.24	-0.66	0.31	0.71	-0.70	0.335		
A	2.51	271.8	1.21	-1.73	-0.47	1.60	-1.76	-0.61	-1.47	0.26	0.88	-0.80	0.309	0.013	-0.017
B	2.00	218.9	2.16	-2.52	1.39	2.33	-2.92	-1.88	-2.34	0.18	2.13	-0.49	0.270	-0.017	-0.010
C	1.50	170.5	0.21	-0.35	2.42	3.49	-3.80	-3.17	-0.28	0.07	3.22	-0.42	0.264	-0.001	-1.331
D	1.00	127.5	-4.32	4.21	4.82	6.36	-6.18	-4.66	4.27	0.06	5.51	-0.76	-0.086	-0.002	-4.057
	Accelelration Phase														
E	1.00	108.6	-7.36	7.29	7.43	9.07	-7.15	-5.90	7.33	0.03	7.39	-0.72	-0.863	-0.020	-6.210
F	1.50	159.4	-1.53	1.48	2.52	3.82	-4.29	-3.33	1.51	0.03	3.49	-0.57	0.318	-0.005	-1.741
G	2.00	214.1	1.56	-1.81	1.12	2.31	-2.76	-1.74	-1.69	0.13	1.98	-0.55	0.266	0.008	-0.020
H	2.50	264.2	0.57	-1.08	-0.23	1.20	-1.45	-0.87	-0.82	0.25	0.82	-0.50	0.336	0.008	-0.006

Table 4.2
Control Plane Deflection Angles and Calculated Effective Plane Angles for Straight Line Test - 2

			Dive Planes		Tail Plane				Dive Plane		Tail Plane comb.			Ang. Disp	
Seg.	**V**	**n**	**$\delta 1$**	**$\delta 2$**	**$\delta 3$**	**$\delta 4$**	**$\delta 5$**	**$\delta 6$**	**δP_D**	**δR_D**	**δP**	**δY**	**δR**	**Roll**	**Pitch**
	m/s	rpm	deg	deg	deg	deg	deg	deg	deg	deg	deg	deg	deg	ϕ, deg	θ, deg
	Deceleration Phase														
A	2.38	287.0	1.71	-2.13	-0.80	0.47	-2.89	0.01	-1.92	0.21	0.64	-1.04	0.804	0.019	0.017
B	2.00	223.9	2.25	-2.58	1.44	2.16	-2.97	-1.68	-2.41	0.17	2.07	-0.50	0.264	0.006	-0.042
C	1.50	173.4	0.60	-0.64	2.12	3.59	-3.81	-3.11	-0.62	0.02	3.16	-0.54	0.301	0.009	-1.183
D	1.00	125.5	-4.59	4.52	4.83	6.54	-5.99	-4.89	4.55	0.03	5.57	-0.70	-0.123	-0.004	-4.055
	Accelelration Phase														
E	1.00	109.0	-7.09	6.96	7.63	8.77	-6.91	-5.83	7.03	0.06	7.28	-0.55	-0.914	0.005	-6.167
F	1.50	155.8	-1.31	1.18	2.73	3.99	-4.17	-3.17	1.24	0.07	3.51	-0.56	0.155	0.014	-1.750
G	2.00	210.8	1.47	-1.67	0.79	1.68	-2.65	-1.78	-1.57	0.10	1.73	-0.44	0.489	0.020	-0.068
H	2.50	263.2	0.46	-0.87	0.10	1.08	-1.37	-0.75	-0.67	0.21	0.83	-0.40	0.233	-0.051	-0.030

Tables 4.1 and 4.2 show that slower speeds (1m/s) required larger plane deflections, in order to maintain level flight at constant forward speed. The combined effect of these plane deflections resulted in larger values of δP and δP_D. From the Tables, it is also seen that the roll attitudes of the vehicle were negligible while the pitch attitudes at slow speeds were significant. Further, the significantly high and positive values of δP_D and δP for slow speed runs indicate that all six control planes were working towards pitching the nose up. Despite all six control planes working hard to bring the vehicle nose-up, the pitch attitude of the vehicle was negative. This could be explained by the fact that the vehicle is normally trimmed nose down and with starboard roll. Nose down (i.e. tail up) trim is to ensure that the antennas mounted on the communications mast come up out of the water in a failsafe condition. Starboard roll is maintained to compensate for the effect of propeller torque. As the speed decreases, the amount of force generated by each control plane is decreased until a point is reached where the net forces are not enough to overcome the vehicle's buoyancy and trim. This explains the reason for a negative pitch attitude despite positive plane deflections during slow

speed, whereas at higher speeds the planes generate sufficient lift force to overcome the innate nose-down characteristic and hence the vehicle has a level attitude.

4.2.3 Estimation of Thrust from Test and Propeller Data

The acceleration-deceleration tests have provided data from which a relationship between the propeller RPM and vehicle forward speed was established. This was shown in Figure 4.5. Also, if the thrust developed by the propeller to push the vehicle at a certain speed can be estimated, this additional and useful information could be incorporated in the hydrodynamic motion simulation model. The information obtained from the test data (Figure 4.5) was not sufficient to estimate the thrust developed by the propeller.

The thrust T and torque Q developed by a propeller are usually expressed as functions of propeller RPM n and are given by:

$$\text{Thrust coefficient, } K_T = \frac{T}{\rho n^2 D_p^4} \tag{4.8}$$

$$\text{Torque coefficient, } K_Q = \frac{Q}{\rho n^2 D_p^5} \tag{4.9}$$

where D_p is the diameter of the propeller and ρ is the density of the water.

The propeller open-water efficiency is derived from the thrust and torque coefficients:

$$\eta_0 = \frac{K_T J}{K_Q 2\pi} \tag{4.10}$$

where J is the advance ratio defined as $J = \frac{V_A}{nD_p}$ (4.11)

while V_A is the average inflow speed to the propeller.

The *MUN Explorer* AUV was propelled by a 0.65 m diameter twin-bladed propeller driven by a Hathaway Emoteq 48 VDC brushless motor coupled to a 3:1 planetary gear. Figure 4.9 shows the propeller open-water diagram consisting of thrust coefficient K_T and torque coefficient K_Q. This was obtained from the manufacturer – International Submarine Engineering Ltd.

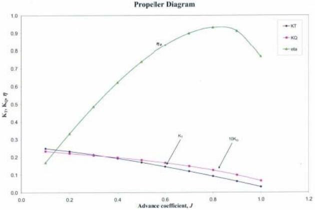

Fig. 4.9 Propeller characteristics diagram showing KT, KQ and h0 versus advance ratio J
(Courtesy: ISE Ltd.)

The open-water diagrams can be used for determining the operating point thrust, torque, and power, generated by the propeller, particularly when the vehicle is moving ahead at a steady speed. Bertram (2000) indicates, that for cases where the speed is changed, so-called four-quadrant diagrams are used. Since we intend to estimate the thrust and torque during the steady straight-ahead motion of the vehicle, the propeller characteristics shown in Figure 4.9 were utilized. Knowing K_T and K_Q values from the Figure 4.9, equations (4.8) and (4.9) were used to estimate the thrust and torque developed by the propeller.

The propeller thrust and torque thus determined were corrected for hull-propeller interaction effects by using appropriate correction factors such as Taylor's *wake-fraction*, ω, and *thrust-deduction* coefficient t. The wake-fraction accounts for the energy lost in the flow behind the vehicle before it enters the propeller while the thrust-deduction coefficient accounts for the increase in thrust required due to the low pressure area ahead of the propeller, which acts on the hull. Both the thrust deduction and wake fraction terms can be accurately determined through model tests but in the absence of such data, they could be approximated as a function of propeller to hull diameter ratio. For instance, see Figure 40 of Allmendinger (1990).

Burcher and Rydill (1994), in addition to the ratio of propeller to maximum hull diameter, also considered the effect of hull tail-cone included angle in calculating the these coefficients ω and t. Figure 4.10 shows the wake fraction as a function of propeller-to-hull diameter ratio and the tail-cone included angle while Figure 4.11 shows the thrust deduction coefficient as a function of the same. The data for both figures were sourced from Burcher and Rydill (1994).

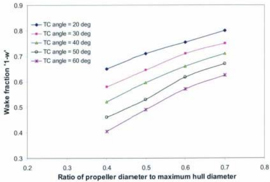

Fig. 4.10 Taylor wake fraction versus propeller size and tail-cone included angle

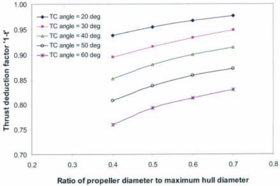

Fig. 4.11 Thrust deduction factor versus propeller size and tail-cone included angle

The *MUN Explorer* had a propeller-to-hull diameter ratio of 0.94 and the tail-cone included angle was estimated to be 44.8°. Clearly, this ratio of 0.94 falls outside the range of the charts shown in Figure 4.10 and Figure 4.11. Nevertheless, extrapolation of the charts provided an approximate idea about the values of ω and t to be used for calculation purposes. In the calculations that follow, these coefficients were calculated to be $\omega = 0.2$ and $t = 0.1$.

Thrust vs. Speed Relationship

The relationship between forward speed and the corresponding propeller RPM during steady straight-ahead motion of the vehicle was already established through Figure 4.5. The thrust developed by the propeller corresponding to each forward speed was estimated by the method discussed above. This is shown in Table 4.3. A curve-fit showing this relationship between forward speed and propeller thrust is also shown in Figure 4.12.

Table 4.3
Thrust and Torque Developed by the Propeller

	V	RPM	n	V_a	$J=V_a/(n.D)$	K_T	K_Q	T [N]	Q [N.m]
Test #1	2.66	294.6	4.910	2.130	0.6673	0.129	0.015	512.0	44.0
	2.50	272.5	4.542	1.999	0.6771	0.126	0.015	428.7	37.1
	2.00	218.9	3.648	1.601	0.6754	0.127	0.015	278.0	24.0
	1.50	170.5	2.842	1.200	0.6493	0.134	0.016	177.5	15.1
	1.00	127.5	2.125	0.800	0.5794	0.151	0.017	112.5	9.2
	1.00	108.6	1.810	0.800	0.6804	0.125	0.015	67.7	5.9
	1.50	159.3	2.655	1.200	0.6951	0.121	0.015	140.9	12.4
	2.00	214.1	3.568	1.599	0.6893	0.123	0.015	257.6	22.5
	2.50	264.3	4.405	2.000	0.6984	0.121	0.015	385.2	33.9
Test #2	2.00	222.8	3.713	1.603	0.6640	0.130	0.015	295.2	25.3
	1.50	173.5	2.891	1.200	0.6384	0.136	0.016	187.6	15.8
	1.00	125.4	2.090	0.801	0.5894	0.149	0.017	107.2	8.8
	1.00	108.8	1.813	0.800	0.6790	0.126	0.015	68.1	5.9
	1.50	155.7	2.595	1.200	0.7114	0.117	0.014	129.8	11.5
	2.00	210.7	3.511	1.599	0.7006	0.120	0.015	243.3	21.4
	2.50	263.1	4.385	2.000	0.7016	0.120	0.015	378.9	33.4

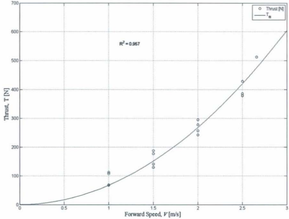

Fig. 4.12 Thrust versus forward speed relationship for the *MUN Explorer* AUV

This relationship between forward speed and thrust was used as a look-up table in the hydrodynamic simulation model for modelling a simple propulsion module.

Bare Hull Drag Coefficient, C_{DB0}

The hydrodynamic motion simulation model, described through Chapter 2, which is based on the *component build-up method*, calculates the hydrodynamic loads on each component separately. In order to calculate the drag on the bare hull, it was necessary to know the bare hull drag coefficient, C_{DB0}. Normally, this coefficient is obtained from tank testing of a scale model of the vehicle. Here, an attempt was made to deduce this drag coefficient data roughly from the resistance of the vehicle.

When the vehicle travels straight-ahead at a constant speed, the drag (resistance) experienced by the vehicle is equal to the thrust, T, developed by the propeller, provided, T, is modified for thrust deduction, t. This is given by the relation:

$$R = T(1-t) \tag{4.12}$$

On the other hand, the resistance of a body to motion through a fluid is generally expressed by the relation:

$$R = \frac{1}{2}\rho C_D A_{ref} V^2 \tag{4.13}$$

where ρ is the density of the fluid, A_{ref} is the reference area of the body, V is the flow speed and C_D is the drag coefficient related to the shape of the body. Equation (4.12) represents the total resistance of the body, which includes all the appendages added to the hull; six control planes in the case of the *MUN Explorer*. Deducting the drag contribution of control planes from the total drag provides a rough estimate of the bare hull drag.

$$R_{BH} = R - R_{CP} \tag{4.14}$$

where R_{BH} is the bare hull resistance and R_{CP} is the resistance from all six control planes. Note that the total resistance, R, incorporates within it the interaction effects between the hull and the appendages since this quantity was calculated from the thrust, T, required to push the whole vehicle. A plot similar to Figure 4.12 can be generated to fit the bare bull resistance data to the forward speed and is shown in Figure 4.13. However, the hull drag coefficient thus estimated will contain some errors due to the interactions from appendages.

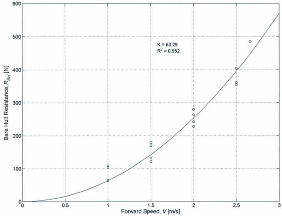

Fig. 4.13 Bare hull resistance versus forward speed relationship for the *MUN Explorer* AUV

As the density of the fluid, reference area and drag coefficient of the body remains a constant, the general expression for resistance (4.13) can be expressed as a function of forward speed in the form

$$R_{BH} = KV^2 \tag{4.15}$$

where $K = \frac{1}{2}\rho C_{DB0} A_{ref}$ in which A_{ref} was the wetted surface area. The value of K was estimated through a basic regression analysis and is shown in Figure 4.13. From the expression for K the drag coefficient for the bare hull, C_{DB0}, was estimated, knowing the reference area of the hull[2], A_{ref}.

[2] See *Appendix – B* for the calculation of wetted surface area of the *MUN Explorer* hull

$$C_{DB0} = \frac{2K}{\rho A_{ref}} = 0.0143$$

4.2.4 Summary of Straight-line Tests

The straight-line tests provided information about some of the steady-state and transient characteristics of the vehicle.

a. It was observed that the propeller RPM, and consequently the thrust; necessary to maintain a certain speed in one direction (deceleration phase) was different from that necessary to maintain the same speed in the opposite direction (acceleration phase) indicating the presence of a current.

b. The in-line current velocity was estimated to be around 0.2 m/s in the south direction and this explained the reason for the increase in propeller RPM observed during the deceleration phase when the vehicle was heading north. The vehicle adjusted its propeller RPM so as to maintain a constant speed-over-ground. This is because the vehicle was operated in a *constant speed* mode. In a vehicle dynamics study where vehicle response is of importance, such as this thesis, it is more appropriate to use the *constant propeller RPM* rather than the *constant speed* mode. This would help capture the vehicle response to environmental effects or external disturbances.

c. The time to accelerate (decelerate) from one speed to another and the distance travelled during this transition period was estimated. As expected, the higher speed regime (transition between 2 m/s and 2.5 m/s) required the maximum distance, with the distance covered during acceleration phase greater than the deceleration phase.

d. The time taken by the vehicle during transition from one speed to another was a maximum when the vehicle decelerated from 1.5 m/s to 1.0 m/s (~ 23 s) while the distance travelled during this transition (~ 5 LOA) was almost equal to the distance travelled by the vehicle during its acceleration from 1.0 m/s to 1.5 m/s.

e. From control plane deflections, it was observed that larger dive plane deflections were needed at slower speeds so as to counteract the inherent nose-down attitude of the vehicle and to maintain a level flight.

f. A relationship between thrust versus forward speed was established, which could be used to develop a simple propulsion module for the hydrodynamic simulation model.

g. A rough estimate of the bare hull resistance was calculated from the knowledge of the thrust developed during steady-state speed, by deducting the resistance due to the appendages from the thrust. An attempt was also made to estimate the drag coefficient, C_{DB0}, of the bare hull based on wetted surface area.

A subset of the results from the data analysis of straight-line tests has already been published in Issac *et al* (2007b).

4.3 Turning Circles Data Analysis

The turning circle is a steady-state manoeuvre in which the vehicle enters a steady turn at a constant speed. Traditionally, a turning circle is performed by deflecting the rudders to a predefined angle and holding them fixed resulting in the vehicle entering a circular path. The turning circle manoeuvres assess the turning ability of a vehicle and also provides information on the effectiveness of the rudder. This may be the case of interest in a real-life mission when the AUV takes a turn at the end of transects or when it circles around a station of interest such as a hydrothermal vent or other geo-physical features. According to the International Towing Tank Conference (ITTC) recommended procedures (ITTC, 2005), the turning circle tests should be performed to both port and starboard side at approach speed with maximum rudder angle and is necessary to maintain the steady turn for at least 540 degrees to determine the main parameters of this trial.

The original plan according to the proposed research was to obtain manoeuvring data for *mild, moderate* and *extreme* cases of manoeuvres. This is defined as circles, which are the outcome of mild, moderate, and extreme or maximum allowable rudder deflections at different forward speeds. However, this was not possible with the *MUN Explorer* as the vehicle controller program only allowed the user to set a radius of turn and forward speed as the input parameters, contrary to rudder angle and forward speed as in the conventional case. The criteria then were to perform circles of different turning radii at a certain speed starting from the least possible radius (10 m) specified by the manufacturer. The list of turning circles that were performed is shown in Table 4.4, along with some of the steady-state parameters that were estimated from the manoeuvring data. All turns were performed to the starboard side. Although one turning mission in each set was planned to be executed to the port side, the outcome of those experiments turned out to be unsuccessful with the vehicle turning to the starboard instead. In addition, it was not possible to complete the entire series of circles at 2 m/s speed due to shortage of test time and battery life.

The turning circle missions were generated using the task verb *circle* of the "FleetManager" software. This demands that the geographical coordinates of the centre of the circle be specified about which the vehicle goes around in a circle of command radius at the command speed. Given the command radius and speed, the control plane deflections necessary for achieving a circle having the command radius are automatically determined and set by the vehicle control system during the mission execution. All circles were performed at a depth of approximately 3 m. In order to account for any possible drift in the trajectory due to currents or other disturbances, all missions were planned to execute 2.5 revolutions. In normal cases, the mission plan file created at the surface console is loaded on to the VCC via radio telemetry and the AUV is allowed to perform one mission at a time. However, to overcome the difficulties encountered in loading the mission files to the vehicle computer one at a time, the entire circle missions were compiled on to a single large mission plan file with each mission demarcated by a unique label number (*entry_label*). This single large mission file was uploaded to the vehicle computer through hard-wire connection before the vehicle was deployed. This method was successful in enabling the vehicle to do several missions consecutively on a given day.

The actual radius of turn, R_a obtained was plotted against the commanded radius R_c and is shown in Figure 4.14. The actual radius R_a obtained from each test was always larger than the commanded radius of turn R_c. The amount ΔR by which the actual radius differed from the command radius, for forward speeds 1.0 and 1.5 m/s, are represented as a factor *f* in the plot shown in Figure 4.15.

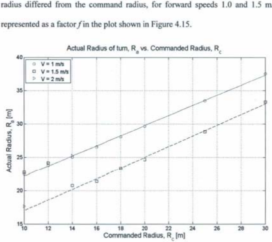

Fig. 4.14 Actual radius, R_a vs. command radius, R_c for forward speeds, V = 1.0, 1.5 and 2.0 m/s

It is observed from Figure 4.15 that the difference in actual radius from the command radius (ΔR) reduced as the command radius grew larger. In other words, the discrepancy between command and actual radii reduced as the radius of turn grew larger. This increase in radius for all runs is expected to have occurred due to some erroneous control gain settings for the control planes; although the exact reason for this discrepancy is unknown. The increment factor, *f*, for forward speeds 1.5 m/s was similar to that for speed 1 m/s for those tests performed on Day-2 (R_c = 10 & 12 m), but for those tests performed on Day 3 (D3), there is a drop in the factor, *f*, for 1.5 m/s speed. Further, when the last two tests in Table 4.4 were performed on Day-4, the vehicle was outfitted with sensors such as the CTD sensor and Rhodamine fluorometer for water column sampling, Niu (2007a), Niu (2007b), as seen in Figure 4.16. The presence of these sensors on the exterior of the body alters the fluid flow around the body consequently affecting the hydrodynamic loads acting on the vehicle. Hence, it may not be appropriate to use these data for validation purposes. As a result, the discussions that follow only contain examples from results corresponding to forward speeds 1 m/s and 1.5 m/s.

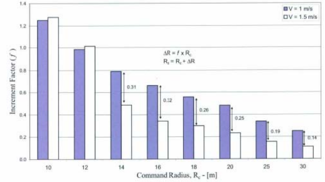

Fig. 4.15 Increment factor (*f*) by which $\mathbf{R_s}$ differ from $\mathbf{R_c}$ at speeds, V = 1 m/s and 1.5 m/s

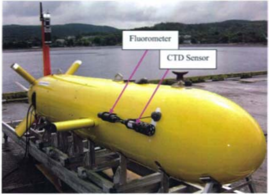

Fig. 4.16 CTD sensor and fluorometer mounted on *MUN Explorer* AUV

4.3.1 Turning Circles: Data Analysis and Observations

Two tests from each set of forward speed (V = 1m/s & 1.5 m/s) are chosen for the purpose of illustration. The turning circle results for command radii (R_c) 12 m and 16 m are chosen. As is evident from Table 4.4, the test for R_c-12 was performed at both speeds on the same day (Day-2), while the test for R_c-16 was performed on two different days (Day-2 & Day-3). The figures 4.17 and 4.18 show the trajectory (XY position) of the vehicle relative to a fixed point on the wharf, which in turn was chosen as the origin of the Earth coordinate system.

The point A in figures 4.17 and 4.18 denotes the point at which the vehicle starts to dive and B is approximately the point at which the vehicle levels off at the command depth. As evident from the figures the vehicle starts the turning mission even before it has reached the command depth which implies that the approach distance allotted in the mission plan was not sufficient to take the vehicle down to the command depth before it actually started the turning mission. As a result, the common parameters of interest in the transient phase of a turning manoeuvre such as, the transfer, advance etc., cannot be properly estimated. Hence in the discussions that follow, only the steady turning portion is analyzed and the steady-state parameters are presented in Table 4.4.

It also appears from figures 4.17 and 4.18 that there is a jump in the position data at certain points and this is prominent at the points that are encircled and an enlarged view is shown in the inset. The position of the vehicle is estimated by DVL using velocity and heading information. Intermittently this position estimate is corrected by position fixes from other instruments such as the DGPS, while the GPS signals are still available. When the vehicle is completely submerged the DGPS ceases to provide this information and the jump in the position data corresponds to the point where the last DGPS position fix was available. Beyond this point, the DGPS aided navigation switches completely to the DVL dead reckoning and hence the trajectory is a smooth curve as there are no more position fixes available from the DGPS to correct the position estimate until the vehicle has surfaced again.

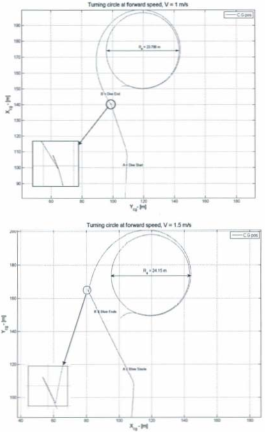

Fig. 4.17 Turning circles performed by the vehicle for a command radius of 12 m at forward speeds, V = 1 m/s & 1.5 m/s

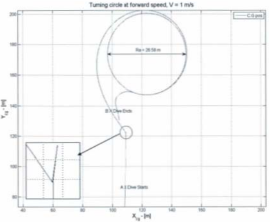

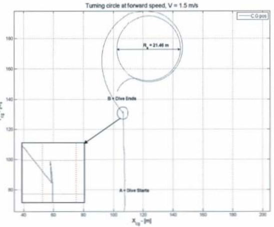

Fig. 4.18 Turning circles performed by the vehicle for a command radius of 16 m at forward speeds, V = 1 m/s & 1.5 m/s

Analysis of Steady-State Turn

A turning manoeuvre can be divided into two portions: an initial *transient* portion where surge, sway and yaw accelerations ($\dot{u}$, $\dot{v}$ and $\dot{r}$) are significant and a *steady* turning portion where the rate of turn and forward speed are essentially constant while the vehicle maintains a circular path. The transient phase of the manoeuvre starts at the instant when the control planes begin to deflect and the vehicle starts responding to the control plane forces and moments. This produces accelerations $\dot{v}$ and $\dot{r}$ of the vehicle, which exist in isolation only momentarily, for they quickly give rise to a drift angle β, and rotation r, of the vehicle. As the vehicle starts to turn accelerations coexist with velocities resulting in the build-up or creation of hydrodynamic force acting towards the centre of the turn. The magnitude of this force acting inwards (to starboard) soon balances the centrifugal force acting outwards (to port) causing the acceleration $\dot{v}$ to cease to grow and eventually be reduced to zero. The transient phase ends with the establishment of the final equilibrium of forces. When the equilibrium is reached, the vehicle settles down to a turn of constant radius thus beginning the *steady* turning phase. Here, the accelerations $\dot{v}$ and $\dot{r}$ are zero but the velocities v and r have non-zero values, [Lewis, 1969].

The sketch in Figure 4.19 shows a schematic diagram of an axisymmetric vehicle undergoing a steady starboard turn. The origin of the body coordinate system is fixed at the center of gravity of the vehicle. The sketch shows the velocity components and the angle of inclination of the vehicle to the incoming flow. R denotes the turning radius with which the body rotates around a center point C with an angular velocity r

about the positive z-direction. The linear velocity components $[u, v, w]$ and the angular velocity components $[p, q, r]$ are relative to the body fixed axis.

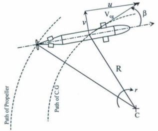

Fig. 4.19 Sketch showing the trajectory of the vehicle during a steady turn

In order to generate a radial force of sufficient magnitude, to turn the vehicle, the hull should be held at an angle relative to the flow. The control plane forces should be capable of holding the vehicle at this angle of attack, called the drift angle, β. This is defined as the angle between the centerline of the vehicle and the tangent to the path at the point concerned; in this case, the C.G of the vehicle.

The angle of attack α and the drift angle β are related to the velocity components by the following relation:

$$\tan\alpha = \frac{w}{u} \text{ and } \sin\beta = \frac{-v}{V} \text{ where } V^2 = u^2 + v^2 + w^2 \qquad (4.16)$$

The angle of attack α is measured with respect to the incoming flow. The incoming flow can be considered to be horizontal as the C.G of the vehicle traverses a horizontal plane. A comparison of the angle of attack α estimated with respect to the horizontal incoming flow and the pitch angle θ measured by the vehicle with respect to the horizontal shows a very close match (see Table 4.4). However, the estimated drift angle β do not show a good match particularly when the set of tests done on different days are compared. There is an abrupt change in the values of β observed for the tests performed on Day-3.

Table 4.4 shows a list of steady-state parameters that were measured, such as control plane deflections, depth, propeller rpm, radius of turn, angular displacements, angular rates etc., as well as estimated parameters such as angle of attack, drift angle and linear velocity components, from the turning circle missions.

The set of figures that follow shows the time-series of parameters corresponding to the tests of turning circles shown in Figure 4.17 and Figure 4.18. These parameters were measured by the various instruments onboard the vehicle. Figure 4.20 shows the time-series for depth profile of the vehicle during a complete mission. The region between points A, B, C & D denotes each phase of the turning manoeuvre. As shown in figures 4.17 and 4.18, AB is the diving phase of the manoeuvre followed by the transient phase BC, which eventually ends up in a steady state of turn, denoted by the region CD. The mean depth was estimated for the steady state range of CD.

TABLE - 4.4

STEADY-STATE PARAMETERS FROM THE ANALYSIS OF TURNING CIRCLES

Sl. No.	Depth d [m]	Speed Va [m/s]	Control Plane Angles: Dive Planes δ1	δ2	Tail Planes δ3	δ4	δ5	δ6	Radius Rc [m]	Ra [m]	RPM	AoA (α) [deg]	Drift (β) [deg]	Angular disp Roll [deg]	Pitch [deg]	Ang. Rates p [deg/s]	q	r	Lin. Vel. Comp u [m/s]	v	w	Turn rate, r'	Day
V_c = 1 m/s																							
1	2.81	1.0	-4.2	4.2	10.3	0.1	-1.8	-12.5	10	22.5	121.4	-4.8	6.5	0.00	-4.81	0.21	0.00	2.56	0.997	-0.114	-0.084	0.200	1
2	2.81	1.0	-4.8	4.8	10.6	0.0	-1.8	-12.6	12	23.8	122.9	-4.9	5.8	-0.01	-4.96	0.21	0.00	2.41	0.997	-0.101	-0.086	0.189	2
3	2.84	1.0	-5.2	5.3	10.2	0.3	-2.4	-12.2	14	25.0	122.4	-5.0	5.2	0.00	-5.06	0.20	0.00	2.30	0.997	-0.092	-0.088	0.180	2
4	2.37	1.0	-5.0	5.1	10.3	0.4	-2.1	-12.3	14	25.1	121.9	-5.0	5.3	0.00	-4.98	0.20	0.01	2.30	0.997	-0.093	-0.087	0.179	2
5	2.82	1.0	-5.1	5.1	10.2	0.9	-2.4	-11.8	16	26.6	121.6	-5.1	5.2	0.00	-5.08	0.19	0.00	2.18	0.997	-0.091	-0.089	0.169	2
6	2.84	1.0	-5.4	5.4	10.1	1.0	-2.7	-11.5	18	28.0	121.6	-5.2	4.9	0.00	-5.13	0.18	0.00	2.05	0.997	-0.085	-0.090	0.161	2
7	2.84	1.0	-5.3	5.3	9.9	1.2	-2.8	-11.6	18	28.1	122.6	-5.1	5.1	0.00	-5.10	0.18	0.00	2.07	0.997	-0.090	-0.089	0.160	2
8	2.83	1.0	-4.9	5.0	9.8	1.6	-2.8	-11.3	20	29.7	118.6	-5.1	5.2	0.00	-5.22	0.17	0.00	1.95	0.996	-0.091	-0.089	0.152	1
9	2.85	1.0	-5.4	5.5	9.7	2.8	-3.5	-10.5	25	33.4	122.2	-5.4	4.0	0.00	-5.40	0.16	0.00	1.70	0.996	-0.069	-0.094	0.135	2
10	2.86	1.0	-5.8	5.8	9.4	2.8	-3.7	-10.3	30	37.5	121.8	-5.3	3.8	0.00	-5.36	0.14	0.01	1.53	0.996	-0.066	-0.093	0.120	2
V_c = 1.5 m/s																							
1	2.84	1.5	-0.4	0.5	8.2	-3.5	1.2	-10.4	10	22.8	172.6	-1.8	6.4	0.00	-1.79	0.12	0.00	3.73	1.500	-0.164	-0.046	0.198	2
2	2.84	1.5	0.6	-0.5	8.4	-3.4	1.7	-10.0	12	24.2	171.9	-1.6	5.6	0.00	-1.57	0.09	0.00	3.49	1.500	-0.148	-0.041	0.186	2
3	2.83	1.5	-1.3	1.3	10.2	-5.2	3.1	-12.2	14	20.8	161.7	-1.8	2.4	0.00	-1.83	0.14	0.01	4.21	1.500	0.063	-0.048	0.216	3
4	2.83	1.5	-1.6	1.6	9.3	-4.5	2.3	-11.4	16	21.5	161.5	-1.9	2.3	0.00	-1.88	0.13	-0.01	3.91	1.500	0.060	-0.048	0.210	3
5	2.84	1.5	-1.8	1.8	8.9	-3.4	1.8	-10.5	18	23.0	161.6	-1.9	2.2	0.01	-1.91	0.12	0.00	3.66	1.500	0.057	-0.049	0.195	3
6	2.84	1.5	-1.9	1.9	8.9	-3.6	1.9	-10.6	18	23.7	161.4	-1.9	2.1	0.00	-1.85	0.12	0.00	3.65	1.500	0.056	-0.049	0.190	3
7	2.83	1.5	-1.7	1.7	8.4	-2.9	1.5	-10.2	20	24.7	161.6	-1.8	2.0	0.00	-1.91	0.10	-0.01	3.45	1.500	0.052	-0.047	0.183	3
8	2.84	1.5	-1.7	1.6	7.7	-1.7	0.6	-9.1	25	28.8	161.5	-1.9	1.7	0.00	-1.88	0.10	0.01	2.99	1.500	0.044	-0.050	0.156	3
9	2.83	1.5	-1.5	1.4	7.1	-0.9	0.2	-8.2	30	33.3	161.5	-1.8	1.5	0.00	-1.81	0.08	0.00	2.59	1.500	0.038	-0.047	0.135	3
V_c = 2 m/s																							
1	2.86	2.0	2.3	-2.6	10.9	-9.3	6.7	-12.1	10	17.6	212.5	0.0	2.7	0.00	-0.03	-0.01	0.02	6.46	2.001	0.094	-0.001	0.255	3
2	2.86	2.0	2.3	-2.6	7.2	-4.7	3.2	-8.4	12	24.2	225.3	0.0	5.5	0.01	-0.01	-0.02	-0.01	4.51	2.000	-0.183	0.000	0.186	4
3	2.88	2.0	2.1	-2.2	6.6	-5.2	3.1	-7.4	14	25.3	230.7	0.0	5.3	-0.01	-0.03	0.04	0.00	4.43	2.005	-0.181	-0.001	0.178	4

Vc = commanded speed; Va = actual speed measured
Rc = commanded radius; Ra = actual radius obtained
u,v,w = linear velocity components during the turn
p, q, r = angular rates measurements obtained directly from the data
r' = non-dimensional turning rate = r^*L/V_a where L = 4.5 m
Drift angle, $\beta = \sin^{-1}(-v/V)$; Angle of attack $\alpha = \tan^{-1}(w/u)$
δ1 = Port Dive plane; δ2 = Stbd Dive plane; δ3 = Port Upper; δ4 = Port Lower; δ5 = Stbd Upper; δ6 = Stbd Lower

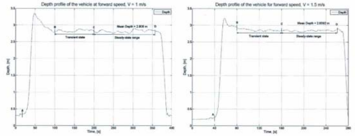

Fig. 4.20 a Depth profile of the vehicle for command radius, R_c = 12 m at forward speeds V = 1 & 1.5 m/s

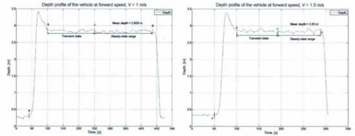

Fig. 4.20 b Depth profile of the vehicle for command radius, R_c = 16 m at forward speeds V = 1 & 1.5 m/s

Figure 4.21 shows time-series of the vehicle speed and corresponding propeller rpm for the four different tests shown above. From all the four tests, it appears that the vehicle maintained a constant speed equivalent to the command speed while negotiating a steady turn. Further, the vehicle maintained this speed during turn without any considerable increase in propeller rpm. Normally, a vehicle moving at a constant speed suffers a loss of speed when it enters a steady turn [Burcher & Rydill, 1994]. This is because the control planes hold the hull at an angle of attack in order to develop the force and moment necessary to turn the vehicle, which comes at a cost of increased drag. This increased drag causes the vehicle to decelerate to a point until it reaches a new steady speed, which could be considerably lower than the constant approach speed. Therefore, theoretically, it is not possible to maintain the command speed during a steady turn without actually changing the propeller rpm, but this pattern was consistent and was observed for all the tests shown in Table 4.4.

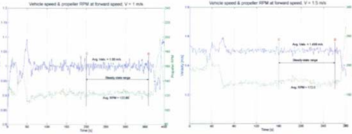

Fig. 4.21 a Time-series of vehicle speed and corresponding propeller RPM of the vehicle for command radius, $R_c = 12$ m at forward speeds V = 1 & 1.5 m/s

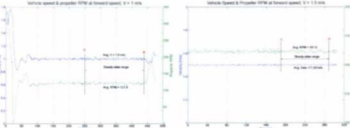

Fig. 4.21 b Time-series of vehicle speed and corresponding propeller RPM of the vehicle for command radius, $R_c = 16$ m at forward speeds V = 1 & 1.5 m/s

It is possible that the drag experienced by the vehicle while negotiating a circle of significantly large diameter-to-length ratio (D/LOA of 10 and more), may not differ much from that experienced on a straight course. This would explain the reason for not observing a considerable increase in the propeller rpm to maintain a constant command speed during the steady turn.

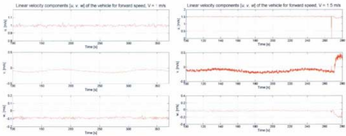

Fig. 4.22a Time-series of the linear velocity components of the vehicle for command radius, $R_c = 12$ m at forward speeds V = 1 & 1.5 m/s

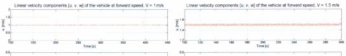

Fig. 4.22b Time-series of the linear velocity components of the vehicle for command radius, $R_c = 16$ m at forward speeds V = 1 & 1.5 m/s

The plots of linear velocity components [u, v, w] for the four tests are shown in Figure 4.22. As described in *Section 4.1.2*, the rate of change of position [x, y, z] of the vehicle C.G in 3-D space gives the global velocity components $[\dot{x}, \dot{y}, \dot{z}]$. The linear velocity components were derived from the global velocity components by a simple coordinate transformation knowing the vehicle attitudes [ϕ, θ, ψ] – the *Euler angles*. The surge velocity, u, thus derived from position estimate, shown in Figure 4.22, is almost equivalent to the command speed V and remains fairly constant throughout the turning manoeuvre further indicating that there was little or no loss of speed during the turn.

As mentioned before, the vehicle attitude and heading information are measured by means of the Watson Attitude Heading Reference System (AHRS) mounted within the pressure hull. This system integrates the angular rates to produce the attitude and heading information. Hence, the angular displacements [ϕ, θ, ψ] and angular velocities [p, q, r] are both available from the mission data. Figure 4.23 and Figure 4.24 shows the time series of these parameters respectively for the entire mission.

It is observed from Figure 4.23 that at speeds of 1 m/s, the vehicle has a nose-down attitude averaging a pitch value of around $\theta = -5^{o}$, while at higher speeds of 1.5 m/s the pitch angle is around $\theta = -2^{o}$. This pattern was similar to what was observed in the straight-line tests where a nose-down attitude was observed for the slow speed regime. As explained in the previous section, this happens as a result of slow manoeuvring speed where the control planes are less effective in generating enough force to counter the inherent nose-down attitude set by weight and buoyancy distribution. Further, the roll motions, ϕ, of the vehicle appear to be negligible for both speeds and different radius of turns. Normally, when a submerged vehicle undergoes a steady turn, the net action of the centrifugal force acting through the C.G of the vehicle and the radial component of the hydrodynamic force acting towards the centre of the circle produces an inward heel angle [Lewis, 1989]. This would be prominent in vehicles with a sail or similar structures of asymmetry such as in submarines. Since the *MUN Explorer* AUV is axisymmetric it is not expected to exhibit significant roll motions during a steady turn.

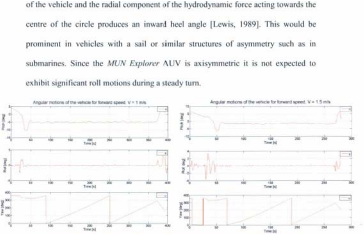

Fig. 4.23 a Time-series of vehicle orientation θ, ϕ, ψ for command radius, R_c = 12 m at forward speeds V = 1 & 1.5 m/s

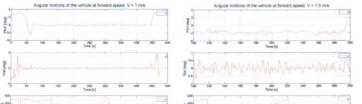

Fig. 4.23 b Time-series of vehicle orientation θ, ϕ, ψ for command radius, R_c = 16 m at forward speeds V = 1 & 1.5 m/s

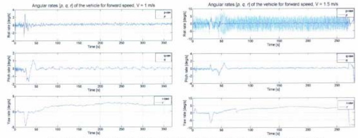

Fig. 4.24 a Time-series of the vehicle angular velocities $[p, q, r]$ for command radius, $R_c = 12$ m at forward speeds V = 1 & 1.5 m/s

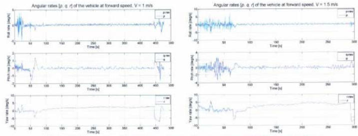

Fig. 4.24 b Time-series of the vehicle angular velocities $[p, q, r]$ for command radius, $R_c = 16$ m at forward speeds V = 1 & 1.5 m/s

The angular velocities or rotational rates $[p, q, r]$ of the vehicle are shown in Figure 4.24. There is a certain amount of noise in the roll rate, p, measured at 1.5 m/s where as both roll and pitch rates are seen to be negligible in the rest of the tests. The most important of these angular rates in a turning manoeuvre is the yaw rate, r, at which the heading changes during a turn.

All the steady-state parameters estimated for the four examples shown in figures 4.20 through 4.24, are the mean values estimated over a time range between C and D shown in Table 4.5. The actual numerical values of the various parameters for all the turning manoeuvres, including the four examples presented above, were provided in Table 4.4.

TABLE - 4.5 Time range for different phases of manoeuvre

Control Inputs			Diving range		Transient range	Steady-state range	
V	R_c	R_a	A	B		C	D
[m/s]	[m]	[m]	[s]	[s]		[s]	[s]
1.0	12	23.8	20	100		200	360
1.5	12	24.2	40	80		160	260
1.0	16	26.6	40	100		250	440
1.5	16	21.5	50	100		190	290

The steady state angle of attack (α) and the drift angle (β) for the four tests were estimated at every instant using the relation given in equation (4.16) and plots of their time-series are shown in Figure 4.25. The steady-state angles of attack (α) estimated from the plot are found to closely match the steady-state values of pitch (θ) measured by the vehicle sensors.

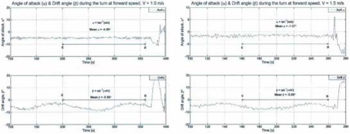

Fig. 4.25 a Angle of attack (α) and drift angle (β) for the turning circle of command radius, Rc = 12m at forward speeds, V = 1 & 1.5 m/s

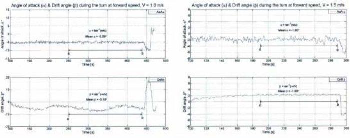

Fig. 4.25 b Angle of attack (α) and drift angle (β) for the turning circle of command radius, Rc = 16m at forward speeds, V = 1 & 1.5 m/s

Next, the control plane angles during the turning manoeuvre are plotted in the figures below. The AUV uses six control planes to manoeuvre in 3D space and since the turning circle is a horizontal plane manoeuvre, the effect of the four tail planes are expected to be predominant while dive planes should have little or no effect on a horizontal plane manoeuvre. However, Figure 4.26 shows that at low speeds (1 m/s), the dive plane deflections are relatively high, around 5°. When expression (4.4) was used to find the effective angle of deflection (δP_D) of the dive planes, it provides a value of around +5°. This implies that the combined effort of the dive plane deflections was to produce a positive pitch attitude on the vehicle.

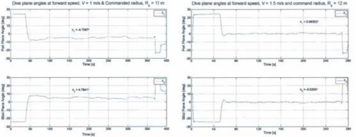

Fig. 4.26 a Dive plane angles for the turning manoeuvres of command radius, R_c = 12 m at forward speeds V = 1 & 1.5 m/s

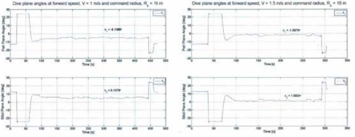

Fig. 4.26 b Dive plane angles for the turning manoeuvres of command radius, R_c = 16 m at forward speeds V = 1 & 1.5 m/s

The 'X'-tail configuration of *MUN Explorer* makes use of all four control planes to manoeuvre in any given plane. Figures 4.27a through 4.27d shows the tail plane deflections of the AUV for the four examples of turning manoeuvres. The mean deflection angles of each control plane for the steady-state phase are estimated and presented in each plot. The plane numberings followed here are the same as shown earlier in Figure 4.1. As all manoeuvres were performed to the starboard, it is evident from the figures that control planes 3 and 6 are the ones chiefly involved in a starboard turn on a horizontal plane.

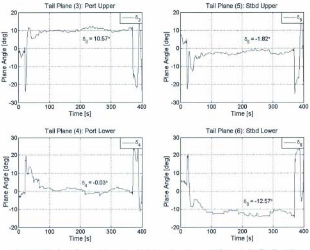

Fig. 4.27 a The four tail plane deflection angles for a turning manoeuvre of command radius, R_c = 12 m at forward speed, V = 1 m/s

Figures 4.27a and 4.27b shows the tail plane angles for the same command radius, R_c – 12 m, performed at forward speeds of 1 and 1.5 m/s respectively. Note that these two runs were performed on the same day: Day-2. From Table 4.5, it is seen that the actual radius of turn obtained from the two runs, although far from the command radius, differed only by 0.4m. The deflections of control planes 3 and 6 dominate the other two planes while producing a starboard turn. Comparing both figures, it can be said that at higher speeds, smaller control plane deflections can produce the same outcome, assuming the environmental conditions to have stayed more or less steady.

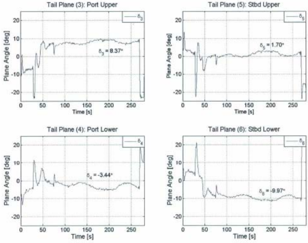

Fig. 4.27 b The four tail plane deflection angles for a turning manoeuvre of command radius, $R_c = 12$ m at forward speed, V = 1.5 m/s

The combined effect of all four planes was calculated using the set of equations (4.1) through (4.3). For instance, the effective pitch angle calculated using expression (4.1) for the example in Figure 4.27a is:

$$\delta P = \frac{10.57 + (-0.03) - (-1.82) - (-12.57)}{4} = 6.23^{\circ}$$

A positive value of δP implies that the given configuration of plane deflections has a tendency to pitch the nose up. Thus the combined effect of dive planes with an effective pitch angle of +5° and tail planes with an effective pitch angle of +6.23° is to produce a nose-up attitude. Despite this effort from all the control planes working to bring a positive pitch, the vehicle attitude was seen to be negative (see Figure 4.23) for slow speeds. This same scenario was observed in the straight-line tests as well. As explained before, these large control plane deflections are a result of the vehicle control system's effort to generate sufficient lift to maintain a level flight. However, due to slow speed the control planes are incapable of generating the necessary lift and hence the large nose-down attitude.

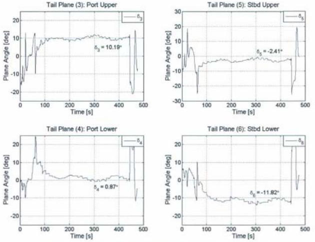

Fig. 4.27 c The four tail plane deflection angles for a turning manoeuvre of command radius, R_c = 16 m at forward speed, V = 1 m/s

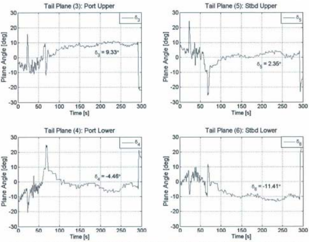

Fig. 4.27 d The four tail plane deflection angles for a turning manoeuvre of command radius, R_c = 16 m at forward speed, V = 1.5 m/s

Similarly, figures 4.27c and 4.27d shows the tail plane angles for command radius R_c – 16 m, at forward speeds of 1 and 1.5 m/s respectively. The pitch attitude (θ) of the vehicle at this speed is found to be around -2°, from Figure 4.23. The effective dive plane angles (δP_D) for this speed are also far less than that for the case of 1 m/s speed, ranging between 0.5° and 1.5°. These smaller deflection angles are effective in generating considerable lift owing to the increased speed. Any further contribution of lift, necessary to maintain a level flight, is complemented by the four tail planes.

The effective yaw angle (δY) produced by the same combination of the four tail plane configurations, seen in Figure 4.27a, is:

$$\delta Y = \frac{10.57 - (-0.03) + (-1.82) - (-12.57)}{4} = 5.34^{\circ}$$

A positive value for δY implies that the given combination of plane deflections has a tendency to produce a positive yaw attitude; in other words a starboard turn. This representation will be found useful in presenting the influence of control plane deflections on various parameters. A complete list of individual steady-state control plane angles, δ_1, δ_2… δ_6, and the effective plane angle produced by their combination is given in Table 4.6.

TABLE - 4.6 Effective Control Plane Deflection for Turning Circles

Radius		Dive Plane Angles				Individual Tail Plane Angles				Effective Plane Angles			
R_c	R_a	δ_1	δ_2	δP_D	δR_D	δ_3	δ_4	δ_5	δ_6	δP	δY	δR	Day
V = 1 m/s		[deg]	[deg]	[deg]	[deg]	[deg]	[deg]	[deg]	[deg]	[deg]	[deg]	[deg]	
10	22.51	-4.17	4.17	4.17	0.00	10.32	0.10	-1.82	-12.51	6.19	5.23	0.98	1
12	23.80	-4.76	4.76	4.76	0.00	10.57	-0.03	-1.82	-12.57	6.23	5.34	0.96	2
14	25.02	-5.23	5.29	5.26	-0.03	10.19	0.34	-2.38	-12.18	6.27	4.91	1.01	2
14	25.09	-5.04	5.06	5.05	-0.01	10.32	0.39	-2.08	-12.26	6.26	5.03	0.91	2
16	26.58	-5.12	5.11	5.12	0.00	10.19	0.87	-2.41	-11.82	6.32	4.68	0.79	2
18	27.97	-5.36	5.36	5.36	0.00	10.10	0.97	-2.70	-11.54	6.33	4.49	0.79	2
18	28.11	-5.28	5.28	5.28	0.00	9.87	1.23	-2.77	-11.60	6.37	4.37	0.82	2
20	29.65	-4.94	4.96	4.95	-0.01	9.76	1.60	-2.83	-11.31	6.38	4.16	0.70	1
25	33.44	-5.42	5.51	5.47	-0.04	9.66	2.79	-3.53	-10.51	6.62	3.46	0.40	2
30	37.54	-5.82	5.83	5.83	0.00	9.41	2.77	-3.70	-10.34	6.56	3.32	0.47	2
V = 1.5 m/s													
10	22.76	-0.41	0.45	0.43	-0.02	8.19	-3.54	1.24	-10.42	3.46	5.85	1.13	2
12	24.15	0.56	-0.53	-0.55	-0.02	8.37	-3.44	1.70	-9.97	3.30	5.87	0.83	2
14	20.80	-1.27	1.28	1.28	-0.01	10.16	-5.23	3.05	-12.19	3.52	7.66	1.05	3
16	21.46	-1.63	1.60	1.62	0.01	9.33	-4.46	2.35	-11.41	3.48	6.89	1.05	3
18	23.03	-1.78	1.75	1.77	0.02	8.87	-3.38	1.78	-10.50	3.55	6.13	0.81	3
18	23.73	-1.93	1.91	1.92	0.01	8.88	-3.58	1.86	-10.62	3.52	6.24	0.87	3
20	24.66	-1.73	1.68	1.71	0.03	8.41	-2.88	1.54	-10.23	3.56	5.77	0.79	3
25	28.84	-1.69	1.61	1.65	0.04	7.69	-1.66	0.62	-9.09	3.63	4.77	0.61	3
30	33.28	-1.48	1.43	1.46	0.03	7.10	-0.86	0.16	-8.19	3.57	4.08	0.45	3
V = 2 m/s													
10	17.64	2.29	-2.56	-2.43	0.14	10.86	-9.29	6.65	-12.11	1.76	9.73	0.97	3
12	24.24	2.33	-2.56	-2.45	0.12	7.22	-4.73	3.22	-8.42	1.92	5.90	0.68	4
14	25.29	2.09	-2.21	-2.15	0.06	6.63	-5.16	3.12	-7.40	1.44	5.58	0.70	4

Information that can be derived from the above data is: what combination of control plane deflections can produce a turning circle of specified radius at a given forward speed? This is presented as a chart in Figure 4.28 for two different speeds: 1.0 m/s and 1.5 m/s. In another sense, the knowledge of the radius of turn and the corresponding tail plane deflections to produce it may be used to validate simulators developed for similar vehicle configurations.

From Figure 4.28a and Figure 4.28b, it was seen that control planes 3 and 6 have the maximum influence on a starboard turn. If only these planes were to act during a turn ($\delta_4 = \delta_5 = 0$), their effect would produce a δY exactly equal to δP, according to the expressions given by equations 4.1 and 4.2. This means that the vehicle may dive or climb as it executes a turn. In other words, the vehicle will be turning on an oblique plane instead of a horizontal plane. The effect of planes 4 and 5 in a starboard turn is to counteract any unwanted pitch and roll motions that may accompany a steady turn in the horizontal plane.

A decrease in the deflection angles of control planes 3 and 6 produces turns of larger radii at both speeds. However, trend in the deflections of planes 4 and 5 during slow speed (1 m/s) is different from the trend in their deflections at high speed (1.5 m/s). At slow speed of 1 m/s, deflection of planes 4 and 5 have an increasing or diverging trend. At this speed the vehicle had a large nose-down attitude and this was countered by the collective effort of the tail planes, apart from the dive planes, which produced an effective pitch angle δP (see Table 4.6). As the radius of turn increases, the

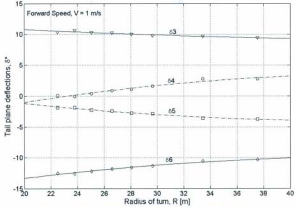

Fig. 4.28a Chart showing tail plane deflections corresponding to various radii of turn at forward speed, V = 1 m/s

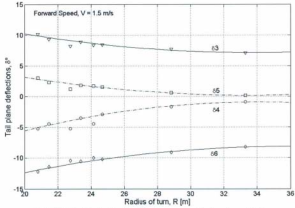

Fig. 4.28b Chart showing tail plane deflections corresponding to various radii of turn at forward speed, V = 1.5 m/s

increase in deflections of planes 4 and 5 are to complement the drop in the other two plane deflections in providing an effective pitch deflection angle δP. In other words, for large radius of turns, smaller deflections of planes 3 and 6 are necessary while at the same time to counter the nose-down attitude, larger deflections of planes 4 and 5 are needed. This accounts for the diverging trend of plane angles δ_4 and δ_5 seen in Figure 4.28a. However, at the higher speed of 1.5 m/s, planes 4 and 5 have a different trend; their deflection decreases or converges to zero as the radius of turn increases. While executing circles of large radius of turn at this speed, the contributions of planes 4 and 5 are hardly needed to generate lift, as the dive planes become more effective. As a result, at this speed, the nose-down attitude was much less than that observed at slow speeds. So the plausible reason why the planes 4 and 5 seem to show a higher deflection at lower radius of turn, in Figure 4.28b, is to counter any unwanted roll motions. In other words, when the vehicle executes smaller radius of turns at higher speeds, the apparent effect of planes 4 and 5 is to bring about roll stabilization.

4.3.2 Radius of Turn, R_a and Rudder Angles δY

Conventionally, the radii of turns are plotted against the rudder angle in order to understand the effectiveness of the rudder in turning the vehicle at a particular speed. Since all the four control planes are involved in a turning manoeuvre here, their combined effect was represented by an individual control plane deflection angle given by the expression (4.1) for δY. The sign taken by these values indicate the tendency of the combination to produce a positive or negative attitude in yaw. On observing Figure 4.29, which represents the variation of turning radius with effective yaw angle δY for both speeds, it is seen that all δY values are positive. A positive value should indicate a starboard turn, which was actually the case with all the experiments. However, the figure looks odd when we realize that for the same effective rudder deflection δY, the higher speed produced a larger radius of turn compared to the slow speed; the opposite is normally expected in manoeuvring tests.

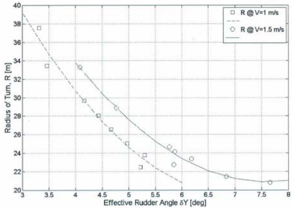

Fig. 4.29 Radius of turn vs. effective yaw deflection angle δY at forward speeds, V = 1 & 1.5 m/s

If only the deflections of planes 3 and 6 were considered for calculating δY during a starboard turn, and the radii plotted against these values, the graph would look as shown in Figure 4.30. This figure clearly shows that for the same effective rudder deflection δY, the higher speed produced smaller radius of turns while slower speed resulted in larger radius of turns. It should be noted that in certain circumstances the other set of planes, (planes 4 and 5) can also be used to perform a starboard turn, as will be seen later in this chapter with the discussion on helical manoeuvre. In such cases, the choice of a pair of planes and their combined effect can become confusing in the calculation of δY. Thus, it would be appropriate to use δY, calculated from all the four different plane angles, as a representative value against which the various parameters like turning rate, *r*, drift angle *β* etc., may be compared.

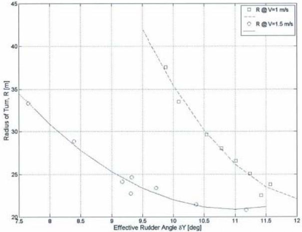

Fig. 4.30 Radius of turn vs. effective yaw deflection angle δY- considering only planes 3 and 6, at forward speeds, V = 1 & 1.5 m/s

Drift angles (*β*) and Turing rates (*r*)

It is apparent from the above descriptions that the various parameters of steady turn can be represented as a variation against rudder deflection with the help of a single effective control plane deflection, δY, as it takes into account the effect of all the four control planes. However, the use of δY has some drawbacks as explained in Figure 4.29 even though they are good indicators of the possible attitude the vehicle may achieve during a manoeuvre. Thus, it is not totally wrong to represent the combination of tail plane deflections by a single effective value. Nevertheless, parameters such as drift angles β, turning rates r etc., vary also with the radius of turn. Therefore, in this scenario, it makes more sense to represent the variations of drift angle and turning rates with respect to the actual turning radius, R_a. Hence in the following figures, the drift angles and turning rates are plotted against the radius of turn R_a.

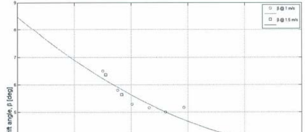

Fig. 4.31 Variation of drift angle β with radius of turn R_a for both speeds

In order to generate a radial force of sufficient magnitude to turn the vehicle, the hull should be held at an angle relative to the flow. The rudder forces should be capable of holding the vehicle at this angle of attack, called the drift angle, β. It is defined as the angle between the centerline of the vehicle and the tangent to the path at the point concerned: in this case, the C.G of the vehicle (see Fig. 4.19). Figure 4.31 shows the variation of drift angle β with radius of turn R_a for turning circles performed at speeds of 1.0 and 1.5 m/s. The trend shows β decreasing as the radius of turn R_a increases. At slow speeds, large drift angles are required to generate the hydrodynamic force necessary to turn the vehicle while at higher speeds the same hydrodynamic force can be generated by a small drift angle. This explains the reason for the spacing between the two curves in Figure 4.31. Further, the drift angle β increases as the radius of turn decreases, regardless of the speed of the vehicle.

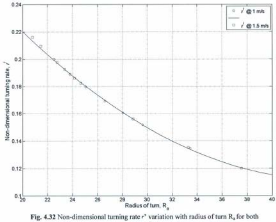

Fig. 4.32 Non-dimensional turning rate r' variation with radius of turn R_a for both speeds

The rate at which the heading changes during a turn - the turning rate, r, is plotted in Figure 4.32 as a variation of radius of turn, R_a. It is related to the speed of the vehicle and the radius of turn as $r = V/R$, where V is the tangential velocity and R is the radius of turn. This quantity can be non-dimensionalised as follows:

$$r' = r\frac{L}{V} = \frac{L}{R} \tag{4.17}$$

The non-dimensional turning rate r' thus becomes a function of just radius R alone, as the overall length of the vehicle L remains a constant.

The value of r' decrease as the radius of turn grows larger. A decrease in radius is brought about by an increase in the effective plane angle deflection δY. Thus it can be inferred that turning rate increases as the plane angle δY increases or is proportional to δY. The equation (4.18) for non-dimensional turning rate r' can be helpful in evaluating the turning rate of the vehicle negotiating a given radius.

$$r' = 0.00018R_a^2 - 0.016R_a + 0.47 \tag{4.18}$$

Starboard and Port Turn

An attempt was made to perform turns to the port side for a particular command radius of R_c-18 m at each forward speed. However, this turned out to be unsuccessful. The mission for port turn was coupled with the mission for the starboard turn at command radius, R_c-18 m, in a single mission plan file. In that way, the vehicle after performing a normal starboard turn was expected to perform a port turn, instead of performing the turns independently, thereby save some battery-life.

Figure 4.33 shows the example of a turning circle performed at a forward speed of 1.5 m/s and at a command radius of 18 m where the vehicle was expected to perform a second circle to the port side, after completing the first. Upon completing nearly 2.5 revolutions about the centre point C_1 to the starboard side, the vehicle was expected to pull out somewhere near point P_1 and head in the direction of the tangent (shown by the arrow) down. Having the centre point C_2 of the second circle defined on the left side of this tangent or the line-of-sight of the vehicle, it was presumed that the vehicle would execute a turn the port about C_2. Unfortunately, this was not the case. The vehicle pulled out of the first circle, moved towards the centre point of the second circle and performed another starboard turn instead of a desired port turn. The trajectory of the vehicle is shown in Figure 4.33. The *dashed* line in the figure represents the expected trajectory.

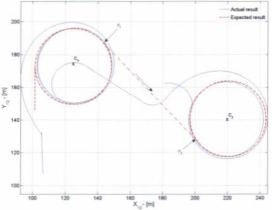

Fig. 4.33 Trajectory from a turning mission performed by *MUN Explorer* at a speed of 1.5 m/s in response to a command to perform a starboard and port turn at a command radius of R_c=18 m.

Although, the attempted methodology for performing a port turn was unsuccessful, it is believed that this issue can be rectified easily by making appropriate changes to the mission plan file.

Figure 4.34 presents a 3-D view of the same manoeuvre. This also gives a 3-D perspective of the rest of the turning circle manoeuvres performed, except that in all other cases the vehicle surfaced at the end of the execution of the first circle.

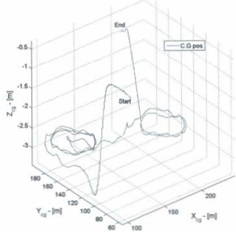

Fig. 4.34 3-D view of the turning mission performed by *MUN Explorer* shown in Figure 4.33

4.3.3 Summary of Turning Circle Manoeuvres

A set of 22 turning circle manoeuvres were performed using the *MUN Explorer* AUV at different speeds of 1, 1.5 and 2 m/s and the results and observations from these were presented through the previous sections. A subset of turning manoeuvres as well as a subset of straight-line test results was published in Issac *et al* (2007b). These tests provided insight into the steady-state behaviour of the vehicle during a turn. Some of the observations made from the above manoeuvres are listed below:

a) The actual radius of turn R_a estimated from the data, from all the tests, were larger than the commanded radius R_c. The large difference between the actual and commanded radius is expected to have occurred due to improper calibration of the control planes. In order to obtain circles of smaller radius of turn, the control planes have to be deflected to their maximum allowable deflection angles (25^o). The maximum deflections observed during the turn were roughly half the allowable deflection. Therefore, it is necessary to investigate and modify that portion of the vehicle control software, which controls the control plane deflection. An alternative option, in an attempt to perform a circle of smaller radius, is to command the vehicle to perform a radius of turn smaller than the manufacturer specified minimum radius (10 m).

b) The speed of the vehicle in the steady turning phase was same as the command speed in all tests and this occurred without any considerable change in the propeller rpm. Theoretically, it should not be possible to have the same speed during a turn as that of the approach speed without actually changing the propeller rpm, but this pattern was consistent with all the tests. It is reasoned that since the radii of turns obtained were too large, with a diameter-to-length (D/LOA) ratio of 10 or more, the drift angle experienced by the AUV may generate drag not much different from that experienced on a straight course. This would explain the reason for not observing a considerable change in propeller rpm during the steady turning phase.

c) The vehicle exhibited negligible roll motion even during the turn and this was consistent with all the tests. Thus, the ability of the control system to maintain a command speed throughout the turn with negligible roll motion ensures steady sampling of data during a mission. This is an essential quality of a sensor platform.

d) Slower speed turning manoeuvres showed a large nose-down attitude. This pattern was the same as that observed during the straight-line tests.

e) From the series of tests, a chart was developed for each of the two different speeds that relate the tail plane deflections necessary to produce a specified radius of turn. This information on control plane angles δ and forward speed V estimated from the turning circle mission are useful as inputs for the hydrodynamic motion simulation model.

f) The results from the turning circles show that from a vehicle performance or application point of view, it is appropriate to operate the vehicle at *constant speed* mode. However, from a vehicle dynamics point of view, as it was the intent of this study, it would be more appropriate to operate the vehicle at a *constant propeller rpm* mode. Using constant propeller rpm helps to capture the vehicle response such as loss of speed during turn, if any.

4.4 Horizontal Zigzag Manoeuvring Analysis

A zigzag manoeuvre is indicative of the control characteristics of the vehicle. It also shows the effectiveness of the rudder in controlling the vehicle. In the case of underwater vehicles, these zigzag manoeuvres or Z-tests can be performed both in horizontal and vertical planes. Traditionally, a horizontal zigzag manoeuvre is performed by deflecting the rudder to a pre-defined angle and holding it until the vehicle heading has changed to that same angle. Then the rudder is deflected to the same angle in the opposite direction and held in place until the vehicle heading changes to that value. This procedure is repeated for three or four cycles [Lewis, 1989]. On the *MUN Explorer* AUV, it is the vehicle computer that controls or sets the rudder angle for a desired mission and the operators had little or no control over it

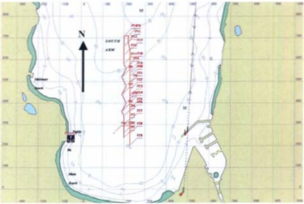

Fig. 4.35 Mission plan for a horizontal and vertical zigzag manoeuvre

when the vehicle was submerged. Hence conventional method of executing a zigzag was not possible and alternative methods had to be devised.

Using the drawing tools and text editors in "FleetManager", the missions were created by defining a route by means of a series of waypoints. This was accomplished by using some geographical task verbs such as *target* and *line_follow*. The zigzags missions were designed for both horizontal and vertical planes and were planned as follows. Both, the horizontal and vertical zigzags were planned by picking points at regular intervals on either side of a straight course in the horizontal plane as well as in the vertical plane, respectively. These missions were executed in such a way that the vehicle on its way North performed a horizontal zigzag and on its way back (South), it performed a vertical zigzag, as shown in Figure 4.35. In this way the available energy storage in the batteries was used as efficiently as possible. The following sub-sections present the results and observations from the horizontal zigzag manoeuvres while the results from the vertical zigzag manoeuvres will be addressed in the next section.

4.4.1 Patterns of Horizontal Zigzag

The horizontal zigzags, designed as shown in Figure 4.35, were performed by allowing the AUV to follow a predefined path at a preset speed. Two different speeds were chosen: 1.5 and 2.0 m/s. A total of six horizontal zigzags were performed during the available test time. Table 4.7 below lists the total number of horizontal Z-tests conducted.

TABLE 4.7
Horizontal Z-Test Plan

Test #	V	Y_O	L_C	Day
	[m/s]	[m]	[m]	
1	1.5	10	160	1
2	2.0	10	160	1
3	1.5	20	160	1
4	2.0	20	160	1
5	1.5	10	80	2
6	1.5	20	80	2

The numbers shown in Table 4.7 were arrived at after having seen the performance of the vehicle in surface trials (see Figure 4.36 & Figure 4.37). Two sample trajectories of the AUV during surface trials of horizontal zigzags are shown in Figure 4.36a & 4.36b. The red lines show the defined path while the green lines are the vehicle trajectory as seen on the "FleetManger" chart in real-time. The real-time trajectory of the vehicle can be tracked when the vehicle was on the surface, as radio telemetry connections could be established then. Once the vehicle is submerged this radio telemetry communication cannot be established and hence the trajectory cannot be tracked. One test (Figure 4.36a) used the task verb *target* and the other used the task verb *line_follow* (Figure 4.36b). The surface trials had amplitude (Y_0) of 10 m and a cycle length (L_C) of 40 m. Amplitudes (Y_0) and cycle lengths (L_C) are defined as shown in Figure 4.38. From surface trials, it was found that the path defined was extremely tight for the vehicle to manoeuvre. Further, the smoothness of the trajectory in Figure 4.36a was an indication to use the task verb *target* over *line_follow* for the entire horizontal zigzag tests. Note that when the vehicle was manoeuvring on the surface, the tail control planes - port upper (Plane -3) and the starboard upper (Plane-5), protrude out of the water and so were not fully effective in generating control forces (see Figure 4.37). It was reasoned therefore that when the vehicle is submerged and when all the four tail planes become fully effective, the trajectory of the vehicle for the defined path would be much more tight or distorted. Based on these observations, it was decided to increase the cycle lengths (L_C) of the path for the actual tests and consequently arrived at the numbers shown in Table 4.7.

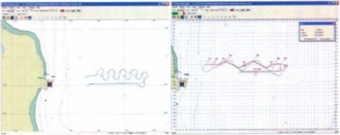

(a) (b)

Fig. 4.36 "FleetManager" chart showing the trajectories of surface trials performed by the AUV upon using *target* and *line_follow* commands

Fig. 4.37 Planes '3' and '5' protrude out of the water surface while *MUN Explorer* performs a surface trial

4.4.2 Trajectory and Heading

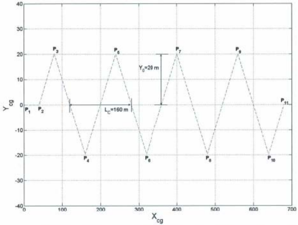

Fig. 4.38 Path defined for a horizontal zigzag with amplitude, Y_0 20m and cycle length L_C 160 m.

Figure 4.38 shows the path defined for the horizontal Z-test represented by tests 3 and 4 of Table 4.7, which had amplitude of 20 m and a cycle length of 160 m. Points P_1, P_2, P_3 etc., are the waypoints picked on the electronic chart of "Fleet Manager". When the mission was executed, the AUV followed a route defined by these waypoints using the *target* command. The task verb *target* was used so as not to put any constraints on the free motion of the vehicle while it navigated through and between waypoints. As a result, the defined path in Figure 4.38 is depicted as a smooth curve in figures 4.39 and 4.40.

The results of the zigzag manoeuvre are speed dependent. In general, the time to reach the successive waypoints decreases with increasing speed while the overshoot width of path and overshoot yaw angle increase with increasing speed [Lewis, 1989], [Lopez *et al.*, 2004]. The responses of the AUV for two different speeds, 1.5 m/s and 2.0 m/s, and two different amplitudes or width-of-path (Y_0 = 10 m & 20 m), that had the same cycle lengths (L_C 160 m), are shown in figures 4.39 and 4.40, respectively. All horizontal zigzags were performed at a depth of approximately 3 m and therefore the position estimates was obtained from DVL, which uses dead reckoning.

From the trajectory of the vehicle shown in figures 4.39 and 4.40 it can be seen that the vehicle passes exactly through the defined waypoints but overshoots the point before turning. The turning occurs only after the vehicle had passed through the waypoint. Thus, there is an overshoot in both x and y directions from the coordinates of the waypoint.

The overshoot in y-direction (Δy) for the case of Y_0-10 & L_C-160 was estimated to be 1.2 m (0.27 LOA) and 1.5 m (0.33 LOA) while in the x-direction (Δx) this offset was estimated to be 5.5 m (1.2 LOA) and 6.3 m (1.4 LOA) at speeds of 1.5 and 2.0 m/s respectively. In these tests (Tests 1 & 2), after hitting the waypoint, the vehicle changed its heading by approximately 28° while following the defined path. Figure 4.41 shows the vehicle's trajectory and heading corresponding to both the speeds. Similarly, the overshoot in the y-direction (Δy) for the case of Y_0-20 & L_C-160 was estimated to be 3.0 m (0.7 LOA) and 3.9 m (0.9 LOA) while in the x-direction (Δx)

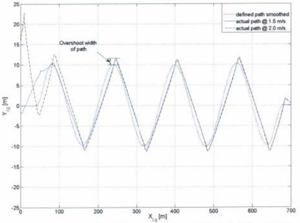

Fig. 4.39 Zigzags performed at two different speeds for the same defined path – Y_0 10 m & L 160 m

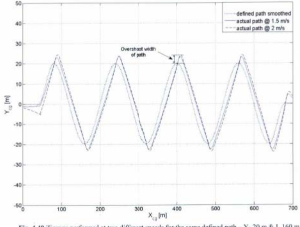

Fig. 4.40 Zigzags performed at two different speeds for the same defined path – Y_0 20 m & L 160 m

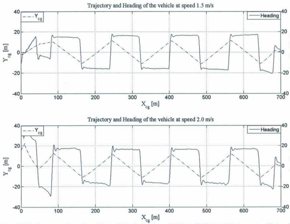

Fig. 4.41 Trajectory and heading of the vehicle for horizontal Z-Test [$Y_0$20, L_C160] at speeds of 1.5 and 2.0 m/s

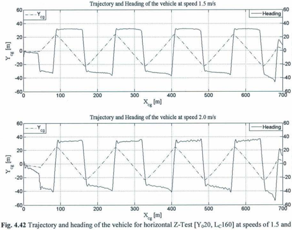

Fig. 4.42 Trajectory and heading of the vehicle for horizontal Z-Test [$Y_0$20, L_C160] at speeds of 1.5 and 2.0 m/s

this offset was estimated to be 8.5 m (1.9 LOA) and 10 m (2.2 LOA) for speeds 1.5 m/s and 2.0 m/s respectively. Here, after hitting the waypoint the vehicle changed its heading by approximately 53°. Figure 4.42 shows the vehicle's trajectory and heading corresponding to both the speeds. It appears from both figures 4.41 and 4.42 that there are periods of constant heading. These periods of constant heading correspond to the portion of the trajectory between two waypoints where the vehicle travels for a considerable distance (14 to 16 LOA) in a straight line. This is not the case in a conventional zigzag manoeuvre where the heading changes continuously and thus forms a sinusoidal pattern. On account of this observation obtained from the first four tests performed on Day 1, it was reasoned that further experiments should be refined by adjusting the width-of-path/amplitude (Y_0) and/or cycle length (L_C), such that the straight line portion of the run between successive waypoints was reduced to give a more realistic zigzag manoeuvre. The latter two experiments (tests 5 & 6) on Day 2 were performed as an attempt to make this change by reducing the cycle length to half while maintaining the same path widths (10 and 20 m).

The response of the AUV to tests 5 & 6 are presented in figures 4.43 and 4.44. It is apparent from figures 4.43 and 4.44 that the modifications in cycle-length (L_C) did indeed produce trajectories that were much closer to a conventional zigzag. This is further evident from Figure 4.45, which depicts the trajectory and heading of the vehicle where the overshoot has increased considerably when compared to the first four trials although the heading still does not resemble a sinusoidal pattern.

As the vehicle travelled a distance of 14 to 16 LOA in a straight line between each waypoint, it was reasoned that the overshoot measures would remain the same regardless of the number of vehicle-lengths-of-travel. In this scenario, it may be more appropriate to look at the time taken by the vehicle to change its course from a positive heading direction to a negative heading direction or vice-versa. From tests 1 & 2 the estimated overshoots (Δx, Δy) happened while the vehicle heading changed from the initial course by approximately 28° and from trials 3 & 4 the estimated overshoots (Δx, Δy) happened while the vehicle heading changed from its initial course by approximately 53°. Table 4.8 below shows a comparison of the values of overshoot width of path (in both x and y directions), average turning time at each waypoint, vehicle-lengths-of-travel during the periods of constant heading and the magnitude of heading change. Any change in the observed values of Δx, Δy, turning time, between tests 1 & 2 was caused by the change in speed of the vehicle by 0.5 m/s, assuming constant conditions. Similarly, any change in the observed values of Δx, Δy, turning time, between tests 3 & 4 resulted from a change in speed of the vehicle by 0.5 m/s as well. In contrast, tests 5 & 6 differed only in their width of path while both tests were performed at the same speed of 1.5 m/s and maintained a reduced cycle length of 80 m.

In test 5, the change in heading of the vehicle is the same as that for the tests 3 & 4 (~ 53°) but the overshoot observed was larger than that for tests 3 & 4. The only difference between test 3 and test 5 is in the straight-line portion of the trajectory between two waypoints. In test 5, the straight-line portion is considerably reduced to 5.8 LOA from an estimated value of 16.4 LOA in test 3, while the vehicle performed the above two zigzags at the same speed and experienced a change in heading through almost the same angle, 53°. Therefore, reducing the cycle length to half, thereby making the turns tighter, had the effect of increasing the overshoot and consequently the turning time. In test 6 the vehicle turned through an angle of around 90° but at the expense of an increase in turning time and overshoot.

TABLE 4.8
Overshoot width of path, turning time and heading change

Test	V	Y_o	L_C	Overhoot		Turn time	Dist. in	Heading
No.	[m]	[m]	[m]	Δx [m]	Δy [m]	[s]	no. of LOA	change
1	1.5	10	160	5.5	1.2	8.5	15.3	28°
2	2.0	10	160	6.3	1.5	9.7	14.1	28°
3	1.5	20	160	8.6	3.0	11.8	16.4	53°
4	2.0	20	160	10.1	3.9	11.1	16.1	53°
5	1.5	10	80	10.2	5.8	19.2	5.8	53°
6	1.5	20	80	11.1	8.9	21.2	8.3	90°

An increase in vehicle speed always increased the overshoot distances for the same defined paths. An increase in the degree or sharpness of turn increased the overshoot width of path and consequently the turning time as well. This is evident from comparing the pair of tests 1 & 2 with the pair 3 & 4. One can also arrive at the same inference by considering tests 5 & 6, where an increase in overshoot and turning time was observed with an increase in sharpness of turn.

An explanation for the cause of increased turning time at regions of sharp turns may be due to: the time to cover the large overshoot distances produced as a result of tight turns and the loss of speed of the vehicle at regions of sharp turns. Thus the large overshoot combined with the loss of speed in a turn can considerably increase the turning time of the vehicle.

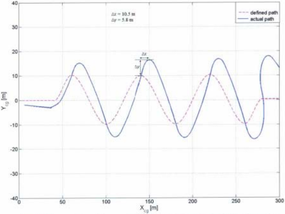

Fig. 4.43 Zigzag performed at a speed of 1.5 m/s for the defined path – Y_0 10 m & L_C 80 m

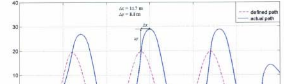

Fig. 4.44 Zigzag performed at a speed of 1.5 m/s for the defined path – Y_0 20 m & L_C 80 m

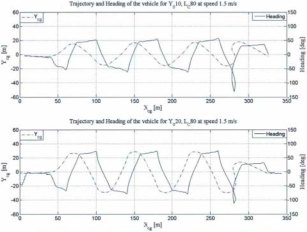

Fig. 4.45 Trajectory and heading of the vehicle for horizontal Z-Tests [$Y_0$10, L_C 80 & $Y_0$20, L_C 80] at speed 1.5 m/s

The speed-loss at a turn, if any, can be estimated by examining the speed profile of the vehicle. Figures 4.46 through 4.48 shows the time series of vehicle speed and corresponding propeller rpm for all the different tests performed.

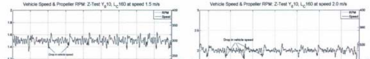

Fig. 4.46 Vehicle speed and propeller RPM for horizontal Z-Tests $Y_0$10, L_C160 at speeds 1.5 and 2.0 m/s

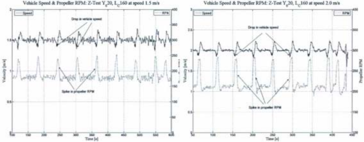

Fig. 4.47 Vehicle speed and propeller RPM for horizontal Z-Tests $Y_0$20, L_C160 at speed 1.5 and 2.0 m/s

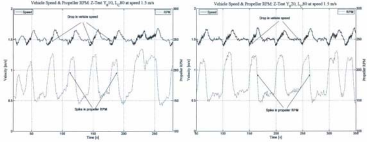

Fig. 4.48 Vehicle speed and propeller RPM for horizontal Z-Tests $Y_0$10, L_C80 & $Y_0$20, L_C80 at speed 1.5 m/s

When analyzing the time-series of vehicle speed and propeller rpm, it is seen that at regions of turn where the vehicle speed drops, the propeller spins at a higher rpm to regain the constant command speed. Hence, it can be deduced that speed-loss does not contribute much to the observed increase in turning time because when there is a drop in speed, the propeller responds immediately by spinning faster. On the other hand, this feedback nature of the propeller, to maintain the command speed, results in the vehicle speed shooting over and above command speed. This contributes to an additional increase in the overshoot distances that would otherwise have been absent if the vehicle were to negotiate the turn at a constant rpm. Therefore, the loss of speed at turns is not the significant factor, which contributes to the observed increase in turning time but the overshoot distance. This emphasizes the need to perform similar manoeuvring tests using constant propeller rpm as the control input rather than constant speed.

4.4.3 Attitude and Control Plane Angles

The vehicle uses all four tail control planes to perform the horizontal zigzag manoeuvre at a constant depth. In general, these four control planes are used for manoeuvring of the vehicle in any given plane – horizontal, vertical or oblique. This is typical of how an 'X' tail configuration works. The deflections of the four planes can generate pitch, roll and yaw motions of the vehicle. In other words, there is always a coupling between motions in the case of an 'X' tail configuration. Therefore, it becomes necessary to define the combined deflections of the four planes in generating each of these motions, by a simple representation. The value δY was taken as the effective single plane deflection, which represented or was assumed to capture the combined effect of all the four planes' deflection in producing a yaw motion of the vehicle. Similarly, δP and δR are the effective single plane deflection, which represent the combined effect of all the four plane deflections in producing pitch and roll motions respectively.

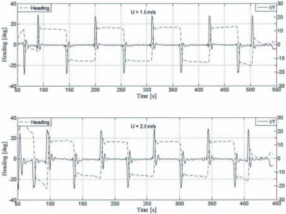

Fig. 4.49 Vehicle heading and effective tail plane deflection δY at speeds of 1.5 & 2 m/s for Z-Tests Y_0 10, L_C160

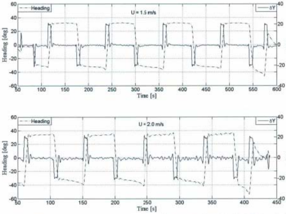

Fig. 4.50 Vehicle heading and effective tail plane deflection δY at speeds of 1.5 & 2 m/s for Z-Tests Y_0 20, L_C 160

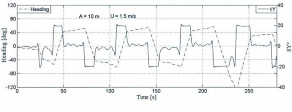

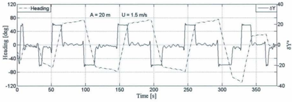

Fig. 4.51 Vehicle heading and effective tail plane deflection δY for Z-Test Y_0 10, L80 & Y_0 20, L_C 80 at speed of 1.5 m/s

Figure 4.49 shows the heading and effective control plane deflection δY, in producing yaw motion when the vehicle followed the zigzag path Y_0-10 and L_C-160 at speeds 1.5 and 2.0 m/s (Tests 1 & 2). Similarly, Figure 4.50 shows the heading and effective control plane deflection when the vehicle followed the zigzag path Y_0-20 and L_C-160 at speeds 1.5 and 2.0 m/s (Tests 3 & 4). From these figures it is seen that the tail planes are not in action for long periods of time. This indicates the region where the vehicle was traveling in a straight line (constant heading). Note that in all cases, the combined effect of four control plane angles, represented by, δY, takes a value close to 20°. This value is more than double the effective deflection angle, δY, encountered in all the turning circle tests. That indicates the vehicle is capable of performing tighter turns of smaller radii. Figure 4.51 shows the same heading and effective control plane deflection angle data from tests 5 & 6. However, in Figure 4.51, where the cycle length was reduced to half, the control planes were deflected and held in position for longer periods of time to achieve the required change in course than the initial four cases. The average turning time for each test was presented in Table 4.8.

An overall picture of the horizontal zigzag manoeuvres in 3D space can be viewed in figures 4.52a through 4.58a. Note that the scales on the three axes are distorted for convenience. A close observation of the figures 4.52a, 4.53a, 4.54a, 4.55a, 4.57a and 4.58a indicate that the vehicle experiences a "wobble" motion at regions of turn. This is categorized by a sudden rise from level flight followed by a dip from the steady path upon changing the course. This effect is found to be larger when the vehicle makes a turn to starboard than for a turn to port.

Figures 4.52b through 4.58b consist of two subplots. The first subplot depicts the depth profile and the effective control plane deflection δY of the vehicle while performing the zigzag manoeuvre at a certain command speed. Although, the values of δY do not apply much to motions in vertical plane or depth changes, they were included in the subplot to identify the regions where the vehicle is negotiating a turn. The second subplot shows the time-series of pitch attitude (θ) of the vehicle and the effective control plane deflections in producing pitch: δP_D and δP.

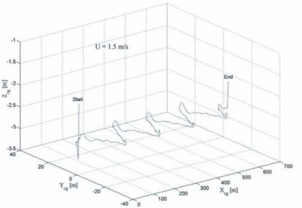

Fig. 4.52a 3-D plots of the horizontal zigzag manoeuvre, Y_0 10, L_C 160 at speed 1.5 m/s

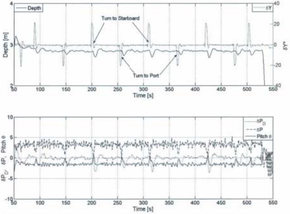

Fig. 4.52b Depth, pitch (θ) and corresponding control plane deflections (δP_D, δP, δY) for the zigzag manoeuvre: $Y_0$10, L160 at speed 1.5 m/s

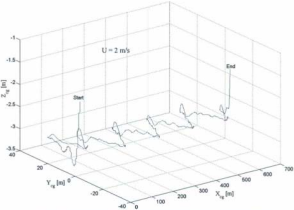

Fig. 4.53a 3-D plots of the horizontal zigzag manoeuvre, Y_0 10, L_C 160 at speed 2 m/s

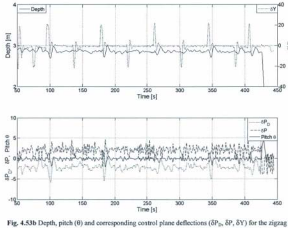

Fig. 4.53b Depth, pitch (θ) and corresponding control plane deflections (δP_D, δP, δY) for the zigzag manoeuvre: $Y_0$10, L160 at speed 2 m/s

It is apparent from the subplot for depth and δY in figures 4.52b and 4.53b that in the periods when the vehicle undergoes a turn (δY is executed) a sudden change in depth also occurs. However, the change in depth is seen to be larger during starboard turns than for port turns. In the subplot, a starboard turn is identified by regions where a positive spike in the value of δY is seen. This tendency can be seen in all the 3-D plots shown in figures 4.52a through 4.58a. When observing the subplots for vehicle pitch attitudes (θ), it is seen that the vehicle maintains a steady pitch attitude of approximately -1.5° (nose-down) at a forward speed of 1.5 m/s and maintains a level or near zero attitude at a forward speed of 2 m/s. As the control planes are responsible for causing these changes in attitude of the vehicle, analysing the control plane deflections may explain the reasons for the change in depth observed at turns.

At the speed of 1.5 m/s, the effective dive plane deflection δP_D was zero for most parts of the test (see Fig. 4.52b) except at certain points corresponding to the regions of turn. At regions of starboard turn δP_D had a maximum value of -3.3° and during port turns δP_D had a maximum value of -2°. On the other hand, the δP value was around $+3.3^{\circ}$ for most parts of the manoeuvre except at turns when the tail planes were deflected for producing the turns. The positive value of δP indicates that the combined effect of tail planes had a tendency to pitch the nose up while the dive plane deflections, δP_D, having a near zero value, do not contribute much to the pitch attitude of the vehicle. The combined action of both the tail planes and dive planes is what holds the vehicle at a steady pitch attitude of -1.5°. A similar tendency can be observed at the speed of 2.0m/s as well (see Fig. 4.53b). In this case, the effective tail plane deflection δP is about $+2^{\circ}$ and the effective dive plane deflections δP_D, unlike the previous case, is about -2° except at regions of turn. These angles indicate that the effective tail plane deflections δP have a tendency to pitch the nose up while the dive plane deflections δP_D, having a value of -2°, tend to pitch the nose down. The combined actions of these two sets of planes hold the vehicle at a level or near zero attitude as seen in Figure 4.53b. At regions of starboard turn the effective dive planes deflection δP_D has a maximum value of -5°, from the steady value of -2°, while at port turns, δP_D has a maximum value of -3°.

Figure 4.54 and Figure 4.55 shows the zigzag manoeuvres Y_0 = 20 m, L_C = 160 m performed by the vehicle at 1.5 m/s and 2.0 m/s respectively. The pattern is similar to that observed in test Y_0 =10 m, L_C = 160 m, shown in figures 4.52 and 4.53. At a speed of 1.5 m/s, the vehicle maintains a steady pitch attitude of -1.5° for most parts of the run except at turns (see Figure 4.52), where a steady δP value of 3.2° was maintained during the entire run except at turns. The dive plane deflections δP_D are nearly zero for most parts of the manoeuvre except at turns. At regions of starboard turn, δP_D has a maximum deflection of about -6° and at regions of port turns δP_D has a maximum deflection of about -3.5°. The combined action of δP and δP_D is what holds the vehicle at a -1.5° pitch attitude. When the vehicle follows the same path at a speed of 2.0 m/s, the pitch attitude of the vehicle is seen to be level or near zero for most parts of the run except for the occasional disturbance happening at regions of turn (see Fig 4.55b). In Figure 4.55b, the effective tail plane deflection δP and the dive plane deflection, δP_D, had non-zero values and also they were not steady when compared to Figure 4.54b. The average tail plane deflection, δP, was around 2.3° and

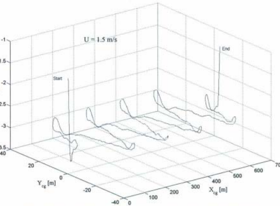

Fig. 4.54a 3-D plots of the horizontal zigzag manoeuvre, Y_0 20, L_C160 at speed 1.5 m/s

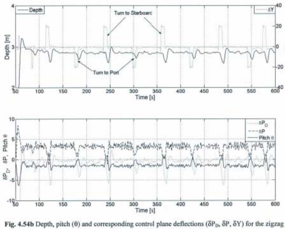

Fig. 4.54b Depth, pitch (θ) and corresponding control plane deflections (δP_D, δP, δY) for the zigzag manoeuvre: Y_0 20, L_C160 at speed 1.5 m/s

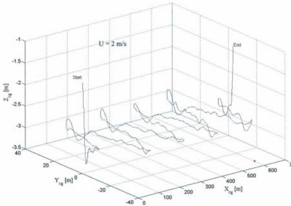

Fig. 4.55a 3-D plots of the horizontal zigzag manoeuvre, Y_0 20, L_C160 at speed 2 m/s

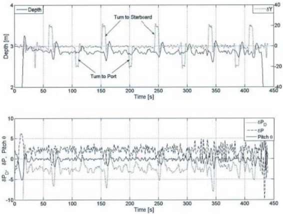

Fig. 4.55b Depth, pitch (θ) and corresponding control plane deflections (δP_D, δP, δY) for the zigzag manoeuvre: Y_0 20, L_C160 at speed 2 m/s

the average dive plane deflection δP_D was around -2.5°. However, at regions of starboard turn, δP_D had a maximum deflection of –6° and at regions of port turn, the maximum deflection was around –3.2°. Figures 4.52 through 4.55 show that at higher speed (2 m/s) the plane deflections are not as steady as was the case at lower speed (1.5 m/s).

In all the above tests, the vehicle experienced a sudden change in depth at turns. These locations were identified as regions near the waypoints where the vehicle negotiated a turn or a change in course. This depth change was more prominent when the vehicle turned to starboard than when it turned to port. This change in depth happens because, when the tail planes are deflected for a starboard or port turn (change in δY), their change also produces a change in δP from that of a steady value. This brings about a change in pitch attitude of the vehicle, which in turn results in a change in depth of the vehicle to an elevated depth level. However, the dive planes react quickly and brings the vehicle back to a steady path after an initial dip.

The change in depth during turns was larger for starboard turns than for turns to port. This also explains the reason for observing higher δP_D values at regions of starboard turn than at regions of turns to port.

It is also possible that the presence of a current in the direction closer to that shown in Figure 4.56 influenced the starboard turn at point P_1 while at the same time pushing the vehicle beyond the line P_2P_3 such that the vehicle struggles to get back on path P_2P_3 by adjusting its heading. This adjustment in heading could be the cause for the slight inclination in the heading observed in figures 4.49 and 4.50, instead of a constant heading. However, it should be noted that an asymmetric operation of the control planes could also produce a similar result.

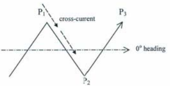

Fig. 4.56 Sketch showing the possible scenario of a cross current

The horizontal zigzags in figures 4.57 and 4.58 show the tests where the cycle length, L_C, was reduced to half (80m) while the vehicle traversed two different widths of path, Y_0: 10 m and 20 m, at a command speed of 1.5 m/s. In general, the depth changes happening at regions of turn in these two cases are more prominent than that observed in the previous two cases at 1.5 m/s shown in figures 4.52 and 4.54.

In test 5 [Y_0 10, L_C 80] (see Figure 4.57), the vehicle maintained an average pitch attitude of -1.6° with an average tail plane deflection δP of 3.5° while the dive planes deflection (δP_D) was nearly zero. However, near regions of turn, the maximum dive plane deflections exceeded -6.5° in order to bring the vehicle back on a level path from an estimated 0.4 to 0.5 m depth change, while turning the course through about 53°.

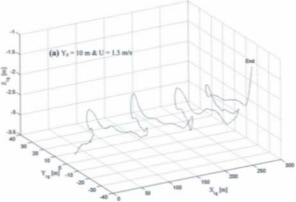

Fig. 4.57a 3-D plots of the horizontal zigzag manoeuvre, Y_0 10, L_C 80 at speed 1.5 m/s

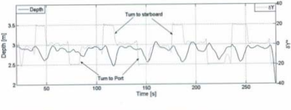

Fig. 4.57b Depth, pitch (θ) and corresponding cortrol plane deflections (δP_D, δP, δY) for the zigzag manoeuvre: Y_0 10, L_C 80 at speed 1.5 m/s

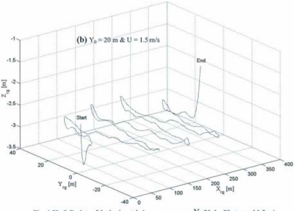

Fig. 4.58a 3-D plots of the horizontal zigzag manoeuvre, Y_0 20, L_C 80 at speed 1.5 m/s

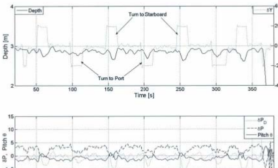

Fig. 4.58b Depth, pitch (θ) and corresponding control plane deflections (δP_D, δP, δY) for the zigzag manoeuvre: Y_0 20, L_C 80 at speed 1.5 m/s

In test 6, [Y_0 20, L_C 80] (see Figure 4.58), the vehicle maintained an average pitch attitude of -1.5^o with an average tail plane deflection δP of 3.4^o while the dive planes deflection, δP_D had near zero values. At regions of turn, the maximum dive plane deflections were around -5^o in order to bring the vehicle back on a level path from an estimated depth change of 0.2 to 0.3 m, while turning the course through about 90^o.

In the last two tests (5 & 6), the tail planes were deflected (δY) for a longer period of time (~ 9 s in test #5 and ~ 14 s in test #6) than in all the initial four tests (~ 5 s). This happened as a result of reducing the cycle lengths thereby making the turns tighter.

4.4.4 Analysis of Turning Parameters

The different turning parameters of interest during an unsteady turn in a horizontal plane manoeuvre are the turning rate, r, drift angle, β and the sway velocity, v. In particular, parameter such as turning rate, r, would be useful indicators of how fast or slow the vehicle can deviate from its course in the event of obstacle avoidance. The variation of these parameters with each other as well as with the control plane deflections, δY, during an unsteady turn like a zigzag in horizontal plane is presented in the following subsections.

a. Turning rates r vs. Control plane deflections δY

The zigzag manoeuvre is an indicator of the efficiency of the control planes to control the vehicle's heading. The ease with which a vehicle can change its course is measured by its turning rate r, which in turn depends on the effectiveness of the control planes. Figure 4.59 thorough Figure 4.61 show the phase-plane plot of turning rate, r, versus the effective control plane deflection, δY, for different speeds and degrees-of-turn. The phase-plane plot was created considering only the turning regions of the trajectory where an apparent rudder deflection and a corresponding turning rate were observed.

Figure 4.59 shows the phase-plane plot of turning rate, r, with respect to effective control plane deflection δY, for the same degree-of-turn (Y_0-10, L_C 160), at two different speeds. Figure 4.60 shows the same for a different degree-of-turn (Y_0-20, L_C 160), at both speeds. In each figure, the only factor that changes is the speed of the vehicle, while it traverses the exact same trajectories. Therefore, any difference observed between the two plots in each figure is the result of change in vehicle speed.

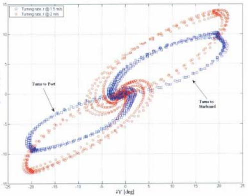

Fig. 4.59 Phase-plane plot of turning rate, r vs. control plane deflection δY for zigzag manoeuvres at speeds of 1.5 and 2.0 m/s (Y_0 10, L_C 160)

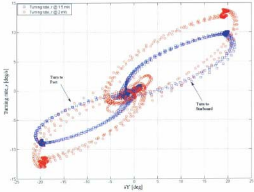

Fig. 4.60 Phase-plane plot of turning rate, r vs. control plane deflection δY for zigzag manoeuvres at speeds of 1.5 and 2.0 m/s (Y_0 20, L_C 160)

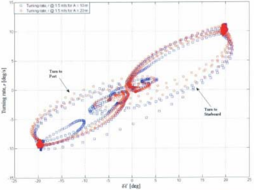

Fig. 4.61 Phase-plane plot of turning rate, r vs. control plane deflection δY for zigzag manoeuvres at different degrees of turn (Y_0 10 & Y_0 20; L_C 80) at the same speed of 1.5 m/s

The width of the loop indicates the stability of the vehicle. The larger or wider the loop, the less stable the vehicle is. A closer look at the figures reveal that the loops for positive rudder deflections or starboard turns are wider and larger than that for the port turns, in almost all the cases. The disturbance noticed in the 3D plots (see Figures 4.52a through 4.58a) during the starboard turns may explain the reason for the instability and consequently the asymmetry in the loops.

Figure 4.61 shows the phase-plane plot of turning rate for two different trajectories (Y_0-10 & Y_0-20), at the same speed. Note that there is no significant difference between the turning rates for the two cases because the loops more or less overlap each other. This indicates that the width-of-path (Y_0 10 or Y_0 20) or in other words the degree-of-turn have hardly any effect on the turning rate of the vehicle but only the speed. Figures 4.62 and 4.63 further prove this point, which is only a different representation of the cases shown in Figures 4.59 and 4.60 where the tests pertaining to the same speed are grouped together. It is clear from those figures that the turning rates remain the same regardless of the degree-of-turn and that indicates the turning rate is dependent only on the forward speed apart from control plane deflection δY which in all tests were deflected to the same maximum values.

b. State-Space Plots

Another important parameter that is of interest during a turn in a horizontal plane is the drift angle or the sideslip angle β of the vehicle. In order to generate a radial force sufficient enough to turn the vehicle, the hull should be held at an angle with respect to the flow. This angle, which the hull makes with respect to the flow, is called the drift

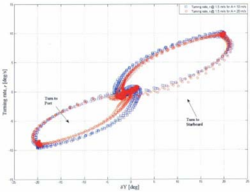

Fig. 4.62 Phase-plane plot of turning rate, *r* vs. control plane deflection δY for zigzag manoeuvres at different degrees of turn (Y_0 10 & Y_0 20; L_C 160) at the same speed of 1.5 m/s

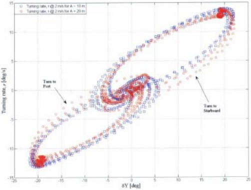

Fig. 4.63 Phase-plane plot of turning rate, *r* vs. control plane deflection δY for zigzag manoeuvres at different degrees of turn (Y_0 10 & Y_0 20; L_C 160) at the same speed of 2.0 m/s

angle or sideslip angle. As a result of this sideslip angle, the vehicle experiences an increased drag, which consequently reduces the speed of the vehicle. It was seen in Figure 4.46 through Figure 4.48 that there was a loss of speed associated with each region of turn but a spike in propeller rpm compensated the loss of speed almost immediately. Just as the turning rate or yaw rate is affected by the control plane deflection, so is the drift angle β of the vehicle.

A different way of visualizing the variation of these three parameters i.e., turning rate r, control plane deflection δY and the drift angle or the sideslip angle β, during a manoeuvre, is through a state-space plot, as all three parameters are interrelated. The time series of these parameters are shown in Figures 4.64a through 4.66b while Figures 4.64b through 4.66b shows their state-space representation. It shows how variation in one parameter affects the other two or vice-versa. The phase-plane plots of turning rate vs. control plane deflection, discussed in the previous subsection, are a special case of this state-space plot. In other words, they are the projection of the state-space plot on to one of the coordinate planes. Similarly, the phase-plane plots of turning rate (r) vs. drift angle (β) as well as drift angle (β) vs. control plane deflection (δY) are also a special case of the state-space plot depending upon along which axis they are viewed at. In all cases, the loops fall in a roughly diagonal plane, which has a positive slope, i.e., as one parameter increases, its effect is to increase the other two parameters as well. Finally, it is observed that the loops corresponding to the more stable manoeuvres seemingly fall on a steeper plane than the others.

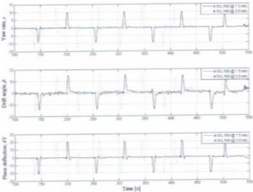

Fig. 4.64a Time series of Yaw rate, Drift angle and control plane deflection for Y_0 10, L_C 160 @ 1.5 and 2.0 m/s

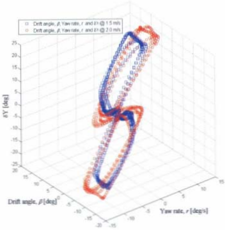

Fig. 4.64b State-space plot of the parameters during turn for Y_0 10, L_C 160 @ 1.5 and 2.0 m/s

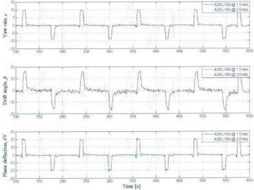

Fig. 4.65a Time series of Yaw rate, Drift angle and control plane deflection for Y_0 20, L_C 160 @ 1.5 and 2.0 m/s

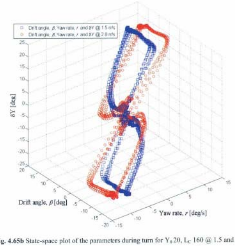

Fig. 4.65b State-space plot of the parameters during turn for Y_0 20, L_C 160 @ 1.5 and 2.0 m/s

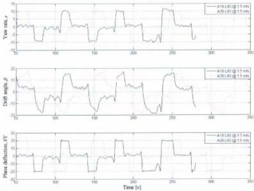

Fig. 4.66a Time series of yaw rate, drift angle and control plane deflection for Y_0 10 & A20, L_C 80 @ 1.5

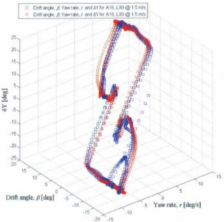

Fig. 4.66b State-space plot of the parameters during turn for Y_0 10 & Y_0 20, L_C 80 @ 1.5 m/s

Sway velocity (v) vs. Drift angle (β)

Another important parameter during a horizontal turn is the sway velocity or the drift velocity, v. The variation of sway velocity v' with respect to the drift angle β is plotted in the Figure 4.67. The sway velocities from all the six different zigzag tests are represented in their nondimensional form and are shown in figures 4.67a, 4.67b and 4.67c. Figure 4.67a shows the sway velocity results when the vehicle followed the same trajectory (Y_0 10, L_C 160) at two different speeds and Figure 4.67b shows the same when the vehicle followed a different trajectory (Y_0 20, L_C 160) at two different speeds. On the other hand, Figure 4.67c shows the variation of sway velocity for two different trajectories or degree-of-turns at the same speed (1.5 m/s). It appears from this figure (4.67c) that for the same speed (1.5 m/s) the degree of turn is immaterial. The data shown in the figures corresponds to the regions of turn and contains only the data selected from those regions.

Further, it is clear from all the tests that there exists a linear relationship between sway velocity and drift angle, given by the following relation:

$$v' = -0.017\beta \qquad (4.19)$$

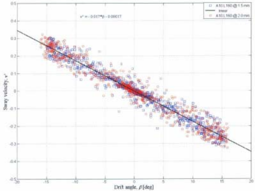

Fig. 4.67a Variation of sway velocity v' vs. drift angle β for Y_0 10, L_C 160 @ 1.5 and 2.0 m/s

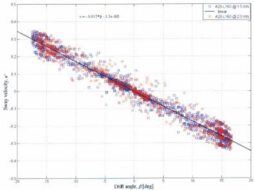

Fig. 4.67b Variation of sway velocity v' vs. drift angle β for Y_0 20, L_C 160 @ 1.5 and 2.0 m/s

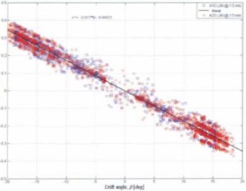

Fig. 4.67c Variation of sway velocity v' with drift angle β for Y_0 10 and Y_0 20, L_C 80 @ 1.5 m/s

4.4.5 Summary of Horizontal Zigzag Manoeuvres

Unlike straight-line tests and turning circles, which are steady-state tests, a zigzag manoeuvre is characteristic of an unsteady manoeuvre. A total of six horizontal zigzag manoeuvres were performed using the *MUN Explorer* AUV during the available test time. The vehicle responses from a few horizontal zigzag manoeuvres described through this section were already published in Issac *et al* (2008). The missions were programmed in such a way that the vehicle was commanded to follow a path defined by a series of waypoints in a zigzag pattern, at two different speeds: 1.5 and 2.0 m/s. some key observations from data analyses of horizontal zigzag manoeuvres are summarized below:

a) Although the zigzag trajectories traced by the vehicle do not resemble exactly a conventional zigzag manoeuvre, it does demonstrate the ability of the AUV to precisely follow a predefined path. Nevertheless, the vehicle's turning ability can be simulated using the hydrodynamic model and the results can be compared with the information available from the actual vehicle over regions of turn.

b) From the initial four tests it was seen that the vehicle travelled a considerable distance in a straight line (constant heading) while following the predefined path. This is not characteristic of a conventional zigzag manoeuvre in which the heading changes continuously, forming a sinusoidal pattern. In an attempt to rectify this, the last two tests were performed by reducing the cycle lengths to half while retaining the same amplitudes or width-of-paths. The modifications in cycle-length (L_C) indeed produced trajectories that seemed much closer to a conventional zigzag, although not exactly. In the event of a need for similar experiments in future vehicle dynamics study, the above information can be used as a guide to refine the experiments by adjusting the amplitude and cycle length.

c) Higher speeds and sharper turns produced larger overshoots and consequently more turning time.

d) The loss of speed during the turn was sharply evident in the zigzag manoeuvres unlike the turning circle manoeuvres. This is because larger drift angles ($\sim 15^{\circ}$) were noticed in horizontal zigzag manoeuvres, which in turn would generate large drag forces that would slow down the vehicle. However, the loss of speed was immediately compensated by a positive spike in the propeller rpm. This once again emphasizes the need for performing the test with constant propeller rpm as the input rather than constant speed-over-ground.

e) The vehicle was slightly unstable during turns to the starboard side than when it turned to the port side. This was further shown by the presence of an asymmetry in the loop for turning rates where the loops characterizing starboard turns were seen to be larger and wider than the ones characterizing the port turns.

f) The turning rate was seen to be affected only by the speed of the vehicle while the rate was not influenced by the sharpness or degree-of-turn. The maximum degree-of-turn or change in heading ever experienced by the vehicle during the test was 90^{o} and hence it is not known whether any further sharp turns would affect it or not. Further, the speed also affected the stability of turn with higher speeds producing more unstable turns than the slower speeds. This was characterized by larger and wider loops for turning rates at higher speeds (2 m/s) than that at slower speeds (1.5 m/s).

4.5 Vertical Zigzag Manoeuvring Analysis

An underwater vehicle needs to be controllable in the vertical plane so as to enable itself to maintain or change depth as required. Zigzag manoeuvres in the vertical plane are often performed with underwater vehicles in order to study their dynamic stability and control in depth changing. With underwater vehicles such as submarines, manoeuvres in the vertical plane are of more significance than those in the horizontal plane as many submarines are restricted to a layer of water, which is of the order of at most two or three ship lengths deep (Molland, 2008). Similarly, underwater vehicles such as AUVs, operate within a depth range, often limited by the depth ratings of the pressure hull or the depth ratings of the instruments onboard the vehicle, whichever is less. Further, an underwater vehicle operating in a vertical plane has to deal with an extra set of forces, viz., the hydrostatic or buoyancy forces. This is different from when it operates in a horizontal plane.

Autonomous underwater vehicles, in many scenarios, operate close to the seabed either mapping the seabed topography or monitoring geophysical features or marine life. While following a rugged seabed terrain at a constant altitude, the AUV may have to make frequent depth changes along its path. This change in depth is facilitated by means of hydroplanes, which as Molland (2008) defines, are control surfaces that are used to control the vertical motion of underwater vehicles.

The depth-changing manoeuvres or the vertical zigzags with *MUN Explorer* were performed by forcing the vehicle to follow a predefined path laid out by a series of waypoints in a zigzag pattern. These paths were generated by picking points at regular intervals on either side of a horizontal-line in a vertical plane. There are two distinct modes by which the vehicle can achieve a depth change, (a) by using the tail planes or (b) by using the dive planes, as will be explained later in this section. As mentioned in Section 4.4, the vertical zigzags were performed in conjunction with the horizontal zigzags (see Figure 4.35). The horizontal zigzags were performed in the South-to-North direction while the vertical zigzags were performed in the North-to-South direction on the return leg. Hence, the origin of the local Earth coordinates had to be arbitrarily chosen as a point on the water surface at the north end of the line. A total of six vertical zigzag tests were performed at varying amplitudes and cycle lengths. Table 4.9 gives a list of these manoeuvring trials performed at two different speeds: 1.5 and 2.0 m/s. The tests were done over a span of three days.

TABLE 4.9
Vertical Z-Test Plan

Test #	V	Z_0	L_C	Command	Type	Day
	[m/s]	[m]	[m]			
1	1.5	1.5	140	*line follow*	A	1
2	2.0	1.5	140	*line follow*	A	1
3	1.5	3.0	140	*line follow*	A	1
4	2.0	3.0	140	*target*	C	3
5	1.5	1.5	60	*target*	B	2
6	1.5	3.0	60	*target*	B	2

4.5.1 Patterns of Vertical Zigzags

Initially, two different vertical zigzag paths were defined which had the same cycle length (L_C) of 140 m but different amplitudes, (Z_0): 1.5 and 3.0 m. The vehicle was commanded to follow these paths at two different speeds of 1.5 and 2.0 m/s thus making a total of four runs. The first four runs shown in the Table 4.9 reflect this. However, preliminary observations made from the three tests performed on Day-1 revealed that the cycle length (140 m) chosen was too large for the given amplitudes;

just as in the case for horizontal zigzags. As a result, two new zigzags were designed by making changes to the previous ones in which the cycle length was reduced to 60 m. The two new paths had amplitudes of 1.5 and 3.0 m while the vehicle traversed them at a speed of 1.5 m/s.

There were two further differences in the vertical zigzags that were planned. As apparent from the Table 4.9, there was already a difference in the cycle length L_C, which was maintained at 140 m for the initial four cases but reduced to 60 m in the remaining two cases. Apart from that, there were two further differences that need to be mentioned. This is illustrated through Figure 4.68 in which the defined paths are termed as Type-A, Type-B and Type-C.

Type-A zigzag paths had a flat base at the crest and trough and the vehicle used the *line_follow* command during the ascent and descent phases of the manoeuvre. It was reasoned, that a vehicle descending the inclined path, say P_6P_7, after hitting P_7, would overshoot it and would need some extra distance allotted so as to regain its upward climb along the path P_8P_9. This was the reason why the flat bases were provided for the initial tests. However, at the end of first day's test it was found that the vehicle did not overshoot as much as was expected. Thus the flat bases provided were of hardly any use and were eliminated in subsequent tests.

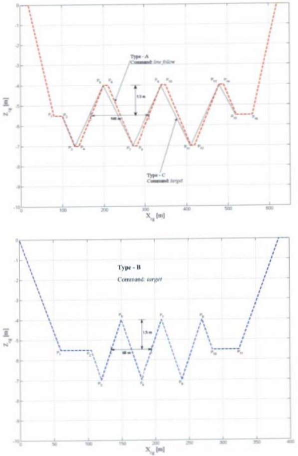

Fig. 4.68 Different types of vertical zigzag paths defined: Type-A, B & C

Type-B zigzag manoeuvres had their cycle lengths reduced to 60 m and the flat bases were removed. The vehicle followed the defined paths using the *target* command. Examples of each of the above mentioned types are shown in the two panes of Figure 4.68. Type-A shown in the first pane is typical of tests 1, 2 & 3 although Test #3 had amplitude of 3 m. Similarly, Type-B shown in the second pane represent tests 5 & 6 although Test #6 had amplitude of 3.0 m.

Test #4 performed on Day-3, had a slight variation from the above mentioned two types: A & B. It was modified from Test #3 (Type-A) by joining the odd-numbered points $P_3P_5P_7P_9$…etc., thereby getting rid of the flat base, as shown by the firm line path in the first pane of Figure 4.68. Hence, the cycle length remained the same as Type-A manoeuvres but the pattern looked like Type-B manoeuvres. Further, the vehicle was commanded to follow this path using the *target* command as in Type-B. This is denoted as a Type-C manoeuvre in Table 4.9 and in Figure 4.68.

Although, zigzag paths have been planned using the *line_follow* and *target* commands, it was later discovered that these task verbs have no distinction between them for executing a mission in the vertical plane, unlike in an horizontal plane. This is because in the vertical plane, the vehicle's depth controller overrides these commands.

The responses of the vehicle to different vertical zigzag manoeuvres listed in Table 4.9 are described through the following subsections.

4.5.2 Vehicle Trajectory and Attitudes

The vehicle's response to the same predefined path, both of Type-A pattern, at two different speeds: 1.5 and 2.0 m/s, are shown in Figure 4.69. This corresponds to tests (1) and (2) in Table 4.9. For both runs, the vehicle used the *line_follow* command. From Figure 4.69 it is obvious that the vehicle did not follow the line exactly but reached the commanded depth quicker than desired. This is because the vehicle decouples vertical control from horizontal control. Although waypoints can be defined in the vertical plane using the *target* or *line_follow* cammands, the depth controller works independent of the geographic (*x, y*) control in the vertical plane. Thus there cannot be a path defined at a particular slope in the vertical plane. This means that the vehicle will climb or dive at a rate determined by the tunings of the vertical PID controller and not in a linear fashion from one point to another. Thus, in Figure 4.69 the vertical control has reached its target (commanded depth) well in advance of the geographic control reaching its (*x, y*) target. Hence, the vehicle travelled a considerable distance (~40 m) in level flight before it executed the next dive or climb phase. This also indicated that the cycle length provided (140 m) was too large for the intended manoeuvre. Even though the vehicle did not follow exactly the defined path, both runs produced trajectories that look similar to each other but with the exception that the manoeuvre at higher speed (2.0 m/s) had a slight overshoot as it reached the new depth level.

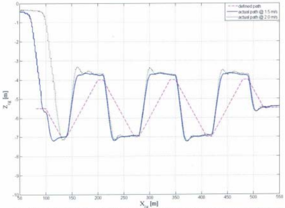

Fig. 4.69 Trajectories of the AUV in response to two different speeds over the same defined path (Z_0 1.5, L_C 140) [Test #1 and 2]

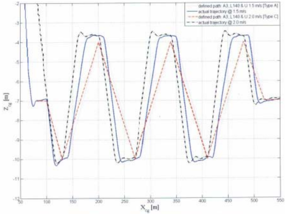

Fig. 4.70 Trajectories of the AUV in response to test #3 and 4 (Z_0 3.0, L_C 140)

Figure 4.70 shows the trajectories of the vehicle corresponding to tests (3) and (4). In this case, the defined paths had the same amplitude (3.0 m) and cycle length (140 m) but were not exactly the same in their pattern. In terms of pattern, Test #3 followed a Type-A pattern zigzag using the *line_follow* command while Test #4 followed a Type-B pattern zigzag using the *target* command. It was modified from Test #3 by eliminating the alternate waypoints or even-numbered waypoints thereby eliminating the flat bases. To signify the slight differences it made with Type-A and Type-B manoeuvres, this particular zigzag was denoted by Type-C in Table 4.9. The results from tests (3) and (4) (see Figure 4.70) look similar to that from tests (1) and (2) (see Figure 4.69) in pattern, except that there is a phase lag between the two trajectories. This happened because of the difference in the defined paths that the vehicle was forced to travel. Here again, the vehicle travels a distance of about 30 m in level flight at the crest and trough indicating that the cycle length provided was still too large for the given amplitude (3m). This emphasized the need for designing new zigzags with shorter cycle length. Consequently, test (5) and (6) were designed.

Apart from vehicle's depth controller overriding the *target* and *line_follow* commands, in terms of hydrodynamic loads acting on the vehicle also, forcing a vehicle to follow an inclined straight line in the vertical plane can be challenging. This is because the depth change is facilitated by the control planes that generate lift, which in turn are dependent on the speed of the vehicle and control plane deflection. The higher the speed, for a given control plane deflection (δ), the faster it ascends or descends and vice-versa. Further, an underwater vehicle manoeuvring in a vertical plane encounters hydrostatic or buoyancy forces. Since AUVs are generally designed to be slightly positively buoyant, this further adds to the problem of forcing the vehicle along a slope in the vertical plane. On the other hand, one could argue that by adjusting the control plane deflection to suitable values, speed being set to a constant, one could 'fly' the vehicle along a predefined inclined path. However, this was not observed to be the case.

Another observation from the same figures is that in all four cases the overshoot of the vehicle from the defined path was significantly small. This is contrary to what is usually expected from a depth-changing manoeuvre and is an extremely important criterion in deciding the operational depths of underwater vehicles; for instance a submarine. For AUVs, the overshoot in the vertical plane could be a concern particularly when the AUV is deployed in shallow waters or operating in close proximity to the seabed.

In test (1) and (2), a certain amount of overshoot happens at the trough for both speeds whereas at the crest (peak), the overshoot occurs only for the higher speed; i.e., at 2 m/s. The maximum overshoot at the crest was estimated to be around 0.25 m. The magnitude of maximum overshoot at the trough was also around 0.25 m for both speeds. Following this initial disturbance, the vehicle stabilized whereafter it followed a level flight at constant depth for about 40 m. This level-flight segment coincides with the flat base of designed path at the trough while the level-flight segment at the crest was off the flat base of the defined path by about 30 cm. This offset from the defined path is not significantly large and is less than half the diameter of the vehicle. It should be noted that the trajectory plotted corresponds to the path traced by the centre of gravity of the vehicle whereas the depth measurements were recorded by the pressure sensor which was located approximately 15 cm below and almost 75 cm forward of the C.G. Hence, in addition to the apparent vertical separation between the centre of gravity and the pressure sensor, any change in pitch or roll attitude of the vehicle would also affect the interpretation of the measured depth.

Tests (3) and (4) which had an amplitude of 3.0 m also produced trajectories of similar pattern as that of tests (1) and (2), except that they had a phase lag which was, as explained before, due to the slight difference in the defined paths. This similarity is despite the fact that the vehicle was driven by two different commands: test (3) by *line_follow* and test (4) by *target* commands. This again shows that there is no distinction between using *target* command and *line_follow* command in the vertical plane. Here again, the level-flight segment at the crest was around 30 cm above the defined path while that at the trough seemed to have coincided with the defined path. The maximum overshoot from this level path at the crest was about 20 cm and at the trough was 25 cm, which occurred only in the case of higher speed (test #4).

The reason for this relatively insignificant overshoot observed in all the above four cases is explained by analysing the control plane deflections and attitude of the vehicle during the manoeuvres. The control plane deflections for each of the four manoeuvres are shown in figures 4.72a through 4.75a. A portion of the time series (100 s to 200 s) from test (1) consisting of one complete cycle (includes a dive and a climb segment) of control plane deflections, shown in Figure 4.72a, is enlarged in Figure 4.71 to show in detail the individual plane deflections during that period. In the first pane, the dive plane deflections δ_1 and δ_2 are shown. The effective single control plane deflection δP_D representing their combined effect is also plotted which overlaps the δ_2-curve. In the second pane, the individual tail plane deflections are plotted along with δP, which is the effective single plane deflection representing their combined effect in producing pitch attitudes.

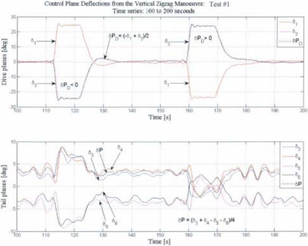

Fig. 4.71 Enlarged view of individual control plane deflections and their combined effects of a portion of the time-series from Test #1 [Z_0 1.5 m, L_C 140 m] at 1.5 m/s
Time Series: 100 to 200 seconds

The effective single tail plane deflection δP representing the combined effect of tail planes δ_3, δ_4, δ_5 and δ_6 in producing a pitch attitude and the effective single dive plane deflection δP_D representing the combined effect of δ_1 and δ_2 in producing a pitch attitude were calculated using equations (4.1) and (4.4) described in *Section 4.1.1*, respectively.

Figure 4.72a and 4.73a show the time series of plane deflections from tests (1) and (2) while Figure 4.74a and 4.75a depict the same from tests (3) and (4) respectively. The first subplot in each figure depicts the dive plane deflections with their combined effect δP_D. The second subplot in each figure shows the four tail plane deflections with their combined effect δP as well. It is apparent from the figures that the dive planes were instrumental in producing the depth change while the tail planes had relatively less role in helping the vehicle change its depth. The role of the tail planes is more like a stabilizer to hold the vehicle at a certain pitch attitude. With the dive planes primarily acting as the devices for depth change, the vehicle follows a gliding motion with a nearly level pitch attitude as it ascends or descends. This can be shown by examining the pitch attitude of the vehicle.

The pitch attitude (θ) and the corresponding angle-of-attack (α) of the vehicle during each of the four trials are shown in figures 4.72b through 4.75b. The angle of attack (α) was estimated using the relation: $\tan\alpha = (+w/u)$, where u and w are the linear components of velocity in the surge and heave direction respectively, estimated as described in *Section 4.1.2.2*. The effective control plane deflections δP_D and δP, already shown in figures 4.72a through 4.75a, are re-plotted in the first subplots of figures 4.72b through 4.75b along with the depth profile of the vehicle. This is to show exactly the actions of the control planes at regions where the depth changes happen. It is clear that the depth change happens in a relatively short period of time and the dive planes are instrumental in bringing about this change. The second subplot shows the time series of pitch attitude (θ) and angle of attack (α) corresponding to the depth profile and effective control plane deflections depicted in the first subplot.

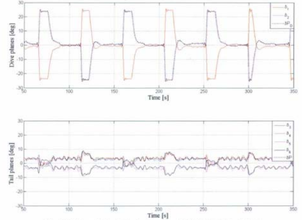

Fig. 4.72a Control plane deflections from Test #1 [Z_0 1.5, L_C 140] at 1.5 m/s

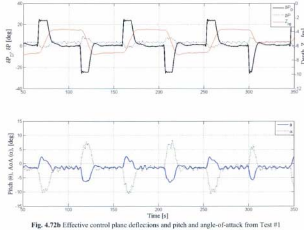

Fig. 4.72b Effective control plane deflections and pitch and angle-of-attack from Test #1 [Z_0 1.5, L_C 140] at 1.5 m/s

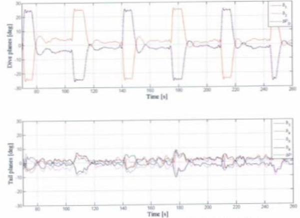

Fig. 4.73a Control plane deflections from Test #2 [Z_0 1.5, L_C 140] at 2.0 m/s

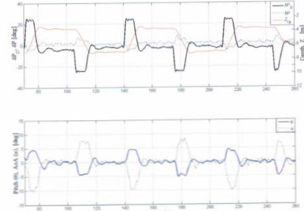

Fig. 4.73b Effective control plane deflections and pitch and angle-of-attack from Test #2 [Z_0 1.5, L_C 140] at 2.0 m/s

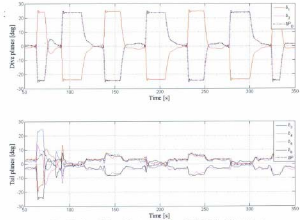

Fig. 4.74a Control plane deflections from Test #3 [Z_0 3.0, L_C 140] at 1.5 m/s

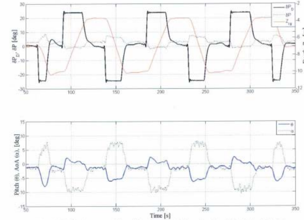

Fig. 4.74b Effective control plane deflections and pitch and angle-of-attack from Test #3 [Z_0 3.0, L_C 140] at 1.5 m/s

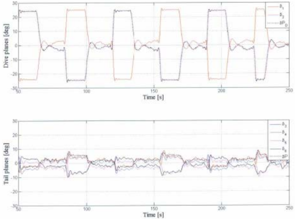

Fig. 4.75a Control plane deflections from Test #4 [Z_0 3.0, L_C 140] at 2.0 m/s

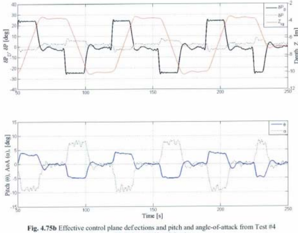

Fig. 4.75b Effective control plane deflections and pitch and angle-of-attack from Test #4 [Z_0 3.0, L_C 140] at 2.0 m/s

Refer to Table 4.10 (page 225) for an estimate of the average magnitude of some of the parameters shown in Figures 72 through 75 at each phase: dive, climb, crest & trough. For a given manoeuvre, the magnitude of pitch (θ) was seen to be larger during the dive than for the climb. On the contrary, the magnitude of angle-of-attack (α) is larger for a climb than for a dive. According to SNAME (1950), the angle of attack (α) is defined as the angle in the plane of symmetry (xz -plane) measured from the projection of the velocity of the origin of the body axes relative to the fluid (tangent to the trajectory in space), to the longitudinal body axis, positive in the positive sense of rotation about the y-axis. Figure 4.76 is a schematic diagram showing the attitudes of the vehicle at each phase during a typical depth-changing mission. The magnitude of maximum pitch attitude observed among all the above cases was between -5° to -6°. This relatively small pitch attitude during its ascent and descent phases imply that the vehicle was in a state of gliding motion rather than diving or climbing with a sharp nose-up or nose-down attitude; whereby it maintained more or less a level pitch attitude during those phases. In other words, it can be described as the vehicle approaching the flow with its 'belly' at an angle rather than 'head-on'. Maintaining a nearly level pitch attitude during ascent or descent increases the drag on the vehicle considerably, thereby damping much of the overshoot that would otherwise have happened in a 'head-on' motion. This explains the reason for the relatively insignificant overshoot observed in all the manoeuvres.

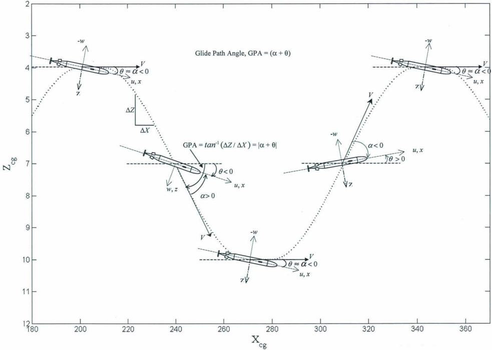

Fig. 4.76 Pitch attitude (θ) and angle of attack (α) of the vehicle during a typical vertical zigzag manoeuvre

As mentioned earlier, there are two ways by which the vehicle can achieve a change in depth and the vehicle controller gives a choice between the two. One is by using the tail planes, whereby it changes the pitch attitude of the vehicle as it advances thus making it dive or climb. In this case the longitudinal axis of the vehicle will be almost inclined to the path of the vehicle. This is termed as the *Depth-by-Pitch* mode. The other method of changing depth is by using the dive planes in which the vehicle pitch attitude remains more or less level as it ascends or descends. This is called the *Depth-by-Heave* mode. In the absence of an operator specifying otherwise, the vehicle uses the default mode, which is the *Depth-by-Heave* mode. This may also be the safest mode to operate the vehicle in the vertical plane as it restricts the depth excursions during a depth-changing mission. Thus, all the vertical zigzags performed have been controlled by the *Depth-by-Heave* mode. This was discovered only after the completion of all the tests and hence there was not a chance to perform any test using *Depth-by-Pitch* mode.

All the initial four tests had large cycle lengths (140 m) which means that for tests (1) and (2), which had an amplitude of 1.5 m, the slope of ascent and descent for the defined path was 1 in 20, and for tests (3) and (4), which had an amplitude of 3.0 m, the slope of the defined path was 1 in 10. However, when analysing the slope of the actual trajectory traced by the vehicle, it is found that the vehicle followed a steeper path than the defined path, with a slope of roughly 1 in 8 and 1 in 6 respectively for tests (1) and (2) while the slope was around 1 in 7 and 1 in 5 respectively for tests (3) and (4), during the climb. During dives, it followed an even steeper path with a slope of roughly 1 in 5 for all the four tests. This resulted in the vehicle reaching the commanded depth quicker than desired, thereby experiencing long segments of level-flight between each climb and dive phases. To eliminate these unwanted segments of level-flight it was decided to do some missions with considerably shorter cycle lengths and as a result tests (5) and (6) were designed. Both runs were performed at the speed of 1.5 m/s while the vehicle traversed the paths using the *target* command. The trajectories from tests (5) and (6) are shown in Figure 4.77 and Figure 4.79 respectively, while the corresponding effective control plane deflections with pitch attitudes and angles of attack are shown in Figure 4.78 and Figure 4.80. By reducing the cycle lengths to 60 m, while retaining the amplitudes at 1.5 m and 3.0 m respectively, the level-flight segment in both cases were considerably reduced.

In test (5), the vehicle traced the defined path very closely with very little overshoots. The designed path in this case had a slope of 1 in 10 while the vehicle followed a steeper path with a slope of 1 in 6.25 during ascent and 1 in 4.5 during descent. This resulted in a level-segment flight at the crest and trough spanning only about 15 m, which was far less than that in the initial four tests. This is clear from the first subplot of Figure 4.78.

The path designed for test (6) turned out similar to a conventional test because the result indicates that the vehicle followed a tight enough course where the control planes never returned to the zero-state anytime during the entire manoeuvre. This is clear from the first subplot of Figure 4.80 where the control planes are continuously engaged in performing the manoeuvre. The path designed, which had a slope of 1 in 5, must have been too tight for the vehicle such that it undershoots the waypoints at the crest by 70 cm while it overshoots the trough a little by 15 cm.

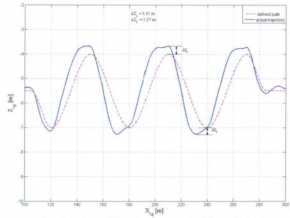

Fig. 4.77 Trajectory of the AUV in response to test #5 [Z_0 1.5, L_C 60] at 1.5 m/s

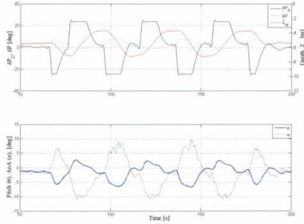

Fig. 4.78 Effective control plane deflections, pitch and angle-of-attack from test #5 [Z_0 1.5, L_C 60] at 1.5 m/s

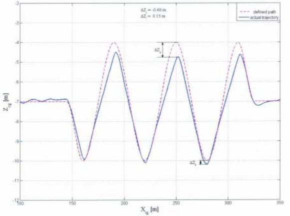

Fig. 4.79 Trajectory of the AUV in response to test #6 [Z_0 3.0, L_C 60] at 1.5 m/s

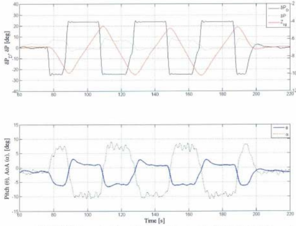

Fig. 4.80 Effective control plane deflections, pitch and angle-of-attack from test #6 [Z_0 3.0, L_C 60] at 1.5 m/s

TABLE 4.10

Parameters Estimated from Vertical Zigzag Manoeuvres

Test Numbers	1	2	3	4	5	6
Designed paths ⟶	**$Z_0$1.5, L_c140**	**$Z_0$1.5, L_c140**	**$Z_0$3, L_c140**	**$Z_0$3, L_c140**	**$Z_0$1.5, L_c60**	**$Z_0$3, L_c60**
Command speeds ⟶	U = 1.5	U = 2.0	U = 1.5	U = 2.0	U = 1.5	U = 1.5
CLIMB						
Change in Depth, ΔZ [m]	-3.20	-3.09	-6.14	-6.17	-3.05	-5.33
Adavance, ΔX [m]	23.98	17.70	40.89	31.06	18.58	30.17
Time to change depth, Δt [s]	16.0	9.0	27.3	15.7	12.0	20.0
Rate of ascent, $\Delta Z/\Delta t$ [m/s]	-0.20	-0.34	-0.23	-0.39	-0.25	-0.27
Slope of ascent, $\Delta Z/\Delta X$ [m/m]	-0.13	-0.17	-0.15	-0.20	-0.16	-0.18
Glide Path Angle (GPA) = $\tan^{-1}(\Delta Z/\Delta X)$	**7.6**	**9.9**	**8.5**	**11.2**	**9.3**	**10.0**
Dive Plane deflection, δP_D [deg]	23.7	24.1	23.7	24.0	23.7	23.7
Eff. Tail Plane deflection, δP [deg]	-1.2	-3.7	-0.9	-2.7	-1.3	-1.0
Pitch, θ [deg]	1.5	4.2	0.8	3.6	1.6	1.0
Angle-of-Attack, α [deg]	-9.8	-9.3	-9.1	-8.8	-9.9	-9.6
Glide Path Angle (GPA) = $\lvert \theta + \alpha \rvert$	**11.3**	**13.5**	**9.9**	**12.5**	**11.5**	**10.6**
CREST						
Level flight segment [m]	46.1	39.48	28.61	28.65	15.03	0.00
Mean depth at the crest, Z_c [m]	3.72	3.67	3.71	3.66	3.73	4.00
Overshoot from mean depth [m]	NIL	0.31	NIL	0.20	NIL	-0.69
Dive Plane deflection, δP_D [deg]	-0.2	-3.1	0.8	-2.1	2.5	0.0
Eff. Tail Plane deflection, δP [deg]	3.3	1.8	3.2	2.1	3.4	0.0
Pitch, θ [deg]	-1.5	0.0	-1.4	0.0	-1.7	0.0
Angle-of-Attack, α [deg]	-1.2	0.0	-1.5	-0.1	-2.2	0.0
DIVE						
Change in Depth, ΔZ [m]	3.28	3.25	6.31	6.22	2.92	5.40
Adavance, ΔX [m]	17.6	18.55	32.73	31.56	13.15	26.09
Time to change depth, Δt [s]	12.0	9.5	22.0	16.0	9.0	17.5
Rate of descent, $\Delta Z/\Delta t$ [m/s]	0.27	0.34	0.29	0.39	0.32	0.31
Slope of descent, $\Delta Z/\Delta X$ [m/m]	0.19	0.18	0.19	0.20	0.22	0.21
Glide Path Angle (GPA) = $\tan^{-1}(\Delta Z/\Delta X)$	**10.6**	**9.9**	**10.9**	**11.1**	**12.5**	**11.7**
Dive Plane deflection, δP_D [deg]	-24.3	-24.5	-24.3	-24.6	-24.1	-24.5
Eff. Tail Plane deflection, δP [deg]	7.1	6.1	6.5	5.4	7.2	7.0
Pitch, θ [deg]	-5.9	-4.5	-6.2	-4.8	-5.9	-6.1
Angle-of-Attack, α [deg]	6.3	7.3	6.7	7.5	6.9	7.3
Glide Path Angle (GPA) = $\lvert \theta + \alpha \rvert$	**12.2**	**11.9**	**12.9**	**12.3**	**12.7**	**13.4**
TROUGH						
Mean depth at the trough, Z_t [m]	6.96	6.95	10.03	9.97	7.00	10.00
Max. Overshoot depth, Z_{max} [m]	7.22	7.18	10.17	10.22	7.28	10.15
Overshoot from the mean depth [m]	0.26	0.23	0.14	0.26	0.28	0.15
Dive Plane deflection, δP_D [deg]	0.8	-1.9	1.7	-1.5	2.7	0.0
Eff. Tail Plane deflection, δP [deg]	3.2	1.7	3.1	2.0	2.3	0.0
Pitch, θ [deg]	-1.5	-0.1	-1.2	-0.2	-0.8	0.0
Angle-of-Attack, α [deg]	-1.6	-0.2	-1.9	-0.2	-1.4	0.0

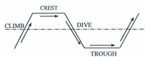

Note: The numbers shown in the Table are mean values of the variables averaged over the number of cycles each test had.
For eg., if Test #1 had 3 climbs, then the rate of ascent is equal to the average of these 3 values.

The above discussion on the slope of ascent or descent, or in other words the glide path angle, can be summarized into a tabular form showing the comparison between the designed slope and the actual glide path slope resulting from all the vertical zigzag manoeuvres. These values, which are already presented in Table 4.10, are condensed to an easy-to-read form in Table 4.11.

TABLE 4.11

Defined slope vs. Actual slope of the Glide Path

Test #	Forward Speed [m/s]	Defined slope		Actual slope	
		Climb	Dive	Climb	Dive
1	1.5	1 in 20	1 in 20	1 in 7.7	1 in 5.3
2	2.0	1 in 20	1 in 20	1 in 5.9	1 in 5.6
3	1.5	1 in 10	1 in 10	1 in 6.7	1 in 5.3
4	2.0	1 in 10	1 in 10	1 in 5.0	1 in 5.0
5	1.5	1 in 10	1 in 10	1 in 6.3	1 in 4.5
6	1.5	1 in 5	1 in 5	1 in 5.6	1 in 4.8

From Table 4.11, test (3) and test (5) have the same design conditions of glide path slope and forward speed. The only difference between them being their cycle lengths; 140 m for test (3) and 60 m for test (5). However, their glide path slopes resulting from the experiments, show some disagreement between each other, particularly during descend. It is unknown whether this disagreement resulted from the tightness of test (5), although both had the same design slope and speed. Further, the values in Table 4.11 can be used as a guideline for designing similar experiments in future. Within the bounds of existing features of the *MUN Explorer* AUV, a reasonably good depth-changing manoeuvre that resembles closely a conventional vertical zigzag manoeuvre can be designed, as proven from these experiments. It can be inferred from Table 4.11 that a path, if defined with a slope of 1 in 5 or closer, can result in a decent vertical zigzag manoeuvre, at least for the case when the vehicle is operated in the *Depth-by-Heave* mode.

Description of terminologies used in Table 4.10

Some important parameters estimated from the vertical zigzag manoeuvres such as the overshoots, effective control plane deflections, pitch angles, angle of attack, rate of ascent and descent etc., corresponding to different phases of the manoeuvres are shown in Table 4.10. The terminologies and notations used in Table 4.10 are described in brief below:

Climb and Dive Phase

i) *Change in depth, ΔZ*: is the vertical distance through which the centre of gravity (C.G) of the vehicle has dropped during a climb or dive phase.

ii) *Advance*, *ΔX*: is the horizontal distance in *x*-direction through which the C.G of the vehicle has traversed as it changed its depth by ΔZ.

iii) *Time to change depth, Δt*: is the time taken by the vehicle to travel through a vertical distance of ΔZ.

iv) *Rate of ascent / descent*: is defined as the rate at which the vehicle changes its depth and is estimated as $\Delta Z/\Delta t$. The vertical displacement ΔZ and the time taken for that displacement Δt are estimated from the steady phase of dive and climb.

v) *Slope of ascent / descent*: is defined as the inclination of the vehicle trajectory or glide path to the horizontal, provided the vehicle is in a steady ascent or descent. In other words, it is the ratio of the change in depth to the change in distance (advance) $\Delta Z/\Delta X$. This slope when expressed as an angle is called the *Glide Path Angle* (GPA). GPA also works out to be the sum of the angle of attack (α) and pitch angle (θ) as depicted in Figure 4.76. The estimates of GPA by these two methods are presented in the

Table. The slope of ascent/descent also gives an idea about how far ahead should the vehicle start its dive or climb so as to reach a specified depth while travelling at a constant speed.

vi) *Effective Plane deflections* δP_D *and* δP: are defined as the effective single control plane deflection representing the combined effect of the dive planes and tail planes respectively, averaged over a period of time during which the vehicle undergoes a steady ascent or descent.

vii) *Pitch* (θ) *and angle of attack* (α): are the attitudes of the vehicle averaged over a period of time during which the vehicle undergoes a steady ascent or descent.

Crest and Trough Phase

viii) *Level flight segment*: is the distance travelled by the vehicle at the crest or trough in a nearly horizontal line between a dive and a climb. This happened as a result of large cycle lengths and was significant in the first four tests.

ix) *Mean depth at the crest,* Z_c *or trough,* Z_t: is the depth at the crest or trough averaged over a period of time for which the vehicle travels in a level flight.

x) *Maximum overshoot depth,* Z_{max}: is the maximum depth to which the vehicle overshoots at the crest or trough before it stabilizes to the mean depth, Z_c or Z_t.

xi) *Overshoot*: is estimated as the distance from the mean depth at crest or trough to the maximum overshoot depth. In other words, it is the difference between Z_{max} and Z_c (or Z_t).

In all the above cases, there is a slight overshoot at the trough while at the crest the overshoot occurs only for higher speeds. The change in depth is produced in a short period of time during which the dive planes in particular are deflected to their maximum values. At regions of depth change where the control planes have maximum deflection, the effective dive plane deflection δP_D and the effective tail plane deflection δP have opposite sense.

From tests (1) and (2), at speeds of 1.5 and 2.0 m/s, the maximum dive plane deflections δP_D for the climb are almost the same (~ 24°) while the tail plane deflections δP have relatively much smaller value but in opposite sense. At 2.0 m/s speed (test #2), δP seems to have a marginally higher deflection angle (~ -3.7°) than that at 1.5 m/s (~ -1.2°). The negative sign implies that the combined effort of the tail planes were to produce a negative pitch attitude or hold the nose down. In other words, when the dive planes were responsible for producing all the lift necessary for the climb, the tail planes tend to hold the vehicle at a near zero pitch attitude. At higher speed (2.0 m/s) the dive planes, having the same deflection, generate more lift, which consequently tend to produce a large nose-up attitude. To counter this, the combined effect of tail planes have a larger negative value than that at 1.5 m/s and hence the observed increase in effective tail plane deflection δP.

At the crest and trough of the trajectory, corresponding to the region of level-flight, a certain amount of tail plane deflections are always present. Hence these deflections are responsible for whatever attitude the vehicle achieved during that period of level flight. From Table 4.10, the pitch attitude and angle-of-attack of the vehicle are almost equal during the level-flight at the crest and trough. This is about -1.5° at 1.5 m/s speed and is almost level (0°) at 2.0 m/s speed. The corresponding dive plane deflections δP_D are 0° and –3° respectively at 1.5 and 2.0 m/s speeds while the tail plane deflections δP are 3.3° and 1.8° respectively. In other words, it is the positive deflections of the tail planes that hold the vehicle at a pitch attitude of –1.5° at 1.5 m/s speed while it is the effort of both tail and dive planes that holds the vehicle at a perfectly level attitude at 2.0 m/s speed.

4.5.3 Rate of Ascent and Descent

The rate of ascent and descent of the vehicle at both speeds during the depth-changing manoeuvres is examined here. This is critical in understanding how far ahead should a vehicle start its dive or climb in order to reach a specified waypoint at a certain depth while moving ahead at a particular speed.

At speeds of 1.5 m/s, it was found that the rate of descent was greater than the rate of ascent. Since the AUV is generally designed to be slightly positively buoyant, one would normally expect the buoyant force to act in favour of the climbing motion of the vehicle and hence a higher rate of ascent. However, the opposite was observed from missions at speeds of 1.5 m/s. The answer to this discrepancy lies in the pitch attitude (θ) of the vehicle during ascent and descent. During a dive, the vehicle maintained a larger pitch angle than that during a climb. The maximum pitch angle during dive was found to be around – 6° while that during a climb was approximately 1.5°. As a result, during a climb, naturally the vehicle experiences an increased drag owing to its nearly level attitude compared to its attitude of –6° during a dive. This explains the reason for the slower rate of climb than dive. This may also explain why an overshoot was observed only at the trough for all speeds while it was observed at the crest only for the higher speed cases.

At speeds of 2.0 m/s, the rate of ascent was equal to the rate of descent. This is because the pitch attitude of the vehicle during both ascent and descent more ore less were of same attitude.

4.5.4 Vehicle Speed and Propeller RPM

The vehicle speed and propeller RPM corresponding to each of the depth changing manoeuvres are shown in figures 4.81 through 4.83. The first pane in each figure shows the depth profile or trajectory of the vehicle while in the second pane the forward speed and corresponding propeller rpm are plotted.

It is seen from the figures 4.81 and 4.82 that throughout an entire manoeuvre, the vehicle maintained roughly a constant forward speed; equivalent to the command speed. However, in every case, the propeller rpm had variations at regions of dives and climbs. This indicates that the propeller had to generate some additional thrust so as to maintain a constant command speed in those regions. Further, this increase in propeller rpm was predominant at the beginning of dives rather than at the beginning of climbs. An underwater vehicle manoeuvring in a vertical plane has to overcome the buoyant force in order to push itself down and hence needs some extra thrust. This generation of extra thrust resulted in the observed increase in propeller rpm during a dive.

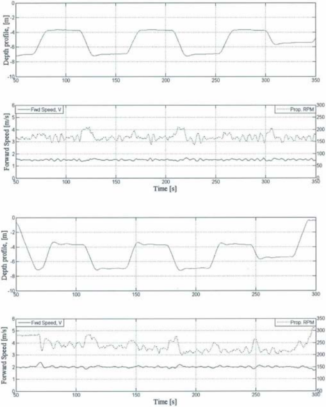

Fig. 4.81 Vehicle speed and corresponding propeller rpm for the vertical zigzag path Z_0 1.5, L_C140) at two different speeds

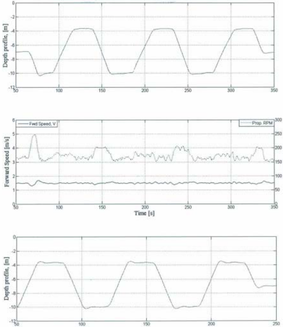

Fig. 4.82 Vehicle speed and corresponding propeller rpm for the vertical zigzag path Z_0 3.0, L_C 140 at two different speeds

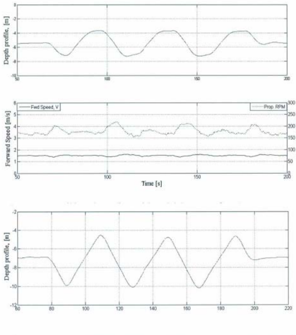

Fig. 4.83 Vehicle speed and corresponding propeller rpm for the vertical zigzag paths Z_0 1.5, L_C 60 and Z_0 3.0, L_C 60 at speed 1.5 m/s

Although the propeller generated an increased thrust at regions of descent, the increased thrust was not responsible for the higher rate of descent observed, discussed in earlier section. This is because the vehicle maintained a constant speed throughout regardless of the propeller rpm. Hence, the only factor, which contributed to the observed increase in rate of descent, was the pitch attitude of the vehicle during the dive.

4.5.5 Phase-Plane Plots of Rate of ascent/descent and Angle of Attack with Control Plane Deflection

The following subsection shows the variation of some of the parameters such as the rate of ascent or descent ($\dot{Z}$), angle-of-attack (α), heave velocity (w) etc., with control plane deflection (δP_D).

(i) *Rate of ascent and descent versus control plane deflection*

The deflection of the control planes is what facilitates the ascent or descent of the vehicle. The rate at which this ascent and descent occurs is dependent on the forward speed of the vehicle. The following figures show the rate of ascent and descent produced by dive plane deflections corresponding to different speeds. Only dive plane deflections are taken into consideration as they are the ones, which predominantly influence the depth change.

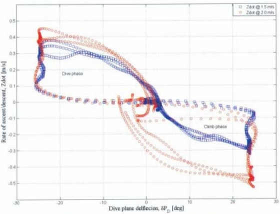

Fig. 4.84 Phase-plane plot of $\dot{Z}$ from the response of the vehicle to the trajectory Z_0 1.5, L_C 140 m at two different speeds.

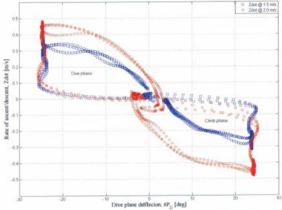

Fig. 4.85 Phase-plane plot of $\dot{Z}$ from the response of the vehicle to the trajectory: Z_0 3.0, L_C 140 m, at two different speeds.

Figures 4.84 and 4.85 show the phase-plane plots of the rate of change of depth ($\dot{Z}$) of the vehicle with respect to dive plane deflection δP_D, at different speeds and trajectories. Each figure shows the responses from the vehicle to two different speeds: 1.5 and 2.0 m/s, while following the same trajectory. Figure 4.84 shows the vehicle's response when following the trajectory with amplitude 1.5 m at 1.5 and 2.0 m/s and Figure 4.85 shows the same when following the trajectory with amplitude 3.0 m. Hence, any difference observed between the two curves in each figure is expected to be caused by the change in speed.

From figures 4.84 and 4.85, the response of the vehicle looks very similar regardless of the trajectory. This makes sense, as the factors that affect $\dot{Z}$ the most are the forward speed V and the dive plane deflection, δP_D. The amplitude or consequently the slope of the path does not have much influence in these cases.

At speeds of 1.5 m/s, it is observed that the loops corresponding to dives are larger than the loops corresponding to climbs while at 2.0 m/s these two loops have roughly the same size. It was shown earlier, in Table 4.10, that the rate of ascent and descent was the same when the vehicle followed the trajectories at 2 m/s speed. This explains the observed similarity in size between the loops at 2 m/s speed. On the other hand, at 1.5 m/s speeds, the rate of descent was found to be greater than the rate of ascent. Consequently, in the figures the loops corresponding to dives are larger. The reason for this discrepancy was primarily attributed to the pitch attitude of the vehicle during the dive (-6.2°) compared to the pitch attitude during climb (0.8°) whereby the vehicle maintained a nearly level attitude, making it difficult to climb. In all the above cases, the loops converge at the origin and clusters of data points can be seen at the origin and at regions of maximum dive plane deflections. To illustrate this point, consider the figures 4.86a and 4.86b.

Figure 4.86a and 4.86b are simply a replication of the Figure 4.85 in which one complete cycle, containing a dive and a climb phase, pertaining to 1.5 m/s speed (test #3) and another pertaining to 2.0 m/s (test #4) respectively, are extracted and plotted with time-markers on it to show the dive plane deflections and corresponding $\dot{Z}$ at different instances of time.

Figure 4.86 shows the sequence in which the operation of dive planes and the corresponding depth-changes happen at each speed. Figure 4.86a corresponds to a portion of the time series from test #3 (Z_0 3, L_C 140 & U 1.5 m/s) consisting of one complete cycle. This cycle can be identified as the region between the time-series 184 s and 257 s in the first subplot of Figure 4.74b. Figure 4.86b, on the other hand, shows one complete cycle from test #4 (Z_0 3, L_C 140 & U 2.0 m/s) and can be identified as the region between time-series 110 s and 180 s in the first subplot of Figure 4.75b.

In the figures 4.86a and 4.86b, the sequence of operations starts with the deflection of dive planes to their maximum angles. This happens at a rapid rate taking only about 1.5 seconds in all cases and is denoted by the sparsely spaced data points on the plot along the horizontal axis. This deflection initiates a depth change, the rate of which shoots up to its maximum value in a few seconds. The vehicle maintains this maximum deflection and maximum rate of ascent/descent for a certain period of time, represented by the cluster of data points at the corners, after which the dive planes

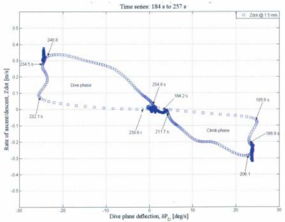

Fig. 4.86a One complete cycle from vertical zigzag Z_θ 3, L_C 140 at 1.5 m/s with time-markers

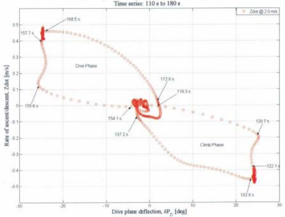

Fig. 4.86b One complete cycle from vertical zigzag Z_θ 3, L_C 140 at 2.0 m/s with time-markers

retract to zero deflection or neutral position. In both figures, there are three regions where there is a clustering of data points: one at the origin where the loops converge and the other two on the diagonally opposite corners of the loops. The cluster at the origin indicates the time when the plane deflections are zero and consequently the vehicle neither dives nor climbs but would 'fly' level. This corresponds to the region of the trajectory at the crest or trough where the level-flight segments are present. The clusters at the diagonally opposite corners of the plot correspond to regions of steady dive and climb when the dive planes are deflected to their maximum angle and held in place such that the vehicle continues to dive or climb at a constant rate.

From all the above cases, as the dive planes were deflected to their maximum allowable angles, the factor which affected the rate of ascent or descent, was mostly the forward speed of the vehicle. The higher the speed the larger the rate of ascent or descent. The effect of the slope of path or the tightness of path was not seen as an influencing factor in all the above cases. In order to investigate the effect of tightness of path on the rate of ascent or descent, the responses from tests (5) and (6) which had a shorter cycle length are considered.

Figure 4.87 shows the rate of change of depth of the vehicle while following two defined paths having the same cycle length (60 m) but different amplitudes (1.5 m & 3.0 m), at a forward speed of 1.5 m/s. The response of the vehicle to the path having an amplitude of 1.5 m (test #5) is very similar in pattern to that of the previous four tests where there are two diagonally opposite loops converging at the origin; the loop corresponding to the dive phase being larger than the loop corresponding to the climb phase. However, the density of the cluster of data points at the origin, representing the

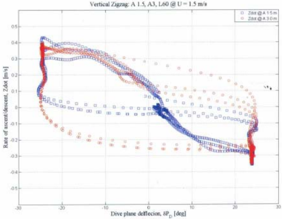

Fig. 4.87 Rate of ascent/descent from test (5) and (6) with respect to dive plane deflection
Vertical Zigzag: Z_0 1.5, L_C 60 and Z_0 3.0, L_C 60 @ U = 1.5 m/s

region of level-flight segments at the crest or trough of the trajectory, was far less. This is because the length of the level-flight segment, in test (5), was considerably shorter than that for the previous four cases. On the other hand, the response of the vehicle to the path having an amplitude of 3.0 m (test #6) is different from all the previous five tests. It consists of a single large loop with two clusters of data on the diagonally opposite corners of the loop. The cluster of data at the origin is completely absent in this case indicating the absence of unwanted level-flight segments. In other words, the manoeuvre was very close to a conventional vertical zigzag manoeuvre where the dive planes deflected from their maximum positive value to the maximum negative value (without stopping at zero deflection) immediately after the vehicle reached a certain defined depth. The clusters of data present at the corners indicate that the inclined path defined was long such that the vehicle remained in a state of steady-dive or climb for a certain period of time. This implies that a conventional zigzag can be designed by making certain adjustments or modifications to the size or slope of the inclined path. Consequently, the parameters of interest during a depth-changing manoeuvre such as overshoot depth, pitch angle, time to correct the attitude etc can be studied.

Pitch angle (θ) versus dive plane deflection (δP_D)

The pitch angle (θ) is the angle which the longitudinal axis of the vehicle makes with the horizontal. The phase-plane plots showing the variation of this parameter, θ, with dive plane deflection, δP_D, at two different speeds are presented in figures 4.88, 4.89 and 4.90. Figure 4.88 shows the results from test (1) and (2) when the vehicle follows the trajectory with amplitude of 1.5 m, at two different speeds. Similarly, Figure 4.88 shows the results from test (3) and (4), when the vehicle follows the trajectory with amplitude of 3.0 m, at two different speeds.

The phase-plane plots of pitch angle also shows that, at speeds of 1.5 m/s, the loops corresponding to climbs are smaller than the loops corresponding to dives. The maximum pitch angle during climb was 1.5° while during dive the maximum pitch angle was -6.0°. The nearly level attitude (1.5°) of the vehicle during climb induces a large angle-of-attack (α) on the vehicle which in turn increases the drag experienced by the vehicle. Consequently, the increased drag inhibits the rate of ascent during a climb. Further, the central clustering of data denoting the neutral position of the dive planes during level-flight, from where the planes are deflected to their maximum

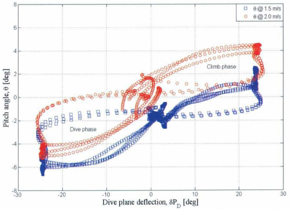

Fig. 4.88 Phase-plane plot of pitch angle (θ) and dive plane deflection (δP_D) for the defined path Z_0 1.5, L_C 140 at speeds of 1.5 and 2.0 m/s

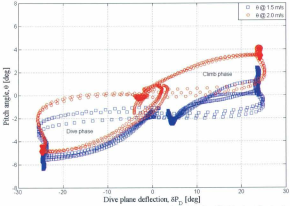

Fig. 4.89 Phase-plane plot of pitch angle (θ) and dive plane deflection (δP_D) for the defined path Z_0 3.0, L_C 140 at speeds of 1.5 and 2.0 m/s

positive and negative values is shifted off the x-axis. It was discovered earlier that the vehicle had a pitch attitude of about -1.5° even during the level-flight segment and this inherent nose-down attitude is what makes the plot to be shifted below the x-axis.

At speeds of 2.0 m/s, it was found that the rate of ascent was equal to the rate of descent (see Table 4.10). This explains the reason for the similarity in size of the loops for dive and climb phases in the above figures. One of the key factors influencing the rate of ascent/descent was recognized as the pitch angle of the vehicle during dive and climb. In this case, the maximum pitch angle attained during the dive is almost equal to that attained during the climb (~ 4°). Moreover, at speeds of 2.0 m/s, sufficient lift is generated so as to hold the vehicle at a level attitude. As a result, there is no apparent asymmetry with the plot about the x-axis.

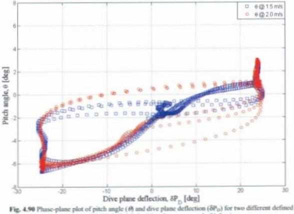

Fig. 4.90 Phase-plane plot of pitch angle (θ) and dive plane deflection (δP_D) for two different defined paths of $Z_0$1.5 & $Z_0$3.0, L_C60 at the same speed of 1.5 m/s

When the cycle length of the defined path was reduced to 60 m, as in the case with test (5) and (6), the resulting phase-plane plots had some difference in its pattern as shown in Figure 4.90. The result from test (5) had two loops with the loop corresponding to climb being smaller than that for the dive.

The result from test (6) had only a single large loop where the dive plane deflections oscillated between the maximum positive and maximum negative deflection angles without stopping at zero deflection or the neutral position. As depicted in Figure 4.76, a positive value of θ indicates that the vehicle is in a state of ascent and a negative value of θ indicates the opposite. Since both runs were performed at 1.5 m/s speed, the maximum pitch angle attained by the vehicle was same in both cases except that in the latter case, when following a tight defined path, the planes oscillated directly between their maximum positive and negative values without having to stop at the neutral position. Figure 4.90 shows that the vehicle has a larger pitch angle during descent (-6°) than during ascent (1.5°). Consequently, the flow approaches the vehicle at a low angle-of-attack during the dive and the drag force generated is less. This enabled the vehicle to dive faster than it climbed, as explained earlier. The asymmetry in the pitch angle during dive and climb is reflected in the figure where the loop as a whole is shifted off the x-axis to the negative pitch angle region.

Angle of attack (α) versus heave velocity (w)

The angle of attack, α is clearly a function of the heave velocity w as it is derived from the relation: $\alpha = \tan^{-1} (w/u)$ and if a general relationship between the two be established, the value of one can be roughly arrived at knowing the other. Figure 4.91

shows the relationship between the angle of attack, α, and heave velocity, w, where the heave velocity is nondimensionalized using the forward speed V ($w' = w/V$). Thus the results from all the six vertical zigzags can be condensed into a single plot showing the relationship between the two variables. From Figure 4.91, it is clear that there exists a linear relationship between α and w', at least for the range within which the tests were performed and the conditions that prevailed, i.e., constant speed at *Depth-by-Heave* mode. A linear fit to the plot generated from the above six tests is provided by the equation:

$$\alpha = 57.5w' \tag{4.20}$$

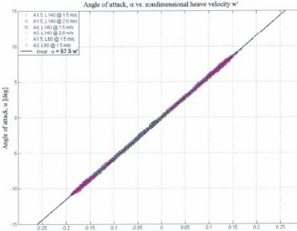

Fig. 4.91 Relationship between angle of attack α and nondimensional heave velocity w' from all the vertical zigzag tests

The forward speed, V, combined with the dive plane deflection, δP_D, is what generated the heave motions in *MUN Explorer* AUV for all tests discussed above. Therefore, if one knows what heave velocity can be expected from a particular combination of forward speed and dive plane deflection, the resulting angle of attack can be estimated from the above equation (4.20). This can be compared against results from simulations in vertical plane for the purpose of validation. Further, rough estimates of drag and lift on the vehicle can also be estimated from the knowledge of angle of attack of the vehicle.

4.5.6 Summary of Vertical Zigzags

The following are some of the key observations inferred from the vertical zigzag manoeuvres using *MUN Explorer* AUV. The vertical zigzag manoeuvres were designed and executed within a band of depth ranging from 4 m to 10 m thus allowing the vehicle a maximum depth excursion of 6 m.

a. From the vertical zigzags, it was observed that the vehicle produced small overshoots that were often less than half the diameter of the vehicle. This was because the vehicle utilized the dive planes for much of the depth-changing manoeuvres as the controller was set to act in the *Depth-by-Heave* mode. This indicates that while operating an AUV in regions of shallow water and at times when it is manoeuvring closer to the seabed, this mode would be the most preferable mode.

b. Even though the task verbs *target* and *line_follow* are used to plan vertical zigzag missions, it is not these commands which determine the path of the vehicle in a vertical plane. In other words, the vehicle controller decouples vertical control from horizontal control which results in the depth controller (z) working independently of the geographic control (x, y). This is the reason why the vehicle achieved the commanded depth much before it reached the waypoint at that level in the initial five tests.

c. The rate of dive was faster than the rate of climb although the opposite would have been expected, since net positive buoyancy should work in favour of the ascending motion of the vehicle. This was explained from the pitch attitudes of the vehicle during the climb and dive. During climb the vehicle had a near zero pitch attitude compared to its pitch attitude during dive. The angle of attack also helps explain this. During the dive, the flow approaches the vehicle at a smaller angle of attack than during the climb. Consequently, the drag experienced by the vehicle is less during a dive than when the vehicle climbs and hence the faster dive rate.

d. At speeds of 1.5 m/s, and when the vehicle is operated in the *Depth-by-Heave* mode, the vehicle can climb roughly at a rate of 0.25 m/s and dive at a rate of 0.3 m/s while at speeds of 2.0 m/s, the vehicle dives and climbs roughly at the same rate of 0.4 m/s. Since dive planes were deflected to their maximum allowable angles in all cases, the only factor controlled the rate is the forward speed V of the vehicle.

e. At speeds of 1.5 m/s, the vehicle attains a pitch angle of 1.5° during the climb and about –6° during the dive, where as at speeds of 2.0 m/s, the pitch angle during dive and climb is almost the same about 4°. This is true only for the case when the vehicle is operated in the *Depth-by-Heave* mode.

f. Further, the information obtained from these trials can be used as a guideline for designing experiments of similar nature in future should a need arise in vehicle dynamics study – perhaps when there is a change in vehicle configuration or when other appendages are added.

4.6 Helix Manoeuvring Data Analysis

The manoeuvres described in the previous sections were all planar manoeuvres; that is, all of the manoeuvres discussed earlier happened in a 2-D plane; either vertical or horizontal. Those types of manoeuvres need not necessarily excite all six degrees-of-freedom (DOF) of motion: surge, sway, heave, roll, pitch and yaw. Therefore, it was necessary to perform a test that would excite all six degrees-of-freedom of motion. Hence, a special mission in 3-D space had to be designed so as to achieve this goal. A turn in the horizontal plane, such as a turning circle, would excite surge, sway and yaw motions in particular and roll motion to a certain degree, depending on the tightness of turn. A depth-changing manoeuvre, on the other hand, would excite heave and pitch motions of the vehicle. Combining the above two conditions in a single mission would possibly result in a 3D manoeuvre that would excite all 6 DOF. In essence, it was intended that a mission be designed such that the vehicle should dive at a constant rate as it turned around in circles. The resulting trajectory would then have the shape of a helix. Experiments of such 3D manoeuvres are few in literature and validations of vehicle model against such 3D manoeuvres are rare. Therefore, a helix manoeuvre was expected to provide some experimental data for testing the validity of a vehicle dynamics model when it is subjected to 6 DOF motions.

The helix manoeuvre is not a conventional or standard manoeuvre. A helix, in mathematical terms, is described as a three dimensional curve, turning about an axis on the surface of a cylinder (or cone) while rising at a constant upward angle from the base. A different but simple way of describing it would be a circle whose start and end points do not meet on the same plane; thus the start and end points have different *z*-

values. This description of helix seemed well within the capability of the mission planner and the vehicle controller in the design and execution of the helix manoeuvre.

The helix manoeuvre was designed as a series of circles to be performed at intervals of 1.5 m depths, which had their centres along a common vertical axis. The design of a mission of this nature seemed possible just by using the geographical task verb *circle* available with the mission planner – "Fleet Manager". This is because each *circle* command takes an input that dictates at what depth the circle should be executed. The mission was performed at a forward speed of 1.5 m/s and the commanded radius of turn was 15 m. By planning the mission in such a way, it was expected that the vehicle would go in circles of 15 m radius, while diving simultaneously, so that it reached exactly 1.5 m below the starting point at the end of one complete revolution. The desired or expected trajectory of the helix manoeuvre is shown in Figure 4.92.

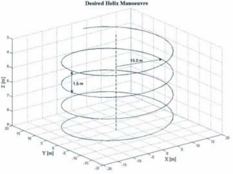

Fig. 4.92 Desired or expected trajectory of the helix manoeuvre

4.6.1 Vehicle Response to Helix Manoeuvre

The helix manoeuvre designed was performed between a depth range of 3 m and 9 m. The mission started at 3 m depth from where the vehicle was expected to spiral down to a maximum depth of 9 m and then spiral back up to 3 m depth, all the while going around in circles. The response of the vehicle to the planned mission is shown in Figure 4.93. It represents the complete mission and is colour coded to demarcate the downward and upward spiral: *blue* indicating the downward spiral and *red* indicating the upward spiral with the changeover taking place at point B. For the purpose of analysis as well as clarity, these two phases of the helix manoeuvre was split into two; the downward spiral as shown in Figure 4.94a and the upward spiral as shown in Figure 4.94b.

It is apparent from the figures that the response of the vehicle to the planned mission did not result in a helix manoeuvre as intended. It was expected that the vehicle would dive continuously as it turned around in circles. Instead, the executed mission looks more like turns followed by dives (climbs) or vice-versa. The vehicle seemed to have performed almost a complete circle at each level before it dropped (or climbed) to the next level to start the next circle and so on. As a result, the combined dive (climb) and turn motion happened only for a short segment of the entire turn, as seen in Figure 4.95. If there exists a region where all six DOF motions can be expected, it is this short segment of dive-and-turn (climb-and-turn) phase. The rest of the turn resembles much like a turning circle or an arc of a circle.

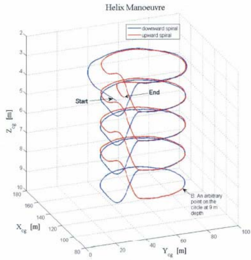

Fig. 4.93 Trajectory traced by the AUV in response to the helix mission

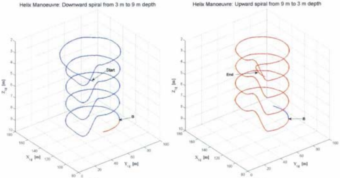

(a) **(b)**

Fig. 4.94 Downward spiral (a) and upward spiral (b) of the helix manoeuvre

From Figure 4.94, it is evident that the vehicle performed turns between depths 3 m and 9 m, in each phase, at intervals of 1.5 m. The last turn at 9 m depth is common to both phases and hence the entire mission consisted of a total of nine turns. This clearly indicates that the depth interval between circles was short for the designed mission. This is one key reason for not achieving the expected helix trajectory. Moreover, the radius of turn at each level was estimated to be around 26.0 m, which was much larger than the commanded radius of 15.0 m. This scenario was seen in the case of turning circles discussed in *Section 4.3* as well, where the actual radius of turn was larger than the commanded radius in all tests. However, the helix manoeuvre when projected to the *XY*-plane or as viewed from top resembles a perfect turning circle manoeuvre, as seen in Figure 4.95. This indicates that the circles at different levels had their centres along the same vertical axis as intended and the vehicle maintained a constant radius at each level although the radius of turn was larger than desired. The perfect overlap between circles at different level shows the vehicle's robust navigational ability. The total time taken by the vehicle to finish one complete revolution was estimated to be around 108 seconds. Figure 4.95 also shows that the region of dive and climb between every level, where six DOF motions are likely to be present, accounts to only a fraction ($1/7^{th}$) of this total time of about 15 to 16 seconds. In essence, the larger than desired radius of turn combined with the close intervals between circles made the dive-and-turn segment look even shorter and posed the major hindrance to performing a successful helix mission. Nevertheless, the dive-and-turn segment of this manoeuvre is of use for the purpose of studying the vehicle dynamics during motions in 3D space.

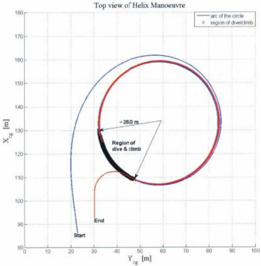

Fig. 4.95 The trajectory of the vehicle in response to helix mission as projected on *XY*-plane

The observations from the above manoeuvre indicate that with some modifications made to the mission, the same approach or procedure can be adopted to achieve a helix manoeuvre. For instance, if the same manoeuvre was designed using just two circles, one at 3 m depth and the other at 9 m depth, the resulting trajectory would have had a larger dive-and-turn segment making the trajectory look more like a helix. Further, reducing the radius of turn would increase the tightness of turn and consequently would excite all six DOFs. Therefore, by reducing the radius of turn and increasing the depth interval between circles, a complete six DOF motion can be achieved, while making sure that the vehicle is deployed in considerably deeper water.

Vehicle Speed and Propeller RPM

The vehicle speed and the corresponding propeller RPM for the entire helix manoeuvre are shown in Figure 4.96. The first half of the time-series represents the downward spiral phase and the latter half corresponds to the upward spiral.

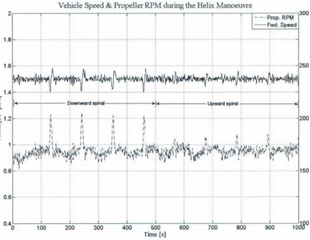

Fig. 4.96 Forward speed and propeller RPM for the entire helix manoeuvre

The vehicle maintained a relatively constant speed of 1.5 m/s throughout with the exception of occasional spikes. These spikes were found to correspond to the regions of dive and climb. The propeller RPM, on the other hand, oscillates slightly about an average value of 167 RPM. The propeller RPM also shows spikes at regions of dive and climb with the spikes corresponding to regions of dive peaking to a little over 200

RPM while that during a climb peaking to about 180 RPM. This scenario was the same as observed in the case of depth-changing manoeuvres discussed in *Section 4.5*, where the propeller had to generate some extra thrust in order to overcome the buoyant force and push the vehicle down, while maintaining roughly a constant forward speed throughout.

Translational and Angular Motions of the Vehicle

The translational components of the velocity u, v and w during the turn and dive motions during the helix manoeuvre are shown in Figure 4.97. The surge velocity u measured is almost equal to the command speed or resultant velocity of the vehicle (1.5 m/s) even during the turn except for the slight disturbance observed from the mean value at regions of dive or climb. No loss-of-speed that is normally expected during a turn was noticed and this is because the propeller RPM was adjusted to keep the speed constant as seen in Figure 4.96. The sway velocity v shows an oscillatory pattern about a mean value of around -0.15 m/s. The heave velocity w, has a mean value of -0.04 m/s throughout the manoeuvre except at regions of dive and climb where it shoots up by an amount of 0.2 m/s to either side of the mean value.

The angular displacements of the vehicle during the manoeuvre are shown in Figure 4.98. In the plot, the flat portion of the curve indicate the steady turning phase at each depth level while the spikes indicate the regions of dive-and-turn The pitch attitude of the vehicle was seen to be -1.5° throughout. This means that the vehicle maintained a slightly nose-down attitude throughout the entire manoeuvre except at regions of dive-and-turn where the pitch angle dropped from -1.5° down to -6° during a dive and it

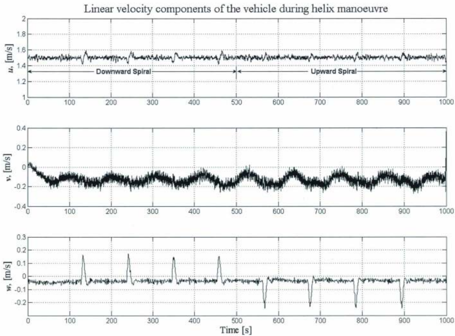

Fig. 4.97 Linear velocity components [u, v, w] of the vehicle during the helix manoeuvre

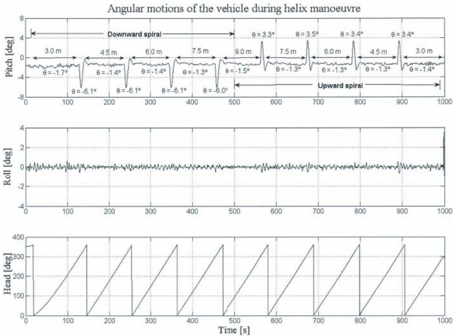

Fig. 4.98 Angular motions [θ, ϕ, ψ] of the vehicle during the helix manoeuvre

increased to 3.5° during a climb. It is this inherent nose-down attitude (θ = -1.5°) that caused the negative heave velocity (w = -0.04 m/s) observed in Figure 4.97. Figure 4.96 also shows that the roll motion of the vehicle was negligible during all those dives and turns.

The translational and angular motions of the vehicle observed here are consistent with the responses of the vehicle observed in similar scenarios earlier. For instance, from the turning circle manoeuvres, described in *Section 4.3*, it was observed that the vehicle neither rolled nor suffered a loss of speed while negotiating the turns; both being typical of a turning vehicle. In almost every case when the vehicle was operating at a forward speed of 1.5 m/s, there was an inherent nose-down attitude of -1.5° to -2.0° attained by the vehicle.

The roll, pitch and yaw rates (p, q, r) of the vehicle during the manoeuvre are shown in Figure 4.99. The roll rate p is negligible. The pitch rate q also is insignificant having a mean of zero except at regions of dive-and-turn where it shows some disturbance from the mean value. The yaw rate, r, has a wavy pattern as it oscillates between 2.5°/s and 4.0°/s while also having a slight disturbance noticeable at regions corresponding to the dive-and-turn segments. An average yaw rate of 3.3°/s was roughly estimated for one complete revolution.

Figures 4.97 and 4.98 in combination, shows the six different DOF that were expected to be excited by performing a helix manoeuvre. However, the response of the vehicle shows that only certain regions, which constituted only a fraction of the entire manoeuvre , excited all six DOF.

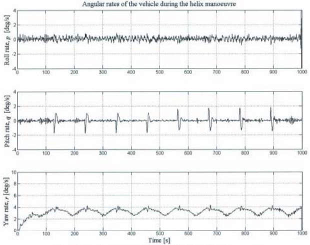

Fig. 4.99 Angular rates $[p, q, r]$ of the vehicle during the helix manoeuvre

4.6.2 Control Plane Deflections

The individual control plane deflections and their combined effects are described through the figures below. Figure 4.100 shows the time series of dive plane deflections, δ_1, δ_2 and their combined effect δP_D. It is evident from the figures that the dive planes are engaged only during the dive-and-turn phase and for the remainder of the mission, they are not used at all. At the dive-and-turn segment, the dive planes are engaged for about 10 seconds. The effective single control plane deflection representing the combined effect of both δ_1 and δ_2 is denoted by δP_D shown in the third pane. In the downward spiral phase, δP_D angles are negative initiating a dive while in the upward spiral phase δP_D values are all positive initiating a climb.

The individual tail plane deflections δ_3, δ_4, δ_5 and δ_6 and their combined effect in producing pitch (δP) and yaw (δY) motions are shown in Figure 4.101. The port upper (δ_3) and lower (δ_4) control plane deflections are shown in the first pane of Figure 4.101 while the starboard upper (δ_5) and lower (δ_6) control plane deflections are shown in the second pane. The effective single control plane deflections representing their combined effect in producing pitch (δP) and yaw (δY) are shown in the third pane.

The effective tail plane deflection in producing pitch, δP, has an average value of 3.2° that remained steady during much of the mission except at regions of dive-and-turn where a peak value of about 7.5° was observed in the downward spiral phase and a negative high of about -3.3° in the upward spiral phase. What makes δP change its peak values from 7.5° in the downward spiral to -3.3° in the upward spiral can be seen from Figure 4.101 as a result of the change in configuration of the four tail plane deflections. A positive value of δP indicates that such a configuration of tail planes tend to pitch the nose up. Therefore, a positive value of δP (7.5°) at regions of dive indicates that the tail planes were merely holding the vehicle from excessive nose-down attitude during the dives; because the dive planes were primarily responsible for the depth-change. During the turns when the dive plane deflection δP_D remained zero, the tail planes maintained an average δP value of 3.2° in an effort to hold the nose up. Despite this effort by the tail planes, the vehicle still had a nose-down attitude of approximately -1.5° during the turn, as seen in Figure 4.98.

The tail planes, in addition to providing a vertical force to pitch the nose up are also engaged in generating a horizontal force that would produce a yaw motion. The effective tail plane deflection in producing yaw, δY, shown in the third pane of Figure 4.101, is what makes the vehicle turn around in circles. Thus, the tail planes perform two functions at the same time. A positive value of δY indicates that it tends to turn the vehicle to the starboard side and a vehicle undergoing a steady turn is expected to hold the control planes at fixed angles. However, the effective single control plane deflection δY in producing yaw have a periodic change with its values oscillating between 4° and 7° showing distinct crest and trough. This indicates that the planes were not held at constant deflection angles but were fluttering. This is exactly what we observe with the time-series of individual control plane deflections shown in Figure 4.101. However, note that only the value of δY changes with time while the same configuration of the tail planes does not produce any appreciable change in δP, except at regions of dive and climb. So the planes must have oscillated in such a manner that δP remained constant. Consequently, this periodic change in δY may very well be the reason for the observed oscillations in sway velocity, v (see Figure 4.97) and yaw rate, r (see Figure 4.99). The smooth periodic nature of δY is disrupted only at instances of dive and climb where spikes are present in conjunction with the peak values of δP.

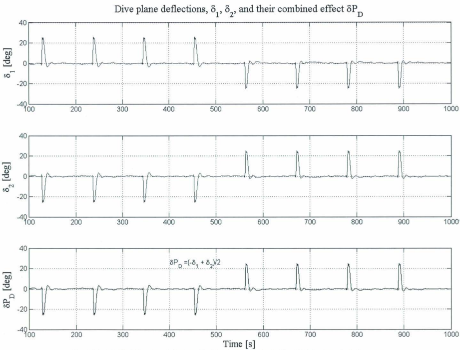

Fig. 4.100 Individual dive plane deflections (δ_1, δ_2) and their combined effect (δP_D) for the entire helix manoeuvre

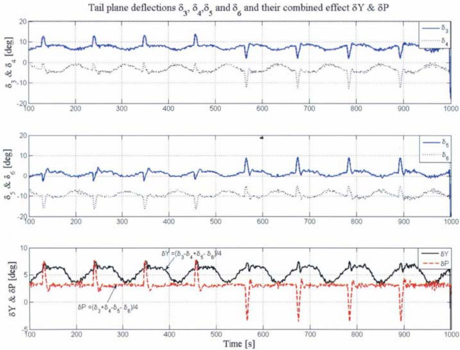

Fig. 4.101 Individual tail plane deflections (δ_3, δ_4, δ_5, δ_6) and their combined effect in producing yaw (δY) and pitch (δP)

The effective single deflection angles δY and δP, at any instant of time, are produced by the same tail planes configuration. Hence, it is plausible that a change in one would affect the other. A plot of δY against δP is shown in Figure 4.102 to see how a change in δY would affect δP or vice versa. In the plot, δY oscillates between 3.5^{o} and 7^{o} depicted by the horizontal portion. The fact that this portion is horizontal implies δP is constant for much of this range. In other words, there is hardly any change in δP induced by a change of δY from 3.5^{o} to 6.0^{o}. The portion of δY beyond 6.0^{o} corresponds to the region of dive or climb where a spike appears in δY in conjunction with the peak values of δP. A 3D plot of a portion of the time-series between 200 and 800 seconds, of δY and δP, is shown in Figure 4.103, which clearly shows the effective tail plane angles during the manoeuvre.

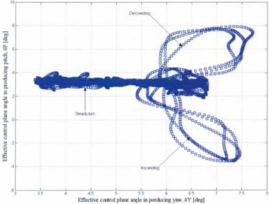

Fig. 4.102 Plot showing the variation of δP with δY for the helix manoeuvre

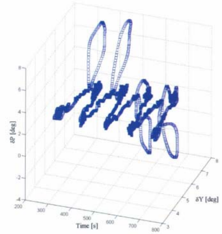

Fig. 4.103 3D plot showing a portion of the time-series of δP vs. δY

The vehicle, during both its downward and upward spiral, was turning to the starboard side. This is evident from Figure 4.94, 4.95 etc. In order to have a starboard turn, δY has to have a positive value. This condition is also met, from Figure 4.101, 4.102 and 4.103, that δY has a positive value throughout. In the *Section 4.3.1* for turning circles, Figure 4.28b (pg. 150) presented a chart showing the tail plane deflections for different radii of turns. It was established there that, at speeds of 1.5 m/s, the diagonally opposite pair of planes 3 and 6 were chiefly responsible for producing a starboard turn while the other pair of diagonally opposite planes 4 and 5 merely acted as roll stabilizers. This scenario is true here with the case of the helix manoeuvre as well (see Figure 4.101), where planes 3 and 6 have the maximum deflection during the entire manoeuvre and be chiefly responsible for producing the starboard turn. However, the pair of planes steering the vehicle during the dive and climb segment of the turns seem to be different. In the downward spiral phase, when the dive planes are engaged to descend the vehicle, planes 3 and 6 are deflected further to produce the turn as well as to produce a positive δP to pitch the nose up. Note that the dive plane deflection δP_D was chiefly responsible for dive and climb and the tail plane deflection δP helps to hold the nose up. However, in the upward spiral phase, when the dive planes are engaged in ascending the vehicle, planes 3 and 6 retract closer to neutral position in an attempt to hold down the nose from excessive pitch angle. During this time, it was the other pair of planes 4 and 5 that were chiefly engaged in steering the vehicle to continue in a starboard turn. The fact that the combination of planes 4 and 5 could produce a starboard turn of exactly the same radius as the combination of planes 3 and 6 indicates that different combination of plane angles can produce the same effect.

It is possible to explain this phenomenon with the help of the expression used to describe the factors δY and δP. If we consider the effect of planes 3 and 6 only while ignoring the effects of 4 and 5 ($\delta_4 = \delta_5 = 0$), the equations[1] for δP and δY will be reduced to the following expressions:

$$\delta P_{3,6} = \left(\frac{\delta_3 - \delta_6}{2}\right) = \delta Y_{3,6} \qquad (4.21)$$

where $\delta P_{3,6}$ and $\delta Y_{3,6}$ indicates the effective single control plane deflection considering planes 3 and 6 only. This relation implies that the pitching moment produced by the

[1] See Equations (4.1) & (4.2) on page 93

deflection of the diagonally opposite planes 3 and 6 is equal to the yawing moment produced by the same combination. Also, note that both are positive, which means, a combination that produces positive pitch moment (nose-up) will produce a positive yaw moment (starboard turn) and vice versa.

Similarly, if we consider the effect of planes 4 and 5 separately, ignoring the effects of planes 3 and 6, the same original equations for δP and δY will be reduced to the following expressions:

$$\delta P_{4,5} = \left(\frac{\delta_4 - \delta_5}{2}\right) \text{ and } \delta Y_{4,5} = \left(\frac{-\delta_4 + \delta_5}{2}\right) \tag{4.22}$$

In other words, the pitching moment produced by the combination of planes 4 and 5 will be equal in magnitude but opposite in sign to the yawing moment produced by the same combination. This means that a combination that produces a positive yaw moment (starboard turn) will also produce a negative pitch moment (nose-down) and vice versa. In the upward spiral phase, when the vehicle was ascending, the role of tail planes, apart from turning the vehicle to the starboard side, was to hold down the nose from excessive positive pitch angle. Hence, the δP should be negative. From the expression for $\delta P_{3,6}$ it is evident that a combination of planes 3 and 6 which produce negative pitch moment would also produce a negative yaw moment which means that the vehicle has to turn to the port side. Since this is not the case with the upward spiral of helix manoeuvre where the vehicle continued its starboard turn, the only option is to use the planes 4 and 5 to produce a positive δY and at the same time produce a negative δP. This explains the reason for the observed change in combinations of planes used during the dive and climb segments of the helix manoeuvre.

Rate of Ascent and Descent

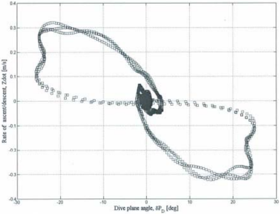

Fig. 4.104 Rate of ascent and descent during the helix manoeuvre performed at a speed of 1.5 m/s

The rate of ascent and descent of the vehicle moving at a forward speed of 1.5 m/s during the helix manoeuvre is shown in Figure 4.104, as a response to the dive plane deflections δP_D. Only δP_D is considered, as it was primarily responsible for dive and climb. The cluster of data points at the middle of the plot corresponds to the time when the vehicle is turning around. At this region, δP_D and $\dot{z}$ are both zero. The loops correspond to the time when the vehicle is in a dive or climb. Note that the loops have a smooth transition between their start and end without having any clusters of data along them, as found in the case of vertical zigzags. In other words, the loops indicate a smooth deflection of the planes from neutral to maximum values and back. This is because, with only 1.5 m of depth to travel, the dive or climb happens in a very short time such that the dive planes are not deflected and held in place to their maximum deflection angle for a long period (see Figure 4.100). The maximum rate of ascent and descent from the figure is almost the same and has a value close to 0.3 m/s.

Pitch and Yaw Attitudes of the Vehicle

In the dive-and-turn segments of the helix manoeuvre, since there is a coupling of heave and yaw motions, parameters such as pitch angle θ, drift angle β, angle of attack α, heave velocity, w, sway velocity, v etc. are expected to be present. The variation of some of these parameters with respect to control variables such as plane deflections and forward speed are present below.

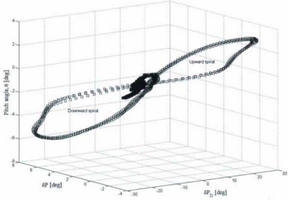

Fig. 4.105 Variation of pitch angle (θ) with control plane deflections δP & δP_D at a vehicle forward speed of 1.5 m/s

The pitch attitude of the vehicle during the entire manoeuvre with respect to control plane deflections is shown in Figure 4.105. Since the tail planes are also involved in helping the vehicle maintain a certain pitch attitude, when the dive planes are engaged in diving or climbing the vehicle, a 3D plot is made showing the variation of pitch angle (θ) against both effective dive plane (δP_D) and effective tail plane deflections (δP).

The maximum pitch angle attained by the vehicle during the dive segment was -6°. This was similar to the pitch attitude attained by the vehicle during vertical zigzags at a forward speed of 1.5 m/s, discussed in *Section 4.5*. However, the pitch attitude of the vehicle during climb (3°), in the case of helix manoeuvre, is somewhat larger that that in the case of vertical zigzags, which was estimated to be around 1.5°. During the vertical zigzag manoeuvres, all the tail planes were solely engaged in assisting with the pitch attitude of the vehicle, but in the case of helix, the tail planes do have an additional role of turning the vehicle as well. This extra job of producing the turn while countering excessive pitch produced the observed difference in pitch angle between the two cases.

The radial force necessary to produce a turn is generated by holding the hull at an angle relative to the flow. This is known as the sideslip angle or the drift angle β. The drift angle β and the angle of attack, α, are angles usually used to express the orientation of the vehicle, which in turn is specified by the velocity components [u, v, w], derived as shown in *Section 4.1.2.2*. SNAME (1950) defines drift angle as the angle to the principal plane of symmetry from the velocity of the origin of the body axes relative to the fluid, positive in the positive sense of rotation about z-axis. The drift angle β was estimated using the relation: $\beta = \sin^{-1}(v/V)$.

The time-series of drift angle β and its variation with sway velocity, v is shown in Figure 4.106. The drift angle shows a periodic pattern as it was found with the case of turning rate, r. It seems to oscillate about a mean value of 5°. The periodic nature of drift angle may be induced by the oscillations of the control plane deflection δY itself.

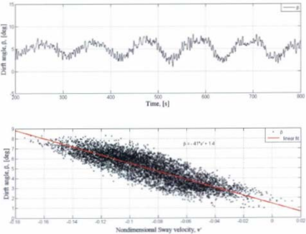

Fig. 4.106 Drift angle β and its variation with non-dimensional sway velocity, v'

The variation of drift angle β with non-dimensionalised sway velocity, v' is also shown in the second pane of Figure 4.106. The sway velocity, v is non-dimensionalised using the relation v/V, where V is the forward speed of the vehicle. A trend is clearly visible from the plot although there is some scatter. The expression for the linear fit is given by:

$$\beta = -41v' + 1.4 \tag{4.23}$$

The above expression (4.23) for drift angle β, denoted as a function of non-dimensional sway velocity, v' comprises the data from the entire helix manoeuvre. This expression is somewhat different from a similar expression (4.19 on pg. 92) derived for drift angle from the horizontal zigzag manoeuvres discussed in *Section 4.4*. The expression (4.19) can be rearranged to have the form of expression (4.23) as:

$$\beta = -58.8v' \tag{4.24}$$

The expression (4.24) from horizontal zigzags implies that the drift angle β is zero when the sway velocity, v is zero. However, this is not the case with the expression (4.23) which implies that when the sway velocity, v is zero; there is still a residual drift angle, β of 1.4°. This discrepancy may be due to the large scatter in the data as the drift angle oscillates with considerable amplitude about a mean value as seen in Figure 4.106. Further, it should be noted that the helix manoeuvre consists of three different segments in conjunction. That is, it consists of a dive-and-turn segment, a steady-turn segment and a climb-and-turn segment. If the drift angles of these three segments are separated and analyzed, the causes for the discrepancy can be further investigated. The variation of drift angle β with nondimensional swayvelocity v' for the three different segments mentioned above are separately identified as shown in Figure 4.107.

The expressions for the drift angle β corresponding to each of the three different segments are as follows:

Steady-turn region: $\beta = -41v' + 1.4$ (4.25a)

Dive-and-turn segments: $\beta = -26v' + 3.1$ (4.25b)

Climb-and-turn segments: $\beta = -23v' + 3.6$ (4.25c)

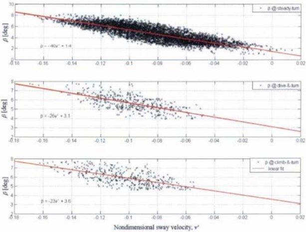

Fig. 4.107 Variation of drift angle β with non-dimensional sway velocity v' at different segments of the helix manoeuvre

The expressions in (4.25) indicate that there clearly exist a difference in drift angle between the steady turn segments and the dive and climb segments. The coupling between the turn-and-dive motions present in dive and climb segments of the helix manoeuvre is what brings about the difference in these expressions. It is reasoned that the fluctuation in drift angle brought about by the periodic variation in tail plane deflections is what creates the large scatter of data.

TABLE 4.12

Comparison of parameters from helix and turning circles							
Type of Manoeuvre	**R_c** [m]	**R_a** [m]	**RPM**	**θ** [deg]	***r*** [deg/s]	**α** [deg]	**β** [deg]
Turning Circle	**14**	20.8	161.5	-1.8	4.2	-1.8	2.4
Helix	**15**	**26.0**	**167.4**	**-1.4**	**3.3**	**-1.4**	**4.7**
Turning Circle	**16**	21.5	161.5	-1.9	3.7	-1.9	2.3

The parameters obtained from the arc of the circle or the steady turn segments of the helix manoeuvre are compared with corresponding parameters obtained from a similar or close to similar steady turn or turning circle experiments, described in *Section 4.3*. Some of these parameters are presented in Table 4.12.

Table 4.12 shows the mean value of some parameters such as the radius of turn, propeller rpm, yaw rate, pitch angle, angle of attack and drift angle obtained from the turning circle manoeuvres with command radii of 14 m and 16 m. The results are compared with the same set of parameters estimated from the steady turning portion of the helix manoeuvre having a command radius of turn of 15 m. There is some discrepancy in the results from both cases, particularly in the response of the vehicle to the command radius and the drift angle. Since both are functions of tail plane deflections, it may be reasoned that the fluctuations in the tail plane deflections caused the discrepancy in the results. These fluctuations in tail plane deflections were described as necessary to maintain a constant δP value, which in turn was responsible for holding the vehicle at a particular pitch attitude.

The angle of attack, α is another parameter used for specifying the orientation of the vehicle. It defines the angle at which the flow approaches the vehicle with respect to the longitudinal axis of the vehicle and is predominant during the ascent and descent of the vehicle in a helix manoeuvre. The variation of this parameter with the heave velocity, w', is shown in Figure 4.108.

The plot shows that there exist a perfect linear relationship between the angle of attack, α and the nondimensional heave velocity, w'. The expression for the linear fit is as follows:

$$\alpha = 57.5w' \tag{4.26}$$

The expression (4.26) is in exact agreement with the result obtained from vertical zigzag tests (4.20) shown in Figure 4. 91. The dive planes were solely instrumental in producing the depth change in both cases. Consequently, it is inferred that the heave velocity, w is completely determined by the forward speed and dive plane deflections of the vehicle and the turn has little to no effect on it. In the case of helix manoeuvre also, the vehicle was operated in the *Depth-by-Heave* mode.

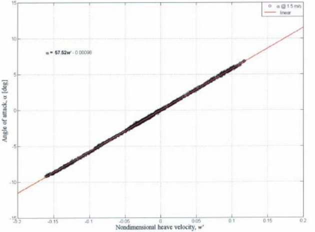

Fig. 4.108 Variation of angle of attack, α with non-dimensional heave velocity, w'

4.6.3 Summary of Helix Manoeuvre

The helix manoeuvre was performed with the intention of doing a 3D manoeuvre, which would excite all six DOF. The response of the vehicle from this manoeuvre will be used to validate the results from simulated response. It was designed as a series of circles being performed at different depths ranging between 3 m and 9 m at intervals of 1.5 m. It can be generally stated that the helix manoeuvre was a combination of depth changing and turning manoeuvres. However, results from the manoeuvre shows that the designed mission did not produce the intended result although some portions of the test can be extracted. Some results from the helix manoeuvres as well as results from a few vertical zigzag manoeuvres were already published in Issac *et al* (2010). The key observations from the helix manoeuvre are listed below.

a. One of the drawbacks with the designed mission was that the intervals between circles were too close such that the manoeuvre looked more like turns followed by dives (or climbs) instead of diving while turning simultaneously. As it was found with the case of turning circles, the actual radius of turn was larger (26.0 m) than the commanded radius of turn (15 m).

b. The vehicle used predominantly the dive planes to change the depth as it was found with the depth-changing manoeuvres. This is because the vehicle was operating in the *Depth-by-Heave* mode.

c. The combined dive-and-turn segment of the manoeuvre took only a fraction of the total time it took for the vehicle to finish one complete revolution. This can be increased by increasing the depth interval between the circles.

d. The vehicle does not experience any loss of speed or roll angle during the turn as it was observed in the case with turning circle manoeuvres.

e. By increasing the depth interval between circles and reducing the radius of turns, a helix manoeuvre of desired characteristics can be designed while following the exact same procedure.

4.7 Conclusions

The following are some of the key observations and conclusions regarding the general performance of the vehicle drawn from the open water manoeuvring trials conducted using the *MUN Explorer* AUV. As mentioned in the beginning, the main purpose of these experiments were to acquire some real vehicle response data from different manoeuvring scenarios such that it can be used to validate the motion responses from a hydrodynamic motion simulation model developed based on the component build-up method. Consequently, a comprehensive set of experiments were planned and executed, which to the best of the author's knowledge were never reported comprehensively in the public domain for any of the seven *Explorer* class AUVs in operation today. The experiments also formed a database for understanding the inherent behaviour of the vehicle and provided valuable information on what remedial measures to be made in future. Some of the manoeuvres that were performed as a part of the open-water trials included straight-line tests or acceleration/deceleration tests, turning circles, horizontal zigzags, vertical zigzags or depth-changing manoeuvres and a helix manoeuvre.

The straight-line tests or the acceleration-deceleration tests were performed by running the vehicle in a straight line consisting of four equal segments, each spanning 100 m long. The vehicle was commanded to travel each segment at a particular speed. In the upward leg of the run, the vehicle started from a speed of 2.5 m/s and decelerated in steps of 0.5 m/s to a speed of 1 m/s with which it travelled the last segment of the line. This formed the deceleration phase of the run. Upon reaching the end of the line, it turned around and starts from the last segment at a speed of 1 m/s and accelerates in steps of 0.5 m/s at each segment, reaching a maximum of 2.5 m/s by the time it reaches the start point of the first segment. This test was repeated making it a replication of the first.

The propeller rpm for the same speed during the acceleration and deceleration phase was found to be different, the difference being predominant at slower speeds indicating the presence of currents. The results showed that there existed an in-line current of 0.2 m/s in the southward direction. The time to accelerate (decelerate) from one speed to another and the distance traveled by the AUV during this transition was also estimated. Further, the stopping distance of the vehicle from an optimum operational speed was also roughly estimated. From the steady-state portion of the manoeuvre, where the speeds remained constant, a relationship between thrust versus forward speed was established, which in turn was used to develop a simple thruster model for the hydrodynamic simulation model. It was observed that slower speed required larger dive plane deflections in order to maintain level flight at constant forward speed. The straight-line tests also demonstrated the ability of the vehicle to follow a predefined path with minimum drift.

A set of 22 turning circle manoeuvres were performed using the *MUN Explorer* AUV at different speeds of 1, 1.5 and 2 m/s and this again provided some insight into the steady-state behaviour of the vehicle during a turn. The analysis and observations from these sets were reported in detail. Only a small subset of the set of tests planned at 2 m/s speed could be completed. The conventional way of performing a turning mission, using forward speed and rudder deflection as the input, was not possible with

MUN Explorer AUV. This was because the operator had no direct control over setting the rudder deflection, as this feature was not built-in to the *MUN Explorer* during the time of test. Hence, the alternative was to use forward speed and radius of turn as the input variables.

The actual radius of turn R_a estimated from the data, in all tests, were larger than the commanded radius, R_c. The speed of the vehicle in the steady turn portion was observed to be equivalent to the command speed in all cases and this happened without any considerable change in the propeller rpm. Theoretically, it is not possible to have the same speed during a turn as that for a straight course without actually changing the propeller rpm. Nevertheless, this pattern was consistent with all the tests. The magnitude of the speed loss in a turn is largely a function of the tightness of the turning circle. It is reasoned that since the radii of turns were large with a diameter-to-length (D/L) ratio of 10 and more, the estimated drift angle experienced by the AUV generates drag not much different from that during a straight course although the exact reason for this behaviour is unknown. As a recommendation, during future experiments, it would be more appropriate to use constant propeller rpm rather than constant speed as the control input such that any change in speed during a turn or dive could be closely estimated. The vehicle exhibited negligible roll motions even during the turn. Thus, the ability of the control system to maintain a command speed through out the turn with negligible roll ensures consistent sampling of data during a mission. As in the case with straight-line tests, the vehicle exhibited a large nose-down attitude at slow speed while it was much less at higher speeds. This is an essential quality of a sensor platform. Finally, the information such as the rudder angle δ and forward speed

V estimated from the turning circle mission would form the inputs for the hydrodynamic motion simulation model.

Zigzag manoeuvres, unlike straight-line tests and turning circles, are characteristics of unsteady manoeuvres. Six horizontal zigzag manoeuvres were performed using the vehicle during the available test time. Here again, due to lack of access to the rudder controls directly, the missions had to designed in an unconventional manner. The vehicle was programmed to follow a defined path laid out by a series of waypoints in zigzag pattern. The angle between the lines formed by these waypoints defined the degree or sharpness of the turn that the vehicle had to negotiate at speeds of 1.5 and 2.0 m/s. Within the range of tests performed, the mildest turn had an angle of about 28^o and the sharpest turn had an angle of about 90^o. These results would form the basis for testing the turning ability of the vehicle simulated using the hydrodynamic motion simulation model.

The ability of the vehicle to precisely follow a predefined path was evident from these horizontal zigzag manoeuvres. The results indicated that the initial trajectories designed had too large cycle lengths such that the vehicle travelled for considerably long distance in a straight line (constant heading) which is not characteristic of a conventional zigzag manoeuvre, where the vehicle changes its heading continuously forming a sinusoidal path. The last two tests were designed in an attempt to rectify this by reducing the cycle length. The result was better trajectories that resembled very close to conventional zigzags. It was observed that higher speeds and sharper turns produced large overshoots and consequently more turning time. Further, the loss of speed during the turn was sharply evident from these manoeuvres unlike the turning circle manoeuvres but the vehicle controller immediately compensated it by adjusting the propeller rpm. This again emphasizes the need for performing the test with constant propeller rpm as the input rather than constant speed. It was also found that the turning rate of the vehicle was influenced by the speed of the vehicle rather than the sharpness of turn, within the range of test conditions. The speed also affected the stability of turns with higher speeds producing more unstable turns than slower speed.

Vertical zigzags or depth-changing manoeuvres formed the next set of unsteady manoeuvring trials performed using the *MUN Explorer* AUV. A total of six tests were performed at speeds of 1.5 and 2.0 m/s. The missions were designed just like the horizontal zigzags by picking points in a vertical plane at regular intervals on either side of a horizontal straight line and were executed within a depth band ranging from 4 m to 10 m thus giving the vehicle a maximum depth excursion of 6 m.

The results from vertical zigzag manoeuvres show that for all the tests performed, the vehicle utilized its dive planes for changing depth and consequently produced overshoots that were rather insignificant for a vehicle of its size. This was because the vehicle controller was set in the *Depth-by-Heave* operational mode, which was also the default mode. The overshoots indicated that the safest mode of operating the AUV in shallow waters or close to seabed is also the *Depth-by-Heave* mode.

The ability of the vehicle to follow an inclined straight line in a vertical plane is questionable unlike in the horizontal zigzag cases where the vehicle exhibited an excellent capability to follow a straight line. This is because the vehicle's depth controller is decoupled from its horizontal or geographic control and therefore one works independently of the other. It was also found that the rate of dive was faster than the rate of climb although the opposite is normally expected due to net positive buoyant force acting in favour of an ascending motion. The cause for this discrepancy was attributed to the pitch attitude of the vehicle during dive and climb. Further, the vehicle maintained the constant command speed throughout an entire manoeuvre and in regions where one would expect a loss of speed it was compensated automatically by an adjustment in the propeller rpm. The above trials provided information about the plausible slopes of path that could be adopted to design future tests of similar nature, which would yield vertical zigzags that resemble a conventional depth-changing manoeuvre. Information about the rate of change of depth at different speeds, while using dive planes, were also presented.

A helix manoeuvre was the last in line to the whole set of open-water trials performed using the *MUN Explorer*. It was performed with the intention of doing a 3D manoeuvre, which would excite all six DOF. However, results from the manoeuvre showed that the designed mission did not produce the intended result although some portions of the manoeuvre did excite all six DOF. It was expected that the vehicle would continuously dive as it turned around in circles. This led to the mission being designed as a series of circles performed at different depths. However, the response from the vehicle showed that it performed almost a complete circle at one level before it dropped to the next level and so on. This was because the interval between the commanded circles was too close. Further, it was found that the turning circles had much larger radius than the commanded radius. In future, tests performed adopting the same procedure can be rectified by reducing the radius of turn and increasing the depth interval between circles in order to achieve a 3D manoeuvre that resembles a helix and thus excite all six DOF.

In the helix manoeuvre also, the vehicle used primarily the dive planes for changing depth and the dive-and-turn segment where all six DOF are likely to be present took only a fraction of the total time it took for the vehicle to finish one complete revolution. This was so because the vehicle controller was set in *Depth-by-Heave* mode. Further, the vehicle did not experience any loss of speed or roll angle during the turn as it was found in the case with turning circles.

As a general conclusion, it can be stated that the *MUN Explorer* demonstrated an excellent capability to follow a predefined path. Since the control over control planes was restricted, all manoeuvres were designed and executed in a way other than the conventional ways. The radius of turn resulting from a manoeuvre was always larger than the commanded radius of turn. In almost every case, slower speeds resulted in the vehicle maintaining an inherent nose-down attitude which unnecessarily required larger dive and tail plane deflections to counter it. The missions involving depth change were all executed using the dive planes as the vehicle controller was set in *Depth-by-Heave* mode. In future, the response of the vehicle to *Depth-by-Pitch* mode can be investigated. The ability of the vehicle to maintain a constant command speed regardless of the type of trajectory and the negligible roll motions exhibited, even during a turn, added with the ability to manoeuvre in a vertical plane without much overshoot is characteristics of a robust control system and is an essential quality of a sensor platform. As a recommendation, it would be more appropriate to use constant propeller rpm as the input rather than constant speed-over-ground so as to capture any information about the change in speed during turns and dives and also from environmental disturbances. As mentioned earlier, a portion of the results from manoeuvring trials described through this chapter has already been peer-reviewed and published in open literature namely Issac *et al* (2007a), Issac *et al* (2007b), Issac *et al* (2008) and Issac *et al* (2010).

Chapter 5

Motion Simulator for the *Explorer* AUV

One of the key objectives of this research was to study the performance of a hydrodynamic motion simulation model for axisymmetric streamlined underwater vehicles, developed based on the component build-up method (CBM). An overriding advantage of using the component build-up method is that the hydrodynamic forces and moments acting on the vehicle can, for the most part, be determined from semi-empirical relations that require only the specification of vehicle geometry and hence they are computationally rapid and inexpensive. Yet another advantage of the component build-up method is that it retains the inherent nonlinear nature of the model and therefore is not limited to a region about the nominal operating (equilibrium) state of the vehicle, an assumption inherent in models, which are linearized for small motions (perturbations), using the Taylor Series Expansion method. However, the CBM does depend on factors that have some physical constraints over the range of vehicle motions. These constraints must be accounted for in the computer model or they constitute limits of validity for the model. The underlying physics of such a fully nonlinear hydrodynamic model, developed for the streamlined AUV C-SCOUT (Canadian Self-Contained Off the shelf Underwater Testbed), was described in Chapter 2. Since no experimental data from free-running trials were available from the C-SCOUT AUV, the experimental data necessary for validating the model was obtained from open-water manoeuvring trials performed using the full-scale *MUN Explorer* AUV. The data analysis and observations from these manoeuvring trials were discussed in Chapter 4. However, along with the *MUN Explorer* AUV, also came the need for development of a computer model specifically tailored for this new vehicle.

A computer model enables the designer to test various design parameters and validate design choices as well as test ideas and algorithms before committing them to hardware. In order to characterize the motion of the physical vehicle, the computer model was developed using MATLAB™ and Simulink ™. The availability of such a hydrodynamic simulation model at Memorial University, developed by Perrault (2002) and Evans (2003) for the C-SCOUT AUV eased the problem of developing a new model for the *MUN Explorer* AUV from scratch. However, necessary modifications were to be made to the existing model in order to capture the geometric features and inertial properties of the *MUN Explorer* AUV. This chapter gives a brief layout of the structure of the existing simulation model and focuses mainly on the modifications that were necessary to make the simulation adapt to the *MUN Explorer* AUV. A second model of the *MUN Explorer* with a different ('+') tail plane configuration was also developed along with the primary model that had 'X' tail configuration. This demonstrates the ease with which a model based on CBM can be reconfigured to adapt to a different vehicle or different configuration.

5.1 The MATLAB™ and Simulink™ Model

The simulation model developed in MATLAB™ and Simulink™ is a modular nonlinear model based on Newton-Euler Equations of Motion for an axisymmetric streamlined underwater vehicle. Simulink™ is a MATLAB graphical top layer which lets you build block diagrams, simulate dynamic systems and evaluate system performance. A block diagram of the existing Simulink model is shown in Figure 5.1.

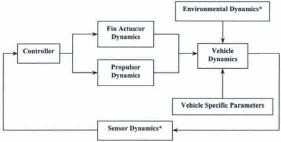

Fig 5.1 Block diagram of the Simulink model

At the heart of the MATLAB™/Simulink™ computer model is a variable time-step integrator, solving a set of six second order differential equations applicable to a large variety of streamlined vehicles. For this reason they are coded as a separate S-*function* while the vehicle specific parameters are generated from an initialization file and held in the workspace while the model is executing. Each of the Simulink blocks in Figure 5.1 is associated with a particular S-file. An *S-function* is a computer language description of a Simulink block, which allows you to add your own blocks to Simulink models[1]. The modular structure of the computer model also allows for the separate development of the actuator and sensor dynamics[*], as well as inclusion of environmental disturbances[*] [Perrault *et al.,* (2000)].

The nonlinear model of the AUV consists of three basic components:

i) The vehicle dynamics

ii) The control actuator dynamics (control plane dynamics, propeller dynamics etc.)

iii) The controller

The *Vehicle Dynamics* block calls a MATLAB script file (m-file), which is a generic implementation of the dynamics of a rigid body in a Newtonian fluid, suitable for any streamlined, axisymmetric body with control planes. These dynamics are the core of the model. As for the *MUN Explorer* AUV, which has its stern planes arranged in an 'X' configuration, a minor modification to this module was necessary in order to incorporate the dynamics for the 'X' tail configuration. The existing vehicle dynamics module for the C-SCOUT AUV handles the cruciform, '+', configuration but not the 'X' configuration. The dynamics of the X-tail configuration and the hydrodynamics of the *Explorer* control planes are discussed in detail in the following section.

All vehicle specific parameters are defined in a MATLAB script file contained in the *Vehicle Specific Parameters* block. This is an initialization file, which must be run first, and only once, to load all the vehicle-specific parameters into the MATLAB

[1] *SIMULINK: Dynamic System Simulation for MATLAB*, Writing S-Functions Ver.-4, The MathWorks Inc., November 2000.

[*] These modules are not used in the model as of now

workspace to initialize the model. This file contains the geometric and inertial parameters specific to the vehicle. As far as this simulation model is concerned, this script file is the one that needs the most updates every time the simulation is to be adapted to a new vehicle. Some of these modifications that are necessary to make the existing model adapt to the *MUN Explorer* AUV are also discussed in the sections that follow after.

5.2 Dynamics of Control Planes in 'X' Configuration

The *MUN Explorer* has a total of six control planes: two dive planes and four tail planes, which enable the AUV to manoeuvre in 3D space. The two dive planes are located on the forward payload section aft of the nose module and forward of the C.G of the vehicle. Also, the dive planes align themselves with the horizontal plane containing the longitudinal axis of the vehicle, at zero deflection. The four tail planes, arranged in an X-tail form, are located on the faired portion of the aft payload section.

5.2.1 X-Tail Configuration: A Brief History and Advantages

Model tests and experience from the past century had indicated that an "X" configuration of the stern planes would be superior to "+" (cruciform) arrangement as it improved the manoeuvrability. An excellent report on the advantages of "X" stern configuration is contained in the paper by Heggstad (1984). It states that the introduction of X-planes in submarine design was originally a US Navy concept, possibly stemming from missile and aerospace activities and was first tried at sea in the USS *Albacore*, following extended model basin tests. From USS *Albacore* sea trials, reported in Jackson (1993), it was demonstrated that an 'X' arrangement of aft control planes gave a much tighter turning circle than with a conventional cruciform arrangement and is an aspect of modern submarine design [Joubert, 2006].

One of the key advantages of having an "X" stern configuration is its ability to achieve a considerable increase in rudder forces without any increase in control surface areas. This can be explained with the help of following figures (5.2) and (5.3), as illustrated in Heggstad (1984).

Figure 5.2 shows schematically the cruciform rudder configuration. If the aft rudders (Planes 2 & 4) and the aft hydroplanes (Planes 1 & 3) are deflected simultaneously to the configuration as shown in Figure 5.2-B, it would result in producing rudder forces, F_y and aft hydroplane forces, F_z, in the horizontal and vertical directions respectively. The resultant of these two forces, F, called the steering force acting at the stern, is the vector sum of F_y and F_z, which will act in the diagonal direction as shown in the figure.

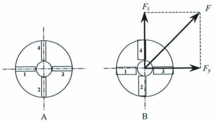

Fig. 5.2 Forces developed by a cruciform stern configuration

From Figure 5.2B, the resultant force, $F = \sqrt{F_y^2 + F_z^2}$

If all control planes have the same area and have the same rudder deflection, then $F_y = F_z$ and hence the above relation can be written as:

$$F = \sqrt{2}F_y = 1.41F_y$$

This means that the steering force acting in the diagonal direction will be greater than the rudder force F_y or hydroplane force F_z by 41%.

If we rotate the configuration shown in Figure 5.2-A as a whole by 45°, the resulting configuration would be the X-stern configuration as shown in Figure 5.3.

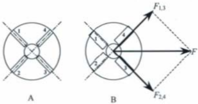

Fig. 5.3 Forces developed by an "X" stern configuration

Here, an increase in rudder force by 41% in the main directions is achieved without any increase in control surface areas. In other words, by adopting 'X'-form, the combined rudder forces in the horizontal and vertical planes are increased.

A further advantage of having the stern planes arranged in 'X' configuration is that the surfaces do not fall in the wake created by the dive planes ahead. In cases when the stern planes operate in a flow disturbed by the foreplanes, such as with '+'

configurations, it is usually appropriate to apply a correction factor to reduce the lift coefficient by about 40% [Hopkin and den Hertog, (1993)], to account for this effect.

5.2.2 Dynamics of Control Planes

The lift and drag forces acting on the control planes are calculated by considering only the chord-wise component of the flow velocity at the centre of pressure of the control plane. In order to calculate the chord-wise flow component as well as to transform the lift and drag forces on control planes into the body-fixed frame, a set of angles, $\alpha, \beta, \alpha', \beta'$, were defined in *Section 2.4* of Chapter 2. These angles, which describe the hull angle of attack and sideslip, were expressed in terms of the local velocities *u*, *v* and *w* (see equations 2.19 and 2.20 in Chapter 2). A similar set of equations can be derived for a body with an 'X' tail configuration. For the purpose of illustration we may use Figure 2.2 of Chapter 2, reproduced here as Figure 5.4, and start our explanation with the dynamics of a cruciform, '+' configuration and thereafter move to the dynamics of 'X' configuration.

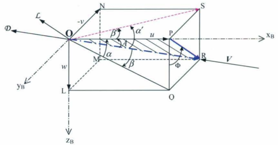

Fig. 5.4 Lift, drag, α and β for a vehicle oriented arbitrarily to the flow
(Figure 2.2 reproduced from Chapter 2)

a) Cruciform Configuration

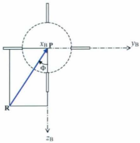

Fig. 5.5 View: looking forward with the approach flow coming from an arbitrary angle of attack. Vector **PR** is the projection of flow-vector **OR** on the y_Bz_B-plane

Figure 5.5 shows the body-fixed frame and the approaching flow, shown in Figure 5.4, when looking from the rear of the vehicle. The rotation angle, Φ, specifies the orientation of the velocity vector **PR** on the body-fixed y_Bz_B-plane. The longitudinal axis (x_B) of the vehicle in the body-fixed frame is perpendicular and directed into the plane of the paper. The circular cross-section of the AUV with stern planes arranged in cruciform (+) configuration is shown superimposed over the body-fixed frame. In the cruciform configuration, the horizontal stern planes are oriented along the y_B-axis and the vertical planes or rudders are oriented along the z_B-axis. The dynamics of the horizontal and vertical control planes have already been discussed in detail in Chapter 2. With regards to the *MUN Explorer* AUV, the dynamics of the dive planes resembles the dynamics of the horizontal stern planes of the C-SCOUT AUV, except that the dive planes are located forward of the C.G of the vehicle. Therefore, the dynamics of the dive planes can be easily modeled using the formulation for the horizontal control planes of the C-SCOUT. This is briefly described below.

In order to calculate the hydrodynamic loads on the dive planes, the velocity of flow at the centre of pressure, V_{CP} of each dive plane is to be determined.

$$V_{CP} = \sqrt{\left(u_{CP}^2 + v_{CP}^2 + w_{CP}^2\right)}$$

$$V_{CP} = \boldsymbol{v}_1 + \boldsymbol{v}_2 \times \boldsymbol{r}_{CP} \tag{5.1}$$

where $\boldsymbol{v}_1$ is the translational velocity of the AUV at the origin of the body-fixed frame, $\boldsymbol{v}_2$ is the angular velocity of the vehicle and $\boldsymbol{r}_{CP}$ specifies the location of the centre of pressure of the dive plane from the origin of the body-fixed frame or in this case the centre of mass of the vehicle.

Since only the chord-wise flow is considered for calculating the hydrodynamic loads acting on the control plane (flow along span being neglected), the flow that is relevant to the dive planes is $V_{CP}\cos(\beta)$ and it falls on a plane parallel to the $x_B z_B$-plane (see Figure 5.4).

$$V_{CP}\cos(\beta) = \sqrt{u_{cp}^2 + w_{cp}^2} \tag{5.2}$$

Horizontal Dive Planes

The drag and lift forces on the dive planes act parallel and perpendicular to the incident flow, $V_{CP}\cos(\beta)$, respectively:

$$\mathcal{D}_{HDP} = \frac{1}{2}\rho C_D A_{CP}\left[V_{CP}\cos(\beta)\right]^2 \tag{5.3a}$$

$$\mathcal{L}_{HDP} = \frac{1}{2}\rho C_L A_{CP}\left[V_{CP}\cos(\beta)\right]^2 \tag{5.3b}$$

where the lift and drag coefficients, C_L and C_D, are functions of the flow angle of attack which is the sum of the deflection of the control plane, δ_{HDP}, added to the angle of attack, α, of the hull. The forces are then rotated about the y_B-axis by $\pi+\alpha$ to express them in the body frame.

$$\begin{bmatrix} X_{HDP} \\ Y_{HDP} \\ Z_{HDP} \end{bmatrix}_B = \begin{bmatrix} \cos(\pi+\alpha) & 0 & -\sin(\pi+\alpha) \\ 0 & 1 & 0 \\ \sin(\pi+\alpha) & 0 & \cos(\pi+\alpha) \end{bmatrix} \begin{bmatrix} \mathcal{D}_{HDP} \\ 0 \\ \mathcal{L}_{HDP} \end{bmatrix}$$

$$\begin{bmatrix} X_{HDP} \\ Y_{HDP} \\ Z_{HDP} \end{bmatrix}_B = \begin{bmatrix} -\cos(\alpha) & 0 & \sin(\alpha) \\ 0 & 1 & 0 \\ -\sin(\alpha) & 0 & -\cos(\alpha) \end{bmatrix} \begin{bmatrix} \mathcal{D}_{HDP} \\ 0 \\ \mathcal{L}_{HDP} \end{bmatrix} \tag{5.4}$$

The angles of attack α, β, α', β' are to be determined for each dive plane and their calculation is made possible from the knowledge of velocity components at the centre of pressures of each control plane, given by the relation in Eq. (5.1). In order to build a second model of the *MUN Explorer* with '+' tail planes the method described in Chapter 2 for the tail planes of C-SCOUT AUV was applied.

b) X-Tail Configuration

The *MUN Explorer*'s tail planes are arranged in an 'X' configuration and in order to formulate the dynamics of such a tail configuration, it is required to introduce an additional reference frame (x_{tp}, y_{tp}, z_{tp}). This new reference frame is aligned with the tail planes, as shown in Figure 5.6, and facilitates the calculation of tail plane forces. These tail plane forces are then transformed into the body-frame by a mere rotation of -45° about the x_B-axis of the vehicle. The x_{tp}-axis coincides with x_B-axis, which is perpendicular to, and directed into, the plane of the paper.

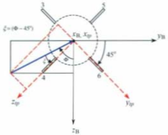

Fig. 5.6 View: looking forward the vehicle arbitrarily oriented to the flow

Figure 5.6 shows the flow conditions experienced by an axisymmetric vehicle with tail planes arranged in 'X' configuration. Since these control planes are oriented at 45° to the body-axis, the angles of attack seen by the planes are different from that seen by the planes arranged in a cruciform, '+', configuration. As discussed in the case with cruciform configuration, only the chord-wise flow is considered for the estimation of lift and drag forces on the control plane, although it is known that any fin for which Φ is not zero is sideslipping, (Hemsch and Neilsen, 1983). It means that the flow which is relevant to control plane 6 (as well as 3) falls in a plane normal to the y_{tp}-axis and the flow that is relevant to control plane 4 (as well as 5) falls in a plane normal to the z_{tp}-axis. The control plane numberings represented here are the same as those used for *MUN Explorer* AUV. In order to find the angle of attack for each fin, the free-stream velocity components along the x_{tp}, y_{tp} and z_{tp} axes should be estimated. Once the expressions for velocity components along the axes are determined, a set of equations, similar to the equations (2.19) through (2.21) of

Chapter 2, can be derived for the case of the 'X' configuration as well. These angles will be useful in determining the angle of attack and sideslip seen by the control planes arranged in an 'X' configuration.

The flow vector on the y_Bz_B-plane of Figure 5.6, is the same as that shown in Figure 5.5, whose magnitude is given by $V\sin(A)=\left(\sqrt{v^2+w^2}\right)$, (see Figure 5.4). This vector was oriented at an angle, Φ, to the z_B-axis, (see Figure 5.5 and Figure 5.4). The same vector, $V\sin(A)$, when viewed from the control plane coordinates (x_{tp}, y_{tp}, z_{tp}), makes an angle ($\Phi - 45^\circ$) with the z_{tp}-axis. If we denote this angle ($\Phi - 45^\circ$) as ξ, this corresponds to a case very similar to that in Figure 5.5, such that the flow vector on the $y_{tp}z_{tp}$-plane has to be rotated by an angle ξ in order to bring it to the z_{tp}-axis. In other words, ξ in the $y_{tp}z_{tp}$-plane of (x_{tp}, y_{tp}, z_{tp}) reference frame corresponds to the roll angle, Φ, in the y_Bz_B-plane of the body-fixed frame (x_B, y_B, z_B); the only difference being that the control plane reference frame is oriented at an angle of 45° from the body-fixed frame. The problem thus simplified can now be visualized by a figure very similar to Figure 5.4, in which the coordinates x_B, y_B, z_B are to be replaced by x_{tp}, y_{tp}, z_{tp} and the roll angle Φ is to be replaced by ξ. The components of the free-stream velocity along the tail plane coordinates x_{tp}, y_{tp} and z_{tp} can then be expressed as:

$$\begin{aligned} u_{tp} &= V\cos(A) \\ v_{tp} &= -V\sin(A)\sin(\xi) \qquad (5.5) \\ w_{tp} &= V\sin(A)\cos(\xi) \end{aligned}$$

A set of angles, similar to that defined by Equations (2.19) and (2.20) of Chapter 2, can now be derived in terms of these velocity components in the tail plane coordinates.

$$\cos\beta_\varphi = \frac{\sqrt{u_\varphi^2 + w_\varphi^2}}{\sqrt{u_\varphi^2 + v_\varphi^2 + w_\varphi^2}} \qquad \sin\beta_\varphi = \frac{-v_\varphi}{\sqrt{u_\varphi^2 + v_\varphi^2 + w_\varphi^2}} \qquad \tan\beta_\varphi = \frac{-v_\varphi}{\sqrt{u_\varphi^2 + w_\varphi^2}} \tag{5.6}$$

$$\cos\alpha_\varphi = \frac{u_\varphi}{\sqrt{u_\varphi^2 + w_\varphi^2}} \qquad \sin\alpha_\varphi = \frac{w_\varphi}{\sqrt{u_\varphi^2 + w_\varphi^2}} \qquad \tan\alpha_\varphi = \frac{w_\varphi}{u_\varphi}$$

$$\tan\alpha_\varphi = \frac{w_\varphi}{u_\varphi} = \frac{V\sin A\cos\xi}{V\cos A} = \tan A\cos\xi \tag{5.7}$$

The alternative set of angles can also be similarly defined as:

$$\cos\alpha'_\varphi = \frac{\sqrt{u_\varphi^2 + v_\varphi^2}}{\sqrt{u_\varphi^2 + v_\varphi^2 + w_\varphi^2}} \qquad \sin\alpha'_\varphi = \frac{w_\varphi}{\sqrt{u_\varphi^2 + v_\varphi^2 + w_\varphi^2}} \qquad \tan\alpha'_\varphi = \frac{w_\varphi}{\sqrt{u_\varphi^2 + v_\varphi^2}} \tag{5.8}$$

$$\cos\beta'_\varphi = \frac{u_\varphi}{\sqrt{u_\varphi^2 + v_\varphi^2}} \qquad \sin\beta'_\varphi = \frac{-v_\varphi}{\sqrt{u_\varphi^2 + v_\varphi^2}} \qquad \tan\beta'_\varphi = \frac{-v_\varphi}{u_\varphi}$$

$$\tan\beta'_\varphi = \frac{-v_\varphi}{u_\varphi} = \frac{-(-V\sin A\sin\xi)}{V\cos A} = \tan A\sin\xi \tag{5.9}$$

In the case of the cruciform '+' configuration, described in Chapter 2, it was seen that the angles β and α' were required to describe the flow velocity that was relevant to the horizontal and vertical control planes, respectively, in order to calculate the lift and drag forces. However, the lift and drag forces are also functions of control plane deflections, δ, added to the angle of attack, α, and angle of sideslip β' of the hull, for the horizontal and vertical control planes respectively.

A parallel approach to that described above can be made for the case of the 'X' configuration, if we consider control planes (3 and 6), oriented along the y_{tp}-axis, to correspond to the horizontal planes of the '+' configuration and that oriented along the z_{tp}-axis (4 and 5) to correspond to the vertical planes of '+' configuration. The angles of attack α_{tp}, β_{tp}, α'_{tp}, β'_{tp} are to be determined for each control plane.

Control Planes (3) and (6)

The flow that is relevant to control planes 3 and 6, oriented along the y_{tp}-axis is represented by $V_{CP}\cos(\beta_{tp})$, where V_{CP}, is the velocity of the flow at the centre of pressure of the control plane. The lift and drag forces on planes 3 and 6 are given by:

$$\mathcal{D}_{3,6} = \frac{1}{2}\rho C_D A_{CP}\left(V_{CP}\cos(\beta_{tp})\right)^2 \tag{5.10a}$$

$$\mathcal{L}_{3,6} = \frac{1}{2}\rho C_L A_{CP}\left(V_{CP}\cos(\beta_{tp})\right)^2 \tag{5.10b}$$

where lift and drag coefficients, C_L and C_D, are functions of the sum of the control plane deflection, $\delta_{3,6}$, and the angle of attack, α_{tp}, (Eq. 5.7) of the hull. The forces are then rotated about the y_{tp}-axis by $\pi + \alpha_{tp}$ to express it in the tail plane reference frame.

$$\begin{bmatrix} X_{3,6} \\ Y_{3,6} \\ Z_{3,6} \end{bmatrix}_{tp} = \begin{bmatrix} \cos(\pi+\alpha_{tp}) & 0 & -\sin(\pi+\alpha_{tp}) \\ 0 & 1 & 0 \\ \sin(\pi+\alpha_{tp}) & 0 & \cos(\pi+\alpha_{tp}) \end{bmatrix} \begin{bmatrix} \mathcal{D}_{3,6} \\ 0 \\ \mathcal{L}_{3,6} \end{bmatrix} \tag{5.11}$$

$$\begin{bmatrix} X_{3,6} \\ Y_{3,6} \\ Z_{3,6} \end{bmatrix}_{tp} = \begin{bmatrix} -\cos(\alpha_{tp}) & 0 & \sin(\alpha_{tp}) \\ 0 & 1 & 0 \\ -\sin(\alpha_{tp}) & 0 & -\cos(\alpha_{tp}) \end{bmatrix} \begin{bmatrix} \mathcal{D}_{3,6} \\ 0 \\ \mathcal{L}_{3,6} \end{bmatrix}$$

The above forces are then transformed from the tail plane reference frame to the body-fixed frame by rotating it counterclockwise about the x_{tp}-axis ($x_{tp} = x_B$) by 45°.

$$\begin{bmatrix} X_{3,6} \\ Y_{3,6} \\ Z_{3,6} \end{bmatrix}_{B} = \begin{bmatrix} 1 & 0 & 0 \\ 0 & \cos\Phi_B & -\sin\Phi_B \\ 0 & \sin\Phi_B & \cos\Phi_B \end{bmatrix} \begin{bmatrix} X_{3,6} \\ Y_{3,6} \\ Z_{3,6} \end{bmatrix}_{tp}$$

$$\begin{bmatrix} X_{3,6} \\ Y_{3,6} \\ Z_{3,6} \end{bmatrix}_{B} = \begin{bmatrix} -\cos\alpha_{tp} & 0 & \sin\alpha_{tp} \\ \sin\Phi_B \sin\alpha_{tp} & \cos\Phi_B & \sin\Phi_B \cos\alpha_{tp} \\ -\cos\Phi_B \sin\alpha_{tp} & \sin\Phi_B & -\cos\Phi_B \cos\alpha_{tp} \end{bmatrix} \begin{bmatrix} \mathcal{D}_{3,6} \\ 0 \\ \mathcal{L}_{3,6} \end{bmatrix} \tag{5.12}$$

Control Planes (4) and (5)

The flow that is relevant to control planes 4 and 5, oriented along the z_{tp}-axis is represented by $V_{CP}\cos(\alpha'_{tp})$, where V_{CP}, is the velocity the of flow at the centre of pressure of the control plane. The lift and drag forces on planes 4 and 5 are given by:

$$\mathcal{D}_{4,5} = \frac{1}{2}\rho C_D A_{CP}\left(V_{CP}\cos(\alpha'_{tp})\right)^2 \tag{5.13a}$$

$$\mathcal{L}_{4,5} = \frac{1}{2}\rho C_L A_{CP}\left(V_{CP}\cos(\alpha'_{tp})\right)^2 \tag{5.13b}$$

where lift and drag coefficients, C_L and C_D, are functions of the sum of the control plane deflection, $\delta_{4,5}$, and the angle of attack, β'_{tp}, (Eq. 5.9) of the hull. The forces are then rotated about the z_{tp}-axis by $\pi+\beta'_{tp}$ to express it in the tail plane reference frame.

$$\begin{bmatrix} X_{4,5} \\ Y_{4,5} \\ Z_{4,5} \end{bmatrix}_{tp} = \begin{bmatrix} \cos(\pi+\beta'_{tp}) & -\sin(\pi+\beta'_{tp}) & 0 \\ \sin(\pi+\beta'_{tp}) & \cos(\pi+\beta'_{tp}) & 0 \\ 0 & 0 & 1 \end{bmatrix} \begin{bmatrix} \mathcal{D}_{4,5} \\ \mathcal{L}_{4,5} \\ 0 \end{bmatrix} \tag{5.14}$$

$$\begin{bmatrix} X_{4,5} \\ Y_{4,5} \\ Z_{4,5} \end{bmatrix}_{tp} = \begin{bmatrix} -\cos(\beta'_{tp}) & \sin(\beta'_{tp}) & 0 \\ -\sin(\beta'_{tp}) & -\cos(\beta'_{tp}) & 0 \\ 0 & 0 & 1 \end{bmatrix} \begin{bmatrix} \mathcal{D}_{4,5} \\ \mathcal{L}_{4,5} \\ 0 \end{bmatrix}$$

The above forces are then transformed from the tail plane reference frame to the body-fixed frame by rotating it counterclockwise about the x_{tp}-axis ($x_{tp} = x_B$) by 45°.

$$\begin{bmatrix} X_{4,5} \\ Y_{4,5} \\ Z_{4,5} \end{bmatrix}_{B} = \begin{bmatrix} 1 & 0 & 0 \\ 0 & \cos\Phi_B & -\sin\Phi_B \\ 0 & \sin\Phi_B & \cos\Phi_B \end{bmatrix} \begin{bmatrix} X_{4,5} \\ Y_{4,5} \\ Z_{4,5} \end{bmatrix}_{tp}$$

$$\begin{bmatrix} X_{4,5} \\ Y_{4,5} \\ Z_{4,5} \end{bmatrix}_{B} = \begin{bmatrix} -\cos\beta'_{tp} & \sin\beta'_{tp} & 0 \\ -\cos\Phi_B\sin\beta'_{tp} & -\cos\Phi_B\cos\beta'_{tp} & -\sin\Phi_B \\ -\sin\Phi_B\sin\beta'_{tp} & -\sin\Phi_B\cos\beta'_{tp} & \cos\Phi_B \end{bmatrix} \begin{bmatrix} \mathcal{D}_{4,5} \\ \mathcal{L}_{4,5} \\ 0 \end{bmatrix} \tag{5.15}$$

The equations (5.12) and (5.15) transforms the lift and drag forces acting on the tail planes, arranged in 'X' configuration, to the body-fixed frame.

Centre of Pressure of Control Planes

The lift and drag forces, described by equations (5.10) and (5.13), act at the centre of pressure (CoP) of each control plane. The *MUN Explorer* AUV's control planes are all identical with a symmetrical section and a rectangular plan-form area. Therefore, the centre of pressure (CoP) of the control plane was assumed to be at the quarter-chord point of the section about midway between the root and tip chord.

5.2.3 Hydrodynamic Characteristics of the Control Planes

The hydrodynamic forces and moments generated by the flow over the control planes can be estimated only by knowing the hydrodynamic/aerodynamic characteristics of that particular airfoil section. The principal aerodynamic characteristics of an airfoil section such as lift, drag and pitching moment are often expressed as coefficients C_L, C_D and C_M respectively. The curves showing these coefficients as a function of angle of attack are known as *characteristic curves*. These characteristics depend on the shape of the profile, the angle of attack α, the aspect ratio AR of the airfoil and the Reynolds Number Re, (Mises, 1959). All six control planes of the *MUN Explorer* are identical, with a NACA 0024 section and have a geometric aspect ratio (AR) of one. The characteristic curves for the NACA 0024 section, to the best of the author's knowledge, were not available from any of the existing literature in the public domain. On the other hand, extensive experimental data was available for the closely related family of NACA 0025 section.

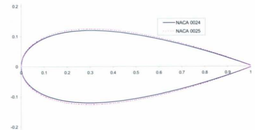

Fig. 5.7 Comparison of NACA 0024 and 0025 profiles

The section profiles of NACA 0024 and 0025 airfoils, generated using the *NACA 4 Digits Series Profile Generator*[2], are compared in Figure 5.7. Since there appears only a minor difference in thickness (~ 1%) between the section profiles of both airfoils, it is assumed that their section characteristics are the same. Therefore, for the purpose of calculating hydrodynamic loads on the control planes of the *MUN Explorer*, which use a NACA 0024 section, the section characteristics of the NACA 0025 airfoil were used.

The section characteristics of NACA 0025 airfoil were available from Bullivant (1940) as well as from Sheldahl and Klimas (1981). For instance, the aerodynamic characteristics of a wing of NACA 0025 section are shown in Figure 5.8, which is reproduced from Figure 5 of Bullivant (1940). The wing had an aspect ratio (*AR*) of six and was tested in the wind tunnel at an average Reynolds Number (*Re*) of 3.2×10^6. Both, the Reynolds number, *Re*, and the aspect (*AR*) reported by Bullivant (1940), were well over the operating range and aspect ratio of the *MUN Explorer* control planes. The operating range of the *MUN Explorer* vehicle (Re_v), calculated based on the overall length of the vehicle, and that of its control planes (Re_{cp}), calculated using the chord length as the reference length, are shown in Table 5.1. Both Bullivant (1940) and Mises (1959) report that the influence of *Re* on the airfoil characteristics is comparatively small while the aspect ratio, *AR*, has significant impact on the 3D wing characteristics. This argument is fairly substantiated by the data from Sheldahl and Klimas (1981), shown in figures 5.9 and 5.10, which depict the lift and drag characteristics, respectively of a wing of infinite aspect ratio (2D)

[2] http://www.ppart.de/aerodynamics/profiles/NACA4.html#

having NACA 0025 section at eight different Reynolds numbers, ranging from 40,000 through 5,000,000, for angles of attack up to 180°.

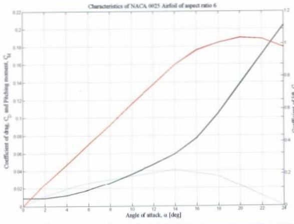

Fig. 5.8 Characteristic curves of NACA 0025 airfoil of AR = 6, reproduced from Bullivant (1940)

Table 5.1 **Operating Reynolds number range of the *MUN Explorer* AUV and its control planes**

V	Re_v	Re_{cp}
1.0	3.3 x 10⁶	266,667
1.5	5.0 x 10⁶	400,000
2.0	6.7 x 10⁶	533,333
2.5	8.3 x 10⁶	666,667

It is evident from the figures that the lift and drag coefficients vary slightly with Reynolds number in the range of angle of attack between 0° to 27° but beyond that the Reynolds number has no influence over the coefficients. If we consider the operating range of the *MUN Explorer* control planes, this difference is apparent only in the range between 10° and 27°. Since we desire a hydrodynamic model that is capable of simulating the full 360° range of angles, it was decided to use the Sheldahl and Klimas (1981) data while the Bullivant (1940) data would provide a complementary source to check the accuracy.

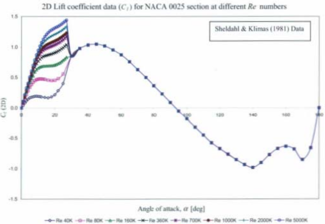

Fig. 5.9 Variation of 2D lift coefficient, C_l with respect to angle of attack (α) for different Reynolds numbers

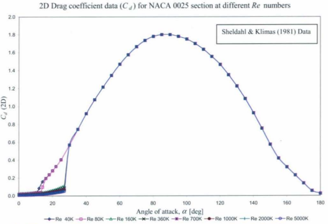

Fig. 5.10 Variation of 2D drag coefficient, C_d with respect to angle of attack (α) for different Reynolds numbers

In order to use the lift and drag data from either of the above two sources with the *MUN Explorer* control planes, it becomes necessary to reduce the data to that corresponding to a 3D wing having the same effective aspect ratio as the *MUN Explorer* control planes. The *effective aspect ratio*, a_e, of the control plane is different from its geometrical aspect ratio and is defined as:

$$a_e = \frac{b_{CP}^2}{A_{CP}}$$

where b_{CP}, is the span (measured as twice the distance from the root to the tip of control plane) and A_{CP}, is the plan-form area of a set of control planes; without including the area inside the hull. Thus, the effective aspect ratio of the *MUN Explorer* control planes, using the above relation, works out to a value of 2.

Reduction of C_L data

The lift curve for the NACA 0025 wing of aspect ratio 6, from Bullivant (1940), can be reduced to that for a wing of aspect ratio 2 using the methods in McCormick (1995).

$$C_{L\alpha} = C_{l\alpha} \frac{AR}{AR + 2\left(\frac{AR+4}{AR+2}\right)} \tag{5.16}$$

$$C_{L\alpha} = C_{l\alpha} \frac{AR}{2 + \sqrt{4 + AR^2}} \tag{5.17}$$

Equations (5.16) or (5.17), developed based on the lifting surface model, provide a more accurate estimate of $C_{L\alpha}$ for wings of low aspect ratio (McCormick, 1995), where $C_{L\alpha}$ is the slope of the lift-curve for the wing or 3D airfoil and $C_{l\alpha}$ is the 2D lift-curve slope.

Provided the lift coefficient, C_L, for a wing of one aspect ratio is known, the lift coefficient for a wing of different aspect ratio, having the same section profile, can be deduced by a simple algebraic operation on Eq. (5.16). The equations (5.18) and (5.19) show the lift coefficient, C_L, for a wing of aspect ratio two, derived by manipulating equations (5.16) and (5.17) respectively.

$$C_{L\alpha(AR=6)} = C_{l\alpha} \frac{6}{6 + 2\left(\frac{6+4}{6+2}\right)} = \frac{12}{17} C_{l\alpha};\ C_{L\alpha(AR=2)} = C_{l\alpha} \frac{2}{2 + 2\left(\frac{2+4}{2+2}\right)} = \frac{2}{5} C_{l\alpha}$$

$$C_{L\alpha(AR=2)} = \frac{17}{30} C_{L\alpha(AR=6)} = 0.567 C_{L\alpha(AR=6)} \tag{5.18}$$

A similar algebraic operation on Eq. (5.17) yields the following result:

$$C_{L\alpha} = C_{l\alpha} \frac{AR}{2 + \sqrt{4 + AR^2}}$$

$$C_{L\alpha(AR=6)} = C_{l\alpha} \frac{6}{2 + \sqrt{4 + 36}} = C_{l\alpha} \frac{3}{1 + \sqrt{10}}; \; C_{L\alpha(AR=2)} = C_{l\alpha} \frac{1}{2 + \sqrt{4 + 4}} = C_{l\alpha} \frac{1}{1 + \sqrt{2}}$$

$$C_{L\alpha(AR=2)} = \frac{1}{3} \left(\frac{1 + \sqrt{10}}{1 + \sqrt{2}} \right) C_{L\alpha(AR=6)} = 0.575 C_{L\alpha(AR=6)} \tag{5.19}$$

The results (5.18) and (5.19) show that the lift coefficients obtained by using equations (5.16) and (5.17) are in very good agreement with each other. Yet another relation that provides a satisfactory correction to lift for change is aspect ratio from AR_1 to AR_2 is provided by Molland & Turnock (2007) and is of the form:

$$\frac{C_{L2}}{C_{L1}} = \frac{(1 + 3/AR_1)}{(1 + 3/AR_2)} \tag{5.20}$$

Equation (5.20) when applied to the current problem provides the relation:

$$C_{L(AR=2)} = \frac{3}{5} C_{L(AR=6)} = 0.6 C_{L(AR=6)} \tag{5.21}$$

Note that the result from Eq. (5.21) is also in good agreement with (5.18) and (5.19).

Equations (5.18), (5.19) and (5.21) indicate that, for a given angle of attack, the lift coefficient of a wing with NACA 0025 section and aspect ratio 2 is about 60 percent (0.6 times) of that of a wing of aspect ratio 6. The effect of aspect ratio is to decrease the slope of the lift curve as the aspect ratio decreases. In other words, low aspect ratio wings require a larger angle of attack than a high aspect ratio wing in order to produce the same lift force. A comparison of lift-curves generated using equations (5.18), (5.19) and (5.21) with the actual Bullivant (1940) data can be seen in Figure 5.11. The numerical value of the slope of the lift curve $\frac{\partial C_L}{\partial \alpha}$, from Bullivant (1940) is 0.062. There is a considerable drop in the slope of the lift curve when the data are reduced from $AR = 6$ to $AR = 2$, as seen in Figure 5.11. The lift curves produced by reducing the data using equations (5.16) and (5.17) have almost the same slope of 0.035 while the relationship given by Eq. (5.20) produced a lift-curve of slope 0.037.

Lift curve reduced from $AR = 6$ to $AR = 2$

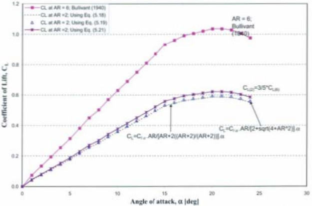

Fig. 5.11 Lift curves for a NACA 0025 wing of aspect ratio 2 deduced from data for a wing of aspect ratio 6 (Bullivant, 1940) using methods from McCormick (1995) and Molland & Turnock (2007)

In order to compare the lift coefficient data from both Bullivant (1940) and from Sheldahl and Klimas (1981), the 2D lift data from the latter source, corresponding to Reynolds numbers 2×10^6 and 5×10^6, were reduced to that for a wing of aspect ratio 6 using equation (5.16). These two data sets were considered to be the closest in Reynolds number range with the 3D wing data from Bullivant (1940), which was tested at an average Reynolds number of 3.2×10^6. The comparison is limited to angles of attack up to 24° because that was the maximum range of data available from Bullivant (1940). Figure 5.12 shows that the experimental data from both sources differed only slightly between each other and hence provides a satisfactory check on the accuracy of the data.

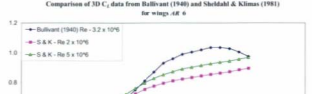

Fig. 5.12 Comparison of 3D lift curves for a NACA 0025 wing of aspect ratio 6 from Bullivant (1940) and that obtained by converting the Sheldahl and Klimas (1981) 2D data to a wing of *AR* 6

Since the operating range of the *MUN Explorer* control planes, shown in Table 5.1, falls within the range of *Re* between 360,000 and 700,000 of Sheldahl and Klimas (1981), it was decided to choose the lift coefficient data corresponding to *Re* 700,000 for use with the *MUN Explorer* control planes. Some characteristics of low aspect ratio planes, typical of AUVs, are that the slope of their lift curves are much reduced from the 2-D cases and that they have a relatively high stall angle of attack [20° to 25°], as reported in studies such as Jones (1952). Figure 5.13 shows the 3D lift coefficient data for a wing of aspect ratio 2 over the range from -180° to +180°. Note that the equation (5.16) used to reduce the 2D lift data to 3D lift data is applicable only to the linear range of the lift curve [McCormick, 1995]. However, here it is assumed to be applicable to the entire range as well.

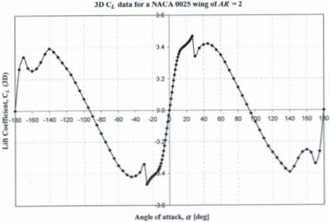

Fig. 5.13 3D lift coefficient, C_L, for a wing of aspect ratio 2 with NACA 0025 section for full 360° range of angles of attack

Reduction of C_D data

The drag coefficient, C_D, of a wing of one aspect ratio may be predicted with considerable accuracy from data obtained from tests on a wing of widely different aspect ratio using the following relations given in Abbott & Doenhoff (1959):

$$C_{D(3D,\alpha')} = C_{D(2D,\alpha)} + \frac{C^2_{L(2D,\alpha)}}{\pi e AR} \tag{5.22}$$

where

$$\alpha' = \alpha_{(2D)} + \frac{C_{L(2D,\alpha_{(2D)})}}{\pi AR} \tag{5.23}$$

is the effective angle of attack at which the flow approaches the 3D wing.

The first term on the right hand side of Eq. (5.22) is often called the coefficient of *parasite drag* or *profile drag*, as it depends on the shape of the profile while the second term in the equation is known as the *induced drag*, which occurs as a result of lift generation and is more pronounced in airfoils of finite aspect ratio. On an airfoil of finite span, the pressure difference between the upper and lower surfaces of the airfoil causes the air to flow from the root of the lower surface, around the tip, towards the root of upper surface. This spanwise flow in combination with the chordwise flow produces a twist to the flow resulting in the generation of vortices along the trailing edge of the airfoil. The resultant velocity thus produced is no longer parallel to the undisturbed stream but has a small downward component; the effect of which is to lower the angle of incidence, α. This induced angled of attack reduces the effectiveness of airfoils to generate lift thus requiring a higher angle of attack, α'. This means that an airfoil with small aspect ratio produces more induced drag than an airfoil with high aspect ratio because the size of vortices will be much reduced in an airfoil of longer span. In other words, induced drag is inversely proportional to aspect ratio.

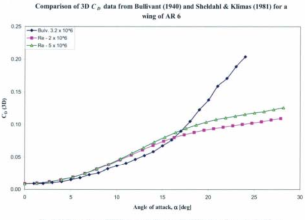

Fig. 5.14 Comparison of 3D drag curves for a NACA 0025 wing of aspect ratio 6 from (Bullivant, 1940) and Sheldahl and Klimas (1981) 2D data converted to *AR* 6

The 3D drag data derived for a wing of aspect ratio six from Sheldahl and Klimas (1981) for Reynolds numbers 2 x 10^6 and 5 x 10^6 were compared with that from Bullivant (1940) measured at a Reynolds number of 3.2 x 10^6. This comparison is shown in Figure 5.14. The plot shows reasonably good agreement up to an angle of attack around 15° before the curves deviate from each other. In the equation (5.22) used to calculate the drag, the Oswald's efficiency factor, *e*, was assumed to be 0.9. The Oswald's efficiency factor is a correction factor that represents the change in drag with lift of a wing when compared to an ideal wing of same aspect ratio and with an elliptic lift distribution.

Figure 5.15 shows the 3D drag coefficient data, C_D, for the control planes of the *MUN Explorer* over the range from -180° to $+180^{\circ}$.

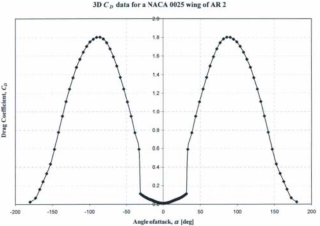

Fig. 5.15 3D drag coefficient, C_D, for a wing of aspect ratio 2 with NACA 0025 section for full 360° range of angles of attack

The lift and drag characteristics of a NACA 0025 wing of aspect ratio 2, shown in Figures 5.13 and 5.15 respectively, were used in the simulation for estimating the hydrodynamic loads on the control planes of the *MUN Explorer* AUV.

The lift and drag forces on the control planes act through the centre of pressure, which was assumed to lie on the quarter chord point, $c/4$.

Summary of Assumptions:

In developing the theory behind the dynamics and hydrodynamics of the *MUN Explorer* control planes, certain assumptions were made. They are summarized as follows:

(i) Only the chord-wise flow was considered for the estimation of hydrodynamic forces on the control planes.

(ii) The interaction between the hull and the control planes was not considered for this study.

(iii) The section characteristics of a NACA 0024 wing were assumed to be the same as that for a NACA 0025 wing.

(iv) The equations (5.16) and (5.22) used to reduce the 2D lift and drag data to 3D data is applicable only in the linear range. However, it was assumed to be applicable for the nonlinear range as well.

These assumptions, of course, are expected to bring some errors in the simulation results.

5.3 Vehicle Specific Parameters: Geometric and Inertial

As mentioned earlier, the vehicle specific parameters such as geometric and inertial properties are all compiled in a MATLAB script file. This file is run at first and only once to initialize the simulation model and load these parameters into the MATLAB workspace. The geometric parameters consist of information pertaining to the vehicle components such as hull, appendages, their shape, size, and location with respect each other etc. A short list of some of the vehicle external geometric parameters and the parameters necessary for the Munk, Allen and Perkins, Hopkins and Jorgensen's formulation for estimating the lift, drag and moment coefficients are shown in Table 5.2. A detailed calculation of these parameters is presented in *Appendix – B*.

Table 5.2

Geometric Parameters of the *MUN Explorer* AUV			
Notation	**Descriptions**	**Value**	**Units**
	Hull		
Ln	Length of semi-ellipsoidal nose	0.69	m
Lp	Length of the parallel mid-body section	2.46	m
Lt	Length of the tail section (faired tail + tail cone)	1.28	m
L	Overal length of the hull	4.43	m
D	Maximum diameter of the hull	0.69	m
A_{csa}	Maximum cross-sectional area of the hull	0.374	m^2
A_{wsa}	Wetted surface area of the hull	8.764	m^2
V_B	Volume of the hull	1.367	m^3
	Hull Parameters for Munk, Allen, Hopkins & Jorgensen's Formulation		
A_p	Plan-form area of the hull	2.698	m^2
x_c	Distance to the centroid of the plan-form area, A_p, from nose tip	2.113	m
x_1	Longitudinal distance from nose to the point where the rate of change of cross-sectional area, dS/dx has the maximum negative value	3.95	m
x_0	Distance to the station on the hull up till which potential flow is valid ($x_0 = 0.378L + 0.527x_1$)	3.783	m
r_{x0}	Radius of the hull at station, x_0	0.228	m
S_{x0}	Cross-sectional area of the hull at station, x_0	0.164	m^2
	Control Planes (NACA 0024)		
b	Half-span of the control plane	0.356	m
c	Chord length of the control plane	0.356	m
t	Maximum chord thickness	0.085	m
A_{cp}	Plan-form area of the control plane	0.126	m^2
AR	Geometric aspect ratio	1	
a_e	Effective aspect ratio, b^2/A_{cp}	2	

Mass and Inertia Properties

The inertial parameters of the vehicle consist of mass and mass distribution properties such as the moments and products of inertia. The simulation model developed here assumes the vehicle to be a rigid body and therefore these parameters are taken to be constants. The *MUN Explorer* is a free-flooding vehicle and part of the mass and inertial properties include the effect of flood-water. The flood-water inside the vehicle actually travels with the vehicle (except in dynamic roll) and is therefore included with the vehicle component masses to give a 'wet' mass. This flood-water also affects the buoyancy, centre of mass, centre of buoyancy and hydrodynamic response of the vehicle. While submerged, these effects are normally static and not time-varying. The term centre of gravity here refers to the C.G of the 'wet' mass. A short list of some of

Table 5.3

Mass and Inertia Properties of the *MUN Explorer* AUV		
Dry mass of the vehicle	630.6	kg
Wet mass of the vehicle	1432.7	kg
Total displacement	1446.3	kg
Net displacement	13.6	kg
Centre of gravity, C.G of the vehicle from nose-tip	2.083	m
Centre of buoyancy, C.B of the vehicle from nose-tip	2.086	m
Longitudinal separation between C.G and C.B (C.G ahead of C.B)	-0.003	m
Vertical separation between C.G and C.B (C.G below C.B)	0.017	m
Static pitch angle	-10.7	deg
Moment of Inertia about the body x- axis, I_{xx}	86.08	kg.m^2
Moment of Inertia about the body y- axis, I_{yy}	1881.71	kg.m^2
Moment of Inertia about the body z- axis, I_{zz}	1877.19	kg.m^2
Product of Inertia, $I_{xy} = I_{yx}$	0.98	kg.m^2
Product of Inertia, $I_{yz} = I_{zy}$	0.29	kg.m^2
Product of Inertia, $I_{zx} = I_{xz}$	3.09	kg.m^2

these parameters is presented in Table 5.3 while details of their calculations can be found in *Appendix - C*.

The values shown in the Table 5.3 were calculated (not measured by experiments) from information provided by the manufacturer in a *Weight-Ballast* file for the very configuration of the vehicle used for the test. The calculations show that the vehicle has an inherent nose-down attitude of about -10°. This happens as a result of the longitudinal separation between the centre of gravity (CG) and the centre of buoyancy (CB), which is about 3 mm (CG forward of CB), in combination with the vertical separation of about 17 mm (CG below CB). It is because of this inherent nose-down attitude that experiments conducted at slow speeds (~ 1 m/s), reported in Chapter 4, had seen pitch angles of about -6° during the run. It was explained that this nose-down attitude was deliberately retained as a fail-safe mechanism to make the telemetry system, mounted on top of the mast at the tail portion of the vehicle, project out of the water when it becomes necessary to communicate with the vehicle while it is at the surface with the mast retracted.

The distribution of mass defines the moments and products of inertia and they were calculated with respect to the body-fixed reference frame, which moves along with the vehicle. This allows us to treat the inertial properties as constant over time. The moments and products of inertia in tensor form, **I**, can be represented as follows:

$$I = \begin{bmatrix} I_{xx} & -I_{xy} & -I_{xz} \\ -I_{xy} & I_{yy} & -I_{yz} \\ -I_{xz} & -I_{yz} & I_{zz} \end{bmatrix} \qquad (5.24)$$

$$= \begin{bmatrix} 86.08 & -0.98 & -3.09 \\ -0.98 & 1881.71 & -0.29 \\ -3.09 & -0.29 & 1877.19 \end{bmatrix}$$

The units of the above matrix are:

$$\text{Units: } \begin{bmatrix} \text{kg.m}^2 & \text{kg.m}^2 & \text{kg.m}^2 \\ \text{kg.m}^2 & \text{kg.m}^2 & \text{kg.m}^2 \\ \text{kg.m}^2 & \text{kg.m}^2 & \text{kg.m}^2 \end{bmatrix}$$

Added Mass of the *MUN Explorer* AUV

In addition to the above parameters, an additional set of parameters called the added mass is essential for the accurate calculation of vehicle accelerations. Added mass is concerned with movement of water external to the hull and it is the hull geometry alone that affects the external flow and is the generator of added mass effects. A detailed study on the sensitivity of added mass to changes in vehicle geometry can be found in Perrault (2002). The added mass must account for accelerations in all the six DOF that result from each of the forces and moments. Therefore, the general form of added mass matrix has 36 elements. However, for any body, there are really only 21 unique elements in the added mass matrix, because of its symmetry about the diagonal [Imlay, 1961].

The added mass terms for the *MUN Explorer* vehicle were estimated numerically by means of an offline program called the ESAM (Estimation of Submarine Added Mass), developed at the Defence Research Establishment Atlantic (DREA) in Dartmouth, Nova Scotia, Canada [Watt, 1988]. The ESAM program calculates all the added mass terms of a deeply submerged multi-component submarine-like rigid body, analytically. ESAM calculates the added mass by approximating the body as a finned prolate spheroid where the vehicle components are replaced by equivalent ellipsoids of same fineness ratio and displaced volumes. The program accounts for the interaction between the hull and appendages while the interactions between appendages are neglected.

$$\mathbf{M}_A = \begin{bmatrix} X_{\dot{u}} & X_{\dot{v}} & X_{\dot{w}} & X_{\dot{p}} & X_{\dot{q}} & X_{\dot{r}} \\ Y_{\dot{u}} & Y_{\dot{v}} & Y_{\dot{w}} & Y_{\dot{p}} & Y_{\dot{q}} & Y_{\dot{r}} \\ Z_{\dot{u}} & Z_{\dot{v}} & Z_{\dot{w}} & Z_{\dot{p}} & Z_{\dot{q}} & Z_{\dot{r}} \\ K_{\dot{u}} & K_{\dot{v}} & K_{\dot{w}} & K_{\dot{p}} & K_{\dot{q}} & K_{\dot{r}} \\ M_{\dot{u}} & M_{\dot{v}} & M_{\dot{w}} & M_{\dot{p}} & M_{\dot{q}} & M_{\dot{r}} \\ N_{\dot{u}} & N_{\dot{v}} & N_{\dot{w}} & N_{\dot{p}} & N_{\dot{q}} & N_{\dot{r}} \end{bmatrix}$$

Added mass matrix for the *MUN Explorer* with 'X' tail configuration

$$= \begin{bmatrix} -15.6 & 0.0 & 0.1 & 0.0 & 0.5 & 0.0 \\ 0.0 & -408.2 & 0.0 & -8.2 & 0.0 & 102.1 \\ 0.1 & 0.0 & -468.2 & 0.0 & -66.8 & 0.0 \\ 0.0 & -8.2 & 0.0 & -43.9 & 0.0 & 3.7 \\ 0.5 & 0.0 & -66.8 & 0.0 & -555.7 & 0.0 \\ 0.0 & 102.1 & 0.0 & 3.7 & 0.0 & -549.8 \end{bmatrix}$$

In addition, added-mass matrix for a hypothetical case of the *MUN Explorer* with "+" tail configuration was also estimated using ESAM. This matrix was used with the second hydrodynamic model developed for the *MUN Explorer*.

Added mass matrix for the *MUN Explorer* with '+' tail configuration

$$= \begin{bmatrix} -15.2 & 0.0 & 0.1 & 0.0 & 0.3 & 0.0 \\ 0.0 & -403.9 & 0.0 & -6.8 & 0.0 & 95.6 \\ 0.1 & 0.0 & -467.3 & 0.0 & -65.4 & 0.0 \\ 0.0 & -6.8 & 0.0 & -43.5 & 0.0 & 1.5 \\ 0.3 & 0.0 & -65.4 & 0.0 & -553.6 & 0.0 \\ 0.0 & 95.6 & 0.0 & 1.5 & 0.0 & -539.9 \end{bmatrix}$$

Note that the second model is obtained by merely rotating the tail planes in 'X' configuration by 45°. This is not expected to produce any change in the mass distribution or moment of inertia of the vehicle but only the added-mass of the vehicle. A comparison of two matrices shows that the differences in the added-mass coefficient values are small. This would be a good justification to use the 2nd model of the *MUN Explorer* with '+' tails for simulating manoeuvres performed by the vehicle with 'X' tail. Consequently, such a study would also give some insights into the possibility of mapping complex 'X' tail actions to simple '+' tail actions.

The units of the elements within the above matrix are as follows:

$$\text{Units:} \quad \begin{bmatrix} \text{kg} & \text{kg} & \text{kg} & \text{kg.m} & \text{kg.m} & \text{kg.m} \\ \text{kg} & \text{kg} & \text{kg} & \text{kg.m} & \text{kg.m} & \text{kg.m} \\ \text{kg} & \text{kg} & \text{kg} & \text{kg.m} & \text{kg.m} & \text{kg.m} \\ \text{kg.m} & \text{kg.m} & \text{kg.m} & \text{kg.m}^2 & \text{kg.m}^2 & \text{kg.m}^2 \\ \text{kg.m} & \text{kg.m} & \text{kg.m} & \text{kg.m}^2 & \text{kg.m}^2 & \text{kg.m}^2 \\ \text{kg.m} & \text{kg.m} & \text{kg.m} & \text{kg.m}^2 & \text{kg.m}^2 & \text{kg.m}^2 \end{bmatrix}$$

The elements of the added mass matrix can be considered constant for a deeply submerged vehicle, such as an AUV. However, they may have frequency dependencies near the free surface or a boundary. In this study a deeply submerged vehicle is assumed.

5.4 Propulsion System

The rear thruster for the existing simulation, described in Chapter 2, was modelled simply as a force exerted along the longitudinal axis of the vehicle. Evans (2003) simulated it as a propulsor with constant power output. In order to model the propeller thrust from the *MUN Explorer* AUV, the thrust versus forward speed relationship shown in *Figure 4.12* of Chapter 4 was used. This relationship was theoretically established (see *Section 4.2.1.3* of Chapter 4) from the propeller rpm versus forward speed data obtained from the straight-line tests conducted using the *MUN Explorer* AUV. This information will be used in the simulation as a look-up table to model the propeller thrust of the vehicle.

The relationship between propeller torque and forward speed was also theoretically established in the same section of Chapter 4, but they were not used for modeling the propulsion system. This is because, during the experiments, it was found that any roll motion induced by external moments or the propeller torques was actively compensated by the vehicle controller using the tail control planes. Since the simulation model at its present state cannot perform adaptive control of the vehicle, introducing this torque information may induce unwanted roll motions in the simulation, which would carry the results further away from the measured data.

5.5 Conclusions

This chapter was aimed at discussing the modifications that were necessary to make the existing simulation model adapt to the *MUN Explorer* AUV. This simulation, developed in MATLAB/Simulink environment, was a modular, nonlinear model. The modular structure of the simulation model ensured that changes were made only to the vehicle-specific parameters module while leaving the remaining modules relatively unchanged. Apart from the vehicle-specific parameters, the major changes that were necessarily incorporated into the *MUN Explorer* simulation were the dynamics of 'X'-tail control planes and the hydrodynamic characteristics of NACA 0024 airfoil sections as discussed in this chapter. In addition, a secondary model of the *MUN Explorer* AUV with an assumed '+' tail configuration was also developed. This second model was developed to conduct a comparative study of the two different tail plane configurations: 'X' tail and '+' tail, in manoeuvring the vehicle. The discussions in this chapter also demonstrate the ease with which a simulation model based on component build-up method can be reconfigured to make it adaptable to another vehicle.

Chapter 6

Model Validation Using *MUN Explorer* Manoeuvring Trials

The major focus of this chapter is to evaluate the performance of the hydrodynamic model developed for the *MUN Explorer* AUV in simulating full-scale manoeuvres. The underlying physics of this hydrodynamic model based on the *component build-up* method, which was originally developed for streamlined axisymmetric underwater vehicles by Nahon (1996), Perrault (2002) and Evans (2003), was described through Chapter 2 and the modifications made thereof to adapt it to the *Explorer* AUV were discussed in Chapter 5. In order to validate the model, the numerical simulations have to be evaluated against the results from sea trials. To achieve this goal, a select number of manoeuvres performed using the *MUN Explorer* AUV, described through Chapter 4, were simulated using the hydrodynamic model.

Out of the whole series of sea trials that were performed, which consisted of straight-line tests, turning circles, zigzags in horizontal and vertical planes, helix, etc., only a small subset of the total number of tests were selected for the purpose of simulation and these are presented in this chapter. The type of manoeuvres chosen for simulation and the comparison of results with the experimental results are described through the following sections. The efficiency and accuracy of the model prediction is assessed by comparing the virtual and real vehicle responses/trajectories as well as by evaluating the error in predicting certain parameters of interest such as the turning radius, turning rates, pitch angles etc.

6.1 Numerical Simulations vs. Sea Trials

In all numerical simulations, the control inputs to the hydrodynamic model were the *forward speed* and *control plane deflections* measured from the experiments at sea. It should be remembered that this procedure is slightly different from the way in which the corresponding experiments were performed at sea. During the sea trials, as reported in Chapter 4, due to lack of direct control over the control planes, the input variables to the *Explorer* vehicle were *forward speed* and *radius of turn* – in the case of turning circles, while *forward speed* and *waypoint follow* were the control inputs to zigzags in the horizontal and vertical planes. All sea trials were performed by commanding the vehicle to operate in *constant speed* mode because it was known that one of the inputs to the hydrodynamic model was the forward speed. However, this choice was made at sea without recognizing that the *constant speed* mode would compensate for any speed variation that occurs during turns and dives due to changes in drag or due to some environmental disturbances such as currents.

In Chapter 4, in order to conveniently represent the control plane deflections for describing the experimental results, a set of expressions which calculated effective single control plane deflection was defined - δY, δP, δR etc. These were called the effective control plane deflection angles, which represented the combined effect of all the tail control planes deflection. The values δY, δP and δR were the effective control plane deflection in producing a yaw, pitch or roll response respectively. Similarly, the combined effect of dive planes in producing pitch and roll was represented by values denoted by δP_D and δR_D, respectively. To see if these representations had any physical meaning or practical use in mapping the complex control plane deflections of an 'X' tail configuration to a '+' tail configuration, the simulations presented here in this Chapter were performed using the second model of the *MUN Explorer* AUV. This model had a '+' tail configuration and used the effective control plane deflection values as its inputs instead of the actual individual control plane deflections recorded during experiments. The actual individual control plane deflections will be used later with the primary model of *MUN Explorer* for a more accurate simulation and is therefore not presented in this chapter at present.

The simulation model was executed as follows. In order to simulate a turn, the effective control plane deflection value of δY is applied to the set of vertical control planes or rudders in the '+' tail model. Similarly, to simulate a dive using stern planes, the effective control plane deflection value of δP should be applied to the set of horizontal stern planes in the '+' model. In manoeuvres, where both δY and δP had significant values, they were applied in combination for the corresponding simulation. The effective plane deflection

δP_D is applied to the dive planes while the effective plane deflections δR and δR_D were never used since these values were negligible in almost all the tests (see Table 4.1 on page 111). Note that, this procedure assumes a vehicle with '+' tail configuration utilizing the effective control plane deflection angles as its control inputs, calculated from the measured deflections of 'X' tail configuration. Some discrepancies in the results are expected because the flow approaching the 'X' tail is different from that approaching a '+' tail, as discussed in Chapter 5. Nevertheless, this will help understand if a direct mapping between deflections of 'X' tail configuration and deflections of '+' tail configuration is possible.

6.1.1 Straight-line Simulations

The straight-line tests were the simplest of all the tests and in an ideal case the only control input required is the forward speed. However, from actual test data, it was found that the vehicle had a nose-down attitude at certain speeds while it was level at certain other speeds. This resulted in the vehicle using its control planes during the straight line tests. Therefore, in the sample straight-line simulations that were performed, the values of δP and δP_D were used. The model was run at four different speeds (1.0, 1.5, 2.0 and 2.5 m/s) corresponding to the *acceleration phase* of the actual Test #1.

TABLE 6.1

Straight-line simulations at constant speeds simulated using the '+' tail model of *MUN Explorer*

V	δP_D	δP	δ_1	δ_2	δ_3	δ_4	δ_5	δ_6	**Pitch angle (θ)**	
m/s	deg	deg	deg	deg	deg	deg	deg	deg	measured	simulated
1.0	**7.3**	**7.4**	-7.4	7.3	7.4	9.1	-7.1	-5.9	-6.2	-
1.5	**1.5**	**3.5**	-1.5	1.5	2.5	3.8	-4.3	-3.3	-1.7	-1.5
2.0	**-1.7**	**2.0**	1.6	-1.8	1.1	2.3	-2.8	-1.7	0.0	-3.2
2.5	**-0.8**	**0.8**	0.6	-1.1	-0.2	1.2	-1.5	-0.9	0.0	-9.1

Note that the propulsion module for the simulator, in its present state, functions as a source of constant power output along the longitudinal direction of the vehicle. Therefore, it was not possible to simulate any change in speed (acceleration or deceleration) at present. Instead, the constant speed straight-ahead motion was simulated and the steady-state pitch attitude of the vehicle at different speeds was compared with the corresponding values from the experiments. Table 6.1 shows the list of control inputs and the measured and simulated outputs.

The values shown in bold in the first three columns of Table 6.1 represent the inputs to the simulator. Here, the effective dive plane deflection, δP_D, and the effective tail planes deflection in producing pitch, δP, were the inputs along with the forward speed. The values of δP_D and δP were calculated from the mean values of the individual control plane deflections δ_1, δ_2, ..., δ_6, measured from the sea trials, using expressions (4.1) through (4.4).

At a forward speed of 1.0 m/s, the vehicle behaviour was erratic with the pitch angle fluctuating between 0^o and -25^o from the initial set value of -10.7^o. This initial pitch value of -10.7^o originate from the longitudinal separation between centre of gravity (CG) and centre of buoyancy (CB) of the vehicle and the net buoyancy of 13.6 kg acting aft of the CG, as calculated and presented in Table 5.3.

At a forward speed of 1.5 m/s, the vehicle maintained a steady pitch angle of -1.5^o, which was very close to the measured value of -1.7^o. However, with time, the vehicle gained depth slightly at a rate of 0.12 m/s.

At a forward speed of 2.0 m/s, the vehicle achieved a steady pitch angle of -3.2° but gained depth at a slower rate of 0.08 m/s. However, when the forward speed was 2.5 m/s the vehicle achieved a steady pitch angle of -9.1° and was seen to dive at a rate of 0.36 m/s. In the actual test, for both speeds 2 and 2.5 m/s, the vehicle maintained a constant depth at near zero pitch angle.

Note that, there is no speed controller or attitude controller built into the simulation model as yet. On the other hand, during the actual test at sea, the vehicle controller continuously adjusted any change in attitude or change in course by adjusting the control plane deflections. This often resulted in fluctuations in control plane deflection about a certain mean value when the vehicle was in a steady state of motion. For instance, in *Section 4.3* of Chapter 4, which describes turning circles, all circles had perfectly smooth trajectories (see Fig. 4.17, 4.18 etc.) but this was produced by plane deflections that were not so smooth (see Fig. 4.27). The measured values indicated by δ_1, δ_2, δ_3, ..., δ_6 in Table 6.1 are averaged value of individual control plane deflection over a period of steady motion. Therefore, using mean values is expected to produce some error particularly when the vehicle has an inherent nose-down attitude of –10.7°.

6.1.2 Turning Circle Simulations

A set of turning manoeuvres were also simulated using the same '+' tail model. The effective control plane deflections δY, δP and δP_D along with the *forward speed* formed the control inputs to the model. Table 6.2 shows the outcome from the turning circle simulations performed at speeds 1 m/s and 1.5 m/s.

TABLE 6.2

Turning circles simulated using the '+' tail model of *MUN Explorer*

V	Rc	δY	δP	δP_D	Ra	Rsim	err.	Drift, β [deg]		Yaw rate, r [deg/s]		Pitch, θ [deg]	
[m/s]	m	deg	deg	deg	m	m	%	mes.	sim.	mes.	sim.	mes.	sim.
1.0	10	**5.2**	**6.2**	**4.2**	22.5	24.9	10.7	6.5	6.8	2.6	1.9	-4.8	-13.0
1.0	12	**5.3**	**6.2**	**4.8**	23.8	24.4	2.5	5.8	6.9	2.4	2.0	-5.0	-12.5
1.0	14	**5.0**	**6.3**	**5.3**	25.0	26.4	5.6	5.3	6.5	2.3	1.8	-5.1	-12.7
1.0	16	**4.7**	**6.3**	**5.1**	26.6	27.7	4.1	5.2	6.2	2.2	1.8	-5.1	-12.7
1.0	18	**4.5**	**6.4**	**5.4**	28.0	28.9	3.2	4.9	6.0	2.1	1.7	-5.1	-13.4
1.0	20	**4.2**	**6.4**	**5.0**	29.7	31.0	4.4	5.2	5.5	2.0	1.6	-5.2	-12.7
1.0	25	**3.5**	**6.6**	**5.5**	33.4	35.9	7.5	4.0	4.7	1.7	1.3	-5.4	-13.3
1.0	30	**3.3**	**6.6**	**5.8**	37.5	37.9	1.1	3.8	4.4	1.5	1.2	-5.4	-15.3
1.5	10	**5.9**	**3.5**	**0.4**	22.8	23.9	4.8	6.4	8.2	3.7	3.6	-1.8	-0.2
1.5	12	**5.9**	**3.3**	**-0.6**	24.2	23.8	1.7	5.6	8.2	3.5	3.5	-1.6	-1.9
1.5	14	**7.7**	**3.5**	**1.3**	20.8	17.1	17.8	2.4	10.7	4.2	5.0	-1.8	0.3
1.5	16	**6.9**	**3.5**	**1.6**	21.5	19.6	8.8	2.3	9.5	3.9	4.3	-1.9	1.0
1.5	18	**6.2**	**3.6**	**1.9**	23.7	22.3	5.9	2.2	8.6	3.7	3.8	-1.9	1.2
1.5	20	**5.8**	**3.6**	**1.7**	24.7	24.1	2.4	2.0	8.1	3.5	3.6	-1.9	1.7
1.5	25	**4.8**	**3.6**	**1.7**	28.8	29.7	3.1	1.7	6.7	3.0	2.9	-1.9	1.6
1.5	30	**4.1**	**3.6**	**1.5**	33.3	35.2	5.7	1.5	5.8	2.6	2.5	-1.8	1.9

Table 6.2 shows the comparison of steady-state parameters such as turning radius, drift angle, turning rate and pitch angle, estimated from the simulation, with measured values from the steady-state phase of the experiments. Only the steady-state phase of the turning circles was simulated because it was found from the analysis of turning experiments data that in several cases the vehicle actually started the transient phase even before it reached the commanded depth. Therefore the approach or transient phase of the manoeuvre was not considered.

Figures 6.1 and 6.2 shows turning circles simulated at speeds 1.0 m/s and 1.5 m/s. These correspond to turns performed at sea for the commanded radius Rc-12 at 1.0 and 1.5 m/s. These two examples were the same two tests (out of the four) chosen for the purpose of illustration in Chapter 4. The attitudes of the vehicle from these two simulations are also shown in Figure 6.3 and Figure 6.4

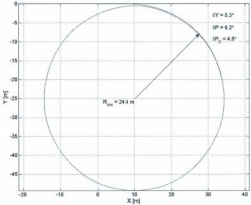

Fig. 6.1 Turning manoeuvre the starboard simulated at 1.0 m/s for the case of Rc-12

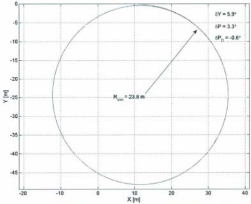

Fig. 6.2 Turning manoeuvre to the starboard simulated at 1.5 m/s for the case of Rc-12

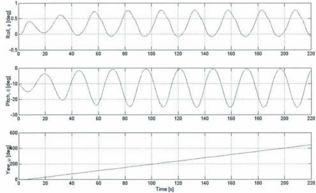

Fig. 6.3 Roll, pitch and yaw attitude of the vehicle at 1.0 m/s for the case of Rc-12, turning to starboard

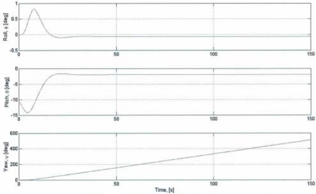

Fig. 6.4 Roll, pitch and yaw attitude of the vehicle at 1.5 m/s for the case of Rc-12, turning to starboard

In the simulation of test Rc-12 at 1 m/s, although the radius of turn obtained is close to the measured radius (2.5% error), the pitch angle of the vehicle oscillated between 0 and -25° from an initial value of –10.7°, as shown in Figure 6.3. On the other hand, from the simulation of the same test Rc-12 at 1.5 m/s, the vehicle attained a steady-state pitch angle of -1.9° which was very close to the measure pitch angle of -1.6° during the steady turning phase. This is seen from Figure 6.4.

All the turning circle experiments performed at speeds 1.0 m/s and 1.5 m/s have been simulated. From Table 6.2, the error associated with predicting the radius of turn for the most cases is found to be less than 10%. The turning rate, r, is also found to be predicted fairly well. The pitch angle of the vehicle appears to be oscillating for slow speed. The initial conditions of inherent nose-down attitude (-10.7°) produced by the separation of CG and CB, combined with the net buoyancy of 13.6 kg, when coupled with the inability of control planes to generate sufficient lift forces during the slow speed manoeuvres is what triggers the oscillatory motion observed. At higher speeds the vehicle has a steady pitch angle comparable to the measured values.

All turning circle experiments reported in Chapter 4 were performed to the starboard side. Although, attempts were made during the sea trials to do a turn to the port side for the case of Rc-18, this turned out unsuccessful. Therefore, a turning simulation to the port side was performed for the case of Rc-12 using the above same model. The trajectory and attitude of the vehicle are shown is Figure 6.5 and Figure 6.6 respectively. The control inputs for this case was the same as that used for the case shown in Figure 6.2, except that the effective control plane deflection δY has a negative value.

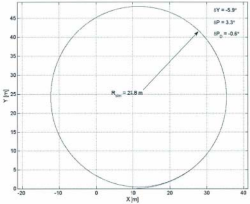

Fig. 6.5 A turning manoeuvre to the port side simulated at 1.5 m/s for the case of Rc-12

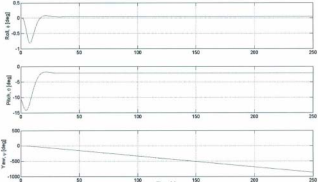

Fig. 6.6 Roll, pitch and yaw attitude of the vehicle at 1.5 m/s during port turn for the case of Rc-12

The results from turning simulation to the port side, which produced results exactly similar to the case in Figure 6.2, indicates the good symmetry of the vehicle simulation model.

6.2 Conclusions

As a preliminary step to evaluating the performance of the hydrodynamic motion simulation model, a set of steady state manoeuvres was simulated at different speeds. Along with forward speed, the simulation used the effective control plane deflections as their control inputs instead of the actual individual control plane deflections. This procedure assumed a vehicle the same as the *MUN Explorer* but with '+' tail configuration utilizing the effective control plane deflection angles calculated from the 'X' tail configuration as its control inputs.

Only simulations from straight-lines and turning circles were presented in this Chapter. The results from the turning simulations show that the error associated with predicting the turning radius for the most part was less than 10%. Other steady state motion parameters such as yaw rate were predicted with reasonably good accuracy. At slow speeds, the vehicle attitude such as pitch angle was found to be oscillating during steady phase of the turn. It appears that the damping forces generated during slow speeds are not sufficient to damp the pitch motions of the vehicle while higher speeds produced large damping forces sufficient enough to damp the pitch motions. This may explain the reason for the observed steady pitch angle during high speeds.

This initial set of simulations addressed steady-state manoeuvres in the horizontal plane only. Simulations of the remaining trials are expected to shed more light on the feasibility of using this model to predict the vehicle behaviour and also establish a performance envelope to the model. This can be established only after the rest of the simulations are completed.

Another goal of this set of preliminary simulations was to investigate if there existed a direct mapping between deflections of an 'X' tail configuration and deflections of a '+' tail configuration. If so, to what degree of accuracy can the motions of a vehicle with 'X' tail configuration be predicted using simulation models with '+' tail configuration. The results from the turning simulations indicate that the usage of effective control plane deflections, in place of actual "X" tail deflections, can produce manoeuvres with reasonable-to-good accuracy.

Chapter 7

Conclusions and Recommendations

The research work addressed in this thesis focused on validating the performance of a motion simulation model, developed based on the *component build-up* method, for axisymmetric streamlined underwater vehicles. The primary objective of this study was to identify how well a motion simulation model based on the component build-up method predicts the performance of a streamlined AUV and what could be the performance bounds of such a model. In order to establish a performance envelope, the model has to be tested against all possible operational scenarios that a real AUV would encounter. The lack of a sufficient or comprehensive set of experimental data from much of the AUV community necessitated the need for an extensive set of experimental data from an operational AUV. Consequently, a wide range of full-scale manoeuvring trials have been performed at sea using an *Explorer* class AUV available at Memorial University and the results and observations from data analysis of the same were reported in detail in Chapter 4.

An overriding advantage of using component build-up method is the simplicity with which it can be developed or adapted from one vehicle to another. This is because the hydrodynamic loads acting on the vehicle are determined from analytical and semi-empirical (ASE) relations, which only require the specification of vehicle geometry and therefore the method is computationally rapid and inexpensive. This prompted the research question of how easily a model based on component build-up method can be adapted to other vehicles or even used to reconfigure the same vehicle. Further, it was also of interest to study the possibility of a mapping between the complex control plane actions of one configuration ('X' tails) to that of another simple configuration ('+' tail).

The first step in answering the above stated objectives was to conduct a number of manoeuvring trials that would resemble the real-life operating scenarios of a typical AUV. A large commercial class AUV available at Memorial University was used for this purpose and an extensive set of experiments were performed at sea. Consequently, a major portion of this thesis focused on presenting the results and observations from data analysis of the vehicle responses to various mission scenarios. The mission scenarios ranged from motions in straight lines to steady and unsteady turns in horizontal planes to motions in vertical planes and in 3-D space. This comprehensive set of data was believed to provide sufficient information to establish the bounds of the hydrodynamic model in all six degrees-of-freedom. In addition to providing an extensive set of data for validation purposes, the results from manoeuvring trails also provided first insights into the *Explorer* class vehicle behaviours to various mission scenarios, which to the best of the author's knowledge were never reported from any of the six other International Submarine Engineering (ISE) *Explorer* class AUVs sold worldwide. This can be considered as a major contribution of this research work.

The next step in accomplishing the research objectives was to develop a computer model specifically tailored for the *MUN Explorer* AUV. This was achieved by modifying and adding necessary features to an existing model of a streamlined underwater vehicle, developed based on the component build-up method, for the C-SCOUT AUV. The modular structure of the simulation model required that only one of its modules needed most of all the changes, which contained the vehicle specific parameters. Therefore, the adaptation of the model from one vehicle to that of another can be done fairly quickly, provided all the information necessary for describing the vehicle-specific parameters are easily available. Further, the work reported here shows that the response of the vehicle to some of these parameters can be very sensitive as described below and care should be exercised in measuring or calculating these parameters.

The geometric and inertial properties of the *MUN Explorer* AUV were calculated from some basic information that was available from the manufacturer (ISE). As far as the work reported in this thesis is concerned, the calculation of these parameters was not trivial. Calculation of geometric properties such as the longitudinal and vertical position of the centre of gravity and centre of buoyancy (LCG, VCG, LCB, VCB) can dramatically affect the hydrostatic pitch angle of the vehicle when it is at rest. For instance, the LCG of the dry vehicle as obtained from the manufacturer was 2.44 m aft of the nose. However, the simulation model uses the 'wet mass' of the vehicle. Therefore, when the effect of floodwater was taken into consideration, the CG shifted forward by about 35 cm. Similarly, the vertical separation between CG and CB was also found to change from a supplied value of 4 cm to an estimated value of 17 mm, when the effect of floodwater was considered. A longitudinal separation between CG and CB by an amount of 3 mm (CB aft of CG) was also estimated. The stated test condition for the sea trials was with 13.6 kg of net positive buoyancy. The longitudinal separation between CG and CB by about 3 mm combined with the net positive buoyancy of 13.6 kg resulted in a static pitch angle of the vehicle by about -10.7° (see Table 5.4). This estimated value of static pitch angle (-10.7°) was not unusual because from the experiments performed at slow speeds (~ 1 m/s), the vehicle was found to maintain a nose-down attitude of around -6°, even when the dive planes were deflected to counteract it. This shows how sensitive the "at rest" condition is to the changes in the location of CG and CB, just by few millimetres.

From the manoeuvring experiments, the actions of the "X" tail control planes were found to be complex with all four control planes being engaged at all times. Further, from the different manoeuvres performed (in particular the helix manoeuvre), it was also found that different configurations of control plane deflections could produce the same effect or vehicle response. This prompted the research question on the possibility of representing the complex actions of the four control planes by a simple single effective control plane deflection. Expressions available from the missile research community were used to estimate the single effective control plane deflections. However, the usefulness of these representations for practical purposes such as mapping the deflections of an 'X' tail control plane configuration to that of a simple '+' tail configuration was unknown, since information in the open literature, to the best of author's knowledge, pertaining to a similar approach was not to be found. To study this, a second model of the *MUN Explorer* with a '+' tail configuration of control planes was developed which used the effective control plane defections estimated from the 'X' tail deflections, as its control inputs. A set of steady-state simulations consisting of straight lines and turning circles were performed using this model and results were presented in Chapter 6. The results from the turning simulations showed that the error associated with predicting turning radius, for the most part, was less than 10%. The turning rate of the vehicle was also predicted with reasonably good accuracy. However, oscillatory pitch motions were noticed at slow speed manoeuvres but at higher speeds the pitch angles settled to a steady state. It may be possible that the forces generated at slow speeds are not sufficient to damp the oscillatory motion. Further, the results from turning simulations also indicate that the usage of effective control plane deflections, in place of actual "X" tail deflections, can produce manoeuvres with reasonable-to-good accuracy. This indicates that the expressions used for mapping "X" tail deflections to "+" tail deflections can be useful in simulating steady-state manoeuvres. Further simulations of unsteady manoeuvres are needed to draw a similar conclusion on the usefulness of such expressions in mapping the control plane actions between two configurations during complex manoeuvres.

It was found from the straight-line simulations, that under the conditions of a net buoyancy of 13.6 kg and static pitch angle of -10.7°, achieving a constant depth trajectory was not possible; instead a descent rate was observed under these conditions. This shows how sensitive the simulation results are to the ballast conditions, and thus, how important it is to know the actual ballast condition used during each run.

In conclusion, while a complete achievement of the stated research objectives is not claimed, a major portion of the work necessary to achieve the stated goals has been accomplished through this thesis work. They are listed as follows:

- Development of two motion simulation models, based on component build-up method for the *MUN Explorer* AUV: one with 'X' tail configuration and the other with '+' tail configuration.

- Collection and analysis of a comprehensive set of experimental data necessary for the validation of the model, obtained by conducting manoeuvring trails at sea.

- The manoeuvring trials also provided first insights into *Explorer* class vehicle responses to different mission scenarios.

On Operational Aspects:

- The AUV was very efficient in following a predefined path and this was seen from straight-line tests and horizontal zigzag tests.

- The AUV was capable of maintaining a constant speed during turns, dives and climbs. Negligible roll motions were noticed even during the turns. The ability to maintain constant forward speed and negligible roll motions ensures consistent sampling of data and is an essential quality of a sensor platform.

- Quickness to make heading changes at different speeds and corresponding overshoots were estimated. This is a desirable feature in obstacle avoidance and the information gathered is useful for developing controllers for obstacle avoidance.

- The insignificant overshoots that were observed from vertical zigzag tests indicate that *Depth-by-Heave* mode is preferable while operating the vehicle in shallow water or close to the seabed. However, this method is not practical when the vehicle is programmed to dive large depth. In such scenarios, the *Depth-by-Pitch* mode should be preferred.

On Simulation Aspects:

- The study presented in this thesis demonstrated the ease with which a model based on component build-up method can be adapted from one vehicle to another. It also showed how the model could be modified to study different configurations of the same vehicle. On the other hand, the work also emphasized the need for the degree of accuracy in estimating various parameters necessary for the model.

- Preliminary results from simulation of steady-state manoeuvres show the possibility of mapping complex "X" tail deflections to simple "+" tail deflections.

Recommendations for Future Work

Recommendations for the Simulation Model

Only a small subset of the experimental manoeuvres was simulated with the motion simulator during the available time. The simulation results reported were performed only in the horizontal plane. The task of setting the performance envelope for the simulation model requires that simulations of all possible manoeuvring scenarios be performed. The preliminary simulation results, presented in Chapter 6, provided reasonably good results despite some deficiencies that are plainly inherent in the existing model. This implies that there is room for improvement of the model and consequently hope for better and more reliable results.

The first step to modifying the hydrodynamic model is to incorporate the interaction effects between hull and appendages. This is expected to improve the simulation predictions, particularly during moderate and extreme manoeuvres.

The existing propulsion module is modeled as a constant power output unit. This could be modified such that a forward speed controller can control the speed of the vehicle by adjusting the thrust developed.

The simulation model can be modified to accept active control plane deflections rather than a constant fixed control plane angle. This feature would enable the model to accept the recorded control plane deflection data from the real vehicle as its input.

Recommendation for Vehicle Operations based on the experiments:

The study shows that from a vehicle performance or application point of view, it is appropriate to operate the vehicle in the *constant speed* mode. This helps the vehicle to maintain a steady command speed throughout and thus collect data at a consistent rate. On the other hand, if the intent of the study is the vehicle dynamics or vehicle response; it is more appropriate to operate the vehicle in the *constant propeller* RPM mode rather than *constant speed* mode. This would capture the vehicle's response to any external disturbance, and factors such as speed loss during a turn or dive, if any.

The radii of turns from all turning manoeuvres were much larger than the commanded radius. This demands an investigation and possibly modification of that portion of the vehicle control software which controls the control plane deflections.

All the depth-changing manoeuvres were performed in the *Depth-by-Heave* mode where the AUV primarily used its dive planes to change depth. Depth changing operations in *Pitch-by-Heave* mode can provide information on the overshoot and pitch angles achieved by the vehicle when the tail planes are used for depth changing.

Bibliography

Abbot I. H., and **von Doenhoff, A. E.** (1959). *Theory of Wing Sections*, Dover Publications, Inc., New York.

Abkowitz, M. A. (1969). *Stability and Motion Control of Ocean Vehicles*, MIT Press.

Allen, H. J. (1949). "Estimation of the Forces and Moments Acting on Inclined Bodies of Revolution of High Fineness Ratio", Research Memorandum RM A9126, National Advisory Committee for Aeronautics (NACA), November 1949.

Allen, H. J., and **Perkins, E. W.** (1951a). "Characteristics of Flow over Inclined Bodies of Revolution", Research Memorandum RM A50L07, National Advisory Committee for Aeronautics (NACA), March 1951.

Allen, H. J., and **Perkins, E. W.** (1951b). "A Study of Effects of Viscosity on Flow Over Slender Inclined Bodies of Revolution", Report 1048, National Advisory Committee for Aeronautics (NACA), March 1951.

Anderson, J.M., and **Kerrebrock, P.A.,** (2004). The Vorticity Control Unmanned Undersea Vehicle [VCUUC]: An Autonomous Robot Tuna. http://draperlab.org/digest2000/paper6.pdf. (accessed on April 2011)

Bachmayer, R. Leonard, N.E., Bhattia. P., Fiorelli, E., and **Graver, J.G**. (2006). "Dynamics, Control and Coordination of Underwater Gliders", in G. N. Roberts & R. Sutton (Eds.), *Advances in Unmanned Marine Vehicles*, The Institution of Electrical Engineers, UK.

Bane, G.L., and **Ferguson, J.** (1987). "The Evolutionary Development of the Military Autonomous Underwater Vehicle", Fifth International Symposium on Unmanned Untethered Submersible Technology, June 22-24, University of New Hampshire, Durham, NH.

Bertram, V. (2000). *Practical Ship Hydrodynamics,* Butterworth – Heinemann, 2000.

Biddle, D. G. (2003). *Inertial Based Control of Kambara Project*, B. Eng. Thesis, Australian National University, June 2003.

Brown, E.D., Gaskell, N.J.J., and **Dering, J.C.** (2000). "The Operation of Autonomous Underwater Vehicles: Recommended Code of Practice", *Society of Underwater Technology (SUT)*, Vol. 1.

Brutzman, d. P., Kanayama, Y., and **Zyda, M. J.** (1992). "Integrated Simulation for Rapid Development of Autonomous Underwater Vehicles", Proceedings of the 1992 Symposium on AUV Technology, pp. 3 – 10.

Buckham, B., Nahon, M., Seto, M., Zhao, X. and **Lambert, C.** (2003). "Dynamics and Control of a Towed Underwater Vehicle System, Part I: Model Development", *Ocean Engineering*, Volume 30, pp. 453 – 470.

Bullivant, W. K. (1940). "Tests of the NACA 0025 and 0035 Airfoils in the Full-Scale Wind tunnel", N.A.C.A Report No. 708.

Burcher, R., and **Rydill, L.** (1994). *Concepts in Submarine Design*, Cambridge Ocean Technology Series – 2, Cambridge University Press 1994.

Butler, B., and **Hertog, V.,** (1993). "Theseus: A Cable-Laying AUV", OCEANS' 93, Proceedings: 'Engineering in Harmony with Oceans', Vol.1, pp. 1210-1213, 18-21 October, 1993.

Craig, J. (1989). *Introduction to Robotics: Mechanics and Control,* Second Edition, Addison-Wesley Publishing Company, Inc., Menlo Park, California, 1989.

Crees, T., Kaminski, C., Ferguson, J., Laframboise, J. M., Forrest, A., Williams, J., MacNeil, E., Hopkin, D., and **Pederson, R.** (2010). "Preparing for UNCLOS – An Historic AUV Deployment in the Canadian High Arctic", IEEE/OCEANS 2010, Seattle, WA, September 20 – 23, 2010.

Critzos, C. C., Heyson, H. H., and **Boswinkle Jr., R. W.** (1955) "Aerodynamic Characteristics of NACA 0012 Airfoil Section at Angles of Attack from 0^o to 180^{o}", NACA TN 3361, 1955.

Curtis, T. (2001a). *The Design, Construction, Outfitting and Preliminary Testing of the C-SCOUT Autonomous Underwater Vehicle (AUV).* M. Eng. Thesis, Memorial University of Newfoundland, 2001.

Curtis, T., Perrault, D., Williams, C. D., and **Bose, N.** (2001b). "Baseline Configuration of the C-SCOUT Autonomous Underwater Vehicle", in 18^{th} Canadian Congress of Applied Mechanics, A. Swamidas, M. R. Haddara and R. Seshadri, Eds., St. John's, NL, June 2001, pp. 251 – 252, Memorial University of Newfoundland.

Curtis, T., **Williams, C. D.**, **Perrault, D.**, and **Bose, N.** (2000). "C-SCOUT: A general-purpose AUV for systems research," in *Proceedings of the 2000 International Symposium on Underwater Technology (UT00),* Tokyo, Japan, May 2000, pp. 73 – 77, IEEE.

Davis, R.E., **Eriksen, C.C.**, and **Jones, C.P.** (2003). "Autonomous Buoyancy-Driven Underwater Gliders", *Technology and Applications of Autonomous Underwater Vehicles,* Taylor and Francis Inc., Edited by G. Griffiths.

de Barros, E. A., **Pascoal, A.**, and **de Sa E.** (2008a). "Investigation of a Method for Predicting AUV Derivatives", *Journal of Ocean Engineering*, vol. 35, pp. 1627 – 1636.

de Barros, E.A., **Dantas, J.L.D.**, **Pascoal, A.M.**, and **de Sa, E.** (2008b). "Investigation of Normal Force and Moment Coefficients for an AUV at Nonlinear Angle of Attack and Sideslip Range", *IEEE Journal of Oceanic Engineering*, Vol. 33, No. 4, pp. 538 – 549, October 2008.

de Barros, E. A., **Pascoal, A.**, and **de Sa, E.** (2004). "AUV Dynamics: Modelling and Parameter Estimation using Analytical, Semi-empirical and CFD Methods", Proceedings of IFAC Conference on Control Applications in Marine Systems, Ancona, Italy.

E. Allmendinger (Ed.), (1990). *Submersible Vehicle Systems Design,* The Society of Naval Architects and Marine Engineers, Jersey City, NJ.

Evans, J. (2003). *Dynamics Modeling and Performance Evaluation of and Underwater Vehicle*, Master's Thesis, McGill University, Montreal, Quebec, Canada.

Evans, J., and **Nahon, M.** (2004). "Dynamic Modeling and Performance Evaluation of an Autonomous Underwater Vehicle", *Ocean Engineering,* Vol. 31, pp. 1835 – 1858.

Feldman, J. (1979). "DTNSRDC Revised Standard Submarine Equations of Motion", David W. Taylor Naval Ship Research and Development Centre, DTNSRDC/SPD-)393-09, June 1979.

Ferguson, J.S. (1998). "The Theseus Autonomous Underwater Vehicle Two Successful Missions", Proceedings of the International Symposium on Underwater Technology, Tokyo, Japan, 15 – 17th April 1998.

Ferguson, J.S. (2003). "Cargo Carrying AUVs", in G. Griffiths (Ed.), *Technology and Applications of Autonomous Underwater Vehicles*, Taylor and Francis Inc.

Ferguson, J.S. (2009). "Under-Ice Seabed Mapping with AUVs", IEEE/OCEANS '09 – EUROPE, Bremen, Germany, 11 – 14 May 2009.

Fossen, T. I. (1991). *Nonlinear Modeling and Control of Underwater Vehicles*, Ph.D. Thesis, Department of Engineering Cybernetics, Norwegian University of Science and Technology, Trondheim, Norway.

Fossen, T. I. (1994). *Guidance and Control of Ocean Vehicles*, John Wiley & Sons, New York.

Funnell, C. (2007). *Jane's Underwater Technology 2006-2007*, Jane's Information Group, 10th Edition.

Gertler, M., and **Hagen, G.R.,** (1967). "Standard equations of motion for submarine simulation", DTNSRDC Report 2510, SR-009-01-01, June 1967, Naval Ship Research and Development Center.

Gertler, M. (1972). "Some Recent Advances in Dynamic Stability and Control of Submerged Vehicles", *Journal of Mechanical Engineering Science,* Vol. 14, No. 7, pp. 14-19.

Goheen, K.R. (1991). "Modeling Methods for Underwater Robotic Vehicle Dynamics", *Journal of Robotic Systems,* Vol. 8, No. 3, pp. 295-317.

Gorski, J.J., Coleman, R.M., and **Haussling, H.J.** (1990). "Computation of Incompressible Flor around the DARPA SUBOFF Bodies", Ship Hydromechanics Department R&D Report, David Taylor Research Centre, DTRC-90/016, July, 1990.

Griffiths, G., Jones, C. P., Ferguson, J., and **Bose, N.** (2007). "Undersea Gliders", *Journal of Ocean Technology*, Vol. 2, No. 2, pp. 64 – 75.

Havard, B. (2004). *Hydrodynamic Estimation and Identification*, M.Sc Thesis, Norwegian University of Science and Technology, NTNU, August 2004.

Heggstad, K. M. (1984). "Why X-form Rudders for Submarines", Maritime Defence, January 1984, pp. 2 – 6.

Hemsch, M. J. and **Neilsen, J. N.** (1983). "Equivalent Angle-of-Attack Method for Estimating Nonlinear Aerodynamics of Missile Fins", *Journal of Spacecraft and Rockets,* Vol. 20, pg. 356 – 362, 1983.

Hemsch, M. J., and **Nielsen, J. N.,** (1986) *Tactical Missile Aerodynamics*, Progress in Astronautics and Aeronautics, Vol. 104, American Institute of Aeronautics and Astronautics, NY, 1986.

Hess, J.L. (1990). "Panel Methods in Computational Fluid Dynamics", Annual review Fluid Mechanics, 1990. http://www.annualreviews.org/aronline. (accessed on June 2008)

Hibbeler, R. C. (1995). *Engineering Mechanics: Statics and Dynamics*, 7th Edition, 1995.

Hoak, D., and **Finck, R. D.** (1978). *USAF Stability and Control DATCOM*, Wright-Paterson Air Force Base, Ohio.

Hopkin, D. and **den Hertog, V.** (1993). "The hydrodynamic testing and simulation of an autonomous underwater vehicle", Proceedings of the Second Canadian Marine Dynamics Conference, 274 – 281.

Hopkins, E. J. (1951). "A Semi-empirical Method for Calculating the Pitching Moment of Bodies of Revolution at Low Mach Numbers", Research Memorandum RM A51C14, National Advisory Committee for Aeronautics (NACA), May 1951.

Humphreys, D. E., and **Watkinson, K. W.** (1983). "Effects of Fin Asymmetry on the Dynamic Response of a Representative Untethered Submersible", Proceedings of the 3rd International Symposium on Unmanned Untethered Submersible Technology, A.R.A.P Technical Memorandum No. 83-8, Vol. 3, pp. 132 – 149.

Humphreys, D.E. (1976). "Development of the equations of motion and transfer functions for underwater vehicles", Report NCSL 287-76, Naval Coastal Systems Laboratory, Panama City, FL, July 1976.

Hwang, Y. L. (2003). "Hydrodynamic Modeling of LMRS Unmanned Underwater Vehicle and Tow Tank Test Validation", Proceedings of the Conference OCEANS '03, Vol. 3, pp. 1425 – 1430, September, 2003.

Imlay, F. H. (1961). "The Complete Expressions for 'Added Mass' of a Rigid Body Moving in an Ideal Fluid", DTMB, Hydromechanics Lab. Research & Development Report, July 1961.

Imlay, F. H. (1961). "The Complete Expressions for Added Mass of Body Moving in an Ideal Fluid", David Taylor Model Basin Report 1528, July 1961.

Imlay, F. H. (1964). "Complete Expressions for Gravitational and Buoyancy Force Terms in the Equations of Motion of a Submerged Body", Naval Ship Research & Development Center Report 1845, July 1964.

Jackson, Capt. H. A. (1993). "The Influence of the USS Albacore on Submarine Design", Paper 2, International Symposium on Naval Submarines, Warship '93, RINA, London, 1993.

Jones, D.A., Clarke, D.B., Brayshaw, I.B., Barillon, J.L., and **Anderson, B.** (2002). "The Calculation of Hydrodynamic Coefficients for Underwater Vehicles", Technical Report, DSTO-TR-1329, July 2002.

Jones, Jr., G. W. (1952). "Investigation of the effects of variations in the Reynolds number between 0.4 x 106 and 3.0 x 106 on the low-speed aerodynamics characteristics of three low-aspect-ratio symmetrical wings with rectangular planforms", NACA Research Memorandum RM L52G18.

Jorgensen, L. H. (1973). "Prediction of Static Aerodynamic Characteristics for Space-Shuttle-Like and other Bodies at Angles of Attack from 0^o to 180^o", National Aeronautics and Space Administration, NASA TN D-6996, Washington, D. C., January 1973.

Joubert, P. N. (2006). "Some Aspects of Submarine Design – Part 2: Shape of a Submarine 2026", Defence Science and Technology Organisation, DSTO-TR-1920, December 2006.

Kalske, S. (1992). *Motion Simulation of Underwater Vehicles*, VTT publications, Technical Research Centre of Finland, Espoo.

Kane, T. R., Likins, P. W., and **Levinson, D. A.** (1983). *Spacecraft Dynamics*, McGraw-Hill, New York, NY.

Lamb, H. (1918). "The Inertia-Coefficients of an Ellipsoid Moving in Fluid", Reports and Memoranda, No. 623, October, 1918.

Lambert, C., Nahon, M., Buckham, B., and **Seto, M.** (2003). "Dynamics and Control of Towed Underwater Vehicle System, Part II: Model Validation and Turn Maneuver Optimization", *Ocean Engineering*, Volume 30, pp. 471 – 485.

Lesieutre, D., Love, J., and **Dillenius, M.** (1996). "High Angle of Attack Missile Aerodynamics Including Rotational Rates – Program M3HAX", Atmospheric Flight Mechanics Conference, San Diego, CA, July 29 – 31, 1996.

Lesieutre, D., Love, J., and **Dillenius, M.** (2002). "Recent Applications and Improvements to the Engineering-Level Aerodynamic Prediction Software MISL3", AIAA 2002-0275, 40th AIAA Aerospace Sciences Meeting & Exhibit, Reno, NV, 14 – 17 January 2002.

Lewis, E. V. (1988). *Principles of Naval Architecture*, Society of Naval Architects and Marine Engineers (SNAME) 1988, Jersey City, NJ, Vol. III, pp. 211.

Lewis, E.V. (1989). *Principles of Naval Architecture*, The Society of Naval Architects & Marine Engineers, Vol. III, pp. 251 – 256.

Lopes, L.A. (1954). "Motion Equations for Torpedos", Navord Report 2090, Underwater Ordnance Department, USA.

Lopez, E., Velasco, F.J., Moyano, E. and **Rueda, T.M.** (2004). "Full-Scale Manoeuvring Trials Simulation", *Journal of Maritime Research*, Vol. 1, No. 3, pp. 37 – 50, 2004.

MacNaughton, A., White, R. H., and **Bendzlowicz, M.** (2005). "Into the Deep End", *International Ocean Systems*, Vol. 9, No. 1, January/February 2005.

Maeda, H., and **Tatsuta, S.** (1989). "Prediction Method of Hydrodynamic Stability Derivatives of an Autonomous Non-Tethered Submerged Vehicle", Eighth International Conference on Offshore Mechanics and Arctic Engineering, The Hague –March 19-23, 1989.

Marani, G., Yuh, J., and **Choi, S.K.** (2006). "Autonomous manipulation for an intervention AUV", in G.N. Roberts & R. Sutton (Eds.), *Advances in Unmanned Marine Vehicles*.

McCormick, B. W. (1995). *Aerodynamics Aeronautics and Flight Mechanics,* 2nd Edition, John Wiley & Sons, Inc., 1995.

McGhee, R. B., Bachmann, E. R., and **Zyda, M. J.** (2000). "Rigid Body Dynamics, Inertial Reference Frames and Graphics Coordinate Systems: A Resolution of Conflicting Conventions and Terminology", Naval Postgraduate School, Monterey, California, November 2000.

Mises, R. (1959). *Theory of Flight*, Dover Publications, Inc., New York.

Molland, A. F. (2008). *The Maritime Engineering Reference Book – A Guide to Ship Design, Construction and Operation*, Butterworth-Heinemann.

Molland, A. F., and **Turnock, S. R.** (2007). *Marine Rudders and Control Surfaces: Principles, Data, Design and Applications*, Butterworth-Heinemann, 2007.

Munk, M. (1924). "The Aerodynamic Forces on Airship Hulls", Report No. 184, National Advisory Committee on Aeronautics (NACA), 1924.

Nahon, M. (1996). "A Simplified Dynamics Model for Autonomous Underwater Vehicles, Autonomous Underwater Vehicle Technology", AUV '96, pp. 373-379.

Nahon, M. (2006). "A Simplified Dynamics Model for Autonomous Underwater Vehicles", *The Journal of Ocean Technology*, Vol. 1, No. 1, 2006.

Niu, H., Adams, S., Husain, T., Bose, N., and **Lee, K. (2007).** "Applications of Autonomous Underwater Vehicles in Offshore Petroleum Industry Environmental Effects Monitoring", 8th Canadian International Petroleum Conference, Calgary, Alberta, Canada, June12 – 14, 2007.

Niu, H., Husain, T., Veitch, B., Bose, N., Adams, S., He, M., and **Lee, K.** (2007). "Ocean Outfall Mapping Using an Autonomous Underwater Vehicle", OCEANS '07, September 29 – October 4, 2007.

Perrault, D. (2002). *Autonomous Underwater Vehicles (AUV) Sensitivity of Motion Response to Geometric and Hydrodynamic Parameters and AUV Behaviors with Control*

Plane Faults, Doctoral Thesis, Memorial University of Newfoundland, St. John's, Newfoundland, Canada.

Perrault, D., Smith, L., Curtis, T., Bose, N., O' Young, S., and **Williams, C. D.** (2000). "A Tool for Modeling Vehicle Behaviour", 2nd NRC-IMD Workshop on Control and Simulation Systems for Underwater Vehicles, 13th & 14th November 2000.

Prestero, T. (2001a). *Verification of a Six-Degree of Freedom Simulation Model for the REMUS Autonomous Underwater Vehicle*, M.Sc Thesis, MIT & WHOI, September 2001.

Prestero, T. (2001b). "Development of a Six-Degree of Freedom Simulation Model for the REMUS Autonomous Underwater Vehicle", OCEANS, Vol. 1 pp 361- 368.

Ray, A., Seshadri, V., Singh, S. N., and **Sen, D.** (2008). "Manoeuvring Studies of Underwater Vehicles – A Review", *International Journal of Maritime Engineering*, Transactions of RINA, Vol. 150, Part A3 2008.

Ridley, P., Fontan, J., and **Cooke, P.** (2003). "Submarine Dynamic Modeling", Proceedings of Australasian Conference on Robotics and Automation, Brisbane, Australia.

Riegels, F. W. (1958). *Aerodynamische Profile,* R. Oldenbourg, Munchen.

Rigaud, V., Louis, J., Ferguson, J. S., Laframboise, J. M., Crees, T., Leon, P., Opderbecke, J., and **Chardard, Y.** (2004). "First Steps in Ifremer's Autonomous Underwater Vehicle Program – A 3000m Depth Operational Survey AUV for Environmental Monitoring", Proceedings of the Fourteenth International Offshore and Polar Engineering Conference, Toulon, France, May 23 – 28, 2004.

Sahin, I., Crane, J.W., and **Warson, K.P.** (1994). "Application of a Panel Method to Hydrodynamics of Underwater Vehicles", Proceedings of the 4th International Offshore and Polar Engineering Conference, Osaka, Japan, April 10-15, 1994.

Sarpkaya, T., and **Isaacson, M.** (1981). *Mechanics of Wave Forces on Offshore Structures*, Van Nostrand Reinhold Company, New York, 1981.

Saunders, A. (2003). *The Effect of Velocity and Orientation on the Simulation and Experimental Characterization of an AUV Tunnel Thruster,* Masters Thesis, University of Victoria, Victoria, British Columbia, Canada, 2003.

Sheldahl, R. E., and **Klimas, P. C.** (1981). "Aerodynamic Characteristics of Seven Symmetrical Airfoil Sections Through 180 Degrees Angle of Attack for Use in Aerodynamic Analysis of Vertical Axis Wind Turbines", SAND80-2114, March, 1981, Sandia National Laboratories, Albuquerque, New Mexico, 118 pages.

Sibenac, M., Podder, T., Kirkwood, W., and **Thomas, H.,** (2004). "Autonomous Underwater Vehicles for Ocean Research: Current Needs and State of the Art Technologies", *Marine Technology Society Journal*, Vol. 38, No. 2

SNAME (1950). "Nomenclature for Treating the Motion of a Submerged Body Through a Fluid", The Society of Naval Architect and Marine Engineers, Technical and Research Bulletin No. 1-5.

Stante, G., Nahon, M., and **Williams, C.D.** (2007). "Simulation of the Performance of an Underwater Glider", 15th International Symposium on Unmanned Untethered Submersible Technology, Durham, NH, USA, 20 to 22 Aug 2007.

Summey, D. C., and **Smith, N. S.** (1981). "The Development and Application of Underwater Vehicle Design Techniques", OCEANS 1981, Vol. 2, pp 1160-1164.

Tam, C., Mills, R., and **Ferguson, J.** (2011). "Delivering on the Promise of the AUV", International Ocean Systems, January/February 2011.

Ward, G. N. (1949). "Supersonic flow past slender pointed bodies," *Quarterly J. Mech. and Applied Math*, vol.2, pt. I, pp. 75 – 97, March 1949.

Watt, G. D. (1988). "Estimates for the Added Mass of a Multi-Component Deeply Submerged Vehicle, Part I: Theory and Program Description", Defence Research Establishment Atlantic (DREA), Technical Memorandum 88/213, October 1988.

Whicker, L. F, and **Fehlner, L. F.** (1958). "Free-stream Characteristics of a Family of Low-aspect-ratio, All-movable Control Surfaces for Application to Ship Design", Report 933, David Taylor Mode Basin (DTMB), Bethesda, MD, December 1958.

Yeo, R. (2008). "Surveying the underside of an Artic ice ridge using a man-portable AUV", International Ocean Systems, Volume 12, No.1, January/February 2008.

International Submarine Engineering (ISE) Technical Manuals

1. ISE-R054-MAN-001-01, MUN Explorer 27-B02-3000 AUV, Operations & Maintenance Manual.
2. ISE-R054-MAN-002-01, MUN Explorer 27-B02-3000 AUV, Control System User's Manual, Release 1.0, 13 June 2006.
3. ISE-R054-SPC-002-01, MUN Explorer 27-B02-3000 AUV, Control System Specification, Release 1.0, 12 April 2006.
4. MUN EXPLORER 27-B02-3000 AUV: Control System Specification, Doc. No. ISE-R054-SPC-002-01.
   http://oceanexplorer.noaa.gov/explorations/08auvfest/logs/may15/may15.html
5. MUN EXPLORER 27-B02-3000 AUV – Technical Manual, Volume V, ACE Documentation.

6. EXPLORER, ISE Web Based AUV DesignInfo, International Submarine Engineering Ltd. (www.ise.bc.ca - accessed on Dec 1, 2007).

List of Publications

Issac, M.T., Bose, N., Williams, C. D., Bachmayer, R. and **Crees, T.** (2010), "Depth-Changing Manoeuvres using the MUN Explorer AUV", proceedings of the 29th American Towing Tank Conference, Annapolis, MD, 11 to 13 August 2010.

Issac, M. T., Adams, S., Bose, N., Williams, C. D., Bachmayer, R. and **Crees, T.** (2008), "Analysis of Horizontal Zigzag Manoeuvring Trials from the MUN Explorer AUV", Proceedings of the OCEANS'08 MTS/IEEE, September 15 to 18, 2008, Quebec City, Québec, Canada.

Azarsina, F., Williams, C.D. and **Issac, M.T.** (2008), "Modelling the Hydrodynamic Sway Force Exerted on the Bare-Hull of an Axi-symmetric Underwater Vehicle in Lateral Acceleration Manoeuvres", Proceedings of the OCEANS'08 MTS/IEEE, September 15 to 18, 2008, Quebec City, Québec, Canada.

Issac, M.T., Adams, S., He, M., Bose, N., Williams, C.D., Bachmayer, R. and **Crees, T.** (2007a), "Manoeuvring Experiments using the MUN Explorer AUV", Proceedings of the Underwater Technology conference, UT'07, Tokyo, Japan, 17 to 20 April, 2007.

Issac, M.T., Adams, S., He, M., Bose, N., Williams, C.D., Bachmayer, R. and **Crees, T.** (2007b), "Manoeuvring Trials with the MUN Explorer AUV: Data Analysis and Observations", IEEE-MTS OCEANS'07 Conference, Vancouver, BC, 29 Sep to 04 Oct, 2007.

Azarsina, F., Williams C.D. and **Issac M.T.** (2007), "Pure Yaw Experiments on a Series of Hull Forms for an Underwater Vehicle: Hydrodynamic Observations and Analysis", Proceedings of the Underwater Technology conference, UT'07, Tokyo, Japan, 17 to 20 April, 2007.

Williams, C. D., Curtis, T. L., Doucet, J.M., Issac, M.T. and **Azarsina, F.** (2006)."Effects of Hull Length on the Hydrodynamic Loads on a Slender Underwater Vehicle during Manoeuvres", Proc. OCEANS'06, MTS/IEEE-Boston Conference, September 18 to 21, 2006.

Williams, C. D., Curtis, T. L., Doucet, J.M., Issac, M.T. and **Azarsina, F.** "Effects of Hull Length on the Hydrodynamic Loads on a Slender Underwater Vehicle during Manoeuvres", Proc. Workshop, International Submarine Hydrodynamics Working Group, September 26 & 27, Arlington, VA.

APPENDIX – A

Vehicle Log File and Mission Plans

A-1 Data Header of the Log File

The parameters that are logged in by the Vehicle Control Computer (VCC) during a typical mission are listed below:

Sl. No	Column	Header	Units
		Clock & Counter	
1	A	vcc_clock_real_seconds	sec
2	B	vcc_log_counter	
		Vehicle Attitudes & Orientation	
3	C	vcc_man_altitude_sp_m_actual	metres
4	D	vcc_pos_altitude_fb_m	metres
5	E	vcc_dvl_altitude_fb_m	metres
6	F	vcc_altimeter_altitude_fb_m	metres
7	G	vcc_man_depth_sp_m	metres
8	H	vcc_pos_depth_fb_m	metres
9	I	vcc_man_heading_sp_deg	deg
10	J	vcc_pos_heading_fb_deg	deg
11	K	vcc_man_pitch_sp_deg	deg
12	L	vcc_pos_pitch_fb_deg	deg
13	M	vcc_man_roll_sp_deg	deg
14	N	vcc_pos_roll_fb_deg	deg
		Vehicle Speed & Thruster RPM	
15	O	vcc_speed_sp_mps	metres/sec
16	P	vcc_speed_fb_mps	metres/sec
17	Q	vcc_thruster_modelled_speed_fb_mps	metres/sec
18	R	vcc_dgps_speed_fb_mps	metres/sec
19	S	vcc_thruster_rpm_sp	rpm
20	T	vcc_thruster_rpm_fb	rpm
21	U	vcc_thruster_rpm_sp_profiled	rpm
		Vehicle Position Information	
22	V	vcc_dgps_longitude_fb	deg
23	W	vcc_dgps_latitude_fb	deg
24	X	vcc_pe_dvl_longitude_fb	deg
25	Y	vcc_pe_dvl_latitude_fb	deg
26	Z	vcc_system_mode_fb	
27	AA	vcc_mission_line_heading	deg
28	AB	vcc_mission_line_offline_distance	metres
29	AC	vcc_mission_line_output_control_heading	deg

Vehicle Control Plane Information			
30	AD	vcc_plane_1_sp_deg	deg
31	AE	vcc_plane_1_fb_deg	deg
32	AF	vcc_plane_2_sp_deg	deg
33	AG	vcc_plane_2_fb_deg	deg
34	AH	vcc_plane_3_sp_deg	deg
35	AI	vcc_plane_3_fb_deg	deg
36	AJ	vcc_plane_4_sp_deg	deg
37	AK	vcc_plane_4_fb_deg	deg
38	AL	vcc_plane_5_sp_deg	deg
39	AM	vcc_plane_5_fb_deg	deg
40	AN	vcc_plane_6_sp_deg	deg
41	AO	vcc_plane_6_fb_deg	deg
Vehicle Power Consumption Information			
42	AP	vcc_battery_fb_volts	volts
43	AQ	vcc_battery_current_fb_amps	amperes
44	AR	vcc_thruster_current_fb_amps	amperes
45	AS	vcc_man_pitch_force_clipped	
46	AT	vcc_man_roll_force_clipped	
47	AU	vcc_man_yaw_force_clipped	
48	AV	vcc_man_depth_force_clipped	
49	AW	vcc_thruster_volts_cmd	volts
50	AX	vcc_hull_temperature_fb_degc	degree Celsius
Vehicle Alarms			
51	AY	vcc_wa_alarm	On/Off
52	AZ	vcc_gf_alarm	On/Off
53	BA	vcc_plane_alarm	On/Off
54	BB	vcc_thruster_alarm	On/Off
55	BC	vcc_battery_alarm	On/Off
Vehicle Pressure Sensor (Paroscientific), DVL Bottom Range & Hull Pressure			
56	BD	vcc_paro_press_fb_psi	
57	BE	vcc_dvl_bottom_range_b1_fb_m	
58	BF	vcc_dvl_bottom_range_b2_fb_m	
59	BG	vcc_dvl_bottom_range_b3_fb_m	
60	BH	vcc_dvl_bottom_range_b4_fb_m	
61	BI	vcc_hull_pressure_fb_inhg	
Position Estimate Feedback from DVL			
62	BJ	vcc_pe_dvl_dr_on	On/Off
63	BK	vcc_pe_speed_fwd_mps	metres/sec
64	BL	vcc_pe_speed_lat_mps	metres/sec
65	BM	vcc_pe_dvl_lat_datum_m	meters
66	BN	vcc_pe_dvl_long_datum_m	meters
67	BO	vcc_pe_dvl_northing_m	meters
68	BP	vcc_pe_dvl_easting_m	meters

Watson AHRS (Pitch, Roll, Heading) Feedback and DVL & DGPS Feedback			
69	BQ	vcc_watson_pitch_fb_deg	deg
70	BR	vcc_watson_roll_fb_deg	deg
71	BS	vcc_watson_heading_raw	deg
72	BT	vcc_watson_heading_fb_deg	deg
73	BU	vcc_dvl_heading_fb_deg	deg
74	BV	vcc_dgps_course_true_fb	deg
75	BW	vcc_dgps_course_magnetic_fb	deg
Control Plane Command Voltage			
76	BX	vcc_plane_1_volts_cmd	volts
77	BY	vcc_plane_2_volts_cmd	volts
78	BZ	vcc_plane_3_volts_cmd	volts
79	CA	vcc_plane_4_volts_cmd	volts
80	CB	vcc_plane_5_volts_cmd	volts
81	CC	vcc_plane_6_volts_cmd	volts
Watson AHRS - Pitch, Roll, Heading rates & Standard Deviation			
82	CD	vcc_watson_pitch_rate_fb_dps	deg/sec
83	CE	vcc_watson_roll_rate_fb_dps	deg/sec
84	CF	vcc_watson_heading_rate_fb_dps	deg/sec
85	CG	vcc_watson_degraded	
86	CH	vcc_watson_pitch_stddev	
87	CI	vcc_watson_roll_stddev	
88	CJ	vcc_watson_heading_stddev	
89	CK	vcc_watson_pitch_rate_stddev	
90	CL	vcc_watson_roll_rate_stddev	
91	CM	vcc_watson_heading_rate_stddev	
92	CN	vcc_altimeter_altitude_fb_m_raw	
93	CO	Time in English units	

A-2 Event Abbreviations:

The Automated Control Engine (ACE) follows a specified pattern or convention in naming the events. Event names can be noun or verb phrases with words separated by underscore. Thus a typical event-name would follow the general form: *system_substem_identifier_description_unit*. The event abbreviations[1] used by ACE and their meanings are listed below:

Event Abbreviations

_amps	amperes
_cmd	command (Boolean: On/Off)
_deg	degrees
_dps	degrees/second (angular rates)
_fb	feedback
_fwd	forward
_lat	lateral (Note: 'lat' also used as an abbreviation of *Latitude* in column 65)
_man	maneuvring
_mps	metres per second
_pos	position
_press	pressure
_psi	pounds per square inch
_rpm	revolutions per minute
_sec	seconds
_sp	setpoint
_vel	velocity

[1] These descriptions are taken from the document *MUN EXPLORER 27-B-02-3000 AUV CONTROL SYSTEM SPECIFICATION* (Document No. ISE-R054-SPC-002-01), prepared by the International Submarine Engineering Ltd.

A-3 Geographical to Rectangular Coordinates Conversion

The following algorithm is used for the conversion of position estimates between geographical and rectangular coordinates and is reproduced from the manufacturer's Technical Manual[2].

The algorithm below converts the X and Y position estimated by the DVL (in metres), to an absolute position in geographic coordinates - *latitude* and *longitude*.

> One degree of Latitude, mpd_lat[3] = 1853.184*60 metres
> Latitude (ϕ) = ϕ_i + input_y/ mpd_lat
> One degree of Longitude, mpd_long[4] = mpd_lat*cos(ϕ)
> Longitude (λ) = λ_i + input_x/mpd_long

where ϕ_i = initial latitude or latitude of the reference point (degrees)

> λ_i = initial longitude or longitude of the reference point (degrees)
> input_x = offset (in metres) estimated by DR – positive east.
> input_y = offset (in metres) estimated by DR – positive north.
> Latitude/Longitude = computed values of current position.

The AUV position information, as estimated by the DVL and obtained from the log files, are in geographical coordinates. To convert the geographical coordinates to Cartesian coordinates, the above algorithm is simply reversed such that the *initial latitude* (ϕ_i) and *initial longitude* (λ_i) becomes the origin *O* of the Earth fixed Cartesian coordinate system. Hence, the current position of the AUV (ϕ, λ) with respect to the initial position (ϕ_i, λ_i) or origin (*O*) can be obtained in Cartesian coordinates (in metres) as follows:

$$X = (\phi - \phi_i).\ \text{mpd\_long};$$

$$Y = (\lambda - \lambda_i).\ \text{mpd\_lat}$$

[2] MUN EXPLORER 27-B02-3000 AUV – Technical Manual, Volume V, ACE Documentation
[3] mpd_lat = metres per degree of latitude
[4] mpd_long = metres per degree of longitude

A-3 Mission Plan Task Verbs

The following are sample mission plan files showing the typical syntax in which the geographical *task_verbs* are applied in planning missions. By using a series of geographic task verbs, a manual route can be defined as a series of waypoints.

Line_follow

```
line_follow,047.388165,-053.132371,3.0,ignore,0.0,dvl,1.5,depth,0.0
           (Latitude, Longitude)                     (speed)
```

Target

```
target, 047.393375,-053.131841,3.0,ignore,0.0,dvl,1.5,depth,3.0
        (Latitude, Longitude)                    (speed)
```

Circle

```
circle, 047.390050,-053.133270, 12.0, rotations,2.5,dvl,1.5,depth,3.0
        (Latitude, Longitude) (Radius)                (speed)
```

A typical *circle* command to turn the vehicle at a radius of 12 m about a centre point for 2.5 revolutions. The geographical coordinates of the centre point are given by the Latitude and Longitude and the point is located at a depth of 3 m below the surface. The vehicle is driven at a speed of 1.5 m/s.

APPENDIX - B

MUN Explorer Geometric Parameters

B-1 BARE HULL

1. Nose Cone

Shape of nose cone: Semi-elliptical in longitudinal section
Length of nose cone, $L_n = 0.69$ m
Maximum diameter or diameter at the base of the nose cone = 0.69 m

Eccentricity of ellipse, $e = \sqrt{1 - \dfrac{b^2}{a^2}} = 0.866$

Surface area[1], $S_n = \pi\left(\left(\dfrac{D}{2}\right)^2 + Ln.\dfrac{D}{2}.\dfrac{1}{e}\mathbf{arcsin}(e)\right)$ (1)

$$= \pi\left(b^2 + \frac{ab}{e}\mathbf{sin}^{-1}(e)\right) = \mathbf{1.2782}\ \mathrm{m}^2$$

Surface area by theoretical formula (1) = **1.2782** m²

Volume of the semi-ellipsoidal nose, $V_n = \dfrac{2}{3}\pi b^2.a = \dfrac{2}{3}\pi 0.345^2 \times 0.69 = 0.1720m^3$

where a and b are semi-major and semi-minor axis.

Calculation check using MAPLE™

Surface area calculation of nose cone section using MAPLE
> restart;

$$y(x) = \frac{b}{a}\sqrt{a^2 - x^2} \text{ (Equation of an ellipse)}$$

y:=0.345/0.69*sqrt(0.69^2-x^2);

$$y(x) = 0.5\sqrt{0.4761 - x^2}$$

y₁:=diff(y,x);

[1] http://en.wikipedia.org/wiki/Spheroid. The same equation is used in C-SCOUT code as well

$$y_1(x) = -0.5\frac{x}{\sqrt{0.4761 - x^2}}$$

> y2:=y1^2;

$$[y_1(x)]^2 = 0.25\frac{x^2}{0.4761 - x^2}$$

> *l*:=sqrt(1+y2);

$$l = \sqrt{1 + 0.25\frac{x^2}{0.4761 - x^2}}$$

> Sn:=2*pi*y**l*;

$$S_n = 1.00\pi\sqrt{0.4761 - x^2}\sqrt{1 + 0.25\frac{x^2}{0.4761 - x^2}}$$

int(Sn,x=0..0.69);

$$S_n = \int_0^{0.69} 2\pi y(x)\sqrt{1 + [y_1(x)]^2}\,dx$$

$$\mathbf{S_n = 0.4068749592\,\pi = 1.2782\ m^2}$$

The surface area obtained from Eq. (1) and by numerical integration is exactly the same.

Nose Cone of the *MUN Explorer* AUV

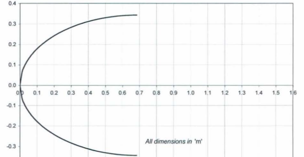

2. Parallel Mid-body Section

The parallel mid-body section can be broken down into three parts: (see Fig. 3.4)

a. Forward payload section
Length of forward payload section, $L_{p1} = 52" = 1.3208$ m
Surface area, $S_{p1} = \pi D \times L_{p_1} = 2.8631$ m^2

Volume of the payload section $= \pi \dfrac{D^2}{4} \times L_{p_1} = 0.4939$ m^3

b. Parallel portion of the Pressure hull
Length of parallel portion of the pressure hull, $L_{p2} = 29.5" = 0.7493 \approx 0.75$ m
Surface area, $S_{p2} = \pi D \times L_{p2} = 1.6258$ m^2

Volume of the pressure hull[2] section $= \pi \dfrac{D^2}{4} \times L_{p2} = 0.2805$ m^3

c. Parallel portion of aft payload section (at the start of tail section)

Length of the parallel portion of the tail, $L_{p3} = 15.5" = 0.3937$ m
Surface area, $S_{p3} = \pi D \times L_{p3} = 0.8534$ m^2

Volume of the portion $= \pi \dfrac{D^2}{4} \times L_{p3} = 0.1472$ m^3

Total Surface Area & Volume of parallel mid-body section

Total length of the parallel mid-body section, $L_p = 52"+29.5"+15.5" = 97" = 2.46$ m
Total external surface area, $S_p = 5.3423$ m^2
Total volume, $V_p = 0.9216$ m^3

[2] This volume is not the actual volume of the pressure hull installed in "Explorer" as the actual volume will have the volume of the two hemispheres attached on either ends. This is only the volume of the parallel portion of the pressure hull.

3. Tail Section

The tail section consists of a faired portion which is the aft payload section followed by a cone section which houses the propeller motor. The two parts are treated separately here:

a. *Faired tail section*

The equation for the faired tail curve[3], $y(x) = -0.1822x^2 - 0.00003x + 0.3429$

$y^2(x) = 0.119025\text{-}0.1257179991x^2\text{-}0.2070\text{e-}4x\text{+}0.3319684\text{e-}1x^4\text{+}0.10932\text{e-}4x^3$

Volume of the faired tail section, $V_{ft} = \int_0^{0.9906} \pi\left[y^2(x)\right]dx = \mathbf{0.2623}\ \text{m}^3$

$x = 0$ to 39" which corresponds to limits 0 to 0.9906 m.

Faired tail portion of the *MUN Explorer* AUV

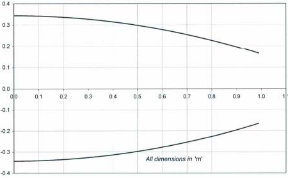

[3] All dimensions are in metres. In the Maple solution instead of the value 0.3429, the value 0.345 is used as it is exactly equal to half of 0.69 m

Calculation check using MAPLE

Volume calculation check using MAPLE

> restart;
> a:=0.345;
>

$$a := .345$$

> b:=-0.1822*x^2;

$$b := -.1822\, x^2$$

> c:=-0.00003*x;

$$c := -.00003\, x$$

> d:=a+b+c;

$$d := .345 - .1822\, x^2 - .00003\, x$$

> e:=expand(d^2);

$$e := .119025 - .1257179991\, x^2 - .00002070\, x + .03319684\, x^4 + .000010932\, x^3$$

> vol:=int(e,x=0..0.9906)*3.141592654;

$$\boldsymbol{vol := .2623118200 \approx 0.2623\ m^3}$$

Surface area calculation check using MAPLE

> restart;
> y:=-0.1822*x^2-0.00003*x+0.345;

$$y(x) = -0.1822\, x^2 - 0.00003\, x + .345$$

> y1:=diff(y,x);

$$y_1 = -0.3644\, x - 0\, .00003$$

> y2:=expand(y1^2);

$$[y_1(x)]^2 = 0.13278736\, x + 0\, .000021864\, x + 0.9\text{x}10^{-9}$$

> *l*:=sqrt(1+y2);

$$l = \sqrt{1.000000001 + 0.13278736x^2 + 0.000021864\, x}$$

> Sft:=2*pi*y**l*;

$$S_{ft} = \int_0^{0.9906} 2\pi(-0.1822x^2 - 0.00003x + 0.0345)\sqrt{1.00 + 0.13278736x^2 + 0.000021864x}\, dx$$

> int(Sft,x=0..0.9906);

$$\boldsymbol{S_{ft} = 0.5754661178\ \pi = 1.8079\ m^2}$$

Surface area of the faired-tail section, $\boldsymbol{S_{ft}}$ = **1.8079** m^2
Volume of the faired tail section, $\boldsymbol{V_{ft}}$ = **0.2623** m^3

b. Tail cone section

The equation of the tail cone is[4], $y(x) = -0.4096x + 0.1641$
Length of the tail cone section (along x-axis), $h = 11.5" = 0.2921$ m
Slant height (along the inclined surface) measured, $s = 12.5" = 0.3175$ m
Slant height (along the inclined surface) calculated[5], $s = \sqrt{(R_1 - R_2)^2 + h^2} = 0.316$ m
Where R_1 = base radius and R_2 = top radius
Radius @ the base section of the cone = 6.46" = 0.1641 m
Radius @ the end section of the cone = 1.75' = 0.0445 m
$y^2(x) = 0.1678x^2 - 0.1344x + 0.02692881$ *(See also Maple solution)*

Volume of the tail cone section, $V_{tc} = \int_0^{0.2921} \pi\left[y^2(x)\right] = 0.0111 \text{ m}^3$

Volume of the tail cone, $V_{tc} = \frac{\pi}{3} h(R_1^2 + R_1R_2 + R_2^2) = 0.0111 \text{ m}^3$

Tail Cone portion of the *MUN Explorer* AUV

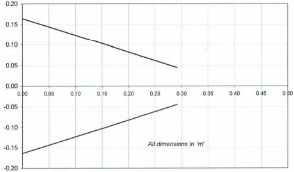

Surface area of cone (*not incl. top & bottom circles*) $= \pi(R_1 + R_2)s$
$= \pi(0.1641 + 0.0445) * 0.316 = \mathbf{0.2071} \text{ m}^2$

Surface area of cone[6], $S_{tc} = 2\pi\frac{(r_1 + r_2)}{2}.l = \pi(0.1641 + 0.0445) \times 0.3175 = 0.2081$ m^2

---

[4] The coefficients in this equation are obtained after converting the values to *metres*.
[5] Formula taken from: *http://mathworld.wolfram.com/ConicalFrustum.html*

Surface area of tail-cone obtained by numerical calculation, $S_{tc} = 0.2068\ m^2$
There is a huge difference between the two values obtained. One uses the inclined length of cone and the other uses length along x-axis.

Total surface area of tail section, $S_t = S_{ft} + S_{tc} = 1.8079 + 0.2071 = 2.015\ m^2$
Total volume of tail section, $V_t = V_{ft} + V_{tc} = 0.2623 + 0.0111 = 0.2734\ m^3$

Calculation check using MAPLE

 # Volume calculation of tail-cone section using MAPLE

> restart;

> a:=0.1641;

$$a := 0.1641$$

> b:=-0.4096*x;

$$b := -0.4096\ x$$

> d:=a+b;

$$d := 0.1641 - 0.4096\ x$$

> e:=expand(d^2);

$$e := .02692881 + 0\ .1678\ x^2 - 0\ .1344\ x$$

> vol:=int(e,x=0..0.2921)*3.141592654;

$$\mathbf{vol := .01105 \approx 0.0111\ m^3}$$

 # Surface area calculation of tail-cone section using MAPLE

> restart;

> $y(x)$=-0.4096x+0.1641;

> y1:=diff(y,x);

$$y_1(x) = -0.4096$$

> y2:=expand(y1^2);

$$[y_1(x)]^2 = 0.1678$$

> l:=sqrt(1+y2);

$$l := 1.0806$$

> Sft:=2*pi*y*l;

$$\text{Sft} := 2.1613\ \pi\ (-0.4096\ x + 0.1641) = 6.7898(-0.4096\ x + 0.1641)$$

> int(Sft,x=0..0.2921);

$$\mathbf{S_{tc} = 0.06582648\ \pi = 0.2068\ m^2}$$

[6] *Calculus: Early Transcendental* – Anton, Bivens, Davis; pg. 492

Total Surface Area of the HULL

Wetted surface area of the nose cone, S_n = **1.2782** m^2
Wetted surface area of the parallel mid-body section, S_p = **5.3423** m^2
Wetted surface area of the faired tail portion, S_{ft} = **1.8079** m^2
Wetted surface area of the tail cone, S_{tc} = **0.2071** m^2

Total wetted surface area (w.s.a) of the hull, A_{wsa} = **8.6355** m^2

Total Volume of the HULL

Volume of the nose cone, V_n = **0.1720** m^3
Volume of the parallel mid-body section, V_p = **0.9216** m^3
Volume of the faired tail portion, V_{ft} = **0.2623** m^3
Volume of the tail cone, V_{tc} = **0.0111** m^3

Total volume of the hull, V = **1.3670** m^3

The complete profile of *MUN Explorer* bare hull is shown in the figure below.

Bare hull profile of *MUN Explorer* AUV

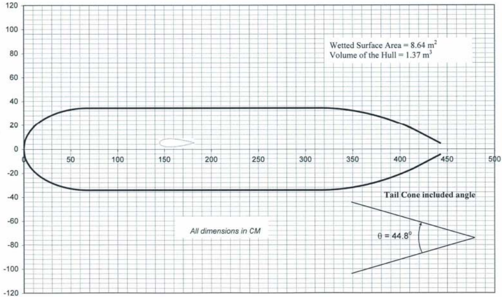

B-2 CONTROL PLANE

There are a total of six control planes for the *MUN Explorer* AUV. All control planes are identical with a NACA 0024 section and have the following geometric parameters:

Chord length, c = 14" = 0.36 m

Half-span, b = 14" = 0.36 m

Maximum thickness of the chord, t = 0.24 x 14" = 3.31" = 0.0853 m

Location of maximum thickness section is at 30% of c = .30 x 14" = 4.2" = 0.11 m

Thickness of root-base along span = 1.5" = 0.0381 m

Geometric aspect ratio, $AR = \dfrac{b}{c} = 1$

Effective aspect ratio, $a_e = \dfrac{b_{CP}^2}{A_{CP}} = 2$

where b_{CP}, is the span, measured as twice the distance from the root to the tip of the control plane and A_{CP}, is the plan-form area of a set of control planes; without including the area inside the hull.

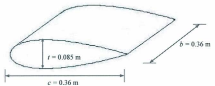

NACA 0024 Profile

B-3 Parameters Essential for the *MUN Explorer* AUV Simulation Model based on Component Build-Up Method

The following are a list of parameters that are essential for the simulation model and are obtained from literature review of the hydrodynamics of the hull and fins used for the AUV. The different parameters with their definitions are listed below.

x – axial distance from the bow of the body to any body station
x_m – axial distance from bow of body to pitching moment center
Length of the vehicle, L = **4.5** m
Volume of the hull, V = **1.3670** m^3
$\mathbf{A}_{ref}$ = reference area or wetted surface area = **8.76352** m^2

$$\mathbf{A}_p = \text{plan-form area}^7 \left(2\int_0^L R dx\right) = A_{p\_nose} + A_{p\_midbody} + A_{p\_tail}$$

$$A_{p\_nose} = \pi \frac{ab}{2} = \frac{\pi \times 0.69 \times 0.345}{2} = \mathbf{0.3739}\ \text{m}^2$$

$$A_{p\_midbody} = 0.69 \times 2.46 = \mathbf{1.6974}\ \text{m}^2$$

$$A_{p\_tail} = 2\int_0^{0.9906}(-0.1822x^2 - 0.00003x + 0.3429)dx + 2\int_0^{0.2921}(-0.4096x + 0.1641)dx$$

$$2\left(\frac{-0.1822x^3}{3} - \frac{0.00003x^2}{2} + 0.3429x + C_1\right)_0^{0.9906} + 2\left(\frac{-0.4096x^2}{2} + 0.1641x + C_2\right)_0^{0.2921}$$

$$C_1 = C_2 = 0$$

$$= 2\left(\frac{-0.1822x^3}{3} - \frac{0.00003x^2}{2} + 0.3429x\right)_0^{0.9906} + 2\left(\frac{-0.4096x^2}{2} + 0.1641x\right)_0^{0.2921}$$

$$= 0.5654 + 0.0609 = \mathbf{0.6263}\ \text{m}^2$$

$$\mathbf{A}_p = A_{p\_nose} + A_{p\_midbody} + A_{p\_tail}$$

$$= 0.3739 + 1.6974 + 0.6263 = \mathbf{2.6976}\ \text{m}^2$$

S_b – cross-sectional area of the base
S_x – cross-sectional area of the hull at a distance of x from the bow or at station x.
Axial distance x_c of the centroid of the plan-form area A_p from the tip of nose

[7] **Allen & Perkins**: A study on effects of viscosity on flow over slender inclined bodies of revolution

Centroid of the semi-elliptical nose cone: $= 0.69 - \dfrac{4 \times 0.69}{3 \times \pi} = \mathbf{0.3972}$ m from nose-tip

Plan-form area of the semi-ellipse: $= 0.3739\ m^2$

Centroid of the parallel mid-body section $= 0.69 + 2.46/2 = \mathbf{1.92}$ m from nose-tip

Plan-form area of the parallel mid-body section: $= 1.6974\ m^2$

Centroid of the faired tail section: $= 0.69 + 2.46 + 0.4436 = \mathbf{3.5936}$ m from nose-tip

Plan-form area of the faired tail section: $= 0.5654\ m^2$

$$\bar{x}_c = \frac{2\int_0^l r(x).x.dx}{2\int_0^l r(x)dx} = \mathbf{0.4436}\ \text{m}$$

Centroid of the tail cone section: $= 0.69 + 2.46 + 0.9906 + 0.1181 = \mathbf{4.2587}$ m

Plan-form area of the tail cone section: $= 0.0609\ m^2$

$$\bar{x}_c = \frac{h(2a+b)}{3(a+b)} = \mathbf{0.1181}\ \text{m; where } a = 2 \times 0.0445;\ b = 2 \times 0.1641$$

Axial distance x_c of the centroid of plan-form area, A_p from nose tip

=

$$\frac{0.3739 \times 0.3972 + 1.6974 \times 1.92 + 0.5654 \times 3.5936 + 0.0609 \times 4.2587}{0.3739 + 1.6974 + 0.5654 + 0.0609} = \frac{5.6987}{2.6976} = 2.1125$$

Thus x_c, the axial distance of the centroid of plan-form area A_p from the nose tip is,

$\boxed{x_c = \mathbf{2.1125}\ \text{m}}$ (Perrault denotes it as x_p)

Hopkins derived equations similar to those of Allen & Perkins, but used different limits of integration for each of the terms in the equations. He integrated the potential terms from the nose to a point x_0 on the body, and viscous flow terms from x_0 to the tail. Allen & Perkins had integrated both sets of terms over the whole length of the hull, and added the results.

The station x_0 can be determined from Hopkins and is given by the following equation:

$$\frac{x_0}{L} = 0.328 + 0.527\frac{x_1}{L}$$

where x_1 is the longitudinal distance from body nose to point at which dS/dx has a maximum negative value.

Estimation of x_0

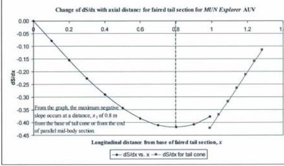

The longitudinal distance of the station where the maximum negative value for dS/dx occurred was estimated to be 0.8 m from the start (base) of the faired tail section. Hence, the longitudinal distance x_1 of this station from the nose is

$$x_1 = 0.69 + 2.46 + 0.8 = 3.95 \text{ m}$$

Hence, $\qquad x_0 = 0.378L + 0.527x_1 = \mathbf{3.7827}$ m

Radius r_{x0}, at station $x_0 = 0.2284$ m

Cross-section area $S_{x0} = \pi r_{x0}^2 = 0.1638 \text{ m}^2$

Plan-form area of that portion of the faired tail section until station $x_0 = \mathbf{0.4043}$ m^2

$$= 2\left(\frac{-0.1822x^3}{3} - \frac{0.00003x^2}{2} + 0.3429x\right)_0^{0.6327} = 0.4043 \text{ m}^2$$

A_{p0}, the plan-form area until station $x_0 = 0.3739 + 1.6974 + 0.4043 = \mathbf{2.4756}$ m^2

Centroid of the plan-form area A_{p0}, is

$$x_{c0} = \frac{0.3739 \times 0.3972 + 1.6974 \times 1.92 + 0.4043 \times 3.4532}{0.3739 + 1.6974 + 0.4043} = \frac{4.8037}{2.4756} = 1.9404 \text{ m}$$

(Perrault denotes it as x_{p0})

APPENDIX – C

MUN Explorer Inertial Parameters

The calculation of Mass, Moment of Inertias and Product of Inertias of the *MUN Explorer* AUV are detailed below:

C-1 Estimation of Wet-Mass, Centre of Gravity (CG) and Centre of Buoyancy of the *MUN Explorer* AUV

The mass of the vehicle in operational condition includes the dry mass of the vehicle with all its components and instruments plus the mass of the flood-water in the flooded space.

Dry mass of *Explorer* as per manufacturer[1] (ISE Ltd.) specification = **630.6** kg

Mass of flood-water

Mass of flood-water = Mass of Hull volume of water – Wt. of water displaced by the Pressure Hull & equipment inside.

Mass of water displaced by the external geometry of the bare hull

$$\nabla = V.\rho_{seawater} = 1.3670 \times 1025 = \mathbf{1401.2} \text{ kg}$$

This does not contain the mass of water displaced by the components external to the hull such as control planes and propeller.

Total displacement of the individual components of the vehicle in seawater = 644.2 kg (ISE supplied). This includes the displacements of external components like the control planes and propeller and hence has to be deducted.

Displacement of the fins and propeller in sea water = (43.3 + 0.7)*1.025 = 45.1 kg

Therefore, **mass of flood-water** = 1401.2 – (644.2 – 45.1) = **802.1** kg

Wet mass of the MUN Explorer

Wet mass of the vehicle = Dry mass + mass of flood-water

$$M = 630.6 + 802.1 = \mathbf{1432.7} \text{ kg}$$

[1] Weight – Balance spread sheet "*MUN_Explorer*_Inertia_Properties.xls" for details supplied by ISE.

Calculation of C.B of the *MUN Explorer* AUV					
C.B of the bare hull	Length	Vol.	Displ.	Centroid	Moment
	[m]	[m3]	[kg]	[m]	[kg.m]
Nose cone	0.69	0.1720	176.3	0.431	76.0
Parallel mid-body section	2.46	0.9216	944.6	1.920	1813.7
Faired tail section	0.99	0.2623	268.9	3.536	950.7
Tail cone	0.29	0.0111	11.4	4.236	48.2
C.B of the bare hull from nose-tip =	**4.43**	**1.3670**	**1401.2**	**2.062**	**2888.6**
Displacements of ext. equipments					
Dive planes			15.9	1.524	24.2
Tail planes			27.0	3.607	97.4
Acoustic transponder			0.3	1.226	0.4
Tow lug, backplate & shackle			0.2	0.737	0.1
Lifting lugs, backplate			0.4	2.388	1.0
GPS antenna			0.3	3.658	1.1
Ethernet radio/antenna			0.3	3.708	1.1
propeller & spinner			0.7	4.420	3.1
			45.1		**128.4**
				2.847	
C.B of *MUN Explorer* AUV from nose-tip			**1446.3**	**2.086**	**3017.0**

Total moment due to displacement =	**3017.0**	kg.m
Total displacement of the vehicle =	**1446.3**	kg
C.B of the vehicle from nose tip =	**2.086**	m

Calculation of C.G of the MUN Explorer AUV					
	Mass	Dist. Of	Moment	Vert.dist	Moment
	[kg]	C.G [m]	[kg.m]	of CG [m]	[kg.m]
Nose cone	201.0	0.442	88.8	0.029	5.8
Forward payload section	431.3	1.210	521.9	-0.002	-1.0
Pressure hull	400.0	2.379	951.6	0.043	17.2
Aft payload section	371.4	3.500	1299.9	0.003	1.2
Tail cone section	29.0	4.202	121.9	0.011	0.3
	1432.7		**2984.1**		**23.5**
C.G of MUN Explorer AUV		**2.083**		**0.0170**	

Total mass of the vehicle =	**1432.7**	kg
Total moment of comp. w.r.t to nose-tip=	**2984.1**	kg.m
C.G of MUN Explorer AUV from nose tip =	**2.083**	m

Net displacement of the vehicle =	**13.6**	kg
Longitudinal separation of CG & CB	**-0.003**	m
Static pitch angle =	**-10.7**	deg

C-2 Estimation of Moments and Products of Inertia

In order to estimate the Moment of Inertia (MI) of the vehicle, the entire vehicle was decomposed into nose, payload, pressure hull, faired tail and tail cone sections with the components that fall within that section. Hence, all components within the nose section are collected together and the C.G and MI of that section were calculated. Similarly, all components within the payload section were collected together and the C.G and MI of that composite section calculated and so on. Finally, the results from all the different sections were added together to obtain the total MI of the vehicle

MOMENT OF INERTIA OF EACH SECTION

a. Nose Cone

Mass of dry nose cone shell of thickness t (5 mm) = 9.32 kg
Displacement of the shell in seawater = 5.2 x 1.025 = 5.33 kg
Mass of equivalent volume (ext. geometry) of seawater = 0.172 x 1025 = 176.3 kg
Mass of water that can be contained inside nose = 176.3 – 5.33 = 170.97 kg
Net displacements of all the equipment inside nose cone = 3.6 kg
Dry weight of the nose cone incl. all components = 34.4 kg
Total mass of nose cone = 170.97-3.6+34.4 = **201.7** kg

Assumption – 1

The semi-ellipsoidal GRP *shell* and the volume of water contained within can be treated as a single *solid* semi-ellipsoid for MI calculations.

Estimate the C.G of the nose section

The C.G of the semi-ellipsoidal shell = 16" from the nose tip or 11" from the base

The C.G of the solid semi-ellipsoidal nose [13] from the base is:

$$\bar{x} = \frac{3a}{8} = 3*0.69/8 = 0.259 \text{ m}$$

Distance of this C.G of the solid nose from the nose tip = 0.69 – 0.259 = 0.431 m

The C.G of the all-inclusive semi-ellipsoidal nose cone is,

$$\bar{x} = \frac{180.29 \times 0.431 + (2.3 - 1.4) \times 0.288 + ... + (21.818 - 1.931) \times 0.567}{201.7}$$

$\bar{x} = \mathbf{0.442}$ **m** from the tip of nose

Mass of nose shell + water contained = 9.32 + 170.97 = **180.3** kg

MI of a solid semi-ellipsoid about x-axis, $I_{xx} = m\dfrac{(b^2+c^2)}{5}$, where $m = \dfrac{2}{3}\pi\rho abc$

When $b = c$ as in the present case, $I_{xx} = \dfrac{4}{15}\pi\rho ab^4$

$$I_{xx} = 180.29\frac{(2\times 0.345^2)}{5} = \mathbf{8.584}\ \text{kg.m}^2$$

MI of the semi-ellipsoid nose about the base[2], $I_{yy} = I_{zz} = \dfrac{1}{5}m(b^2+a^2)$

$$= \frac{1}{5}m(b^2+a^2) = \frac{1}{5}(180.29)(0.345^2+0.69^2) = \mathbf{21.46}\ \text{kg.m}^2$$

Total MI of (Shell + Water), I_{xx} = **8.584** kg.m^2
Total MI of (Shell + Water), I_{yy} = **21.46** kg.m^2
Total MI of (Shell + Water), I_{zz} = **21.46** kg.m^2

The station point of base of nose cone is at 1.751 m forward of the C.B of the vehicle. The C.G of the nose cone with all equipment and flood-water is 0.246 m forward of the station point but the C.G of the nose cone just filled with water is 0.259 m forward of the base.

Thus the moment of inertia of the nose shell about x, y and z-axes (w/o equipment) passing through the C.G can be obtained as below:

$$I_{yy} = I_{zz} = \bar{I}_G + m\bar{x}^2$$
$$21.46 = I_G + 180.29*0.259^2$$
$$\bar{I}_y = \bar{I}_z = \mathbf{9.37}\ \text{kg.m}^2\ \&\ \bar{I}_x = \mathbf{8.584}\ \text{kg.m}^2$$

Moment of Inertia of the nose cone just filled with water w.r.t the C.G of the vehicle is as follows:

$$I_{xx} = \bar{I}_x + m\bar{r}^2 = 8.584 + 180.29\times 0.017^2 = \mathbf{8.64}\ \text{kg.m}^2$$
$$I_{yy} = \bar{I}_y + m\bar{r}^2 = 9.37 + 180.29 \text{ x } 1.652^2 = \mathbf{501.4}\ \text{kg.m}^2$$
$$I_{zz} = \bar{I}_z + m\bar{r}^2 = 9.37 + 180.29 \text{ x } 1.652^2 = \mathbf{501.4}\ \text{kg.m}^2$$

[2] **Meriam, J. L.,** *DYNAMICS*, pg. 382

Product of Inertia of the Nose Cone

The PI of the nose cone was estimated using the parallel axis theorem. First, the product of inertia of the nose cone filled with water is calculated w.r.t the C.G of the nose cone, and then it's transformed to the C.G of the vehicle. The nose cone filled with water being symmetrical about xy and xz plane, the PI about C.G of nose cone $\bar{I}_{xy} = \bar{I}_{xz} = \bar{I}_{zy} = 0$. The PI of the nose cone w.r.t the C.G of the vehicle is calculated using the relation:

$$I_{xy} = \bar{I}_{xy} + m.d_x d_y$$

where d_x and d_y are x and y distances of the C.G of the nose cone from planes planes yz and xz respectively.

For the above nose cone section, the PI I_{xy}, I_{yz}, I_{zx} are:

$$\boxed{\begin{array}{l} I_{xy} = 1.6 \text{ kg.m}^2 \\ I_{yz} = 0.3 \text{ kg.m}^2 \\ I_{zx} = 3.2 \text{ kg.m}^2 \end{array}}$$

Assumption – 2

The moment of inertia contribution from the altimeter, trim weights and other equipment can be calculated by considering them as PInt masses, so that the equation $I = m.r^2$ can be used.

The moment of inertia produced by equipments within the nose cone should be added but their MI due to its displacement has to be deducted from the MI value obtained for inner volume completely filled with water.

b. Forward Payload Section

The forward payload section is 52" (1.32 m) long having a diameter of 0.69m giving a total external volume of 0.494 m^3. This section contains a semi-hemispherical portion of the Al pressure hull, which has to be deducted from the volume, and consequently the mass of the water occupied by that volume.

Mass of the cylindrical payload shell = **24.3** kg
Displacement of the cylindrical shell in seawater = 13.6 x 1.025 = 13.94 kg
Mass of equivalent volume (ext.) of water = 0.494 x 1025 = 506.35 kg
Mass of water that can be contained within the shell = 506.35 – 13.94 = 492.41 kg

Volume of the semi-hemispherical shell
Displacement of the pressure hull in sea water = 511.1 x 1.025 = 523.88 kg
Total vol. of pressure hull = 523.88/1025 = 0.511 m^3
Vol. of the parallel section of pressure hull (29.5") long = 0.280 m^3
Vol. of the spherical end-caps = 0.511 – 0.280 = 0.231 m^3
Vol. of hemispherical shell within payload section = 1/2 x 0.231 = 0.115 m^3
Mass of water displaced by that volume = 0.115 x 1025 = 117.88 kg
Actual mass of water contained by the payload section = 492.41 – 117.88 = **374.53** kg
Mass of cylinder shell + floodwater - water displaced by the hemi-sphere
= 24.3 + 374.53 = **398.83** kg[3]

Apart from this the equipment present within the shell also displaces the contained water which is estimated to be 10.0 kg thus giving 398.83 – 10 = 388.83 kg.
Dry weight of complete payload section[4] = 67 kg [*This includes the dive planes*]
Total mass of the forward payload section = 67 + 388.83 –24.3-16.6= **414.7**
[*This excludes the dive planes, which are outside of the GRP hull*]
Outer radius[5] of hemi-spherical shell = 0.34 m

<u>*Estimate the C.G of the Section*</u>

For the purpose of calculation of C.G, the dive planes & all external components have to be considered as well. Hence the total weight of payload section with these external components = 67 kg considered.

[3] This total (398.83 kg) contains the wt. of water that would otherwise be there if the equipments are absent. Hence the actual mass of flood water would be this value minus the displacements of equipment.
[4] This value should not contain the weight of dive planes that are actually outside of the payload section.
[5] This value of radius (0.34 m) found in the "ISE MUN AUV Specification.doc" may not match with the value estimated from the volume of hemi-spherical shell obtained. However, considering the geometry of the vehicle, only a size less than or equal to 0.34 m can fit within the GRP hull and hence this value is adopted for MI calculation. Also the estimated value of radius (~0.38 m) may be due to some projections for connectors and other stuffs on the surface of the pressure hull.

The station point of base (end-point) of the payload section is 79" (2.0066 m) from nose.

C.G of (Shell + Water) unit from the nose tip = 0.69 + 1.321/2 = **1.351** m

C.G of the hemi-spherical shell is, $\frac{3}{8}r = \frac{3}{8} \times 0.34 =$ 0.1275 m from the base of the payload section.

C.G of this hemi-sphere from the tip of nose cone = 0.69+1.321-0.1275 = **1.884** m

C.G of the forward payload section from the tip of nose =

$$\bar{x} = \frac{516.71 \times 1.351 - 117.88 \times 1.884 + ...\Sigma m_i \times x_i}{431.6} = \mathbf{1.21}\ \text{m}$$

Mass of the composite unit = 24.3 + 492.41 = 516.71 kg

MI of dry shell about x-axis = $m.r^2$ = 24.3 x 0.345^2 = **2.89** kg.m^2

MI of water contained about x-axis, $I_{xx} = \frac{1}{2} m.r^2 = \frac{1}{2}$ x 492.41 x 0.345^2 = **29.31** kg.m^2

Total MI about x-axis of (Shell + Water) = 2.806 + 29.307 = **32.11** kg.m^2

MI of the composite unit about y and z-axes passing through the mid-point (C.G) of the composite unit:

MI of the shell about y and z – axes passing through the C.G of the section

$$I_{yy} = I_{zz} = \frac{1}{12} m(6r^2 + l^2) = \frac{1}{12} \times 24.3(6 \times 0.345^2 + 1.321^2) = \mathbf{4.98}\ \text{kg.m}^2$$

MI of the flood water about y and z – axes passing through the C.G of the section

$$I_{yy} = I_{zz} = \frac{1}{12} \times m(3R^2 + l^2) = \frac{1}{12} \times 492.41(3 \times 0.345^2 + 1.321^2) = \mathbf{86.17}\ \text{kg.m}^2$$

Total MI of (Shell + water) about y and z-axes passing through the C.G of the section

= 4.938 + 86.26 = **91.14** kg.m^2

MI of the hemi-spherical section[6] about x-axis,

$$I_{xx} = \frac{2}{5}m.r^2 = \frac{2}{5}\times -117.88\times 0.34^2 = \mathbf{-5.45}\ \text{kg.m}^2$$

MI of the hemi-spherical section about y and z-axes passing through the C.G of the hemi-sphere is,

$$I_{yy} = I_{zz} = 0.259.mr^2 = 0.259 \times -117.88 \times 0.34^2 = \mathbf{-3.53}\ \text{kg.m}^2$$

Moment of Inertia of the cylindrical shell about y and z-axes passing through the C.G of the vehicle can be estimated using the parallel-axis theorem

$$I_{Gxx} = I_{xx} + m\bar{r}^2 = 2.89 + 24.3\times 0.017^2 = \mathbf{2.9}\ \text{kg.m}^2$$

$$I_{Gyy} = I_{yy} + m\bar{r}^2 = 4.98 + 24.3\times 0.73^2 = \mathbf{17.93}\ \text{kg.m}^2$$

$$I_{Gzz} = I_{zz} + m\bar{r}^2 = 4.98 + 24.3\times 0.73^2 = \mathbf{17.93}\ \text{kg.m}^2$$

The Moment of the Inertia of the cylinder of water w.r.t C.G of the vehicle,

$$I_{Gxx} = I_{xx} + m\bar{r}^2 = 29.31 + 492.5\times 0.017^2 = \mathbf{29.45}\ \text{kg.m}^2$$

$$I_{Gyy} = I_{yy} + m\bar{r}^2 = 86.17 + 492.5\times 0.73^2 = \mathbf{348.62}\ \text{kg.m}^2$$

$$I_{Gzz} = I_{zz} + m\bar{r}^2 = 86.17 + 492.5\times 0.73^2 = \mathbf{348.62}\ \text{kg.m}^2$$

Moment of Inertia of the hemi-sphere about the C.G of the vehicle[7]

$$I_{Gxx} = I_{xx} + m\bar{r}^2 = -(5.45 + 117.88\times 0.017^2) = \mathbf{-5.48}\ \text{kg.m}^2$$

$$I_{Gyy} = I_{yy} + m\bar{r}^2 = -(3.53 + 117.88\times 0.197^2) = \mathbf{-8.11}\ \text{kg.m}^2$$

$$I_{Gzz} = I_{zz} + m\bar{r}^2 = -(3.53 + 117.88\times 0.197^2) = \mathbf{-8.11}\ \text{kg.m}^2$$

Total Moment of Inertia of the forward payload section with water about the C.G of the vehicle,

$\boldsymbol{I_{xx}}$ = 2.9 + 29.45 - 5.64 = **26.71** kg.m^2
$\boldsymbol{I_{yy}}$ = 17.93 + 348.62 - 8.21 = **358.34** kg.m^2
$\boldsymbol{I_{zz}}$ = 17.93 + 348.62 - 8.21 = **358.34** kg.m^2
$\boldsymbol{I_{xy} = I_{yz} = I_{zx} = 0}$

---

[6] **Fowler, B.**, *Dynamics: Engineering Mechanics.* (Inside of last cover page.)
[7] This MI of this volume has to be deducted from the previous composite unit and hence the negative values.

MI and PI of Dive Planes

The moment of inertias of control planes (dive planes) were estimated using some approximate methods. A plan view of the dive plane is shown below. The C.G of the plane is 1.524 m behind the nose-tip and is off centered as shown in the figure. Assume that the mass of the plane is equally divided along yz-plane.

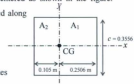

Mass of one dive plane = 8.3 kg
Mass of region $A_1 = A_2 = 4.15$ kg
The dive planes are considered as rectangular flat plates of mass 8.3 kg having a C.G offset as shown.

$I_{xx} = 0.088$ kg.m^2
$I_{yy} = 0.102$ kg.m^2
$\rho_1 = 4.15/(0.3556\text{x}0.2506) = 16.6$ kg/m^2
$\rho_2 = 4.15/(0.3556\text{x}0.105) = 111.15$ kg/m^2

This result was used to calculate I_{yy}, I_{zz} was also calculated in a similar way by assuming a small element of area *dxdy* and summing up the MIs of each element with respect to a vertical axis passing through the CG.

$I_{zz} = 0.095$ kg.m^2

Since the control planes are symmetric about xy-plane as well as the xz-plane, the PI I_{xy}, I_{zx} and I_{yz} are zero.

MI and PI of Acoustic Telemetry Transducer

The LinkQuest acoustic telemetry transducer is not considered as a point mass, rather it was considered as a solid cylinder having the following dimensions[8]:

Overall length, l = 286 mm = 0.286 m
Housing diameter, d = 144 mm = 0.144 m; r = 0.072m;
Weight in air = 7.6 kg
Weight in water = 4.1 kg

[8] http://www.link-quest.com/html/uwm4000.htm

However, the weight measurements given in the Weight-Ballast sheet issued by the ISE is different from these values and hence the ISE given values are used instead of the LinkQuest manufacturer values.

Weight in air = 12.0 kg

Weight in water, $m = 12 - 5.5 = 6.5$ kg

$$I_{xx} = I_{yy} = \frac{1}{4}mr^2 + \frac{1}{12}ml^2 = 0.0527 \text{ kg.m}^2$$

$$I_{zz} = \frac{1}{2}mr^2 = 0.0169 \text{ kg.m}^2$$

The MI of the transducer about a parallel set of axes passing through the C.G of the vehicle can be estimated using the *parallel axis theorem*.

---

c. Pressure Hull

The pressure hull structure consists of a hollow cylindrical section of 29.5" (~0.75 m) long with two hemi-spherical end caps on either side, each 0.34 m deep. The thickness of Aluminium pressure hull is t = 1.14 cm. *The mass distribution of the pressure hull is assumed to be uniform.* This section also contains batteries and lead blocks (to simulate empty spaces of batteries), which can be considered as rectangular blocks and the MI of a rectangular block may be applicable to it as well.

The total mass of the pressure hull = 215.2 kg

Assumption: The mass contribution of each component is roughly estimated as a ratio of their apparent surface area[9], i.e, A_{cyl}/A_{shp}.

Total surface area of pressure hull = $\pi dl + 4\pi r^2 = \pi 0.69 \times 0.75 + 4\pi \times 0.345^2$
$= 1.626 + 1.496 = 3.122$ m²

Contribution of *cylindrical* portion = $\frac{1.626}{3.122} \times 215.2 =$ **112.08** kg

Contribution of each *end-cap* (hemi-spherical portion) = $\frac{1}{2} \times \frac{1.496}{3.122} \times 215.2 =$ **51.56** kg

Moment of Inertia of the hollow aluminum cylinder of thickness t = 1.14 cm.

MI of the hollow cylinder about x-axis, $I_{x1} = m.r^2 = 112.08 \times 0.345^2 =$ **13.34** kg.m²

[9] Since the pressure hull is hollow and behaves as a shell, it would be more appropriate to choose the surface area of the shell than to choose the volume of the shell while calculating the mass contributions.

MI of the same about y and z-axes passing through its C.G, $I_{yy} = I_{zz} = \frac{1}{2}mr^2 + \frac{1}{12}ml^2$

$$I_{yy} = I_{zz} = \frac{1}{2}112.08 \times 0.345^2 + \frac{1}{12}112.08 \times 0.75^2 = \mathbf{11.92}\ \text{kg.m}^2$$

The geometric centre of the hollow cylinder ($l/2$ = 14.75"= 0.375 m) is 2.386 m from the nose. Hence, the C.G of the hollow cylinder is 0.303 m (30 cm) behind the actual C.G of the vehicle (2.083).

Moment of Inertia of the hollow cylinder about x-axis through C.G,

$$I_{xx} = 13.34 + 112.08 \times 0.017^2 = \mathbf{13.37}\ \text{kg.m}^2$$

Moment of Inertia of the hollow cylinder about y-axis through C.G,

$$I_{yy} = \bar{I}_y + m\bar{r}^2 = 11.92 + 112.08 \times 0.303^2 = \mathbf{22.21}\ \text{kg.m}^2$$

Moment of Inertia of the hollow cylinder about z-axis through C.G,

$$I_{zz} = \bar{I}_z + m\bar{r}^2 = 11.92 + 112.08 \times 0.303^2 = \mathbf{22.21}\ \text{kg.m}^2$$

Moment of Inertia of the hemispherical ***forward end-cap***

MI of the hemi-sphere about x-axis, $I_{xx} = \frac{2}{3}mr^2 = \frac{2}{3} \times 51.56 \times 0.34^2 = \mathbf{3.97}\ \text{kg.m}^2$

MI of the hemi-sphere about y and z-axes passing through the C.G of hemi-sphere is,

$$I_{yy} = I_{zz} = \frac{5}{12}mr^2$$

$$I_{yy} = I_{zz} = \frac{5}{12} \times 51.56 \times 0.34^2 = \mathbf{2.49}\ \text{kg.m}^2$$

C.G of the hemi-spherical shell is $x = r/2 = 0.17$ m. The distance of geometric centre of the forward end-cap from the C.G of the vehicle = 0.242 m and –0.017m high.

Moment of Inertias of the *forward end-cap* w.r.t C.G of the vehicle are

$$I_{xx} = \bar{I}_x + m\bar{r}^2 = 3.97 + 51.56 \times 0.017^2 = \mathbf{3.99}\ \text{kg.m}^2$$

$$I_{yy} = \bar{I}_y + m\bar{r}^2 = 2.49 + 51.56 \times 0.242^2 = \mathbf{5.51}\ \text{kg.m}^2$$

$$I_{zz} = \bar{I}_z + m\bar{r}^2 = 2.49 + 51.56 \times 0.242^2 = \mathbf{5.51}\ \text{kg.m}^2$$

Moment of Inertia of the ***aft end-cap***

The distance of C.G of the *aft end-cap* from the nose tip = 2.931 m

The distance of C.G of the *aft end-cap* from the C.G of the vehicle = 0.848 m

Moment of Inertias of the *aft end-cap* w.r.t C.G are,

$$I_{xx} = \bar{I}_x + m\bar{r}^2 = 3.974 + 51.56 \times 0.017^2 = \mathbf{3.99}\ \text{kg.m}^2$$

$$I_{yy} = \bar{I}_y + m\bar{r}^2 = 2.49 + 51.56 \times 0.848^2 = \mathbf{39.57}\ \text{kg.m}^2$$

$$I_{zz} = \bar{I}_z + m\bar{r}^2 = 2.49 + 51.56 \times 0.848^2 = \mathbf{39.57}\ \text{kg.m}^2$$

Total Moment of Inertia of the Aluminum pressure hull shell about the C.G of the vehicle

$$I_{xx} = 13.37 + 3.99 + 3.99 = \mathbf{21.35}\ \text{kg.m}^2$$
$$I_{yy} = 22.21 + 5.51 + 39.57 = \mathbf{67.29}\ \text{kg.m}^2$$
$$I_{zz} = 22.21 + 5.51 + 39.57 = \mathbf{67.29}\ \text{kg.m}^2$$

The C.G of the pressure hull weighing 215.2 kg can be assumed to be at the geometrical centre of the pressure vessel (mid-point of Al cylindrical section) itself, which is 2.386 m from the tip of the nose.

Batteries, Lead Blocks and Battery Tray:

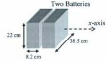

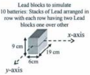

Batteries:

Moment of Inertia of the two batteries and 10 lead blocks assumed to be a rectangular block.

Mass of two batteries, $m = 23.5$ kg

Dimensions of individual batteries, $a = 38.5$cm, $b = 22$ cm & $l = (8.2\text{x}2+1.6) = 18$ cm

MI of the rectangular block about x-axis, $I_{xx} = \frac{1}{12}m(a^2 + b^2)$

$$I_{xx} = \frac{1}{12} \times 23.5 \times (0.385^2 + 0.22^2) = \mathbf{0.385}\ \text{kg.m}^2$$

MI of the rectangular block about y-axis, $I_{yy} = \frac{1}{12}m(b^2 + l^2)$

$$I_{yy} = \frac{1}{12} \times 23.5 \times (0.22^2 + 0.18^2) = \mathbf{0.158}\ \text{kg.m}^2$$

MI of the rectangular block about z-axis, $I_{zz} = \frac{1}{12}m(a^2 + l^2)$

$$I_{zz} = \frac{1}{12} \times 23.5 \times (0.385^2 + 0.18^2) = \mathbf{0.353} \text{ kg.m}^2$$

The C.G of the battery assembly is 0.34 m aft of the C.G of the vehicle and 0.06 below the CG. The MI of the battery assembly w.r.t the C.G of the vehicle are:

$$I_x = \bar{I}_x + m\bar{r}^2 = 0.385 + 23.5 \times 0.085^2 = \mathbf{0.555} \text{ kg.m}^2$$
$$I_y = \bar{I}_y + m\bar{r}^2 = 0.158 + 23.5 \times (0.69^2 + 0.085^2) = \mathbf{11.516} \text{ kg.m}^2$$
$$I_z = \bar{I}_z + m\bar{r}^2 = 0.353 + 23.5 \times 0.69^2 = \mathbf{11.541} \text{ kg.m}^2$$

Lead Blocks:
Mass of 10 rows of lead blocks = 110.7 kg

Dimensions of the whole array of 10 lead block stacks, a = 19cm, b = 9 cm & l = 82 cm. This array of lead blocks has their C.G at 13.5 cm below the C.G of the vehicle or 15 cm below the C.B of the Vehicle.

MI of lead blocks about x-axis, $I_{xx} = \frac{1}{12} \times 110.7 \times (0.19^2 + 0.09^2) = 0.408 \text{ kg.m}^2$

MI of the rectangular block about y-axis,

$$I_{yy} = \frac{1}{12} \times 110.7 \times (0.09^2 + 0.82^2) = 6.278 \text{ kg.m}^2$$

MI of the rectangular block about z-axis,

$$I_{zz} = \frac{1}{12} \times 110.7 \times (0.19^2 + 0.82^2) = 6.536 \text{ kg.m}^2$$

The C.G of the array of lead block is 0.18 m aft of the C.G of the vehicle and 0.135 m below the CG. The MI of the lead-block array w.r.t the C.G of the vehicle are:

$$I_x = \bar{I}_x + m\bar{r}^2 = 0.408 + 110.7 \times 0.11^2 = \mathbf{1.758} \text{ kg.m}^2$$
$$I_y = \bar{I}_y + m\bar{r}^2 = 6.278 + 110.7 \text{ x } (0.17^2 + 0.11^2) = \mathbf{9.478} \text{ kg.m}^2$$
$$I_z = \bar{I}_z + m\bar{r}^2 = 6.536 + 110.7 \times 0.17^2 = \mathbf{9.781} \text{ kg.m}^2$$

Battery Tray:

The battery tray is assumed to be a thin plate.
Weight of the battery tray = 2.8 kg with dimensions a = 100cm & b = 38.5cm

MI of the thin rectangular plate, $I_{xx} = \frac{1}{12} mb^2 = \frac{1}{12} \times 2.8 \times 0.385^2 = 0.035 \text{ kg.m}^2$

MI of the thin rectangular plate, $I_{yy} = \frac{1}{12} ma^2 = \frac{1}{12} \times 2.8 \times 1.0^2 = 0.233 \text{ kg.m}^2$

MI of the thin rectangular plate, $I_{zz} = \frac{1}{12}m(a^2 + b^2)$

$$= \frac{1}{12} \times 2.8 \times (0.385^2 + 1.0^2) = 0.268 \text{ kg.m}^2$$

The C.G of the array of lead block is 0.10 m forward of the C.G of the vehicle and 0.16 m below the CG. The MI of the lead-block array w.r.t the C.G of the vehicle are:

$$I_x = \bar{I}_x + m\bar{r}^2 = 0.035 + 2.8 \times 0.186^2 = \mathbf{0.132} \text{ kg.m}^2$$
$$I_y = \bar{I}_y + m\bar{r}^2 = 0.233 + 2.8 \times (0.25^2 + 0.186^2) = \mathbf{0.509} \text{ kg.m}^2$$
$$I_z = \bar{I}_z + m\bar{r}^2 = 0.268 + 2.8 \times 0.186^2 = \mathbf{0.45} \text{ kg.m}^2$$

Product of Inertia:

The products of inertia of a body are measures of *symmetry* or *dynamic imbalance*. If a particular plane is a plane of symmetry, then the products of inertia associated with any axis *perpendicular* to that plane are **zero**. The product of inertia of the Battery tray assumed as a thin plate, about the C.G is all zeros. $I_{xy} = I_{yz} = I_{zx} = 0$

d. Aft Payload

The aft payload section consists of a portion of the parallel mid-body section immediately behind the pressure vessel combined with the faired tail section forming a single unit. Hence the total volume of this unit is equivalent to the volume of the cylindrical aft portion plus the volume of the faired tail portion. Also embedded in this section is the aft hemi-spherical section of the pressure vessel, which is to be deducted from the flood volume of water.

Dry weight of the aft payload section = 19.545 kg
Displacement of the aft payload section in seawater = 10.919x1.025 = 11.192 kg
Total exterior volume = 0.1472 + 0.2623 = 0.4095 m^3
Mass of equivalent (ext.) volume of water = 0.4095 x 1025 = 419.736 kg
Mass of water that can be contained within = 419.736 – 11.192 = 408.54 kg
Mass of dry shell + water = 408.54 + 19.545 = **428.085** kg

Mass contributed by the cylindrical portion of the aft section $= \dfrac{0.1472}{0.4095} \times 428.1$

=153.88 kg

Mass contributed by the faired tail portion of the aft section $= \dfrac{0.2623}{0.4095} \times 428.1$

=274.20 kg

Volume of water displaced by the aft-hemisphere of pressure hull = -0.115 m^3
Displacement by the hemisphere = -0.115 x 1025 = **-117.88** kg
Displacement of equipments *within* the shell = **-20.2** kg
Net weight of dry shell + flood water = 428.085 – 117.88 – 20.2 = 290.01 kg
Dry weight of all equipments (*exclude shell but incl. 4 tail planes*) = 100.9 –19.5 = 81.4 kg
Total mass of the aft payload section = 290.01 + 81.4 = **371.41** kg

The location of C.G of the cylindrical portion of the aft section from nose tip = 2.953 m
The location of C.G of the faired tail section from the nose tip = 3.536 m
The location of C.G of the hemisphere from nose tip = 2.883 m

Cylindrical portion of the aft payload section
MI of the cylindrical portion of the aft section filled with water, which is 15.5" (0.3937 m) long and has the C.G at 116.25" (2.953 m) from the tip of the nose.

MI of the same about x-axis, $\bar{I}_z = \frac{1}{2} mR^2 = \frac{1}{2} \times 153.9 \times 0.345^2 = \mathbf{9.159}$ kg.m^2

MI of the same about y and z-axes, $\bar{I}_x = \bar{I}_y = \frac{1}{12} m(3R^2 + h^2)$

$$\bar{I}_x = \bar{I}_y = \frac{1}{12} \times 153.9 \times (3 \times 0.345^2 + 0.3937^2) = \mathbf{6.567} \text{ kg.m}^2$$

The C.G of this unit is located 0.51 m aft of the C.G of the vehicle and is above the C.G by 0.04 m. The moment of inertia of the same unit w.r.t the C.G of the vehicle is:

$$I_{CGx} = I_x + m \times (y^2 + z^2)$$
$$= 9.159 + 153.9 \times 0.04^2 = \mathbf{9.405}\ \text{kg.m}^2$$
$$I_{CGy} = I_y + m \times (x^2 + z^2)$$
$$= 6.567 + 153.9\,(0.51^2 + 0.04^2) = \mathbf{47.27}\ \text{kg.m}^2$$
$$I_{CGz} = I_z + m \times (x^2 + y^2)$$
$$= 6.567 + 153.9\,(0.51^2 + 0.0^2) = \mathbf{47.025}\ \text{kg.m}^2$$

Faired tail portion (FTP) of the aft payload section

The faired tail portion has it C.G at 3.536 m from the tip of the nose.

MI of the FTP[10] about x-axis, I_x = **12.308** kg.m^2

MI of the FTP about x-axis, $I_y = I_z = \frac{1}{4}{*}mr^2 + m.x^2 = \frac{1}{2}{*}12.308 + 60.21 = \mathbf{66.37}$ kg.m^2

This I_y & I_z are MI about the base of the FTP and hence the I_y & I_z about the C.G of the FTP should be identified which is 0.386m aft of the base of FTP.

$$66.37 = \bar{I}_G + 274.2 \times 0.386^2 = \mathbf{25.52}\ \text{kg.m}^2$$

Therefore I_y & I_z about the C.G of the FTP = 25.52

MI about the C.G of the vehicle

$$I_{CGx} = I_x + m \times (y^2 + z^2)$$
$$= 12.308 + 274.2 \times 0.04^2 = \mathbf{12.747}\ \text{kg.m}^2$$
$$I_{CGy} = I_y + m \times (x^2 + z^2)$$
$$= 25.52 + 274.2(1.10^2 + 0.04^2) = \mathbf{355.10}\ \text{kg.m}^2$$
$$I_{CGz} = I_z + m \times (x^2 + y^2)$$
$$= 25.52 + 274.2(1.10^2 + 0.0^2) = \mathbf{354.66}\ \text{kg.m}^2$$

MI of the hemispherical portion of the pressure hull

MI of the hemi-spherical section[11] about *x*-axis,

$$I_{xx} = \frac{2}{5} m.r^2 = \frac{2}{5} \times -117.88 \times 0.34^2 = \mathbf{-5.45}\ \text{kg.m}^2$$

MI of the hemi-spherical section about *y* and *z*-axes passing through the C.G of the hemi-sphere is,

$$I_{yy} = I_{zz} = 0.259.mr^2 = 0.259 \times -117.88 \times 0.34^2 = \mathbf{-3.53}\ \text{kg.m}^2$$

---

[10] See Appendix-II for derivation

[11] **Fowler, B.**, *Dynamics: Engineering Mechanics.* (Inside of last cover page.)

The C.G of the hemi-spherical portion is 0.44 m aft and 0.04m above the C.G of the vehicle.

$$I_{CGx} = I_x + m\times(y^2 + z^2)$$
$$= -(5.45 + 117.88 \times 0.04^2) = \mathbf{-5.639}\ \text{kg.m}^2$$
$$I_{CGy} = I_y + m\times(x^2 + z^2)$$
$$= -[3.53 + 117.88(0.44^2 \times 0.04^2)] = \mathbf{-26.893}\ \text{kg.m}^2$$
$$I_{CGz} = I_z + m\times(x^2 + y^2)$$
$$= -[3.53 + 117.88(0.44^2 \times 0.0^2)] = \mathbf{-26.70}\ \text{kg.m}^2$$

MI of the RDI Workhorse DVL

The RDI Workhorse DVL can be approximated as a cylinder of following dimensions[12]:

Height = 244.5 mm, Diameter = 201.9 mm

Since the instrument is bottom looking, the height h dimension corresponds to the z-axis of the vehicle and I_z corresponds to the MI estimated w.r.t this axis.

MI about x and y axes passing through the C.G of the DVL is

$$\bar{I}_x = \bar{I}_y = \frac{1}{12}m(3R^2 + h^2) = \frac{1}{12}\times 14.5(3\times 0.101^2 + 0.2445^2) = 0.109\ \text{kg.m}^2$$
$$\bar{I}_z = \frac{1}{2}mR^2 = \frac{1}{2}\times 14.5\times 0.101^2 = 0.074\ \text{kg.m}^2$$

---

e. Tail Cone

Dry weight of tail cone = 1.53 kg
Volume of water that can be contained = 0.0111 m3
Weight of water displaced by the volume = 0.0111 x 1025 = 11.378 kg
Displacement of shell in sea water = 0.857x1.025 = 0.878 kg
Actual weight of water that can be contained = 10.50 kg
Total weight of the shell + water = 10.5 + 1.53 = **12.03** kg
Displacement of the inside equipment = 9.9 kg
Net weight of the dry shell + flood water = 12.03 – 9.9 = 2.13 kg
Dry mass of all equipments (*excluding shell*) = 25.05 kg
Total mass of the tail cone section = 2.13 + 25.05 = **27.18** kg

[12] Dimensions taken from: www.rdinstruments.com/datasheets/workhorse_nav_ds_lr.pdf. Accessed 31-03-08.

MI of the Thruster Assembly

The propulsion motor consists of 3 solid cylindrical pieces in tandem. The MI of the entire unit is estimated by clubbing the MIs of each individual piece that has different dimensions.

Dry weight of thruster assembly = 22.6 kg

Displacement of the same = 9.3 kg

This mass is distributed to the 3 cylindrical pieces of the thruster assembly in the ratio of their volume as:

Wt. of V_1 = 12.095 kg

Wt. of V_2 = 8.777 kg

Wt. of V_3 = 1.728 kg

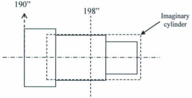

Dimensions of 3 pieces

	l (in)	d (in)	Vol	Wt. / piece
Piece-I	4.35	8.52	0.0041	12.09
Piece-II	6.96	5.74	0.0030	8.78
Piece-III	4.87	3.04	0.0006	1.73

Assumption:

Consider the 3 pieces together as a single solid cylinder (imaginary cylinder) having the same volume and mass with a chosen diameter. The diameter here can be chosen as the diameter of the middle piece (5.74"). The centre of the cylinder can be arbitrarily positioned to coincide with the C.G of the thruster assembly and the length of such a cylinder can be determined knowing the volume.

Total volume of the 3 pieces = 0.0076 m^3

Length of a cylinder of $\phi = 5.74"$ and having the same volume = $\frac{0.0076 \times 4}{\pi \times 0.146^2} = 0.454$ m

The midpoint (CG) of this imaginary cylinder of length 0.454 m and diameter 0.146 m can be assumed to coincide with the C.G of the thruster assembly as given in [10] = 2.11 m aft of the C.G of the vehicle.

MI of the imaginary solid cylinder about its own axes:

$$\bar{I}_x = \frac{1}{2} mR^2 = \frac{1}{2} \times 22.6 \times 0.073^2 = 0.060 \text{ kgm}^2$$

$$\bar{I}_y = \bar{I}_z = \frac{1}{12} m(3R^2 + h^2) = \frac{1}{12} \times 22.6(3 \times 0.073^2 + 0.454^2) = 0.418 \text{ kg.m}^2$$

MI of the thruster assembly about the C.G of the vehicle is:

$$I_{xG} = \bar{I}_x + m\bar{r}^2 = 0.060 + (22.6\text{-}9.3)(0^2 + 0.017^2) = \mathbf{0.064} \text{ kg.m}^2$$

$$I_{yG} = \bar{I}_y + m\bar{r}^2 = 0.418 + (22.6\text{-}9.3)(2.11^2 + 0.017^2) = \mathbf{58.57} \text{ kg.m}^2$$

$$I_{zG} = \bar{I}_z + m\bar{r}^2 = 0.418 + (22.6\text{-}9.3)(2.11^2 + 0.0^2) = \mathbf{58.56} \text{ kg.m}^2$$

Estimation of MI of the Frustum of Tail Cone

In order to estimate the MI of the frustum, the tail cone shell + the flood water is assumed as a single unit of solid mass = 12.03 kg. This works out to a density, r = 1083.78 kg/m^3. The base radii of the frustum are a = 0.1641m and b = 0.0445 m. The method of MI estimation adopted here is by subtracting the MI of the smaller cone of radius 0.0445 m from the bigger cone of radius 0.1641 m.

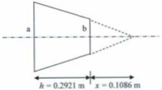

Mass of cone-1 = 12.2489 kg

Mass of cone-2 = 0.2443 kg

C.G of the frustum from the base (a) = 0.0955 m.

The MI of the Cone are:

$$I_{xx} = \frac{3}{10} mr^2 = 0.0988$$

$$I_{yy} = I_{zz} = \frac{3}{20} mr^2 + \frac{3}{80} m(h+x)^2 = 0.1231 \quad \text{kg.m}^2$$

Distance of the C.G of the frustum from the C.G of the vehicle

= 2.083 – (0.69+2.46+0.9906+0.0955) = -2.153 m

Thus the mass of the conical frustum with flood water acts at a distance 2.153 m aft of the C.G of the vehicle.

MI of the frustum w.r.t the C.G of the vehicle.

$I_{xG} = I_{xx} + M.d^2 = 0.0988 + 12.03(0^2 + 0.017^2) = 0.2$ kg.m^2

$I_{yG} = I_{yy} + M.d^2 = 0.1231 + 12.03(2.15^2 + 0.017^2) = 56.113$ kg.m^2

$I_{zG} = I_{zz} + M.d^2 = 0.1231 + 12.03(2.15^2 + 0^2) = 56.109$ kg.m^2

Moment of Inertia of the *MUN Explorer* AUV

I_{xx}	86.08	kg.m^2
I_{yy}	1881.71	kg.m^2
I_{zz}	1877.19	kg.m^2
I_{xy}	0.98	kg.m^2
I_{yz}	0.29	kg.m^2
I_{zx}	3.09	kg.m^2